Self-Assembly Peptide based Double-Network Hydrogel

A thesis submitted to the University of Manchester for the degree of

Doctor of Philosophy

in the Faculty of Science and Engineering

2023

Zixuan Liu

Department of Chemical Engineering

School of Engineering

Content

List Of Tables

List Of Figures

Abbreviations

SAP: Self-assembly Peptide

SAPH: Self-assembly Peptide Hydrogel

DN: Double-network

pI: Isoelectric point

Oligo: Oligonucleotide

Material

KF8K: Peptide sequence: KFEFKFEFKK

F8: Peptide sequence: FEFKFEFK

F9: Peptide sequence: FEFKFEFKK

V8: Peptide sequence: VEVKVEVK

V9: Peptide sequence: VEVKVEVKK

A8: Peptide sequence: AEAKAEAK

FITC: Fluorescein 5-isothiocyanate

Dabcyl: 4-((4-(dimethylamino)phenyl)azo)benzoic Acid

TCEP: tris(2-carboxyethyl)phosphine

ACN: Acetonitrile

TFA: Trifluoroacetic Acid

DMSO: Dimethyl sulfoxide

THT: Thioflavin T

Mal: Maleimide

Equipment

CD: Circular Dichroism

FTIR: Fourier Transform Infra-Red

XRD: X-ray diffraction analysis

TEM: Transmission electron microscope

AFM: Atomic force microscopy

RP-HPLC: Reversed-Phase High-Performance Liquid Chromatography

MALDI-TOF: Matrix-assisted laser desorption/ionization-time of flight mass spectrometry

NMR: Nuclear Magnetic Resonance

Abstract

Hydrogels are a type of material composed of a network of hydrophilic polymer chains that can absorb and retain large amounts of water. They have several advantages, including high water content, durability and biocompatibility. Therefore, this makes them suitable for use in medical applications such as controlled drug release and matrix for tissue engineering.

In the past decade, peptide (short chains of amino acids) has become to a prevalent material for preparing hydrogels. Compared to the synthetic compounds and other natural molecules, sequence designability, precise identification, structural rigidity and minimal toxicity are the advantages of peptide as blinding blocks of hydrogel. Through the physical interactions between peptide monomers, well-designed peptides self-assemble to the three-dimensional networks, resulting in the formation of the hydrogel.

KF8K (sequence: KFEFKFEFKK) is an example of a self-assembling peptide hydrogel. This peptide self-assembles to β-sheet to form the fibres and network. It has several unique properties, involving biocompatibility, biodegradability, and tunable mechanical properties, which make it useful in various biomedical applications, such as tissue engineering and drug delivery. However, there are still several shortcomings in the KF8K hydrogel, including the unsatisfied mechanical stiffness for cell culture.

Therefore, in this project, the KF8K self-assembly peptide was blended with other different sequence self-assembly peptides (SAPs), gelatin and oligonucleotide to produced the blending hydrogels with an improved but controllable stiffness,

First, the KF8K peptide was physically mixed with the similar but different sequence peptide (F9) and same sequence but opposite chirality peptide (D-KF8K) for blending hydrogel. The blending hydrogels underwent the FITC-DABCYL fluorescent quenching reaction in order to explore how the different peptide monomers assemble. The F9 monomers were found to be homogeneously assembled with KF8K monomers while D-KF8K monomers were separated with L-KF8K monomers in the fibre. Unfortunately, there was not stiffness improvement observed in L-KF8K and F9 or D-KF8K blending hydrogel. However, a homogenous stiffness hydrogel with separately assembled monomers was accessible by blending the L-KF8K and D-KF8L.

Subsequently, KF8K and gelatin blending hydrogel formed a double-network structure with an improved but controllable stiffness. The two networks were seen under microscopy. Blended hydrogels were also characterised in term of stiffness between 10 to 40 °C to prove the mixture did not significantly affect the temperature responsibility of gelatin. The blending hydrogel was observed with decrease stiffness with increased temperature.

Finally, there still was stiffness improvement found in the KF8K and oligonucleotide blending hydrogel. The oligonucleotide monomers are also able to self-assemble to chains by Watson-Crick rule. The chains were connected to the KF8K fibres by the peptide-oligonucleotide conjugate. Therefore, the KF8K fibres were further linked by oligonucleotide chains for a higher stiffness.

Declaration

I declare that this research is the result of my own work except as cited in the references and no portion of the work in the thesis has been submitted in support of an application for another degree or qualification of this or any other university or other institute of learning.

Copyright Statement

i. The author of this thesis (including any appendices and/or schedules to this thesis) owns certain copyright or related rights in it (the “Copyright”) and s/he has given The University of Manchester certain rights to use such Copyright, including for administrative purposes.

ii. Copies of this thesis, either in full or in extracts and whether in hard or electronic copy, may be made only in accordance with the Copyright, Designs and Patents Act 1988 (as amended) and regulations issued under it or, where appropriate, in accordance with licensing agreements which the University has from time to time. This page must form part of any such copies made.

iii. The ownership of certain Copyright, patents, designs, trademarks and other intellectual property (the “Intellectual Property”) and any reproductions of copyright works in the thesis, for example graphs and tables (“Reproductions”), which may be described in this thesis, may not be owned by the author and may be owned by third parties. Such Intellectual Property and Reproductions cannot and must not be made available for use without the prior written permission of the owner(s) of the relevant Intellectual Property and/or Reproductions.

iv. Further information on the conditions under which disclosure, publication and commercialisation of this thesis, the Copyright and any Intellectual Property and/or Reproductions described in it may take place is available in the University IP Policy (seehttp://documents.manchester.ac.uk/DocuInfo.aspx?DocID=24420), in any

relevant 12 Thesis restriction declarations deposited in the University Library, The University Library's regulations (see http://www.library.manchester.ac.uk/about/regulations/) and in The University's policy on Presentation of Theses.

Acknowledgements

First of all, I would like to express my heartfelt gratitude to all the individuals who have contributed to the completion of this thesis.

My sincere thanks and appreciation go to my supervisor, Prof. Aline Miller and Prof. Alberto Saiani. whose insightful suggestions and encouragement have given me much guidance in PhD research. It has been a great privilege and joy to have them as my mentor. I am honored to have benefited from their exceptional personality and diligence, and I will always treasure their teachings. My gratitude to them knows no bounds.

I would like to express my sincere gratitude to Dr. Cosimo Ligorio, Dr. Xinyi Zhu and Dr. Xiaoxia Huang for their unwavering patience, assistant and support. I would also like to thank all the members of the Polymers and Peptides groups for their support, Dr. Siyuan Dong, Dr Cong Ding, Ms., Andong Liu, Mr. Albert Ginjaume and Mr. Niall Mahon for their help and support, and for making an enjoyable studying and researching environment.

In addition, many thanks go to my family and friends for their unfailing love and unwavering support.

Finally, I am really grateful to all those who devote much time to reading this thesis and give me much advice, which will benefit me in my later study.

1. Chapter 1. Introduction

1.1. General Introduction

Hydrogels are a fascinating class of materials that have garnered significant attention in recent years due to their unique properties and potential applications in various fields [1]. It is a three-dimensional network of hydrophilic polymers that can absorb large amounts of water, resulting in a gel-like material. They are essentially water-swollen polymer networks that can be engineered to possess specific mechanical, chemical, and physical properties. Hydrogel can be designed to have the biocompatibility and similar mechanical properties to soft tissues and are therefore used in a variety of applications such as wound dressings, drug delivery systems, and contact lenses [2]. Additionally, hydrogels have been found to be used in zwiculture [3], where they are used as soil conditioners to retain moisture in the soil. With their high-water content and ability to mimic the behaviour of living tissues, hydrogels have become an important material in various fields.

Hydrogels can be classified by their raw materials, including synthetic hydrogels and natural hydrogels. The former a made from synthetic polymers such as polyethylene glycol (PEG) and polyacrylamide (PAA) [4]. One of the key advantages of synthetic hydrogels is their ability to be engineered to possess specific properties such as swelling ratio, mechanical strength. However, there are some potential limitations of synthetic hydrogels, such as the potential for toxicity and immune reactions. Therefore, natural hydrogels are proposed, for example, collagen, alginate, and chitosan. They are biocompatible and biodegradable, making them ideal for use in biomedical applications.

So far, the use of self-assembly to produce sequence-dependent materials has become a prevalent strategy in recent years [5] due to its ability to produce highly ordered structures. Hydrogels are an example of what can be prepared by self-assembly. Self-assembly is a bottom-up approach that produces materials through the spontaneous assembly of ingredients under suitable triggers, simplifying the material production process by merely mixing disordered molecules and applying a stimulus. The self-assembly is driven by noncovalent interactions such as hydrophobic forces, hydrogen bonds, and electrostatic forces. These weaker physical interactions determine the thermodynamic properties of the material and result in a thermodynamic equivalent. The self-assembled structures are usually highly ordered, unlike those produced by chemical reactions [6], making self-assembly widely used in the preparation of sequence-dependent materials [7].

Self-assembly peptide hydrogels have been attracting increasing research interest due to their potential applications in biomedical fields [8] and their key role in amyloid diseases [9]. Designed peptides self-assemble into regular structures under suitable triggers, resulting in the formation of fibres, networks, and hydrogels. Researchers have produced a series of self-assembly peptide hydrogels based on protein secondary structures, such as α-helix [10] and β-sheet [11]. The secondary structure determines the three-dimensional arrangement of local segments in long peptide chains and is maintained by physical interactions. The hydrogen bond is one of the most common ones maintaining the secondary structures, which also plays a role in driving the self-assembly [12]. For instance, in α-helix, hydrogen bonds between the oxygen atoms in carboxyl groups and hydrogen atoms in amide groups along the helix direction maintain the helix structure. Besides, hydrogen bonds between carboxyl and amide groups also drive the formation of β-sheet.

A family of β-sheet relying on self-assembly peptide hydrogel has been well-researched recently [13,14]. β-sheet is one of the most general secondary structures. Excellent biological properties, recoverability and easy preparation are its advantages [15]. KF8K (sequence: KFEFKFEFKK) is a typical example of this family. With triggering from suitable pH, KF8K peptides fold to β-sheets and form hydrogel immediately. The self-assembly and hydrogelation of KF8K occur at a pH of 7. For most of biological and medical applications, a neutral pH is desired [16]. However, a shortcoming of KF8K hydrogel is its stiffness for cell culture. Therefore, to achieve a self-assembly peptide hydrogel with both neutral hydrogelation pH and improved stiffness, double-network hydrogels have been proposed as a potential solution.

In recent years, there has been a huge development in the research about double-network (DN) hydrogels with good biocompatibility and mechanical properties [17]. The main research directions aim to improve the poor mechanical properties of conventional hydrogels and to expand their potential applications in various fields [18]. Recent research includes fully chemically cross-linked DN hydrogels, hybrid physical/chemical cross-linked DN hydrogels and fully physically cross-linked DN hydrogels [17]. These DN hydrogels offer significant advantages in terms of mechanical properties, structure and biocompatibility.

1.2. Aims

Therefore, this project attempts to create double-network hydrogels based on the β-sheet family self-assembly peptide. The double-network (DN) hydrogels will chase a higher and controllable mechanical strength compared to the basic self-assembly peptide hydrogel. Meanwhile, the double-network hydrogels are also looking forward to holding the excellent

biological properties of the peptide hydrogel so that the hydrogel can be used as the matrix for cell culture and drug deliver.

Besides, this project still tries to explore the change in the microstructure of self-assembly peptide and its fibre morphology after blending in DN hydrogel. The β-sheet is the key structure of the self-assembly peptide in that the variations in it will be clearly explored.

Finally, it is also planned to explore the potential applications for the double-network hydrogels, for example, as the ink for 3D-bioprinting.

Reference

[1] Ahmed E M. Hydrogel: Preparation, characterization, and applications: A review. Journal of advanced research, 2015, 6(2): 105-121.

[2] Sharma S, Tiwari S. A review on biomacromolecular hydrogel classification and its applications. International journal of biological macromolecules, 2020, 162: 737-747.

[3] Neethu T M, Dubey P K, Kaswala A R. Prospects and applications of hydrogel technology in agriculture. Int. J. Curr. Microbiol. App. Sci, 2018, 7(5): 3155-3162.

[4] Van Berkum S, Dee J T, Philipse A P, et al. Frequency-dependent magnetic susceptibility of magnetite and cobalt ferrite nanoparticles embedded in PAA hydrogel. International journal of molecular sciences, 2013, 14(5): 10162-10177.

[5] Ikkala O, ten Brinke G. Functional materials based on self-assembly of polymeric supramolecules. science, 2002, 295(5564): 2407-2409.

[6] Cölfen H, Mann S. Higher-order organization by mesoscale self-assembly and transformation of hybrid nanostructures. Angewandte Chemie International Edition, 2003, 42(21): 2350-2365.

[7] Knorowski C, Travesset A. Materials design by DNA programmed self-assembly. Current Opinion

in Solid State and Materials Science, 2011, 15(6): 262-270.

[8] Smith K H, Tejeda-Montes E, Poch M, et al. Integrating top-down and self-assembly in the fabrication of peptide and protein-based biomedical materials. Chemical Society Reviews, 2011, 40(9): 4563-4577.

[9] Gazit E. A possible role for π-stacking in the self-assembly of amyloid fibrils. The FASEB Journal, 2002, 16(1): 77-83.

[10] Kulkarni K, Habila N, Del Borgo M P, et al. Novel materials from the supramolecular self-assembly of short helical β3-peptide foldamers. Frontiers in Chemistry, 2019: 70.

[11] Saiani A, Mohammed A, Frielinghaus H, et al. Self-assembly and gelation properties of α-helix versus β-sheet forming peptides. Soft Matter, 2009, 5(1): 193-202.

[12] Bordo D, Argos P. The role of side-chain hydrogen bonds in the formation and stabilization of secondary structure in soluble proteins. Journal of molecular biology, 1994, 243(3): 504-519.

[13] Gao J, Tang C, Elsawy M A, et al. Controlling self-assembling peptide hydrogel properties through network topology. Biomacromolecules, 2017, 18(3): 826-834.

[14] Wychowaniec J K, Moffat J, Saiani A. Quantitative nanomechanical properties evaluation of a family of β-sheet peptide fibres using rapid bimodal AFM. Journal of the mechanical behavior of biomedical materials, 2021, 124: 104776.

[15] Wychowaniec J K, Smith A M, Ligorio C, et al. Role of sheet-edge interactions in β-sheet self-assembling peptide hydrogels. Biomacromolecules, 2020, 21(6): 2285-2297.

[16] Michl J, Park K C, Swietach P. Evidence-based guidelines for controlling pH in mammalian live-cell culture systems. Communications biology, 2019, 2(1): 1-12.

[17] Haque M A, Kurokawa T, Gong J P. Super tough double network hydrogels and their application as biomaterials. Polymer, 2012, 53(9): 1805-1822.

[18] Chen Q, Chen H, Zhu L, et al. Fundamentals of double network hydrogels. Journal of Materials Chemistry B, 2015, 3(18): 3654-3676.

2. Chapter 2. Literature Review

This section attempts to provide a literature review of the self-assembly peptide-based double-network hydrogel. The literature review helps to provide a historical and theoretical context to understand the evolution of ideas and theories in the current development of hydrogel and double network. The areas where there is a lack of knowledge and information can define what needs to be studied in more detail.

Besides, the β-sheet relying self-assembly peptide family is employed as the first and basic network in this project. Therefore, the present achievement in the field of the β-sheet self-assembly peptide hydrogel is demanded to be identified clearly to demonstrate that there is a gap about the self-assembly peptide hydrogel in current knowledge that needs to be filled. It indicates the targets in this project.

Finally, the literature about the current hydrogel materials allows to choose the most appropriate methods and material in the project. The well-researched biological hydrogelation material is the potential candidates for the second network ingredient in this project. It provides the necessary background and context to conduct meaningful and impactful research.

In summary, the literature review in this chapter reveals the result and shortcoming of present researching, giving the detail about the reliable researching target, methods, and materials.

2.1. Hydrogel

A hydrogel is a three-dimensional network of hydrophilic polymer chains that can absorb and retain large amounts of water or biological fluids. The polymer chains are crosslinked to form a gel-like structure that can hold the water molecules within its network. Hydrogels first appeared in 1954 when Wichterle and Lim created the first synthetic hydrogels [1]. In the past 50 years, hydrogels have received considerable attention due to hydrogels containing a significant amount of water but do not dissolve in water [2]. This unique feature is due to the hydrophilic groups in the hydrogel's hydrophobic backbone. These hydrophilic groups interact with water molecules, resulting in high water absorbance. Meanwhile, the hydrophobic backbone forms a network that contributes to the insolubility of hydrogels. The balance driven by the interactions between the hydrogel's network and fluid molecules allows for the expansion of the network. The intensity of these interactions also determines some of the properties of the produced hydrogel, including diffusion characteristics and mechanical strength [3].

The formation of hydrogel typically includes three fibre crosslinking mechanisms involving physical entanglements, ionic interactions, and chemical crosslinks shown in figure 2.1 [4]. A series of mechanisms are involved in the physical entanglements, including thermal condensation (gelatin) and self-assembly. For example, thermodynamic factors such as solubility changes and the hydrophobic interaction can drive fibre entanglement and cross-link. Meanwhile, the ionic interaction by coulomb force also allows the ions to act as a bridge connecting the polymers together. Further, when the chemical bonds connect the monomers, the method is called chemical cross-linking. However, at present, there has been renewed interest in cross-linking through the combination of various interactions, for example, self-assembly [5].

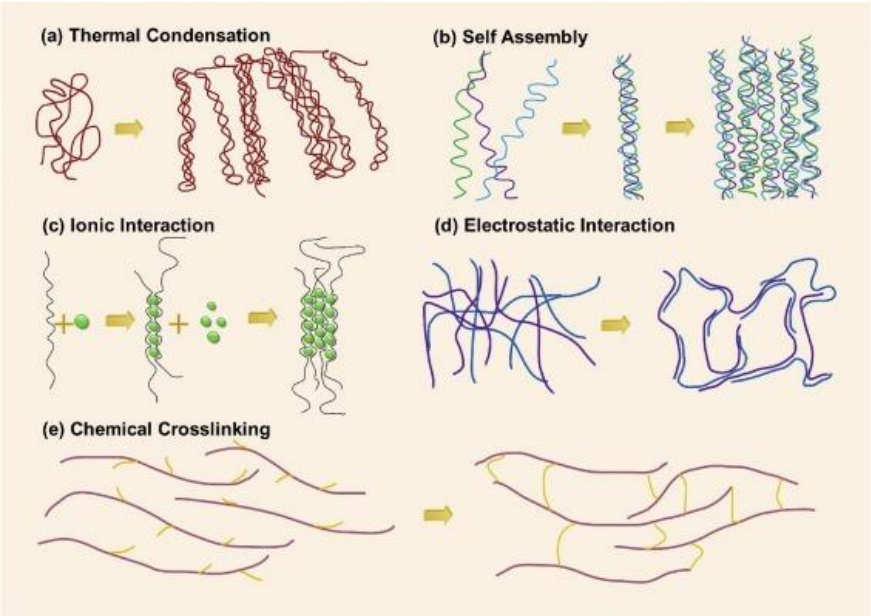

Figure 2-1 The crosslinking strategies for hydrogel [4]

Therefore, because of the difference between physical and chemical interactions, Hydrogels prepared by different mechanisms and strategies have different properties [6]. Currently, the shortcoming of physical entanglement in hydrogel is that the properties of hydrogel highly depend on the inherent properties of the fibre's monomer. In the design of physical cross-linking hydrogels, the choice of polymer decides the properties of the hydrogel. The interactions between the monomers must be strong enough to maintain the semi-permanent network. Hydrophobic, electrostatic and hydrogen bonding are example forces that connect the monomers and maintain the network. Therefore, since most physical interaction is reversible, the family of hydrogels can rebuild the interaction and structure spontaneously after breaking, including hydrogen bonds and ion coulomb force.

As an alternative, hydrogels formed by chemical formation methods show better versatility and are easier to control their properties. Chemical crosslinking utilises covalent bonding between polymer molecules, creating connection. Crosslinking is formed by the addition of small crosslinker molecules to finish polymer-polymer conjugation, photosensitisers, or enzyme-catalysed reactions.

However, high strain recoverability is the main shortcoming of chemical crosslinking hydrogels. The chemical bonds are commonly short of reversibility, needing activation energy to complete the reaction.

Natural hydrogel materials have been well-investigated and researched for a long time. In agriculture, they can slowly release pesticides and agrochemicals such as phosphate fertilisers [7]. They also increase efficiency and reduce runoff while improving water retention in drier soils such as sandy loam. Natural hydrogels are also popular in food, for example, gelatin in jelly and cake preparation. The applications in tissue engineering are its new development. The advantage of natural hydrogel includes well biocompatibility, biodegradability and non-toxicity. These materials include agarose, methylcellulose, hyaluronic acid, gelatin, chitosan, elastin-like polypeptides and other polymers of natural origin [7].

Recently, synthetic hydrogels have been proposed and well-researched because their functions and properties can be well-defined through modification [8]. Initially, research on synthetic hydrogels focused on relatively simple chemical cross-linked polymer networks to study their fundamental characteristics, such as swelling/deswelling kinetics and equilibrium. The applications of synthetic hydrogels are also a prevalent research topic, including in ophthalmology and drug delivery.

At present, synthetic hydrogels based on natural molecules are receiving increasing attention from researchers [9]. It is seen as combining the advantages of both natural and synthetic hydrogels. Additionally, as hydrogel research develops, research interests have shifted from simple to "responsive" networks. At this stage, various hydrogels have been developed that can respond

to changes in environmental conditions, such as pH, temperature, and electric and magnetic fields [10].

Hydrogels have been studied for various applications, including soft contact lenses [11], and drug delivery. By varying the concentration of polymer monomer or crosslinking density, the storage modulus of a hydrogel can be controlled between 10 Pa to 3 MPa, in the range of about five orders of magnitude [12]. The stiffness variability makes hydrogels also attractive for biomedical applications, where matching the mechanical properties of the implant to the surrounding tissue is critical [13].

Currently, hydrogel is one of the primary materials used in biological and medical applications [14]. Its porous network structure and excellent water absorption make it ideal for mimicking the microenvironment of human tissue. By adjusting its properties, a hydrogel can mimic different tissues and organs. Biosensing, drug delivery, cancer treatment, and regenerative medicine [15] have been popular applications for hydrogel in recent decades. Recently, evidence suggested that polymer-modified natural hydrogel has both wide functions and excellent biological properties, making it popular in the biological and medical fields. For example, natural gelatin has been modified by the methacryloyl group to Gelatin methacryloyl (GelMA) [16] through a chemical reaction.

GelMA hydrogels closely resemble some basic properties of native extracellular matrix (ECM) due to the presence of cell attachment and matrix metalloproteinase-responsive peptide motifs [17]. That two compositions allow cells to proliferate and spread in GelMA-based scaffolds. When exposed to light irradiation, GelMA cross-links to form hydrogels with tunable mechanical properties [17].

2.2. Peptide

Peptides are compounds formed by the linking of α-amino acids through peptide bonds. They are intermediate products of protein hydrolysis. When two amino acid molecules are dehydrated and condensed together, the resulting compound is called a dipeptide. Analogously, there are also tripeptides, tetrapeptides, pentapeptides, etc. A peptide consisting of three or more amino acid molecules is known as a polypeptide.

Amino acids are the building blocks of proteins and peptides. They are organic compounds that contain both an amino group ($-NH_2$) and a carboxyl group (-COOH). The side chains decide the type of amino acids. Amino acids generally exist in the form of zwitterions in aqueous solutions or crystals. A zwitterion refers to an amino acid molecule containing both NH^{3+} and COO^- ions, which can release or accept protons. This makes amino acids amphoteric, meaning they can have either a positive or negative charge depending on the pH of their environment. There is a specific pH called the isoelectric point (pI). The positive and negative charges are equal at that pH value, resulting in a zero net charge. The pI is important in peptides and proteins because the charge state of the amino acids affects the 3D structure and properties of the peptide or protein.

On the other hand, amino acids can be divided into α-, β-, γ-, and w-... amino acids based on the location of the amino group on the carbon chain. α-amino acids, which are the building blocks of natural peptides and proteins, are compounds in which the amino group is attached to the α-carbon atom. α-carbon atom is the carbon atom next to the carboxyl group. They are typically colourless crystalline solids with melting points higher than those of corresponding carboxylic acids or amines, typically between 200-300 °C [18]. All amino acids, except glycine, are optically

active. The amino acids found in natural proteins are all L-form. They are usually soluble in water but insoluble in organic solvents.

Peptides widely exist in the human body [19] which are involved in hormones, nerves, cell growth, and reproduction. They play a crucial role in regulating physiological functions [20], activating enzyme systems [21], controlling DNA transcription [22], and affecting specific protein synthesis. Peptides also act as neurotransmitters and transportation tools for nutrients, vitamins, and other beneficial elements to various cells, organs, and tissues in the body.

Despite peptides being much less long than proteins, the secondary structure of proteins can be observed in polypeptides. The secondary structure is the partial 3D structure of a peptide chain, including α-helices, β-sheets, and β-turns. The combination of many secondary structure units consists of the 3D structure of a whole peptide chain, which is the tertiary structure of a protein. α-helix is a right-hand helix block maintained by hydrogen bonds. The hydrogen bond is formed between the amide hydrogen atom of each residue in the same peptide chain and the carbonyl oxygen atom on the fourth residue located after it. The side chains of all amino acids in the α helix are placed outside the framework except the proline. α-helix still involves several types based on the parameter difference, such as the radius or number of amino acids in each circle.

Another common secondary structure is the β-sheet. In typical β-sheets, two or more amino acid chains (peptide chains) or different parts of the same peptide chain form a parallel or anti-parallel arrangement to form a "strand." Hydrogen bonds hold these strands together and can be either parallel or antiparallel. If the C-terminus (the end of an amino acid chain with carboxyl group) of all strands is on one side, it is called a parallel β-sheet. Otherwise, it is an anti-parallel β-sheet (Figure 2.2). There are differences in hydrogen bond angles and length between the two β-

sheets. In the antiparallel β-sheet, the hydrogen bond is parallel. As a result, without the angle, the anti-parallel β-sheet is more stable (e.g., high temperature). The best example of the β-sheet-rich protein is silk fibroin, which is one of the most potent natural materials [23]. Additionally, there are specific β-sheets such as β-turns, where proline is an essential amino acid. Since the side chain of proline contains a ring structure, there is an angle between the amine group and the carboxyl group of lysine. Usually, in protein, the β-turn plays the role of a bridge connecting the α helix and the β-sheet.

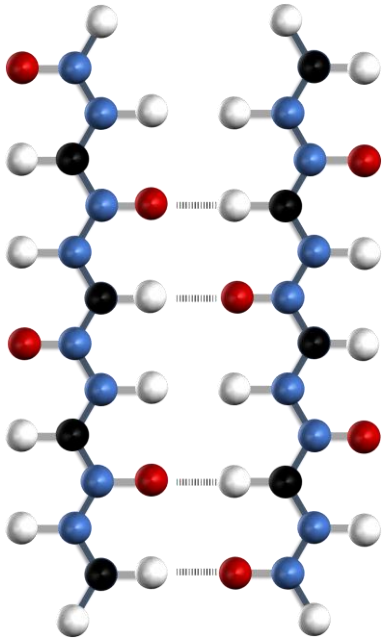

Figure 2-2 Structure of anti-parallel β-sheet

Combining various types of secondary structures can result in a large number of three-dimensional structures for peptide chains. These structures, when combined, comprise a complex protein.

Additionally, the development of designed sequence peptides has driven demand for synthetic peptides. One popular method for synthesising peptides is solid phase peptide synthesis (SPPS), proposed by R. Bruce Merrifield [24]. The steps for SPPS are given in figure 2.3. This method

uses chloromethyl polystyrene resin as an insoluble solid-phase carrier. An amino acid, whose amino group is protected by a blocking group (X), is covalently linked to the solid-phase carrier. Under the action of trifluoroacetic acid, the protective group of the amino group is removed. Therefore, the first amino acid is attached to the solid phase carrier. The carboxyl group of the second amino acid is then activated by N, N'-dicyclohexylcarbodiimide (DCC, Dicyclohexylcarbodiimide). The amino group of the second amino acid is also blocked by (X). The amino group of the first amino acid reacts with the carboxyl group in the second amino acid, forming peptide bonds, resulting in a dipeptide. This peptide bond formation reaction is repeated to grow the peptide chain from the C-terminus to the N-terminus until the desired length of the peptide chain is created. Lastly, the protecting group X is removed, and the ester bond between the peptide chain and the solid support is hydrolysed with HF to obtain the synthesised peptide.

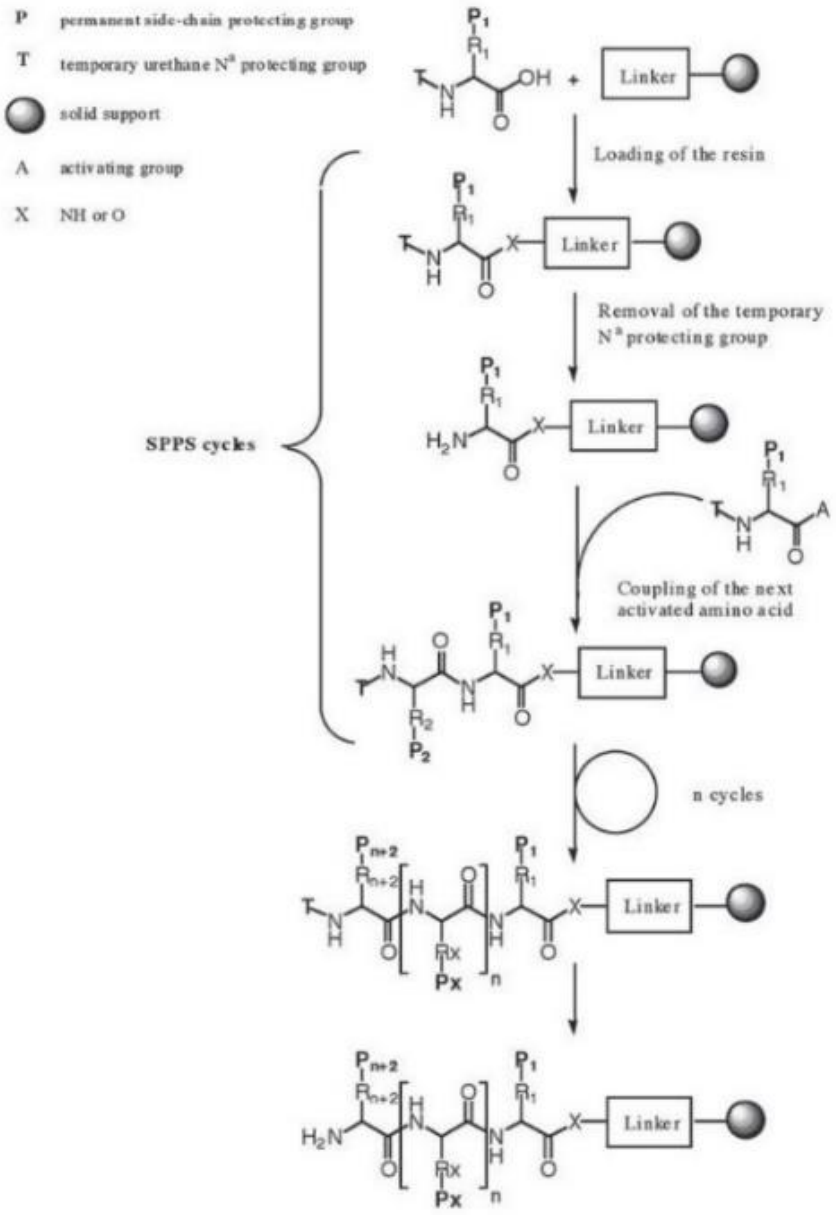

Figure 2-3 Process of solid-phase peptide synthesis [25]

The advantages of the solid-phase synthesis are primarily reflected in the fact that both the initial reactants and products are attached to the solid-phase support. This allows all reactions to be carried out in a single reaction vessel, making it convenient for automated operations. Additionally, high-yield products can be obtained by using excess reactants, and the product is easily separable.

2.3. D-Amino Acid Peptide

In the 20 natural amino acids, except for Glycine, amino acids are optically active due to the presence of chiral carbons. In biochemistry, based on glyceraldehyde, they are divided into D-type and L-type according to the absolute configuration of the molecule. The amino acids that make up natural proteins are all L-shaped.

Every chiral molecule has a mirror symmetry isomer. The isomers are unable to be superimposed but closely linked to each other, similar to two hands. Typically, the carbon atom with four different substituents is accepted as one of the most common chirality centres in biological macromolecules. In amino acids, the carbon atom connects to a carboxyl group, an amide group, a hydrogen atom and a side chain. Therefore, the amino acid is a chiral molecule. The side chain of Glycine is also a hydrogen atom, which means it is not a chiral molecule. To distinguish the two opposite molecules, the isomer causes the plane of polarised light rotating clockwise is called dextrorotatory. On the contrary, the counter-clockwise one is said to be levorotatory. Generally, the L- and D-isomers have the same physical and chemical properties except for the rotation direction of polarised light and their interactions with other chiral molecules.

A D-amino acid is an amino acid in which the steric carbon α of the amino group has the D configuration. For the amino acids in most natural proteins and peptides, their carbon has the L configuration. However, D-amino acids are occasionally observed in proteins derived from ribosome modification [26]. They are defined as a new type of post-translational response that transforms L-amino acids into D-configuration. Much research suggests that bacteria and microorganisms produce and release D-amino acids originally [27]. Meanwhile, a growing body of

literature has investigated the conversion of L-amino acids to D-amino acids, which is widely observed in the food industry [28]. High temperatures, strong acids, or alkalis are accepted to drive the conversion process.

At present, there is a large volume of published studies describing the role of D-amino acids as drugs. D-serine is reported to represent the endogenous ligand for the binding site in brain areas, and it is considered to be liked with schizophrenia. This means D-serine holds the potential to diagnose and treat schizophrenia [29]. Several studies also reported a link between D-alanine and cellular osmotic pressure. Alzheimer's patients were found to have over two times higher D-alanine concentrations compared to the control group [30]. Additionally, D-proline and D-Leucine are also observed to have links to the human nervous system and hormone secretion [31]. On the other hand, D-amino acid-containing antibiotics are also used to overcome drug resistance [32].

Due to the fact that most proteins in vivo are composed of L-amino acids, a replacement by D-amino acid in proteins is proposed as a strategy to extend the lifetime of proteins in drugs and drug delivery [33]. Well-designed D-amino acid peptides self-assemble to form a hydrophobic core that stores the drug. The fibre network helps the slow release of drugs while also protecting them against proteolysis in vivo [34]. Drugs encapsulated in D-amino acids forming hydrogels have shown better selectivity and antitumor efficiency with lower toxicity [35]. Another strategy is to chemically connect drugs to D-peptide fibres, and it is reported that the presence of D-peptide networks increases the drug's selectivity to target cells [36].

The wide application of D-amino acid-based hydrogels in drug delivery has driven more research on the influence of the D configuration on fibres and networks in hydrogels. Designing

hydrogel based on the protein's secondary structure is one of the most popular strategies at present.

As a result, the impact of D-amino acids on the secondary structure is attracting increasing research. Literature has investigated the influence of an L-to-D amino acid replacement in an α-helix peptide. In that peptide, a single D-amino acid presented in a 14-mer amphipathic L-peptide completely disrupted the formation of α-helix and hydrogel. The result suggests that consistent chiral amino acid is asked in the assembly of α-helix [124]. In the case of β-sheet family peptides, the introduction of D-amino acids also disrupted the formation of β-sheet. However, the influence varies in different sequence peptides. The replacement in di-phenylalanine disrupted the self-assembly as intermolecular interaction was reduced and interfered [37]. A well-designed 16-mer peptide was also reported to completely lose its β-sheet after the introduction of D-amino acid [38]. L- and D- hybrid peptides show the worse formation of β-sheet and lose hydrogelation.

2.4. Self-assembly

Typically, self-assembly is characterised by three main features: 1) the self-assembled structure must be more ordered than the individual components; 2) the self-assembly process is driven by weaker physical interactions, such as Van der Waals forces and hydrogen bonds, rather than chemical bonds; 3) the basic unit of construction includes not only atoms and molecules, but also nano- and micro-scale structures with different chemical compositions, structures, and functions.

Molecular self-assembly is accepted as a process of molecular rearrangement under thermodynamic equilibrium conditions where molecular recognition, components, and solvents play a critical role in maintaining the assembled structure (figure 2.4). In the thermodynamic

equilibrium of self-assembly, it is typically seen as the result of a balance between depletion attraction and interparticle dipole-dipole interactions. The depletion attraction is an entropic force that is caused by the overlapping of molecules' excluded volumes, creating more space for dissolution [41]. The interparticle dipole-dipole interactions also contribute to the self-assembly process [42].

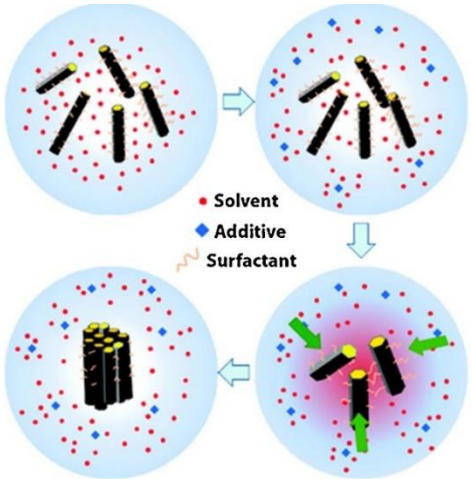

Figure 2-4 The steps of self-assembly Top left: self-assembly molecules were dissolved into solvent. Top Right: Additive was added into the assembly system. Below Right: target molecules start to assemble. Below Left: the finish of self-assembly. [40]

Molecular recognition refers to the process in which a specific receptor selectively binds to a substrate or donor to produce a specific function, including the mutual recognition of geometric size and shape between molecules. The non-covalent interactions, such as hydrogen bonds and π-π interactions, also contribute to the recognition. By utilising the recognition and binding characteristics of molecules, targeted structures can be designed with high efficiency and selectivity. Additionally, when multiple molecules with recognition sites are combined, they will find the most stable and closest position to each other and form aggregates of higher-order structures that surpass the function of a single molecule.

The components in self-assembly ingredients significantly impact the structure of self-assembled supramolecular aggregates because they provide the sites that determine the interactions driving the self-assembly. For example, hydrophobic groups provide hydrophobic force, and hydroxyl groups provide hydrogen bonds [43]. The relationship between the component and its corresponding interaction allows the designing of materials with specific assembly structures. Ideally, a well-designed component can self-assemble into different structures by changing the environmental conditions, such as net charge.

On the other hand, most studies on self-assembled systems are carried out in solution. The solvent plays a crucial role in forming self-assembled systems because it provides mobility for molecules to assemble. Both the nature and the structure of the solvent can lead to significant changes in the self-assembled architecture. Any solvent that breaks non-covalent bonds may affect the self-assembly process, including the type, density, pH, and concentration of the solvent [44].

2.5. Self-assembly Peptide Hydrogel (SAPH)

The literature has highlighted the self-assembly of well-designed peptide molecules for functional materials, such as fibres, 3D scaffolds, membranes, and particularly hydrogels [45]. Self-assembly of hydrogels is typically achieved by physical interactions such as Van der Waals forces, hydrophobic bonds, and Coulomb forces. Chemical bonds are also partially involved in the assembly, like ionic and covalent bonds. However, most peptide hydrogels are formed by noncovalent bonds due to their reversibility [46]. Under the interactions, well-designed peptide chains are able to fold into specific structures with target functions.

As a material formed by natural peptides, the biological properties are considered as one of the main benefits of peptide hydrogel. Firstly, much research proves the excellent biodegradability of self-assembly peptide hydrogels by enzymes, such as proteases [47]. Proteases disrupt peptide bonds in proteins and polypeptides to release free amino acids or shorter peptides. This means that the self-assembly peptide hydrogel (SAPH) does not require additional operations after being injected in vivo. Furthermore, when the peptide hydrogel is used as a tissue recovery matrix, spontaneous biodegradation is required to fix the formation of the new cell-secreted extracellular matrix [48]. Secondly, the natural ingredient contributes to the high biocompatibility of SAPH, allowing for a wide range of applications in biology and medicine, such as drug delivery and cell and tissue culture [49]. The literature has highlighted the use of SAPH as a matrix for nerve cells [50] and eye cells [51].

The idea of preparing hydrogels by self-assembling short peptides stems from the amyloid-like supramolecular structures that are formed by the accumulation of β-sheet structures [52]. Based on the phenomenon, the artificial fibres were created by the accumulation of di-phenylalanine (FF), which forms β-sheet. An example of this design is the dipeptide FΔF, which contains an α, β-dihydroxyphenylalanine (ΔF) residue that drives the dipeptide to assemble into the β-sheet fibres and, further, network [53]. Furthermore, 9-fluorenylmethyloxycarbonyl (Fmoc)-protected modification in FF monomer was also reported to help hydrogel perform better interpenetration in scaffolds and carry drugs as a delivery medium [54].

For the longer peptide, the family of FEFK (F is Phenylalanine, E is Glutamic Acid, K is Lysine) based self-assembly peptide hydrogels have been widely studied. F8 (FEFKFEFK Figure 2.5 (C)) is the primary example of this type of hydrogel. With triggering from suitable pH, F8 peptides fold to

β-sheets and form hydrogel immediately (figure 2.5 A). The self-assembly in F8 is the result of hydrophobic force, hydrogen bond, electrostatic force and π-π stacking [55]. The phenylalanine (F) shows strong hydrophobicity driving the hydrophobic force. The hydrophobic surfaces of peptide residues always try to bury themselves by being close to other hydrophobic surfaces to avoid exploring them into aqueous [127]. Meanwhile, the benzene ring in F also makes a contribution to the formation of π-π stacking. The first amino acid is not limited to F, but also works for all aromatic amino acids that provide a benzyl ring and hydrophobicity for the peptide. However, phenylalanine is primarily used due to its highest hydrophobicity among the 20 natural amino acids. The charge of the amino acid is also known to be an important factor in the self-assembly process. F is non-charged, but E and K are positively and negatively charged, respectively. The electrostatic force prevents the aggregation of the peptide and further precipitation. Typically, the hydrogel forms when the peptide holds 1 to 2 charges [128], and the self-assembly of this family of peptides is triggered by pH.

Additionally, the sequence is not strictly defined and can be slightly modified without interfering with the self-assembly process [56]. F9 (FEFKFEFKK Figure 2.5 D) and KF8K (KFEFKFEFKK Figure 2.5 B) also self-assemble into hydrogels. However, modifying the sequence changes the charge distribution in the peptide chain, causing a shift in the hydrogelation pH. The addition of lysine enhances the positive charge in the peptide chain to maintain one positive charge at pH 7, theoretically. However, the addition of one lysine in F9 does not have the desired effect and F9 also transformed into a hydrogel at pH 4.5. Therefore, KF8K (KFEFKFEFKK) is proposed which forms a clear hydrogel between pH 6.5 and 8. The structure of KF8K is shown in figure 2.5 (B). The presence of lysine in the peptide hydrogel facilitates hydrogelation at neutral pH (figure 2.5 C), but it also weakens the hydrogel's stiffness. The addition of one more lysine in the N-terminal before

phenylalanine interferes with the π-π stacking and hydrophobic interaction between peptide monomers, making the KF8K hydrogel less stiff than the F9 and F8 hydrogels [15]. Meanwhile, several studies have investigated the relationship between hydrogel properties and its peptide sequence. The change in the hydrophobicity surface can lead to a twist in the final hydrogel [57]. Additionally, the inclusion of extra amino acids can add new features to the self-assembly peptide, such as Cysteine (C) for reaction sites with maleimide and Histidine for anti-bacterial properties.

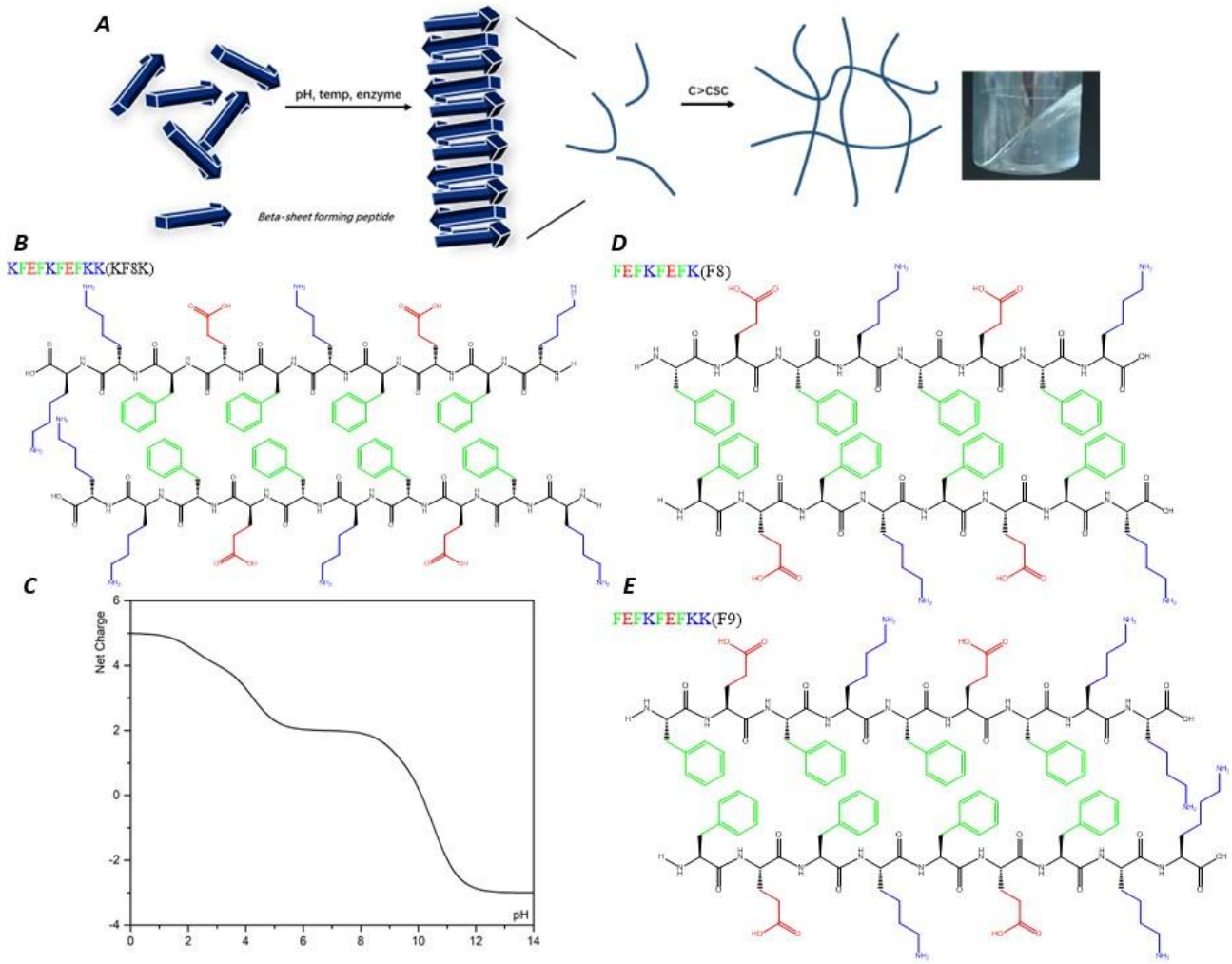

Figure 2-5 (A) The process and hydrogelation pathway of β-sheet family peptide (B) The structure of KF8K (KFEFKFEFKK) (C) The net charge of KF8K against pH (D) The structure of F8 (FEFKFEFK) (E) The structure of F9 (FEFKFEFKK)

In addition to this, there are still other self-assembled peptide hydrogels that rely on β-sheet. One example is MAX1 (H2N-VKVKVKVKV^{D}PPTKVKVKVKV-CONH2), which has a secondary structure of a β-hairpin. In the sequence, V is Valine, P is Proline, and T is Threonine. The design strategy includes alternating charged and uncharged residues with a large amount of hydrophobic amino acids [58]. The specific ring-shaped side chain in the proline helps achieve the β-hairpin in assembly. Before assembly, the MAX1 is in a random coil, but it can transform to a β-hairpin with a designed trigger, such as pH, ions, or temperature. The hydrogel is compatible with fibroblast cells, promoting attachment to the hydrogel scaffolds. Additionally, the MAX1 hydrogel supports fibroblast proliferation without a significant effect on the mechanical properties of the hydrogel [28].

Ac-$(XKXK)_2$-NH_2 (X is set to Valine, Isoleucine, Phenylalanine, and Cyclohexylalanine) is another self-assembly peptide capable of generating a hydrogel [59]. The assembly of this peptide is mainly driven by hydrophobicity and π-π stacking from the aromatic group, while lysine plays a role in initiating self-assembly. The net charges in lysine prevent assembly. As a result, the suitable pH where lysine is uncharged is the trigger for assembly. Another example of an alternative positively and negatively charged amino acid residue self-assembly peptide is RADA16-I (RADARADARADARADA, where A is Alanine, R is Arginine, and D is Aspartic acid), which is an ionic self-complementary peptide that can form a stable β-sheet structure [60]. Alanine side chains form a hydrophobic core that contributes to the stabilisation of the β-sheet by its hydrophobicity force. The alternative oppositely charged arginine and aspartate side chains aggregate with corresponding ones in adjacent β-strands, providing sites allowing for electrostatic attraction [61].

For peptide hydrogels, the peptide sequence and the assembly environment are the two critical factors for the completion of self-assembly and hydrogel.

The peptide chain's sequence is the primary factor in determining whether a peptide chain can self-assemble to form a hydrogel and its properties. For example, the above Ac-$(XKXK)_2$-NH_2 peptide self-assembles to different structures with different X, as shown by FTIR spectra [61]. The successful self-assembly peptide examples in the above paragraphs suggest that peptides with a high amount of hydrophobic amino acids are a critical design for self-assembly, as the hydrophobic force is strong enough that play a key role in peptide assembly. On the other hand, in terms of hydrophilic amino acids, their charged condition also deeply influences the result of self-assembly. As a result, the peptide sequences with the hydrophilic amino acids show sensitivity to pH. For example, the ----++++ peptide chain (with - being acidic amino acid and + being basic amino acid) self-assembles to different shapes with pH. However, there is no variation for the --++--++ peptide chain against pH [62]. This is explained by the fact that the ---- and ++++ generate charged cores whose surface activities vary with the pH change. Furthermore, the ratio between hydrophilic and hydrophobic amino acids largely determines the solubility of peptides which is known to be a factor influencing the self-assembly process.

On the other hand, environmental conditions and self-assembly are also closely linked. Various environmental triggers have been reported to influence the self-assembly process. Temperature, pH, and ionic concentration are three of the most researched factors [63]. Chemical and physical interactions are sensitive to temperature, particularly physical interactions, due to their reversibility and sensitivity to energy. Ionic concentration typically influences peptide chains maintained by charged amino acids. High ionic concentrations mask the electrostatic force in

solution, weakening the attraction and exclusion between molecules, which may lead to precipitation.

pH also plays an irreplaceable role in the self-assembly of peptides, particularly in Coulomb force-driven peptides [64]. Acidic amino acids are negatively charged at high pH, while basic amino acids are positively charged at low pH. pH has a significant impact on the charges in amino acids. The data from several studies suggest that the net charges and their distribution are important determinants of Coulomb force and hydrogen bond [65]. The above ----++++ peptide (- being acidic amino acid and + being basic amino acid) is one example whose shape is spheres under lower pH but transforms to fibres when the pH increases to 11 [62]. A specific pH is also required to trigger the self-assembly of the MAX1 and FEFKFEFKK peptides to form hydrogel [66].

Finally, regardless of the peptide sequence, peptides need to reach a certain concentration threshold for hydrogelation, known as the critical hydrogel concentration (CHC). The CHC is determined by multiple factors, including peptide sequence and environmental conditions (such as pH or ionic strength) [67].

2.6. Gelatin

Gelatin is a peptide derived from collagen. It is also a candidate for hydrogel formation. Gelatin is a mixture of single or multiple peptide chains produced from the denaturation of collagen. The monomer forms triple helices in aqueous solutions [68]. Same to collagen, glycine, proline, and 4-hydroxyproline residues are the major amino acids in gelatin. In particular, glycine residues appear in every three amino acids. Figure 2.6 shows the general amino acid sequence of gelatin, which is Ala-Gly-Pro-Arg-Gly-Glu-Hyp-Gly-Pro. In the sequence, Hyp is hydroxyproline that has one more hydroxyl group than proline. It is not a proteinogenic amino acid. Collagen

molecules are helices formed by three polypeptide chains intertwined with each other. During the production of gelatin, the collagen molecule helix is denatured and decomposed into an α-component containing a single polypeptide chain (α-chain) and a β-group composed of two α-chains. There still is a small amount of the γ-component composed of three α-chains. Besides, the molecular chain fragments smaller than the α-component or larger than the γ-component still exist [69]. As a result, it can be seen that gelatin is a polydisperse system with certain molecular weight distribution. The molecular weight distribution of gelatin varies with different producing process conditions, which affects the physical and chemical properties of gelatin. Gelatin is also known for its excellent hydrogelation ability and biocompatibility. The physical interactions maintaining the network also make gelatin hydrogel being sensitive to temperature, melting at around 35 °C. However, its poor recoverability and lack of anti-bacterial properties limit gelatin to be used in biological and medical areas [70].

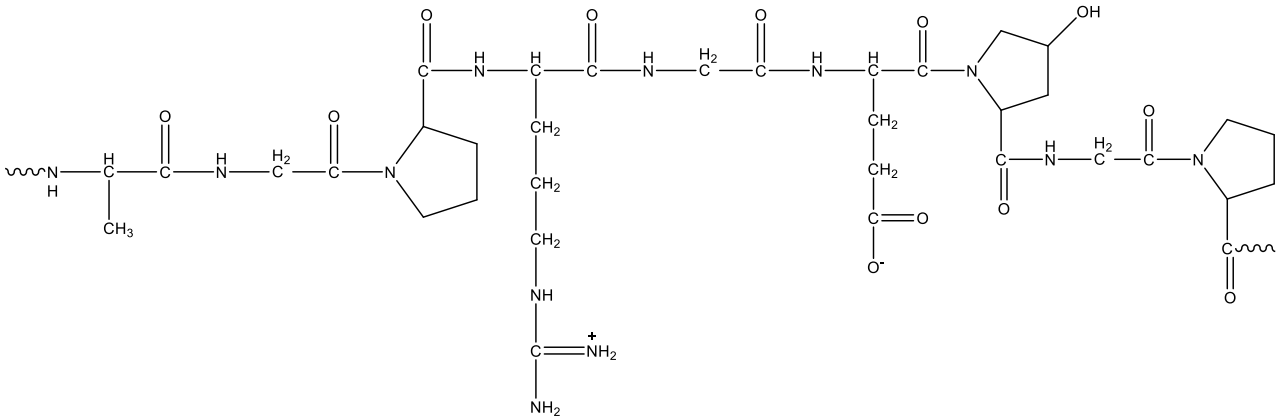

Figure 2-6 the Structure of Gelatin

The production of gelatin begins with the denaturation of collagen from the skin, bones, and tissues of animals, such as pigs, chickens, and fish. However, the gelatin from different sources shows slight differences in amino acid percentages. Particularly the fish gelatin has a lower amount of proline. The difference in amino acid ratio results in fewer amount of hydrogen bonds

in gelatin monomers. Thus, there is a decrease in stiffness and melting point in fish gelatin hydrogel. At present, pigs and chickens are more popular in gelatin production [71]. In the production process, the animal parts are cut into small pieces, degreased, and treated with acid or alkaline to release collagen first. However, due to different treatment strategies, the structure of the produced gelatin varies, leading to differences in the properties of gelatin. Gelatin produced through acid treatment is called type A and has a pI point of 6-9. On the contrary, type B is the gelatin produced through alkaline treatment and has a pI point of 5. Besides the difference in pI, type B is also reported to have a higher crosslinking temperature and slower degradation than type A [72].

When gelatin forms hydrogel, the secondary structure from collagen, the triple helix, is maintained. The short polypeptide chains are connected to the adjacent two polypeptide chains by hydrogen bonds, particularly in the proline-rich zone of polypeptide chains. Then the three peptide chains entangle tightly with each other forming the triple helix structure [73]. When the concentration of gelatin is above the threshold, the helix will accumulate, producing fibrils and networks that trap water molecules, forming a hydrogel. The principle of gelatin hydrogelation has been explained by several theories, such as the kinetic aggregation model [74]. In this theory, water serves as a continuous phase and is in hydrodynamic equilibrium with dispersed gelatin networks. Water is present in the gelatin network as both bonded water, which is bonded to gelatin molecules, and free water. The equilibrium is influenced by temperature, which is the reason for the sol-gel conversion of gelatin hydrogel [75]. The melting point of gelatin is typically around 35°C, but it requires a lower temperature to transform back to hydrogel, below 10°C. When the gelatin hydrogel is cooled below 0°C, the internal water will freeze and gradually expands until freezing the hydrogel.

So far, the non-toxic and digestible properties of gelatin make it widely used in the food industry and drug delivery [76]. Target drugs can be encapsulated into gelatin hydrogels that melt at 37°C after injection in vivo, resulting in drug release. Gelatin can also be combined with thrombin to create a clotting system for hemostasis at injury sites [72]. Additionally, gelatin is also used as a filter in air and water treatment to remove microorganisms [77].

2.7. Oligonucleotide

An oligonucleotide (Oligo) is a short, synthetic strand of nucleotides. Nucleotides are the building blocks of DNA and RNA. It consists of a nitrogen-containing base (adenine (A), thymine (T), cytosine (C), or guanine (G) in DNA; adenine, uracil (U), cytosine, or guanine in RNA), a sugar molecule (deoxyribose in DNA; ribose in RNA), and a phosphate group. Oligonucleotides are typically 10 to 50 nucleotides in length and are used in a variety of applications, such as PCR amplification [78], DNA sequencing [79], and diagnostic testing [80].

The oligonucleotide chains can pair with another complementary chain by the Watson-Crick rule. The principle states that Adenine always pairs with Thymine (T) in DNA and Guanine (G) in RNA. And Guanine always pairs with Cytosine (C) with strict selectivity. The paring process is driven by π-π stacking and particular hydrogen bonds. In DNA, there are two hydrogen bonds in A-T pairing and three in G-C pairing, bringing a more robust connection in the G-C group.

Temperature is one of the most popular factors that influence the pairing process. As the double-strand is maintained by hydrogen bonds which are highly sensitive to high temperatures, there is a threshold temperature when the double-strand oligonucleotide starts to separate. The temperature is called melting temperature Tm, which is approximate $T_m(\,℃) = 2 \times (A + T) +$

$4 \times (G + C)$ in DNA [81]. G-C-rich oligonucleotides have better stability at high temperatures since there are more hydrogen bonds between the G-C pairing.

Oligonucleotides absorb ultraviolet (UV) light at a characteristic wavelength due to the presence of nitrogenous bases in their structure. The absorbance spectrum of an oligonucleotide typically shows a peak between 260 and 280 nm, with the precise wavelength depending on the specific sequence and length of the oligonucleotide. The absorbance at 260 nm is particularly useful as it is relatively specific for double-stranded DNA and RNA. The ratio of absorbance at 260 nm to 280 nm (A260/A280) is commonly used to assess the purity of nucleic acid samples. Generally, a ratio of 1.8 or higher indicates that the sample is pure DNA or RNA [82], while a ratio lower than 1.8 indicates the presence of contaminants such as proteins or salts.

2.8. Oligonucleotide hydrogel

Like peptides, oligonucleotides are also reported as natural self-assembly molecules that can produce hydrogels by utilising the Watson-Crick base pairing rule [83]. The oligonucleotide chains pair with other complementary chains by base pairing, forming an overlapped lattice structure. The accumulation of the lattice structure will be the fibres and network.

Similar to peptide hydrogels, the biocompatibility and biodegradability of oligonucleotide hydrogels are primary benefits. Additionally, an interesting property of DNA hydrogels is that their hydrogelation can be reversed by temperature variation, as the base pairing is strongly temperature-dependent [125]. This means that the pairing will be broken by heating above the melting temperature. Therefore, DNA hydrogels are generally thermosensitive, and the length of the double-stranded DNA (dsDNA) determines the sensitivity to temperature. Based on the nucleotide's chemical and physical properties, many DNA hydrogels have been designed to fulfil

specific demands. For example, it has been proved that thymine (T) can pair with Hg^{2+} to generate a T-Hg^{2+}-T pair, which is stronger than an A-T pair by Watson-Crick pairing. Poly-T DNA hydrogel has been created to detect and remove mercury ions at the same time [84].

Typically, DNA hydrogel is divided into two groups: hybrid DNA hydrogels and pure DNA hydrogels. Pure DNA hydrogels form scaffolds by the assembly of branched and linear DNA units. It has been reported that well-designed three different sequence single-stranded DNA chains can form a Y-shaped structure containing two functional domains. One domain has two cytosine-rich areas. The other is the pairing zone for the formation of the Y shape (Figure 2.7). The three single-stranded DNA chains form the double-stranded DNA by bases pairing in this zone. All Y-shaped units are connected with other Y units by base pairing in the cytosine-rich stretches [85]. This DNA hydrogel is also pH-triggered, as in high pH, the cytosine-rich stretches switch to a random coil, which stops the connection between Y-shape units [85]. Relying on this pH-triggered property, it is easy to control the hydrogel to carry or release molecules, for example, as a drug delivery system.

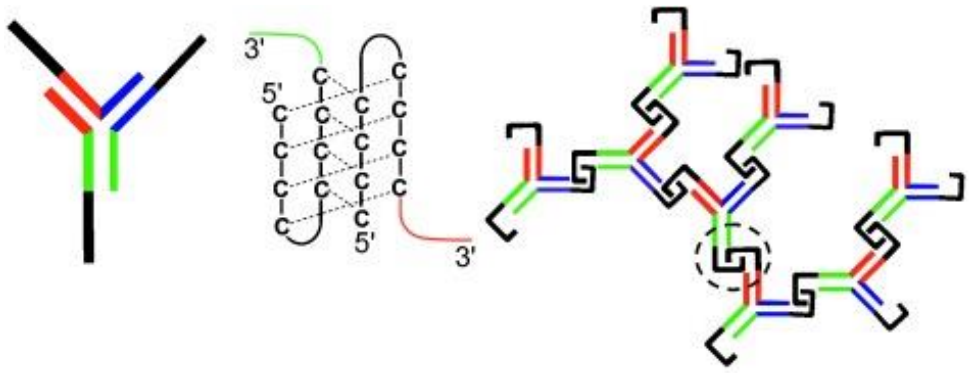

Figure 2-7 Structure of Y shape unit (left) and diagram for unit's connection (right) [85]

Linear double-stranded DNA (dsDNA) with sticky ends is also proposed for hydrogel production. The assembly units contain two oligomers, oligo 1 (O1) and oligo 2 (O2), which are 30 bp in length and able to pair with each other to form a dsDNA block. The block also has

complementary arms on two sides for self-assembly. The dsDNA blocks can connect with each other by the complementary arms, resulting in the formation of hydrogel scaffolds and fibres [86].

Additionally, a DNA-responsive DNA hydrogel were also created, which can change shape in response to the specific DNA signal (figure 2.8) [87]. The units of this hydrogel are two hairpin DNAs, H1 and H2. The units have different domains, but both were precisely designed with complementary arms to produce blocks, fibres and hydrogel. The hydrogel expansion can be induced when there are compatible outside hairpin DNAs presenting. The compatible DNA can insert the blocks changing the length of the fibres. As a result, the hydrogels formed by this hybrid system can swell after the presence of a target DNA signal, leading to a change in shape [87].

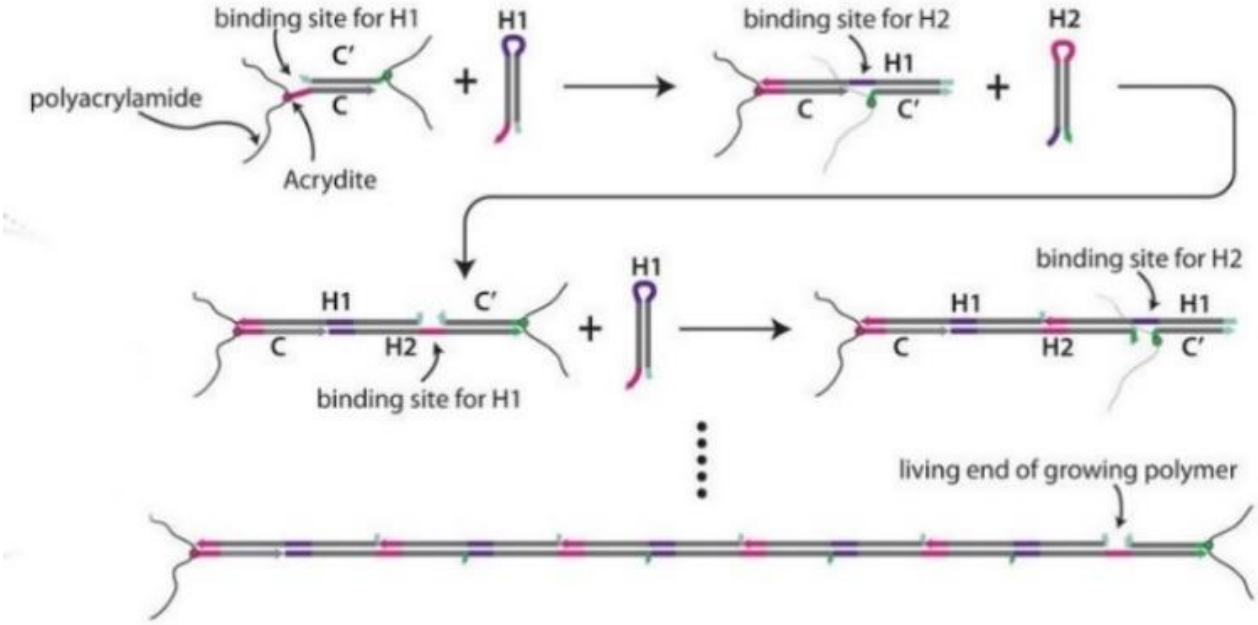

Figure 2-8 The process for hairpin DNAs units self-assemble to hydrogel [87]

On the other hand, in hybrid DNA hydrogels, DNA strands are typically fixed onto a framework as the secondary network. The framework polymer can be biological molecules or chemical polymers. The advantage of the former is retaining brilliant bio-properties, such as polypeptide [88] or protein [89]. Example of chemical polymers includes polyacrylamide [90] and

graphene oxide [91]. The hybrid hydrogel with a chemical framework typically shows better mechanical stiffness. This strategy reduces the demand for DNA, as it only plays a role as additional cross-linkers.

A polypeptide-DNA hydrogel for 3D printing was reported [88]. Poly (L-glutamic acid240-co-γ-propargyl-L-glutamate20) (p(LGA240-co-PLG20) is used as the backbone. All backbones are grafted five to six single-strand DNAs (ssDNA) by copper(I) catalysis. Other double-stranded DNAs (dsDNAs) with sticky ends are added to connect the ssDNAs like bridges. This mechanism allows polypeptide frameworks to be connected and generate a network. This hydrogel has valuable properties for use as a 3D printing ink, including enough mechanical strength for printing more precise structure and no obvious shrinking or swelling phenomena during printing. A particular advantage is its rapid hydrogelation, allowing the ink to dry quickly and avoid interference during later printing [88].

Similar to peptide-DNA hydrogels, there are also protein-DNA hydrogels. For example, human serum albumin (HSA) was selected as the backbone which is modified with PEG arms to increase the water content. The DNA crosslinker is DL1, which is composed of three single-stranded DNAs (S-1, S-2 and S-3) with sticky ends that can link the multiple protein-PEG frameworks together [92]. The sticky end of DL1 can also be connected to crosslinkers (such as DL2) to allow connection to up to two proteins. Based on these sites, modification of the hydrogel can be completed easily.

Interestingly, RNA-based self-assembly hydrogels have also been reported. The hydrogel is composed of an RNA-triple-helix scaffold. RNA-triple conjugates to the dendrimers forming stable triplex nanoparticles. The nanoparticle forms an RNA-triple helix adhesive scaffold in the presence of dextran aldehyde [93]. In particular, the RNA in this hydrogel is miRNA, which has been shown to shrink cancer cells. Therefore, the hydrogel formed by miRNA retains the ability to treat cancer.

Additionally, the hydrogel acts as a delivery vehicle for miRNA and shows great selectivity for certain tissues [93].

Relevantly, RNA chains are less stable than DNA chains because of an additional oxygen atom in RNA. This oxygen atom causes RNA double chains to not form a helix-like DNA. The helix is a key factor for DNA's stability as DNA nucleotides can hide their fragile parts in the centre of the helix and expose their more stable parts on the outside. Additionally, the presence of this oxygen atom creates a hydroxide group on the 2' carbon atom of RNA, whereas DNA has a hydrogen atom in this position. Hydroxide groups are more chemically active than hydrogen atoms. The higher stability makes DNA be a stronger material than RNA for hydrogel formation, except in cases where specific RNAs have additional functions.

2.9. Double Network

Double-network (DN) hydrogels are a type of hydrogel that is made by mixing a soft and a rigid network together. The soft network provides flexibility, while the rigid network provides mechanical strength. The unique combination of the two networks allows for the creation of hydrogels with controllable mechanical properties, such as high toughness and stiffness, making them useful in biomedical applications [64]. The "sacrificial bonds" in the rigid network are designed to break under stress, dissipating energy and preventing the hydrogel from breaking.

The Interpenetrating polymer network (IPN) is a proposed structure formed by two polymers interpenetrating with each other in the form of a network [95]. In IPN, at least one polymer is chemically cross-linked, and another polymer interpenetrates through the network of the former polymer. No covalent bond is formed between the two polymer networks. IPN hydrogels have a two-component network structure, which allows for both a large swelling ratio and good

mechanical properties. The advantages make them promising for use in biomedical tissue engineering, adsorption, and separation [96]. The double-network hydrogel can be seen as a specific IPN hydrogel. In DN hydrogel, the two components both crosslink to the network with interpenetration.

Typically, the two networks in a Double-network (DN) hydrogel interpenetrate with each other, resulting in a more dense and complex structure than single-network hydrogels. The interactions between the networks can be both physical and chemical, and DN hydrogels can be divided into fully physical, fully chemical, and hybrid types. The fully chemical method was mainly used in early research, with examples such as PAMPS/poly(N-isopropylacrylamide-co-acrylamide) [PAMPS/P(NIPAAm-co-AAm)] DN hydrogel, which achieved a 50-fold improvement in stiffness compared to single network hydrogels [97]. However, over-dense crosslinking can harm the network, leading to deterioration with strain increase [98]. The irreversibility of covalent bond breaking restricts the recoverability of DN hydrogel, which is highly demanded in biological and medical applications [99]. Additionally, the toxicity of the crosslinker can also be an issue in terms of biocompatibility.

Therefore, the physical and chemical crosslinking hybrid DN hydrogels are proposed. The first network is still crosslinked by covalent bonds, providing high rigidity. However, the second soft network is maintained by physical interactions such as hydrophobic forces, hydrogen bonds, electrostatic forces, and Van der Waals forces. The dynamic and reversible physical interactions contribute to the self-healing and ductility of the hydrogel. An example of this type of DN hydrogel is the Ca^{2+}-alginate/PAAm hydrogel, where PAAm is chemically linked, and calcium ions act as a bridge connecting alginate molecules by electrostatic force [100]. Another example is the hybrid

Agar/PAAm DN hydrogel, which is composed of hydrogen-bonded agar as the soft network [101]. Additionally, on the PVA/PAAm hybrid DN hydrogel, PVA can form a microcrystalline structure providing physical crosslinking sites in networks. Further physical crosslinking strengthens the stiffness of DN hydrogel [102]. These hydrogels both are based on PAAm, suggesting that one chemically crosslinked network is the potential to blend with different secondary networks undergoing different physical crosslinking strategies.

However, the presence of a chemically crosslinked network still limits the recoverability of hydrogels due to the irreversibility of the inevitable chemical bond breaking. As a result, completely physical crosslinked DN hydrogels are designed. The two networks both are crosslinked by the above discussed physical interactions. Besides, since there is no extra crosslinker, the non-toxicity is another benefit of this type of DN hydrogel. One of the examples is the poly(4-styrene sulfonate-co-methyl-uracil-imidazolium) chloride (PSS-MUI) and gelatin DN hydrogel. The PSS-MUI crosslinks through Fe^{3+} ion-ligand interactions in PSS-MUI and gelatin is the hydrogen bonding [103]. There still is an example of the hydrophobic force and hydrogen bond driving physical DN hydrogels. However, unfortunately, the stiffness of these hydrogels is limited due to the weaker energy and stability of physical crosslinking compared to covalent bonds. Gelatin hydrogels do not perform well in strength at high temperatures. Currently, several gelatin-based DN hydrogels have been produced with better high-temperature mechanical stiffness, such as the Gelatin/polyacrylamide DN hydrogel [96] and the Gelatin/gellan gum DN hydrogel [104].

The β-sheet family SAP can also be involved in the DN hydrogel. There is a poly- acrylamide (APM) and SAP hybrid DN hydrogel (figure 2.9) [105]. Its first network consists by poly- acrylamide (APM), which crosslinks by chemical bonds. The self-assembly peptide fibres, which consist of K, F

and E, are the secondary soft network. Meanwhile, the acrylamide and bis-acrylamide are also modified into peptide and APM monopoly. The two modified groups play the role of connecting two networks together. The mixing hydrogel shows a series of excellent mechanical properties, including high stiffness and compressibility, quick stress relaxation, large energy dissipation, strain stiffening, and fast high strain-breaking recovery.

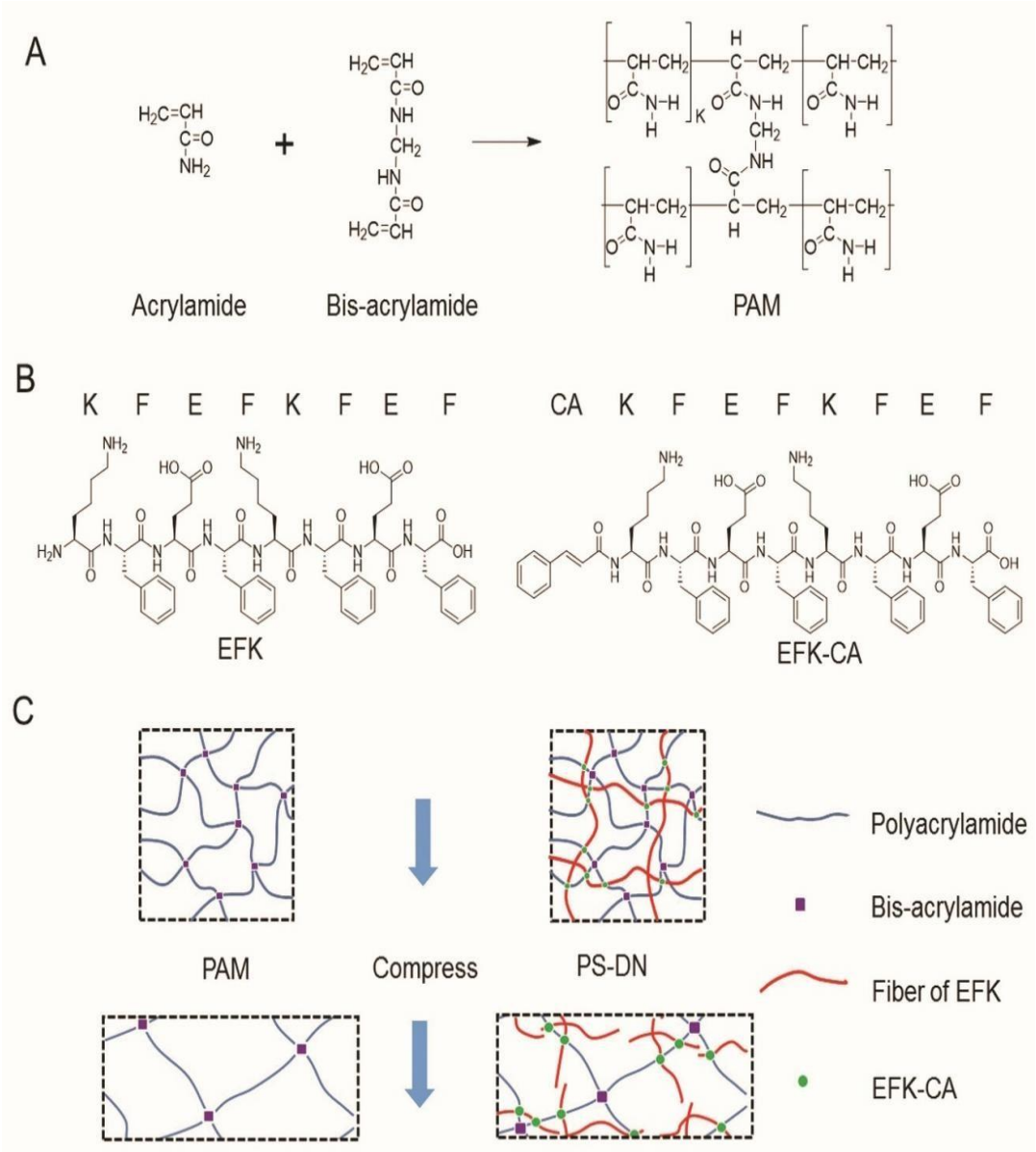

Figure 2-9 The process in producing two-level network hydrogel. (A) the reaction for acrylamide network crosslinking. (B) The structure of peptide network and crosslinker. (C) The structure of the two-level hydrogel [105]

In summary, the design of double-network hydrogels is a target-driven process. Hydrogels that prioritise mechanical strength typically use more covalent bonds for cross-linking. However, hydrogels used for injection and cell culture are more commonly prepared using physical interactions for better recoverability. The design process involves balancing these factors to meet specific targets and demands.

2.10. Applications

2.10.1 3D bio-printing

The excellent mechanical properties and printability of hydrogel make it widely used as an ink in 3D bio-printing, particularly in bio-printing due to its biological properties. The ink in 3D printing is typically demanded to have efficient mechanical properties and no swelling or shrinking after injection which leads to deformation. In addition, precise printing controllability, appropriate biological properties, high-speed hydrogelation, and geometrical uniformity are also necessary for 3D bioprinting ink.

Peptide-based self-assembly hydrogel has been used as the printing material to print well-defined 3D cell-laden constructs with variable stiffness and improved structural integrity. In printing, this hydrogel has not been observed to shrink or swell, decreasing the possibility of shape deformation. Further, the printed objects have a cell-friendly microenvironment for cell culture and proliferation [106].

On the other hand, double network hydrogels have also been employed as inks in 3D bioprinting. One example is the above-discussed DNA-polypeptide hydrogel, which crosslinks by short oligonucleotides (figure 2.10) [88]. In the printing process, the main backbone and linker are

separately injected through two nozzles. Ink A is the backbone solution and ink B is the crosslinker oligonucleotide. The two inks form a stable hydrogel in a short time after the meeting. Therefore, this 3D printing system works like a common 2D printing process, spraying ink and drying ink [88]. In terms of application, the cell culture media printed by this system not only fulfils basic cell demands but also shows the ability to prevent cell settlement and aggregation. At the same time, the printed media still keeps its biodegradability, being easily deformed by proteases and DNases.

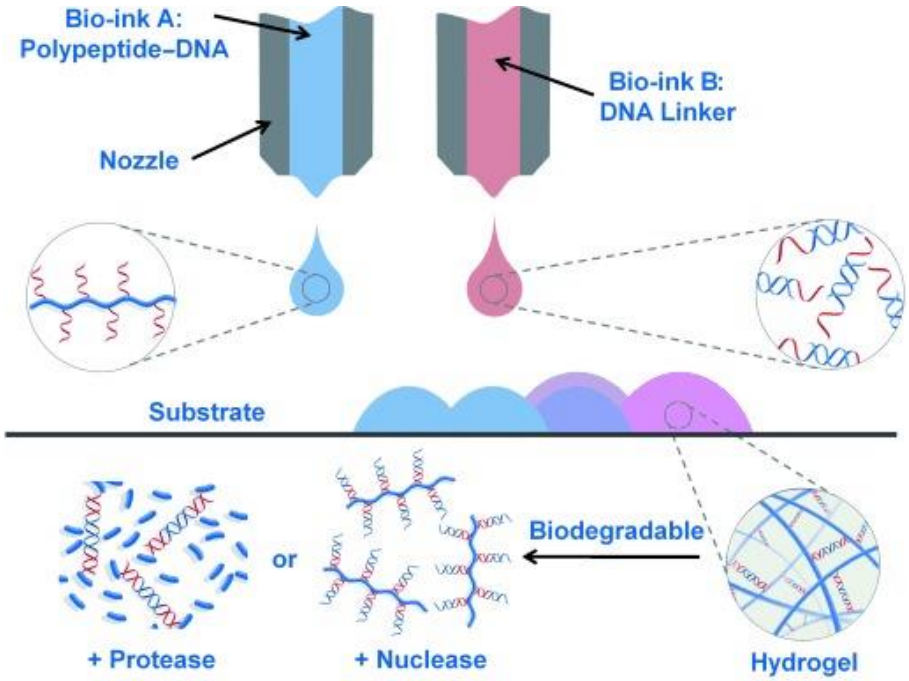

Figure 2-10 A two-ink 3D printing system. Up: The schematic for 3D-bioprinting. Below, the schematic for hydrogel structure [88]

Besides, an adamantane hydrogel (Ad) and β-cyclodextrin hydrogel (CD) based printing system was also designed. The two inks link together through guest-host bonds (between Ad and β-CD moieties). By controlling the mixture ratio, the properties of the hydrogel can be altered, allowing them to be used to print different types of bio-objects [107]. Two inks are also modified by methacrylates (blue) and guest-host molecules (purple). It generates the first physical crosslinking and a secondary chemical crosslinking between methacrylates under UV light exposure [107].

2.10.2 Soft Electronic Devices

Typically, major electronic devices are solid and hard material. However, cells or tissues are made of soft materials, such as the heart or brain [108]. An electrically conductive, soft, stable, stretchable, and biocompatible material [109] is demanded not only in medicine but also in wearable devices. Furthermore, it holds the potential to be used as the skin of robots, which still require high voltage and high-frequency standability [110], and transparency [111] in the material.

Ionic conductive hydrogel is a potential solution for soft electronic devices. The system is composed of two electrodes, a dielectric, and an electrolyte. An electrical double layer is generated at the surface between the electrode and electrolyte [112]. This layer plays the role of separating ions and electrodes, preventing electrochemical reactions, similar to a capacitor containing ions. The movement of ions in the electrolyte between the two layers enables the transmission of electrical signals. The polyacrylamide hydrogel is the matrix of the system, containing NaCl as the electrolyte. The hydrogel has also been proven to have excellent transmittance and stretchability.

Another design involves blending conductive polyaniline (PANI) precursor into a poly(acrylic acid) (HAPAA) hydrogel matrix. In the hydrogel, not only is the high-strain recoverability of HAPAA well preserved but an improvement in stiffness is also observed. At the same time, the presence of PANI enables the movement of electrons and provides electrical conductivity in the soft hydrogel [126].

A wearable electronic skin is also proposed prepared by MXene ($Ti_3C_2T_x$ T is transition metal dichalcogenides) and polyvinyl alcohol (PVA) double-network hydrogel. The addition of MXene causes the enhancement of the conductivity and self-healability of the hydrogel [113].

2.10.3 Medical Application

Tissue engineering is a field of medicine and biology that involves the use of biologically active substances to reconstruct or repair damaged or diseased organs and tissues through in vitro cell culture and tissue construction methods.

A poly(acrylic) acid (PAA) and alginate double network (DN) hydrogel is proposed as an artificial cartilage tissue. The two networks are crosslinked under ultraviolet light [114]. The double-network hydrogel is further mixed with nano-silica to increase compressive strength and fracture toughness, decrease cross-linking density, and reduce the friction coefficient. The physical properties, including swelling ratio and mechanical properties, have also been clearly tested. Additionally, the biocompatibility was also proven by the results from adipose stem cell culture [114].

Meanwhile, the hydrogel is also employed in the artificial joint as a lubricant releaser to decrease wear debris. The hydrogel is a carbon dots/poly(ethylene glycol)/chitosan/sodium glycerophosphate (CDs/PEG/CS/GP) composite hydrogel. It can release CD, PEG and GP as lubrication. The biological results indicate that this material is safe and biocompatible [115].

Besides, vaccines are also a potential application of hydrogel. Traditional vaccines are based on live or attenuated viruses, which hold potential risks in safety (figure 2.11) [116]. A safer alternative is proposed which is composed of antigen DNA into a hydrogel carrier as a vaccine to trigger the immune response. Peptide hydrogel is one of the potential carriers. Because the raw material of this new vaccine is DNA and peptide, it can be degraded by DNases and peptidases easily. In a recent paper, a DNA-hydrogel vaccine has been proven to be valid in triggering a strong immune response in HIV [117].

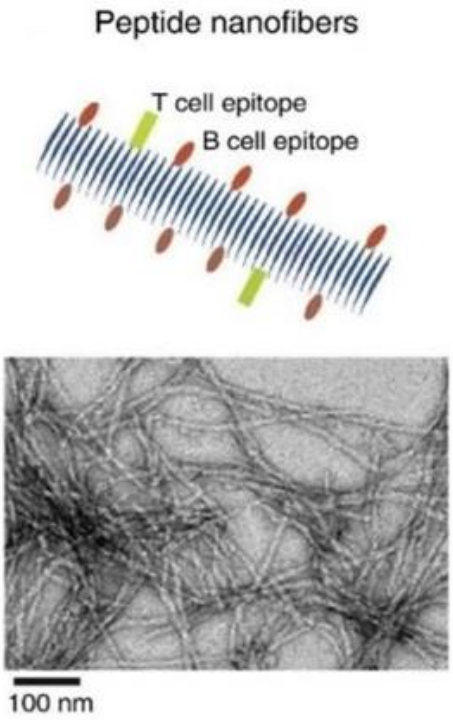

Figure 2-11 An example of peptide-based hydrogel vaccine. Up: the schematic for the vaccine. Below: the TEM image for the peptide hydrogel network. [106]

2.10.4 Biosensor

The biosensor is a system that is designed to detect and respond to a specific biological substance or entity, such as a protein, enzyme, or cell [118]. These sensors typically use a biological recognition element to bind to the target substance and generate a measurable signal, such as a change in electrical current or fluorescence. These sensors can be used for a variety of applications, including medical diagnostics, environmental monitoring, and basic research. Biosensors still is a popular application for hydrogel. For example, by establishing an interface through self-assembly hydrogel and using an enzyme-based electrochemical sensor, a cell monitor can be achieved to report physiological and pathological information [119].

Light can also trigger the formation of a hydrogel. Therefore, the hydrogelation or not can be a signal responding to light. For instance, a cysteine residue-based light trigger has been built to

control the start of a β-hairpin containing hydrogel. The cysteine residue is fixed onto the hydrophobic surface and does not interfere with the β-hairpin folding. Furthermore, an α-carboxy-2-nitrobenzyl is introduced into this cysteine. The presence of α-carboxy-2-nitrobenzyl prevents β-hairpin folding as designed, which is necessary for self-assembly. However, UV light is able to release the α-carboxy-2-nitrobenzyl, allowing the peptide to fold and self-assemble [120]. Thus, the hydrogel responds to UV light by hydrogelation.

In self-assembly peptide hydrogel, the pH value can be measured by the hydrogelation result. Peptide monomers remain in solution when the pH is not in the designed hydrogelation range, but at a suitable pH, partial charges in amino acids are removed, leading to hydrogelation. Additionally, the hydrogel can also be used as a sensor for ion concentration. High ionic strength can mask charge effects [121]. An example of a pH sensor is a histidine-containing peptide hydrogel, where histidine is positively charged when pH is below 6.5, preventing the peptide from forming the necessary structure. On the contrary, in an alkaline environment, this effect will no longer be present.

Besides, relying on the specific thymine(T)- Hg^{+}- thymine(T) reaction, a poly T DNA hydrogel is prepared able to convert to gel from liquid when it gets in touch with Hg ions. [122]. Finally, the DNA-responsive DNA hydrogel proposed in the above paragraph is also a DNA sensor which can change shape after a specific DNA signal [123].

2.11. Objective

This project attempts to create double-network hydrogels based on a self-assembly peptide (KF8K). This double-network (DN) hydrogel is designed to have a higher and controllable mechanical strength compared to the peptide hydrogel. The excellent biological properties of the

peptide hydrogel also try to be retained in the DN hydrogel. The aim is attempted to be achieved by three different ways.

First, the blending hydrogel by different sequences self-assembly peptides will be established. It tries to blend the similar sequence peptides (F9 and F8) and the same sequence but opposite chirality peptide (D-KF8K) into L-KF8K peptides to form blending hydrogels. The influence from the peptide mixture ratio to the hydrogel will be clearly revealed, including hydrogelation pH, microstructures, fibre morphology and mechanical property. Meanwhile, the distribution of peptide monomers will also be verified by a fluorescence quenching reaction. In this case, peptides with a similar sequence are expected to be homogeneously mixed with L-KF8K while D-KF8K will assemble separately from L-KF8K to form a double-network hydrogel.

Subsequently, the second objective is designing hybrid hydrogels consisting of gelatin and self-assembly peptides (KF8K). The improved and controllable stiffness is the primary target. Besides, it also attempts to achieve good temperature sensitivity, antibacterial properties and recoverability after stress breaking in the hybrid hydrogel. The gelatin-SAP hydrogel is planned to work as the ink for 3D printing. Additionally, the change in the microstructure and fibre morphology after blending will also be explored by microscopy.

Finally, it is tried to establish the hybrid hydrogel consisting of the oligonucleotide and self-assembly peptide. An oligonucleotide and peptide consisting of conjugate is tried to be produce by the maleimide-thiol reaction to connect the two biopolymers' network. The success of the reaction is planning to be proved by the characterisations, including MALDI-TOF, NMR and FTIR. And the pairing of the oligonucleotide will be shown by the UV spectroscopy. In the hybrid hydrogel, the oligonucleotide is looking forward to linking the peptide fibre further through the

conjugate to strengthen the hydrogel. The stiffness of the hybrid hydrogel will be tested by rheometer.

In summary, the project is tried to produced double-network hydrogels based on a self-assembly peptide, KF8K. The DN hydrogel will be produced by three different strategies. A clearly comparison between the three types of the double-network hydrogels is targeting to be achieved in this project.

Reference

[1] Ruiz R, Kang H, Detcheverry F A, et al. Density multiplication and improved lithography by directed block copolymer assembly. Science, 2008, 321(5891): 936-939.

[2] Brannon-Peppas, Lisa, and Ronald S. Harland, eds. *Absorbent polymer technology*. Elsevier, 2012.

[3] Buwalda S J, Boere K W M, Dijkstra P J, et al. Hydrogels in a historical perspective: From simple networks to smart materials. Journal of controlled release, 2014, 190: 254-273.

[4] Unagolla J M, Jayasuriya A C. Hydrogel-based 3D bioprinting: A comprehensive review on cell-laden hydrogels, bioink formulations, and future perspectives. Applied materials today, 2020, 18: 100479.

[5] Mahler A, Reches M, Rechter M, et al. Rigid, self-assembled hydrogel composed of a modified aromatic dipeptide. Advanced Materials, 2006, 18(11): 1365-1370.

[6] Bernstein, L.S. ; Grillo, A.A. ; Loranger, S.S. ; Linder, M.E. Journal of Biological Chemistry, 16 June 2000, Vol.275(24), pp.18520-18526

[7] Klein M, Poverenov E. Natural biopolymer-based hydrogels for use in food and agriculture. Journal of the Science of Food and Agriculture, 2020, 100(6): 2337-2347.

[8] Madduma-Bandarage U S K, Madihally S V. Synthetic hydrogels: Synthesis, novel trends, and applications. Journal of Applied Polymer Science, 2021, 138(19): 50376.

[9] Gyles D A, Castro L D, Silva Jr J O C, et al. A review of the designs and prominent biomedical advances of natural and synthetic hydrogel formulations. European Polymer Journal, 2017, 88: 373-392.

[10] Li Y, Huang G, Zhang X, et al. Magnetic hydrogels and their potential biomedical applications. Advanced Functional Materials, 2013, 23(6): 660-672.

[11] Xinming L, Yingde C, Lloyd A W, et al. Polymeric hydrogels for novel contact lens-based ophthalmic drug delivery systems: A review. Contact Lens and Anterior Eye, 2008, 31(2): 57-64.

[12] Oyen M L. Mechanical characterisation of hydrogel materials. International Materials Reviews, 2014, 59(1): 44-59.

[13] Stem Cells and Biomaterials for Regenerative Medicine[M]. Academic Press, 2018.

[14] Wang Y, Cao H, Wang X. Synthesis and characterization of an injectable ε-polylysine/carboxymethyl chitosan hydrogel used in medical application. Materials Chemistry and Physics, 2020, 248: 122902.

[15] Mandal A, Clegg J R, Anselmo A C, et al. Hydrogels in the clinic. Bioengineering & Translational Medicine, 2020, 5(2): e10158.

[16] Yue K, Trujillo-de Santiago G, Alvarez M M, et al. Synthesis, properties, and biomedical applications of gelatin methacryloyl (GelMA) hydrogels. Biomaterials, 2015, 73: 254-271.

[17] Yue K, Trujillo-de Santiago G, Alvarez M M, et al. Synthesis, properties, and biomedical applications of gelatin methacryloyl (GelMA) hydrogels. Biomaterials, 2015, 73: 254-271.

[18] Li W, Wu X, Qi C, et al. Study on the relationship between the interaction energy and the melting point of amino acid cation based ionic liquids. Journal of Molecular Structure: THEOCHEM,

2010, 942(1-3): 19-25.

[19] Nässel D R, Larhammar D. Neuropeptides and peptide hormones[M]//Neurosciences-From Molecule to Behavior: a university textbook. Springer Spektrum, Berlin, Heidelberg, 2013: 213-237.

[20] Bhandari D, Rafiq S, Gat Y, et al. A review on bioactive peptides: Physiological functions, bioavailability and safety. International Journal of Peptide Research and Therapeutics, 2020, 26(1): 139-150.

[21] Vermeirssen V, Van Camp J, Verstraete W. Bioavailability of angiotensin I converting enzyme inhibitory peptides. British Journal of Nutrition, 2004, 92(3): 357-366.

[22] Hupp T R, Sparks A, Lane D P. Small peptides activate the latent sequence-specific DNA binding function of p53. Cell, 1995, 83(2): 237-245.

[23] Strtjther Arnott, S. David Dover and Arthur Elliott. J. Mol. Biol. 1967 Vol.30, pp.201-208

[24] Mitchell A R. Bruce Merrifield and solid-phase peptide synthesis: A historical assessment. Peptide Science, 2008, 90(3): 175-184.

[25] Amblard M, Fehrentz J A, Martinez J, et al. Methods and protocols of modern solid phase peptide synthesis. Molecular biotechnology, 2006, 33(3): 239-254.

[26] Genchi G. An overview on D-amino acids. Amino Acids, 2017, 49(9): 1521-1533.

[27] Naganuma T, Iinuma Y, Nishiwaki H, et al. Enhanced bacterial growth and gene expression of D-amino acid dehydrogenase with D-glutamate as the sole carbon source. Frontiers in microbiology, 2018, 9: 2097.

[28] Hayase F, Kato H, Fujimaki M (1975) Racemization of amino acid residues in protein of poly(L-amino) acids during roasting. J Agric Food Chem 23:491–494

[29] Sacchi S, Rosini E, Pollegioni L, et al. D-amino acid oxidase inhibitors as a novel class of drugs for schizophrenia therapy. Current pharmaceutical design, 2013, 19(14): 2499-2511.

[30] Fisher G H, D'Aniello A, Vetere A, et al. Free D-aspartate and D-alanine in normal and Alzheimer brain. Brain research bulletin, 1991, 26(6): 983-985.

[31] Hamase, K., Konno, R., Morikawa, A., and Zaitsu, K.(2005) Biol. Pharm. Bull., 28, 15781584.

[32] Albert C, Pohn G, Lóki K, Salamon S, Albert B, Sára P, Mándoki Z, Jánosné Csapó, Csapó J (2007) Effect of microorganism on free amino acid and free D-amino acid contents of various dairy products. Poljoprivreda 13:192–193

[33] Ohide H, Miyoshi Y, Maruyama R, et al. D-Amino acid metabolism in mammals: biosynthesis, degradation and analytical aspects of the metabolic study. Journal of Chromatography B, 2011, 879(29): 3162-3168.

[34] Liang G, Yang Z, Zhang R, et al. Supramolecular hydrogel of a D-amino acid dipeptide for controlled drug release in vivo. Langmuir, 2009, 25(15): 8419-8422.

[35] Yang C, Chu L, Zhang Y, et al. Dynamic biostability, biodistribution, and toxicity of L/D-peptide-based supramolecular nanofibers. ACS applied materials & interfaces, 2015, 7(4): 2735-2744.

[36] Li J, Kuang Y, Gao Y, et al. D-amino acids boost the selectivity and confer supramolecular hydrogels of a nonsteroidal anti-inflammatory drug (NSAID). Journal of the American Chemical Society, 2013, 135(2): 542-545.

[37] Li X, Du X, Li J, et al. Introducing D-amino acid or simple glycoside into small peptides to enable supramolecular hydrogelators to resist proteolysis. Langmuir, 2012, 28(37): 13512-13517.

[38] Luo Z, Wang S, Zhang S. Fabrication of self-assembling D-form peptide nanofiber scaffold d-EAK16 for rapid hemostasis. Biomaterials, 2011, 32(8): 2013-2020.

[39] Xing Y, Cheng E, Yang Y, et al. Self-assembled DNA hydrogels with designable thermal and enzymatic responsiveness. Advanced Materials, 2011, 23(9): 1117-1121.

[40] Thorkelsson K, Bai P, Xu T. Self-assembly and applications of anisotropic nanomaterials: A

review. Nano Today, 2015, 10(1): 48-66.

[41] D. Baranov, A. Fiore, M. van Huis, C. Giannini, A. Falqui, U. Lafont, H. Zandbergen, M. Zanella, R. Cingolani, L. Manna Nano Lett., 10 (2010), pp. 743-749

[42] T.D. Clark, J. Tien, D.C. Duffy, K.E. Paul, G.M. Whitesides J. Am. Chem. Soc., 123 (2001), pp. 7677-7682

[43] Thorkelsson K, Bai P, Xu T. Self-assembly and applications of anisotropic nanomaterials: A review. Nano Today, 2015, 10(1): 48-66.

[44] Korevaar P A, Schaefer C, de Greef T F A, et al. Controlling chemical self-assembly by solvent-dependent dynamics. Journal of the American Chemical Society, 2012, 134(32): 13482-13491.

[45] Levin A, Hakala T A, Schnaider L, et al. Biomimetic peptide self-assembly for functional materials. Nature Reviews Chemistry, 2020, 4(11): 615-634.

[46] Zhang S. Fabrication of novel biomaterials through molecular self-assembly. Nature biotechnology, 2003, 21(10): 1171-1178.

[47] Raza F, Zafar H, Zhu Y, et al. A review on recent advances in stabilizing peptides/proteins upon fabrication in hydrogels from biodegradable polymers. Pharmaceutics, 2018, 10(1): 16.

[48] Giano M C, Pochan D J, Schneider J P. Controlled biodegradation of Self-assembling β-hairpin Peptide hydrogels by proteolysis with matrix metalloproteinase-13. Biomaterials, 2011, 32(27): 6471-6477.

[49] Jayawarna V, Ali M, Jowitt T A, et al. Nanostructured hydrogels for three-dimensional cell culture through self-assembly of fluorenylmethoxycarbonyl–dipeptides. Advanced materials, 2006, 18(5): 611-614.

[50] Liang L, Xu X D, Chen C S, et al. Evaluation of the biocompatibility of novel peptide hydrogel in rabbit eye. Journal of Biomedical Materials Research Part B: Applied Biomaterials, 2010, 93(2):

324-332.

[51] Black K A, Lin B F, Wonder E A, et al. Biocompatibility and characterization of a peptide amphiphile hydrogel for applications in peripheral nerve regeneration. Tissue Engineering Part A, 2015, 21(7-8): 1333-1342.

[52] Maji, S. K. et al. Amyloid as a depot for the formulation of long-acting drugs. PLoS Biol. 6, e17 (2008).

[53] Panda, J. J., Mishra, A., Basu, A. & Chauhan, V. S. Stimuli responsive self-assembled hydrogel of a low molecular weight free dipeptide with potential for tunable drug delivery. Biomacromolecules 9, 2244–2250 (2008).

[54] Huang, R., Qi, W., Feng, L., Su, R. & He, Z. Self-assembling peptide–polysaccharide hybrid hydrogel as a potential carrier for drug delivery. Soft Matter 7, 6222–6230 (2011).

[55] Ligorio C, Zhou M, Wychowaniec J K, et al. Graphene oxide containing self-assembling peptide hybrid hydrogels as a potential 3D injectable cell delivery platform for intervertebral disc repair applications. Acta biomaterialia, 2019, 92: 92-103.

[56] Mohammed, Amran ; Miller, Aline F. ; Saiani, Alberto; Saiani, A. Macromolecular Symposia, April 2007, Vol.251(1), pp.88-95

[57] Elsawy M A, Smith A M, Hodson N, et al. Modification of β-sheet forming peptide hydrophobic face: effect on self-assembly and gelation. Langmuir, 2016, 32(19): 4917-4923.

[58] Laverty G. Stimuli-Responsive Biomolecular Hydrogels for Medical Applications[M]//Hydrogels. CRC Press, 2018: 284-300.

[59] Bowerman, CJ ; Liyanage, W ; Federation, Aj ; Nilsson, Bl. Biomacromolecules, 2011 Jul, Vol.12(7), pp.2735-2745

[60] Ye Z, Zhang H, Luo H, et al. Temperature and pH effects on biophysical and morphological

properties of self-assembling peptide RADA16-I. Journal of peptide science: an official publication of the European Peptide Society, 2008, 14(2): 152-162.

[61] Cormier A R, Pang X, Zimmerman M I, et al. Molecular structure of RADA16-I designer self-assembling peptide nanofibers. ACS nano, 2013, 7(9): 7562-7572.

[62] Hong, Yooseong ; Legge, Raymond L ; Zhang, S ; Chen, P; Hong, Yooseong (correspondence author) ; Hong, Yooseong (record owner). Biomacromolecules, 2003 Sep-Oct, Vol.4(5), pp.1433-1442

[63] Kopecek, Jindrich; Kopecek, Jindrich (correspondence author) ; Kopecek, Jindrich (record owner). Nature, May 23, 2002, Vol.417(6887), pp.388-9, 391

[64] Rajagopal K, Lamm M S, Haines-Butterick L A, et al. Tuning the pH responsiveness of β-hairpin peptide folding, self-assembly, and hydrogel material formation. Biomacromolecules, 2009, 10(9): 2619-2625.

[65] Niemann T, Stange P, Strate A, et al. Like-likes-Like: Cooperative Hydrogen Bonding Overcomes Coulomb Repulsion in Cationic Clusters with Net Charges up to Q=+ 6e. ChemPhysChem, 2018, 19(14): 1691-1695.

[66] Kretsinger J K, Haines L A, Ozbas B, et al. Cytocompatibility of self-assembled β-hairpin peptide hydrogel surfaces. Biomaterials, 2005, 26(25): 5177-5186.

[67] Roberts D, Rochas C, Saiani A, et al. Effect of peptide and guest charge on the structural, mechanical and release properties of β-sheet forming peptides. Langmuir, 2012, 28(46): 16196-16206.

[68] Alipal J, Pu'Ad N A S M, Lee T C, et al. A review of gelatin: Properties, sources, process, applications, and commercialisation. Materials Today: Proceedings, 2021, 42: 240-250.

[69] Veis A, Anesey J, Cohen J. The characterization of the γ-component of gelatin. Archives of

biochemistry and biophysics, 1962, 98(1): 104-110.

[70] Bello A B, Kim D, Kim D, et al. Engineering and functionalization of gelatin biomaterials: From cell culture to medical applications. Tissue Engineering Part B: Reviews, 2020, 26(2): 164-180.

[71] Said M I. Role and function of gelatin in the development of the food and non-food industry: A review[C]//IOP Conference Series: Earth and Environmental Science. IOP Publishing, 2020, 492(1): 012086.

[72] Liu D, Nikoo M, Boran G, et al. Collagen and gelatin. Annual review of food science and technology, 2015, 6: 527-557.

[73] Duconseille A, Astruc T, Quintana N, et al. Gelatin structure and composition linked to hard capsule dissolution: A review. Food hydrocolloids, 2015, 43: 360-376.

[74] Ki C S, Baek D H, Gang K D, et al. Characterization of gelatin nanofiber prepared from gelatin–formic acid solution. Polymer, 2005, 46(14): 5094-5102.

[75] Karim A A, Bhat R. Fish gelatin: properties, challenges, and prospects as an alternative to mammalian gelatins. Food hydrocolloids, 2009, 23(3): 563-576.

[76] Aramwit P, Jaichawa N, Ratanavaraporn J, et al. A comparative study of type A and type B gelatin nanoparticles as the controlled release carriers for different model compounds. Materials Express, 2015, 5(3): 241-248.

[77] Harguindeguy M, Antonelli C, Belleville M P, et al. Gelatin supports with immobilized laccase as sustainable biocatalysts for water treatment. Journal of Applied Polymer Science, 2021, 138(2): 49669.

[78] Jarman S N, Ward R D, Elliott N G. Oligonucleotide primers for PCR amplification of coelomate introns. Marine Biotechnology, 2002, 4: 347-355.

[79] Tillib S V, Mirzabekov A D. Advances in the analysis of DNA sequence variations using

oligonucleotide microchip technology. Current Opinion in Biotechnology, 2001, 12(1): 53-58.

[80] Yershov G, Barsky V, Belgovskiy A, et al. DNA analysis and diagnostics on oligonucleotide microchips. Proceedings of the National Academy of Sciences, 1996, 93(10): 4913-4918.

[81] Guagliardi A, Napoli A, Rossi M, et al. Annealing of complementary DNA strands above the melting point of the duplex promoted by an archaeal protein. Journal of molecular biology, 1997, 267(4): 841-848.

[82] Lida Z, Changhe J, Weihong Z, et al. MicroRNA differential expression profile in cholangiocarcinoma cell line and normal bile duct cell line. Life Science Journal, 2011, 8(4).

[83] Marsh T C, Henderson E. G-wires: self-assembly of a telomeric oligonucleotide, d (GGGGTTGGGG), into large superstructures. Biochemistry, 1994, 33(35): 10718-10724.

[84] Dave N, Chan M Y, Huang P J J, et al. Regenerable DNA-functionalized hydrogels for ultrasensitive, instrument-free mercury (II) detection and removal in water. Journal of the American Chemical Society, 2010, 132(36): 12668-12673.

[85] Cheng E, Xing Y, Chen P, et al. A pH-triggered, fast-responding DNA hydrogel. Angewandte Chemie International Edition, 2009, 48(41): 7660-7663.

[86] Nöll T, Schönherr H, Wesner D, et al. Construction of Three-Dimensional DNA Hydrogels from Linear Building Blocks. Angewandte Chemie, 2014, 126(32): 8468-8472.

[87] Cangialosi A, Yoon C K, Liu J, et al. DNA sequence–directed shape change of photopatterned hydrogels via high-degree swelling. Science, 2017, 357(6356): 1126-1130.

[88] Li C, Faulkner-Jones A, Dun A R, et al. Rapid formation of a supramolecular polypeptide–DNA hydrogel for in situ three-dimensional multilayer bioprinting. Angewandte Chemie, 2015, 127(13): 4029-4033.

[89] Wu Y, Li C, Boldt F, et al. Programmable protein–DNA hybrid hydrogels for the immobilization

and release of functional proteins. Chemical communications, 2014, 50(93): 14620-14622.

[90] Nagahara S, Matsuda T. Hydrogel formation via hybridization of oligonucleotides derivatized in water-soluble vinyl polymers. Polymer Gels and Networks, 1996, 4(2): 111-127.

[91] Xu Y, Wu Q, Sun Y, et al. Three-dimensional self-assembly of graphene oxide and DNA into multifunctional hydrogels. ACS nano, 2010, 4(12): 7358-7362.

[92] Wu Y, Li C, Boldt F, et al. Programmable protein–DNA hybrid hydrogels for the immobilization and release of functional proteins. Chemical communications, 2014, 50(93): 14620-14622.

[93] Conde J, Oliva N, Atilano M, et al. Self-assembled RNA-triple-helix hydrogel scaffold for microRNA modulation in the tumour microenvironment. Nature materials, 2016, 15(3): 353-363.

[94] Nonoyama T, Gong J P. Tough double network hydrogel and its biomedical applications. Annual Review of Chemical and Biomolecular Engineering, 2021, 12: 393-410.

[95] Banerjee S, Siddiqui L, Bhattacharya S S, et al. Interpenetrating polymer network (IPN) hydrogel microspheres for oral controlled release application. International journal of biological macromolecules, 2012, 50(1): 198-206.

[96] Zou Z, Zhang B, Nie X, et al. A sodium alginate-based sustained-release IPN hydrogel and its applications. RSC advances, 2020, 10(65): 39722-39730.

[97] Means A K, Shrode C S, Whitney L V, et al. Double network hydrogels that mimic the modulus, strength, and lubricity of cartilage. Biomacromolecules, 2019, 20(5): 2034-2042.

[98] Chen Q, Zhu L, Chen H, et al. A novel design strategy for fully physically linked double network hydrogels with tough, fatigue resistant, and self-healing properties. Advanced Functional Materials, 2015, 25(10): 1598-1607.

[99] Yang J, Li Y, Zhu L, et al. Double network hydrogels with controlled shape deformation: A mini review. Journal of Polymer Science Part B: Polymer Physics, 2018, 56(19): 1351-1362.

[100] Sun J Y, Zhao X, Illeperuma W R K, et al. Highly stretchable and tough hydrogels. Nature, 2012, 489(7414): 133-136.

[101] Sarkar N, Sahoo G, Swain S K. Nanoclay sandwiched reduced graphene oxide filled macroporous polyacrylamide-agar hybrid hydrogel as an adsorbent for dye decontamination. Nano-structures & nano-objects, 2020, 23: 100507.

[102] Rong Q, Lei W, Chen L, et al. Anti-freezing, conductive self-healing organohydrogels with stable strain-sensitivity at subzero temperatures. Angewandte Chemie International Edition, 2017, 56(45): 14159-14163.

[103] Das S, Martin P, Vasilyev G, et al. Processable, ion-conducting hydrogel for flexible electronic devices with self-healing capability. Macromolecules, 2020, 53(24): 11130-11141.

[104] Nässel D R, Larhammar D. Neuropeptides and peptide hormones[M]//Neurosciences-From Molecule to Behavior: a university textbook. Springer Spektrum, Berlin, Heidelberg, 2013: 213-237.

[105] Sun W, Xue B, Li Y, et al. Polymer-supramolecular polymer double-network hydrogel. Advanced Functional Materials, 2016, 26(48): 9044-9052.

[106] Raphael B, Khalil T, Workman V L, et al. 3D cell bioprinting of self-assembling peptide-based hydrogels. Materials Letters, 2017, 190: 103-106.

[107] Highley C B, Rodell C B, Burdick J A. Direct 3D printing of shear-thinning hydrogels into self-healing hydrogels. Advanced Materials, 2015, 27(34): 5075-5079.

[108] Kim D H, Lu N, Ma R, et al. Epidermal electronics. science, 2011, 333(6044): 838-843.

[109] Rosset S, Shea H R. Flexible and stretchable electrodes for dielectric elastomer actuators. Applied Physics A, 2013, 110(2): 281-307.

[110] Pelrine R, Kornbluh R, Pei Q, et al. High-speed electrically actuated elastomers with strain greater than 100%. Science, 2000, 287(5454): 836-839.

[111] Hu L, Yuan W, Brochu P, et al. Highly stretchable, conductive, and transparent nanotube thin films. Applied Physics Letters, 2009, 94(16): 161108.

[112] Keplinger C, Sun J Y, Foo C C, et al. Stretchable, transparent, ionic conductors. Science, 2013, 341(6149): 984-987.

[113] Zhang J, Wan L, Gao Y, et al. Highly stretchable and self-healable MXene/polyvinyl alcohol hydrogel electrode for wearable capacitive electronic skin. Advanced Electronic Materials, 2019, 5(7): 1900285.

[114] Lin H R, Ling M H, Lin Y J. High strength and low friction of a PAA-alginate-silica hydrogel as potential material for artificial soft tissues. Journal of Biomaterials Science, Polymer Edition, 2009, 20(5-6): 637-652.

[115] Lu H, Lv L, Ma J, et al. Carbon dots intensified poly (ethylene glycol)/chitosan/sodium glycerophosphate hydrogel as artificial synovium tissue with slow-release lubricant. Journal of the Mechanical Behavior of Biomedical Materials, 2018, 88: 261-269.

[116] Wen Y, Collier J H. Supramolecular peptide vaccines: tuning adaptive immunity. Current opinion in immunology, 2015, 35: 73-79.

[117] Joint United Nations Programme on HIV/AIDS. UNAIDS report on the global AIDS epidemic; http://www.unaids.org/globalreport,2010

[118] Ziegler C, Göpel W. Biosensor development. Current opinion in chemical biology, 1998, 2(5): 585-591.

[119] Lian M, Chen X, Lu Y, et al. Self-assembled peptide hydrogel as a smart biointerface for enzyme-based electrochemical biosensing and cell monitoring. ACS applied materials & interfaces, 2016, 8(38): 25036-25042.

[120] Haines L A, Rajagopal K, Ozbas B, et al. Light-activated hydrogel formation via the triggered

folding and self-assembly of a designed peptide. Journal of the American Chemical Society, 2005, 127(48): 17025-17029.

[121] Ulijn R V, Smith A M. Designing peptide based nanomaterials. Chemical Society Reviews, 2008, 37(4): 664-675.

[122] Xu S, Chen L, Li J, et al. Novel Hg2+-imprinted polymers based on thymine–Hg2+–thymine interaction for highly selective preconcentration of Hg2+ in water samples. Journal of hazardous materials, 2012, 237: 347-354.

[123] Liang L, Xu X D, Chen C S, et al. Evaluation of the biocompatibility of novel peptide hydrogel in rabbit eye. Journal of Biomedical Materials Research Part B: Applied Biomaterials, 2010, 93(2): 324-332.

[124] Wieduwild, R.; Tsurkan, M.; Chwalek, K.; Murawala, P.; Nowak,M.; Freudenberg, U.; Neinhuis, C.; Werner, C.; Zhang, Y. Minimal, peptide motif for non-covalent peptide–heparin hydrogels. J. Am. Chem. Soc., 2013, 135 (8), 2919-2922.

[125] Cohen S A, Simaan-Yameen H, Fuoco C, et al. Injectable hydrogel microspheres for sustained gene delivery of antisense oligonucleotides to restore the expression of dystrophin protein in duchenne muscular dystrophy. European Polymer Journal, 2022: 111038.

[126] Su G, Yin S, Guo Y, et al. Balancing the mechanical, electronic, and self-healing properties in conductive self-healing hydrogel for wearable sensor applications. Materials Horizons, 2021, 8(6): 1795-1804.

[127] Amorín M, Castedo L, Granja J R. New cyclic peptide assemblies with hydrophobic cavities: the structural and thermodynamic basis of a new class of peptide nanotubes. Journal of the American Chemical Society, 2003, 125(10): 2844-2845.

[128] Ligorio C, Hoyland J A, Saiani A. Self-assembling peptide hydrogels as functional tools to

tackle intervertebral disc degeneration. Gels, 2022, 8(4): 211.

[129] Michl J, Park K C, Swietach P. Evidence-based guidelines for controlling pH in mammalian live-cell culture systems. Communications biology, 2019, 2(1): 1-12.

[130] Wychowaniec J K, Smith A M, Ligorio C, et al. Role of sheet-edge interactions in β-sheet self-assembling peptide hydrogels. Biomacromolecules, 2020, 21(6): 2285-2297.

3 Chapter 3. Experimental Section

In this chapter, the fundamental theories and principle of the techniques employed in this project will be discussed. The characterisation, microscopy, rheometer and 3D printer are involved.

3.1. Rheometer

An Oscillatory Rheometer is an instrument that measures the viscosity and elasticity of fluids or solids by monitoring their mechanical response to an external force [1]. It is considered a superior choice for materials whose viscosity cannot be defined as a constant value, such as viscoelastic substances, as it allows for the dynamic testing of samples. This means that varying impacts are applied to the samples periodically by the rheometer, and the responses from the specimens are monitored and collected in real time.

Viscoelastic materials have been gaining increasing research interest as they display both viscous and elastic characteristics in the deformation process [2]. Viscoelasticity has been well-researched in the past two decades, with a wide range of applications and research on polymers and bio-macromolecules [3]. Viscoelastic materials perform between solid and fluid materials. It means that in viscoelastic materials, there is a response hysteresis between strain and stress [4].

Viscosity is typically observed in fluids and is the macroscopic result of internal friction primarily caused by molecular interactions, including hydrogen bonds and Vander Waals forces. The internal friction causes molecules to follow the movement of surrounding molecules, leading to strain with hysteresis, resulting in a time-dependent strain ratio in a viscous fluid. The interactions leading to the internal friction are influenced by temperature, resulting in viscosity exhibiting temperature sensitivity - generally, the higher the temperature, the lower the viscosity. Numerically, viscosity is defined as the ratio between shear stress (τ) and velocity gradient (du/dy), as shown in Eq 1.

$$\mu = \frac{\tau}{\frac{du}{dy}} \tag{1}$$

where μ is viscosity, τ is shear stress and du/dy is velocity gradient [5].

In that, shear stress is defined as the shear force in a unit area coplanar with a material cross-section. The number of shear stress is in Eq 2. The direction always verticalizes with the normal of the forced surface.

$$\tau = \frac{F}{A} \tag{2}$$

where F is the shear force and A is the area in the forced surface. In the experiment, the measure of viscosity can be is called the modulus of viscosity.

Typically, a material that exhibits a linear strain response to stress is defined as a Newtonian fluid. This means that the viscosity of a Newtonian fluid is constant and does not change with the shear rate. Otherwise, non-Newtonian liquids involve those with varying viscosity in response to stress. The most common example of a Newtonian fluid is water.

On the other hand, elasticity is the ability of a material to return to its original shape after being deformed by an applied force. It is a property of solids, and it is the opposite of plasticity, which is the ability of a material to be permanently deformed without breaking. Ideally, elastic solids exhibit strain immediately when loaded with stress. In the experiment, the measure of elasticity is called the modulus of elasticity.

In recent decades, there has been particular interest in the cone-and-plate rheometer (figure 3.1), due to the small angle of the cone head [6]. This angle, typically smaller than 3 degrees, creates a smaller space between the head and plate for the sample to fill, making it more suitable for small volume samples, such as biological samples. Additionally, the small sample amount also contributes to achieving more uniform heat transfer and temperature distribution in the sample and producing a constant shear rate, avoiding the need to make assumptions to simplify result calculations [7].

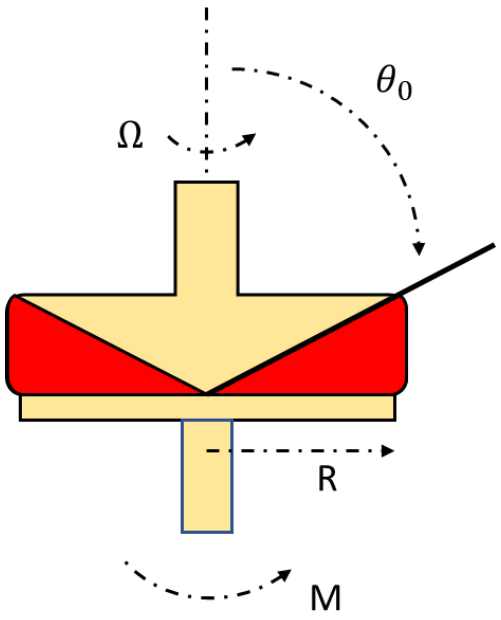

Figure 3-1 The structure of the cone-and-plate rheometer

The viscosity measurement is achieved by applying an angular velocity from the cone's top head and measuring the torque in the material. The shear viscosity can be calculated using Equation3.

$$\eta = \frac{\tau}{\dot{\gamma}} \tag{3}$$

where η is the shear viscosity, τ is the stress and $\dot{\gamma}$ is the shear rate.

In the cone-and-plate, stress presents as Eq 4.

$$\tau = M \times \frac{3}{2\pi R^3} \tag{4}$$

in that, M is the torque that can be measured by the machine. R is the radius of the cone head.

The shear rate is a constant in the cone-and-plate rheometer, which is in Eq.

$$\dot{\gamma} = \frac{\Omega}{\theta_0} \tag{5}$$

in that, Ω is the angular velocity while θ_0 is the top angle of the cone head.

Therefore, the final viscosity can be acquired by Eq. in cone-and plate rheometer [8].

$$\eta = \frac{3\theta_0 M}{2\pi R^3 \Omega} \tag{6}$$

Currently, many researchers have also used rheometers to measure the storage modulus and loss modulus of hydrogel samples, revealing the stiffness and strain limitations of the material. The storage modulus (G'), also known as the elastic modulus, is typically observed in solid materials and demonstrates recovery after deformation, such as in a sponge. On the other hand, the loss modulus (G'' or viscous modulus) is a characteristic of liquids [9]. Therefore, the ratio of these two moduli provides information on how closely the hydrogel resembles a solid or a fluid.

The measuring process involves applying a sine function stress to the sample and monitoring the strain. Typically, simple harmonic stress is applied to the sample and the strain is monitored (figure 3.2).

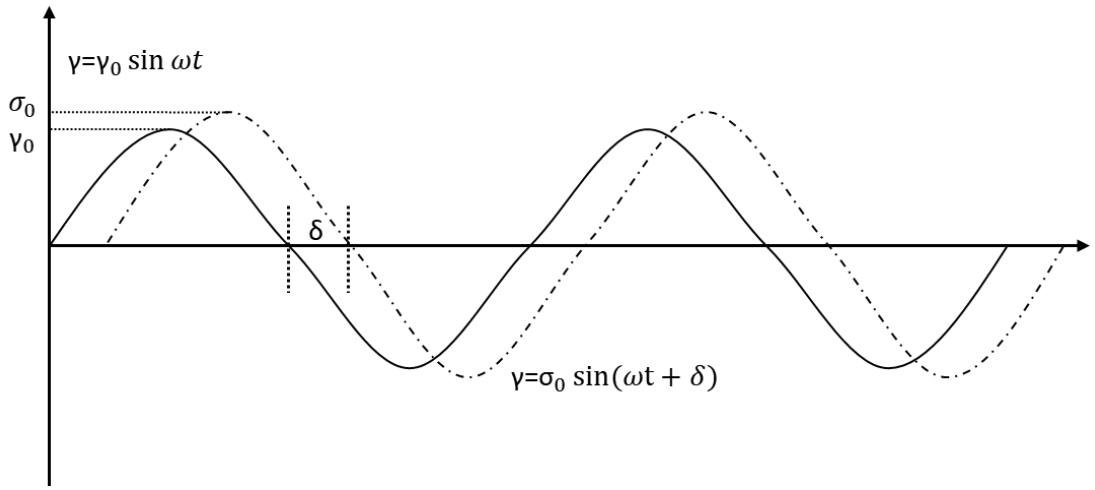

Figure 3-2 Curve of simple harmonic waveforms for stress input (solid line) and strain output (dash line)

By comparing the stress and strain curves, the complex modulus (G* = stress/strain) and phase difference (δ) are obtained.

$$\gamma=\gamma_0 \sin \omega t \tag{7}$$

$$\gamma=\sigma_0 \sin(\omega t+\delta) \tag{8}$$

Because the storage modulus is an instantaneous response to stress, while the loss modulus has a delay, the two vertical vectors of the complex modulus correspond to the storage and loss modulus, respectively. They are given by formula 9, 10 and 11 [10].

$$G^*=\frac{\sigma_0}{\gamma_0} \tag{9}$$

$$G'=G^* \times \cos\delta \tag{10}$$

$$G''=G^* \times \sin\delta \tag{11}$$

The moduli remain stable when the stress is relatively low, which is known as the linear viscoelastic region (LVR) [11]. However, if the stress reaches a threshold at which the response strain is no longer a perfect simple harmonic curve, the moduli start to change and the corresponding stress (strain) is considered the limiting point.

3.2. X-Ray Diffraction (XRD)

X-ray diffraction is an analytical technique that uses the diffraction of X-rays in a specific direction to identify the dimensions of molecular structures and chemical bonds in crystalline molecules. Since its invention in the 1920s, it has been widely used in crystal analysis, such as determining the size of atoms and the dimensions of chemical bonds [12]. Additionally, X-ray diffraction is also used to study biological macro-molecules such as proteins and DNA because of their regularly ordered structures, similar to crystal substances [13]. As a result, X-ray diffraction spectra can be used to confirm the presence of spatial structures and predict their parameters, such as distances.

Obviously, X-rays play a key role in X-ray diffraction measurements. X-rays are high-energy electromagnetic waves (radiation) with a wavelength range of 0.01 to 10 nanometres, possessing energy and penetration abilities between ultraviolet and gamma rays. Typically, X-rays are produced by the collision of high-speed electrons with metal in a vacuum tube. Electrons are emitted from a hot cathode and accelerated by a high-voltage electric field until they reach the target metal, which is placed in the anode. Tungsten (W) and its alloy are commonly used as the target metal for X-ray production in medical applications [14]. Copper (Cu) is the primary target metal used in crystallography analysis, including X-ray diffraction instrumentation [15]. The X-ray produced by the electron-metal collision process produces two dominant wavelengths, Kα and Kβ,

resulting from the jump of electrons from the L shell to the K shell and the M shell to the K shell. In a Copper target, Kα is 1.54184 Å and Kβ is 1.39222 Å [16].

The basic principle of X-ray diffraction is that the molecules of the sample act as a space diffraction grating for X-rays [17]. X-rays undergo reflection and diffraction as they interact with the electrons. Diffraction occurs when a wave encounters an object or hole whose size is smaller than the wavelength, causing the surface of the object or hole to become a wave source, emitting a new wave with the same frequency and amplitude but a different direction from the original wave. Additionally, wave diffraction is often accompanied by interference between the incident wave and the diffracted wave, meaning that the two waves superpose to create a new waveform. The resultant wave can have a higher, lower, or the same amplitude depending on the amplitude, frequency, and phase of the original waves. If the optical path difference of the two waves is a multiple of the wavelength, the wave peaks will be in the same position, resulting in an increase in signal intensity, which is observed as a peak in the X-ray diffraction spectra.

Bragg's Law describes the dimensions of the crystal lattice (figure 3.3). The simplified formula, based on the simplified crystal lattice model, is shown in Eq 12. The signal intensity peaks occur when the optical path difference between the diffraction and incident waves is an integer multiple of the wavelength.

$$n\lambda = 2d \sin\theta \tag{12}$$

where λ is the wavelength of the x-ray, d is the size or length and θ is the incident angle of the x-ray. n is any positive integer [18].

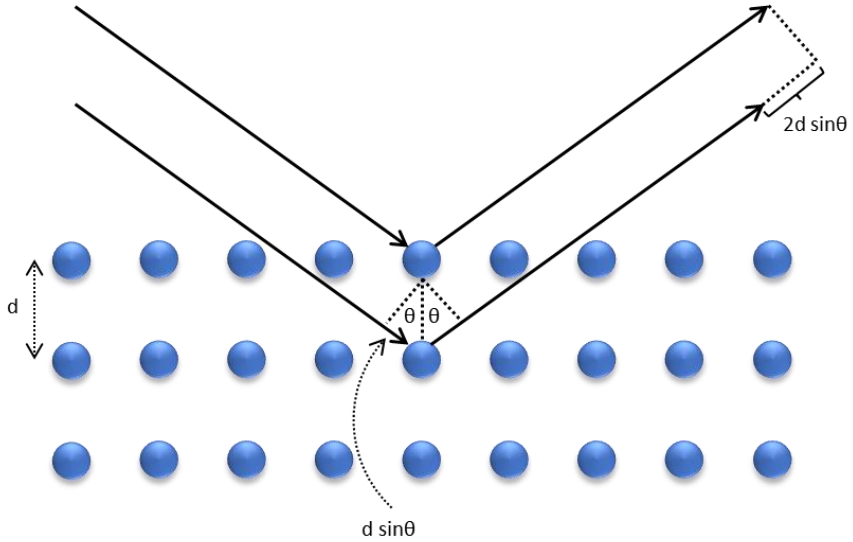

Figure 3-3 Schematic of Bragg diffraction

In order to obtain a single wavelength X-ray for XRD, a graphite monochromator is used to absorb the Kβ rays, ensuring that only Kα (1.54184 Å) reaches the sample. During the measurement process, the X-ray tube is moved around the sample to provide varying X-ray injection angles to the sample surface. The diffraction waves are recorded and monitored by a detector and are transformed into a diagram of peak intensity versus injection angles.

3.3. Atomic Force Microscope (AFM)

AFM, or atomic force microscope, is a type of scanning probe microscope (SPM) that creates images through physical interactions between a probe and a sample surface [19]. SPMs, such as AFM, differ from beam microscopes in several key aspects, such as not requiring a vacuum environment and not being affected by beam diffraction, which leads to improved resolution. In the case of AFM imaging, the probe need not come into direct contact with the sample but instead interacts with the sample's molecules or atoms through physical interactions. This results in a deformation of the cantilever. The deformation is recorded as the probe moves and is used to create an image. Typically, the image created by AFM shows the depth distribution of the sample

surface, as the deformation of the probe is determined by the probe's distance to the sample because of the distance-dependent nature of the critical interactions in AFM [19].

The Van der Waals force is one of the most significant physical interactions contributing to AFM imaging [69]. This force results from the fluctuating polarisations of atoms and molecules. This interaction is relatively weaker than ionic or covalent bonds, with an energy range of 0.4 to 4 kJ/mol [20]. The interaction is primarily caused by the electrostatic attraction between the dipoles of molecules or atoms, which are caused by the structure of partial charges (permanent dipoles) and temporary non-uniform electron distributions (temporary dipoles). The Van der Waals force is considered a short-distance interaction, as the attraction between transit dipoles becomes less significant at longer distances due to its relatively weak intensity [20].

Depending on the polarisation of the interacting molecules or atoms, van der Waals forces can be subdivided into three types: directional, inductive, and dispersive forces (also known as London forces). Directional forces occur between polar molecules that display a permanent dipole. However, inductive forces are usually observed between polar and non-polar molecules. Polar molecules induce a shift in the electron density of non-polar molecules, creating a temporary dipole attraction. Finally, dispersion forces dominate the van der Waals interactions between non-polar molecules. Research has revealed that the most likely cause of this force is the temporary dipole formed by the temporary electron density asymmetry caused by electron motion [21].

In the context of AFM imaging, the traditional method of imaging involves bringing the probe in close proximity to the sample surface and monitoring the deflection of the probe to create a contour of the sample. This method is known as the contact mode. However, due to the small probe-sample gap, the probe can easily come in contact with the sample surface, damaging both

the probe and the sample. To improve the lifetime of the probe and the repeatability of samples, a non-contact mode has been developed where the probe is positioned around 3 nm away from the sample surface and kept in vibration at a constant frequency using a cantilever. The interaction between the probe and the molecules reduces the frequency of vibration, which is monitored and recorded. However, the presence of a liquid meniscus layer on some sample surfaces can still cause the probe to come in contact with the sample surface. To overcome this, the tapping mode is used, where the probe performs an up-down movement at a high frequency. Usually, a feedback loop is used to maintain constant values for amplitude by moving the probe up or down as it rasters across the surface. It is the measurement of these up and down adjustments that provides the surface height map. As a result, the contours of the sample are constructed by measuring the amplitude variations at all (x, y) positions [19].

A well-designed structure is required to complete the imaging process in AFM, as shown in Figure 3.4. The probe is fixed in a cantilever close to the sample surface, and a laser beam illuminates the probe to monitor the variance and is reflected into a photodiode. AFM completes imaging by scanning the sample surface with the probe in the cantilever. When the probe bends due to the interaction with the sample surface, the laser reflected in the probe into the photodiode changes and can be recorded. The cantilever is then adjusted back, restoring the laser signal.

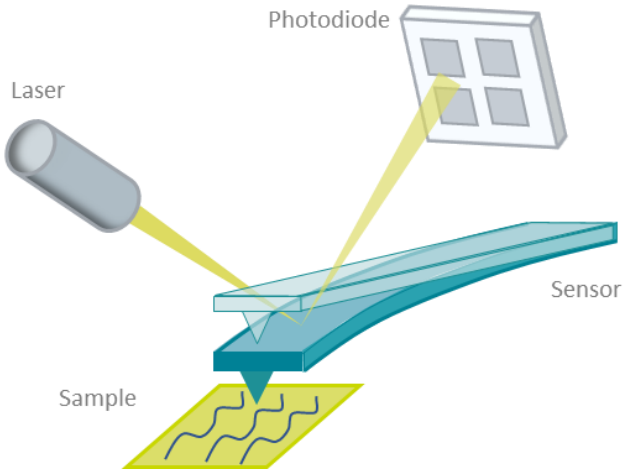

Figure 3-4 Schematic of AFM probe in imaging [70]

3.4. Anti-bacterial Assay

Anti-bacterial assay refers to the technique of measuring and monitoring the inhibitory effects of microorganisms' proliferation. With the use of a plate reader, several samples can be screened at the same time over a continuous and long period. The bacteria and target measuring compounds are set into the well-plate testing by the plate reader successively. One of the most well-known methods to assess bacterial concentration is OD 600, which is the visible light absorbance at 600 nm wavelength. The advantage of this wavelength is that spherical bacteria show the highest absorbance at 600 nm. Besides, bacteria are the unique substance causing significant absorbance at this wavelength, producing proportional absorbance to bacterial concentration [22]. However, this method is limited to spherical bacteria only, including yeast [23]. Those irregular shaped bacteria, such as actinomycetes, are not available as the shape is known to be a factor impacting light absorbance. The advantage of OD 600 measurement is that 600 nm wavelength light does not influence the growth or behaviour of bacteria, allowing for continuous monitoring.

UV (Ultraviolet) is a type of electromagnetic wave with a wavelength between 200 and 400 nm. Substances exhibit varying UV absorbance abilities at different wavelengths, making it possible to predict molecular structure based on the wavelength of absorbance peaks. The Beer-Lambert law [24] formulates the number of absorbances, which is Eq 13.

$$A = \varepsilon cL = -\log {}^{I}/_{I_0} \tag{13}$$

where A is the absorbance, ε is the absorption coefficient, c is the molar concentration of the solution, L is the path length of the cuvette, I_0 is the intensity of incident light, I is the intensity of transmitted light.

The growth of bacteria can typically be divided into four phases according to the bacteria proliferation speed: lag phase, exponential phase, stationary phase, and death phase. The lag phase is loosely described as the period of no obvious increase in bacterial concentration at the beginning, when bacteria prepare for growth followed by proliferation with redundant resources in the exponential phase. During this period, the density of bacteria increases exponentially without any limitation due to resource shortcoming. Once resources reach a threshold where nutrition is not rich enough to support unlimited proliferation, the increase in bacterial concentration begins to slow down. The stationary phase occurs when the growth rate further declines to around zero, meaning the number of bacteria spreading is close to death. Finally, when resources become too scarce to support the existing bacteria, the number of microorganisms begins to decline with time, indicating the end of the system, known as the death phase. Typically, assay tests cover the process between the lag phase and the stationary phase, making sure the exponential phase is included, which is the focus of anti-bacterial tests due to the highest proliferation ratio during this period.

In terms of assay design, E. coli was chosen to evaluate its anti-bacterial ability because it is defined as a model organism in research. The major advantage of E. coli is that it can be not only easily grown and cultured but also inexpensively in a laboratory [25]. Well-researched is another benefit, including being the first organism to have its complete genome sequence published [26]. In terms of biological classification, E. coli is a Gram-negative, facultatively anaerobic, rod-shaped bacterium, and its major strains have been proven to be harmless.

3.5. Circular Dichroism Spectrum

Circular dichroism (CD) is the dichroism of circularly polarised light. It presents as the differential absorption of left- and right-handed light. The difference in electron spins angular momentum monitored in left-hand and right-hand light gives rise to the circular dichroism. Therefore, circular dichroism is also called electron spin angular momentum dichroism [27]. Clearly, the CD spectrum is a spectrum based on the CD phenomenon used to measure the absorbance difference between two directions of circularly polarised light.

Light is a transverse wave with its oscillation direction being vertical to its advance. Non-polarized light, which is commonly seen in daily life, has a random oscillation direction. However, polarized light (figure 3.5), which has been studied extensively, has a specific oscillation direction giving it useful optical properties, such as dichroism. Polarised light can be further divided into linear polarised light, which has an unchanging oscillation direction, and circular or elliptical polarised light, which has a rotating oscillation direction. Combining two circular polarised lights with the same amplitude and frequency but opposite directions can produce linear polarised light. Therefore, the linear polarised lights are the light source of CD spectroscopy [28].

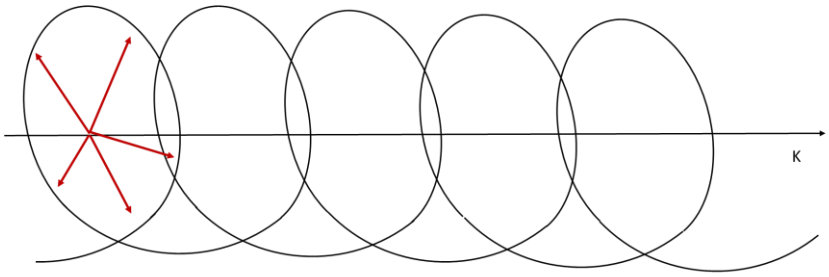

Figure 3-5 Schematic of polar light

When linear polarised light passes through chiral molecules, it is divided into left- and right-hand circular polarised light, with different absorbance levels. The absorbance difference results in a phase difference and amplitude variance between the two circular polarised lights. The different absorbance leads to the combination light being elliptically polarised light. Based on this phenomenon, CD spectroscopy was developed to monitor the produced elliptically polarised light to assess the absorbance difference, which provides information about the structure of chiral substances.

Many researchers widely use CD spectroscopy in the analysis of biological molecules, as a high percentage of dextrorotary and levorotary ingredients are present in biological molecules, including the peptide bonds connecting amino acids in peptides and proteins [27]. As a result, distinct protein secondary structures also exhibit unique CD spectra, as the direction of peptide bonds changes with the peptide chain folding structure. The most well-researched secondary structures, such as α-helix and β-sheet, both produce distinct CD spectra, which are used as standard curves for CD spectra analysis. Based on the standard curve, regression fitting can determine the percentage of secondary structures, revealing the 3D composition of peptides or proteins.

The intensity of CD is given in Eq. [29]

$$CD = A_l - A_r = \Delta A \tag{14}$$

where A_l and A_r are the absorption of left- and right-hand light. Meanwhile, the definition of ellipticity in polarised reflection light is Eq. [29]

$$\theta = \tan^{-1}\frac{I_L - I_R}{I_L + I_R} = 32.98° \times \Delta A \tag{15}$$

where I_L and I_R are the amplitude of left- and right-hand light. There is a very simple conversion between elliptical and absorption differences after a series of mathematical treatments. Using the Lamber-Beer law, the elliptical can be written as in Eq. [29]

$$\theta = 32.98° \times cl \times (\varepsilon_l - \varepsilon_r) \tag{16}$$

The CD spectrum equipment gives linear polarised light with a series of wavelengths and monitors the ellipticity of the polarised light after the sample absorption. The CD spectrum is the ellipticity of the reflected light against the light wavelength.

3.6. Nuclear Magnetic Resonance (NMR)

NMR stands for Nuclear Magnetic Resonance. Nuclear Magnetic Resonance is a physical phenomenon where atoms with odd numbers of protons or neutrons respond to electromagnetic signals in a high-intensity, constant magnetic field. Therefore, NMR is a technique used in chemistry and physics to study the structure and properties of molecules. It relies on the magnetic properties of atomic nuclei to provide information about the atoms in a molecule. In NMR spectroscopy, a sample is placed in a strong magnetic field and exposed to a radio frequency pulse. The nuclei in the sample absorb energy from the pulse and emit it in a characteristic frequency, which can be used to determine the chemical structure and properties of the molecule. Several factors, including the type of chemical bonds and adjacent atoms, can affect the frequency of the

signal from the target atom. NMR is widely used in various fields, such as medicine, biology [30], materials science [31], and environmental science. In material science, NMR is regarded as a well-known tool proving the achievement of chemical reactions, as the variance in chemical bonds causes the difference in relevant signals [32].

The magnetic field from atom spin has made a contribution to the NMR signal. All nucleons consisting of atoms present spin with intrinsic angular momentum similar to classic spheres. The angular momentum S is quantum via the relation.

$$S = \hbar\sqrt{s(s+1)} \tag{17}$$

where s is the spin quantum number which can only be an integer and half-integer while $\hbar$ is the reduced Planck constant. For the atom with an even number of protons and neutrons, the overall spin quantum number is zero as the spin quantum numbers are both 1/2 in proton and neutron. For the non-zero S atoms, there are magnetic dipole moments, μ, presenting given by

$$\mu = \gamma S \tag{18}$$

γ is the gyromagnetic ratio. Therefore, the magnetic moment only practices in the odd number of protons or neutrons atoms leading to the NMR being only observed in the atoms with the odd number of protons or neutrons.

For atoms with non-zero magnetic moments, if the direction of the spin magnetic moment differs from the given magnetic field, the spin magnetic moment precesses due to the force from the magnetic field, which appears as the oscillation of the spin axis. The frequency of precession is constant in a constant magnetic field for certain atoms. However, this consistency depends on the element, chemical bonds, and adjacent atoms. For example, there is a difference in the NMR

spectra of carbon atoms in methane and chloroform. As a result, the number of frequency-responding signals gives information about the number of atoms in different states, which can be used to determine the structure of a molecule and distinguish between isomers.

Hydrogen (^{1}H) and carbon 13 (^{13}C) are the two most commonly used atoms in NMR spectroscopy [33], particularly hydrogen, due to their widespread presence in biological molecules. Typically, deuterium oxide and deuterium-containing chloroform are popular polar and non-polar solvents in ^{1}H NMR measurements to avoid interference from hydrogen atoms in the solvent. The signal peak area, chemical shift, and spin coupling/spin splitting in NMR spectra can identify the structure. The signal peak area is in proportion to the number of hydrogen atoms in the same chemical environment. In terms of chemical shift, the electron shielding from adjacent atoms on a hydrogen atom is responsible for the chemical shift, which separates the signals in the NMR spectrum, providing information to identify the peaks. Therefore, even though both atoms are hydrogen, there are still variations in signals when the hydrogen atoms are in different chemical environments. Similar to FTIR, the signals at specific chemical shifts have been used to distinguish structures by comparing them with standard curves or peaks. On the other hand, spin coupling/spin splitting is similar to chemical shift but is attributed to the shielding from nearby protons. In NMR spectra, spin splitting generally results in the splitting of a signal peak into several smaller peaks, which also helps to predict the structure of molecules [34].

3.7. Fluorescence Spectroscopy

Fluorescence spectroscopy, also known as fluorescence analysis or electromagnetic spectroscopy, involves the use of excitation and emission spectra. When the detected emission wavelength is fixed and a series of excitation beams are applied across the sample, the excitation

spectrum is obtained [35]. In contrast, in the emission spectrum (the typical fluorescence spectrum), the excitation light wavelength is kept constant while the detection wavelength is varied. The measurement process involves exposing molecules or atoms to a beam of light, typically ultraviolet but also visible light, which excites their electrons to a high energy level. When the electrons return to their previous energy level, they emit light, which is detected.

As discussed above, when an electron is excited by a light beam and relaxes by emitting a photon instead of changing spin, fluorescence light occurs at a longer wavelength than the excitation light. The figure 3.6 gives the schematic for electron activation and Illumination. Electrons in the ground state, S_0, absorb a photon from the excitation light, gaining energy and becoming excited to a higher energy level, S_2^*.

$$S_2^* = S_0 + he_{em} \tag{19}$$

where h is the Planck's constant, e_{ex} is the energy in proton from excitation light [36].

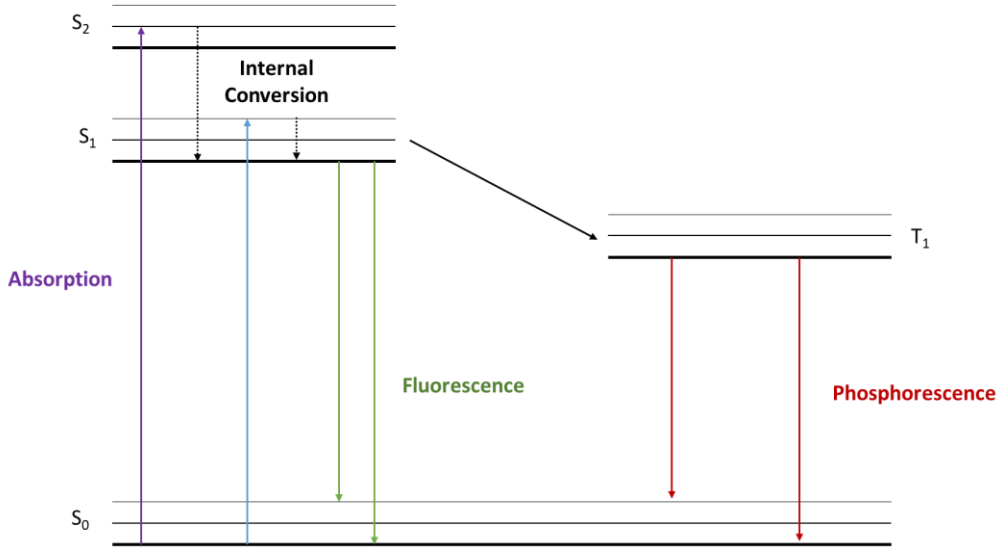

Figure 3-6 Schematic of fluorescence releasing

When the S_2^* molecules interact and transfer energy to the solution molecules by the non-radiation process, for example, internal conversion, the energy dissipation presents in excites molecules by heating. The S_2^* molecules relax to a lower vibration level, S_1^*. The fluorescence molecules release a photon, which emits fluorescence light finishing the relaxation process from the excitation state to the ground state.

$$S_1^* = S_0 + he_{ex} \quad (20)$$

where e_{em} is the energy of the photon in fluorescence light. The fluorescent process is given by

$$S_0 + he_{ex} = S_1^* \rightarrow S_2^* = S_0 + he_{em} \quad (21)$$

Due to the energy dissipation from S_2^* state to S_1^* state, the emission photons are lower in energy in comparison to photons in excitation beam, exhibiting longer wavelength in emission light.

Meanwhile, increasing research on the quenching of fluorescence has been carried out, which demonstrates that molecules emit weaker intensity fluorescence, or even no fluorescence when they are in close proximity to a chromophore at a preferred distance [37]. The quencher can interfere with both the excitation and emission process through several different mechanisms. If the quencher forms a non-fluorescent compound with the fluorescence molecule, for example, a complex, then the emission will not be observed. Furthermore, a number of studies have revealed that quenching relies on Förster Resonance Energy Transfer (FRET), where excited molecules transfer energy to nearby receiver molecules, losing energy and not emitting light [38]. Fluorescence quenching reactions are now commonly used in distance-related experiments, for example, by connecting a fluorescence and quencher on opposite sides of a composite.

Fluorescence spectroscopy typically involves a light beam source, a filter that isolates incident light, and a detector generally set in vertically with the light source to avoid the interference of incident light as much as possible. 300-800 nm is known as the typical wavelength range for the spectroscopy coving near ultraviolet and visible light, which are the excitation wavelength for general fluorescence molecules. In the test, the measuring region of the excitation spectrum is demanded in a lower number than the fixed emission wavelength whereas the target zone stays in a higher wavelength than the excitation beam in the emission spectrum.

3.8. Matrix-assisted laser desorption/ionization-time-of flying (MALDI-TOF)

MALDI-TOF, short for Matrix-assisted laser desorption/ionization time-of-flight, is a type of mass spectrometry that is used to determine the mass-to-charge ratio of ions. This technique has been widely used in isotope separation and the structure prediction of biological macromolecules such as peptides [39]. In MALDI-TOF, samples in various states, including gas, liquid and solid, are ionized using techniques such as electron bombardment. The ions are then propelled through an electromagnetic field, and the time it takes for them to travel a certain distance is measured, which reveals their mass-to-charge ratio.

The ionisation system is one of the critical components of MALDI-TOF mass spectrometry. The system of ionization is typically classified as hard ionization and soft ionization, depending on the energy transferred to sample molecules. A major advantage of hard ionization, particularly electron beam bombardment, is the high degree of fragmentation, giving more detailed information about the sample's structure. However, it requires a high vacuum due to the fragility of electron filament in the atmosphere. On the other hand, soft ionization provides a higher integrity of the target molecules, which closely approximates their molecular weight, and is widely

used in the verification of reaction products. MALDI is considered a member of the soft ionization methods, where the sample is embedded in a laser-absorbing matrix, which releases small fragments upon exposure to a laser [40]. MALDI is a popular choice for ionizing biological molecules, as it avoids over-fragmenting fragile biomolecules [41]. The process of MALDI (figure 3.7) typically consists of three steps: 1) Mixing a suitable matrix solution with the sample and drying the mixture on a plate; 2) exposing the matrix to laser irradiation, causing both the sample and matrix to be ablated and desorbed; 3) protonating or deprotonating the sample molecules in the high-temperature ablation gaseous atmosphere.

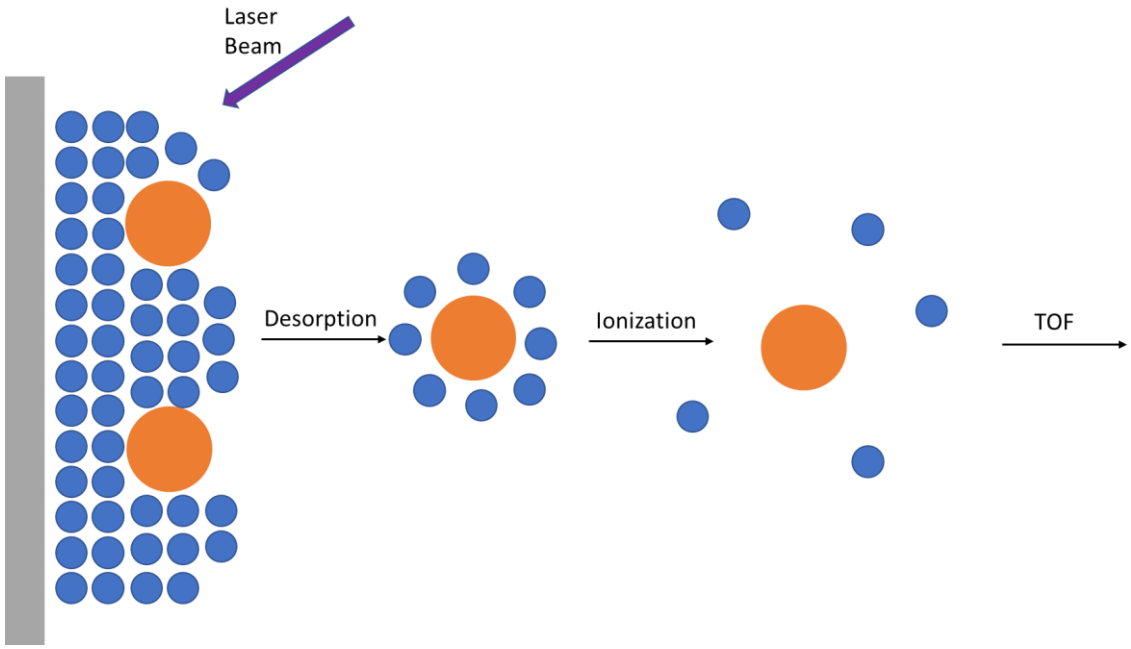

Figure 3-7 Schematic for the process of ion releasing from the matrix

Following ionization, ions enter the electromagnetic field doing motion driven by Lorentz force (magnetic field force) and electric field force, giving the formula 21 and 22.

$$F_M = qvB \tag{22}$$

$$F_e = Eq \tag{23}$$

where F_M and F_e are Lorentz fore and electric field force respectively, q and m are charge and mass of ion respectively, B is intensity of magnetic field and E is intensity of electric field. The direction of the Lorentz force is always perpendicular to the direction of velocity, while the electric force follows the direction of the electric field. In Time-of-Flight (TOF) measurements, the electric field accelerates the particle and serves to measure m/z. However, the magnetic field is not necessary and is only switched on when it is necessary to screen the m/z of the particles. In the equipment, two parallel plates are used, where the electric field are applied parallel to the plates. Ions are accelerated by the electric field and detected by the time it takes for them to cross the plate region. The electric potential energy and kinetic energy are given by Eq 23 and 24.

$$E_p = qU \tag{24}$$

$$E_k = \frac{1}{2}mv^2 \tag{25}$$

In process, all potential energy converts to kinetic energy, meaning the equal of two formulas.

$$\frac{1}{2}mv^2 = qU \tag{26}$$

Due to the pathway of the plates being known and time across the region being available by detection, velocity can be replaced by length (d) and time (t)

$$v = \frac{d}{t} \tag{27}$$

After a simple mathematical re-formation, the mass-to-charge ratio is shown in Eq 27.

$$t = \frac{d}{\sqrt{2u}}\sqrt{\frac{m}{q}} \tag{28}$$

Therefore, according to the detected flying time, we can infer the mass-to-charge ratio of ions.

Under well-designed MALDI methods, samples are ionized with only one positive or negative charge, making it possible to predict the molecular weight (Mw). Furthermore, high molecular weight samples (over 10 KDa) can be analysed with a better resolution by using two electromagnetic fields in succession. This is achieved by reflecting ions back after the first drift. Therefore, the MALDI-TOF technology is currently used in the analysis of biological reactions, measuring molecular weight to predict the composition of products [42].

3.9. Ultraviolet Spectroscopy (UV)

Ultraviolet (UV) radiation is a family of electromagnetic radiation with a wavelength between 10 nm and 400 nm, which is shorter than the wavelength of visible light. Because of the shorter wavelength, UV light has higher electromagnetic energy than visible light, which can break down short DNA or RNA molecules. As a result, UV is widely used in sterilization. In laboratories, electric arcs or specialized lights, such as mercury-vapour lamps, are commonly used as sources of UV radiation [43].

Ultraviolet spectroscopy refers to electromagnetic spectroscopy that covers the ultraviolet and adjacent visible regions. Similar to infrared spectroscopy, both reflection and absorption spectra are available in UV spectroscopy. In UV spectroscopy, chromophores are essential, which means molecules or ions that absorb in the UV region. Chromophore substances absorb protons from UV radiation, acquiring energy to excite their electrons to higher energy orbitals. There are four types of transitions occur: π–π^*, n–π^*, σ–σ^*, and n–σ^*. The Beer-Lambert law explains the relationship between absorbance intensity and the concentration of chromophore substances in the sample solution, and the path length of the cuvette. The wavelength of UV peaks is used to

characterize the structure of organic molecules because different bonds exhibit various electron transition types, corresponding to various absorption wavelengths.

UV spectroscopy is widely used in the estimation of purification and concentration of biomacromolecules [44], such as peptides, proteins, nucleotides, RNA, and DNA. The absorbance at different wavelengths, such as 210 nm for peptides [45], 280 nm for proteins [46], and 260 nm for nucleotides, is used to determine the concentration and purity of the samples. The 280 nm is the absorbance wavelength of the aromatic amino acids, involving tyrosine, phenylalanine, and tryptophan [46]. Meanwhile, the purines and pyrimidines in nucleotide have conjugated double bonds whose UV absorbance is in the 260 nm [47]. Additionally, the proportion of OD 260 to OD 280 is used as a standard to measure the purification of nucleotides from proteins, and the OD260/OD230 ratio is used to detect pollution from salts or organic compounds. Furthermore, the hyperchromic effect of UV spectroscopy is employed to test the pairing of nucleotides, as paired nucleotides show lower UV absorbance than unpaired ones, which results in a decrease in OD 260 when single strand DNA or RNA forms a double strand.

3.10. High-performance liquid chromatography (HPLC)

High-performance liquid chromatography (HPLC) is known as a technique in analytical science able to achieve specific molecule separation, identify, and quantify of each component in a mixed system, relying on the difference in solubility of component [48]. It was employed not only in analysis the purification of purchased peptide powder but also for the conjugate separation from peptide and oligonucleotide after reaction. Compared to traditional liquid chromatography, the higher pressure from the pump is the primary advantage of HPLC making contribution to a better

separation ability due to the particle size in column can be smaller which decides the ability to distinguish between compounds.

In HPLC, the sample is injected into the system and is then passed through a column packed with the stationary phase, typically silica or resin. The molecules in the sample interact differently with the stationary phase based on their chemical properties, leading to the separation of the components in the sample. The separated components are then detected and quantified using a variety of detection methods such as UV-Vis, fluorescence, or mass spectrometry. HPLC is a widely used technique in the pharmaceutical and biotechnology industries [49], as well as in food and environmental analysis. It has the ability to separate and quantitate compounds that are difficult to separate by other methods. Additionally, HPLC is also highly sensitive and able to detect trace amounts of compounds, making it a powerful tool in analytical science.

The interaction of the mobile phase (sample) with the stationary phase (separation column) is the main factor affecting the separation of the sample. The chemical surface on the particles (stationary phase) interacts with the sample molecules, influencing their solubility and rate of passing through the column. Based on the difference in rate, the components are separated by the time in HPLC, which is called retention time. A series of physical or chemical interactions between the mobile and stationary phase, including chemical affinity, hydrophobicity, ionic force, porous size, as well as polarity, causes the variation in retention time between chemical species. Polar-based column involves both normal-phase HPLC and reversed-phase HPLC, which is a type of HPLC employed in this experiment whose stationary phase is non-polar while the mobile phase is polar. In that column, the more polar substance will stay in for a shorter retention time.

Typically, the mobile phase in HPLC involves a combination of water and an organic solvent, for example, acetonitrile [50]. It may also contain acids like trifluoroacetic acid or salts such as lithium perchlorate, to aid in separating the sample components. The composition of the mobile phase can be constant or varied. The varied composition mobile phase is known as gradient elution, which can give a quicker separation of the mixture system. The benefit of gradient elution is the high separation efficiency of target components with distinct affinities to the stationary phase. Typically, the percentage of organic solvent in the mobile phase is changed from a low level to a higher level. It may also contain acids like trifluoroacetic acid or salts such as lithium perchlorate, to aid in separating the sample components.

In the term of equipment, commonly, HPLC is main consisted by pump, sample injector, column, detector, degasser and temperature controller (figure 3.8). In that, the pump is one of the most important parts of the liquid chromatography system, mainly to pump the solvent from the storage into the mobile phase system, and to keep the flow as well as pressure stable under high pressure. Meanwhile, another key section in HPLC is the column mainly used to separate components in mixtures relied by the interaction introduced in above paragraph. Stainless steel-cased columns are commonly employed due to its resistance to many solvents while typically filled by silica or polymer gels. Moving to the detector, it is designed to expose the components separated by the chromatographic column. When the present of target analyte can change the composition of the eluate leading to the peak in detector spectrum. The detector can measure this difference and convert it into an electrical signal for the record. There are many kinds of detectors, such as ultraviolet-visible light detectors, fluorescence detectors and electrochemical detectors [51].

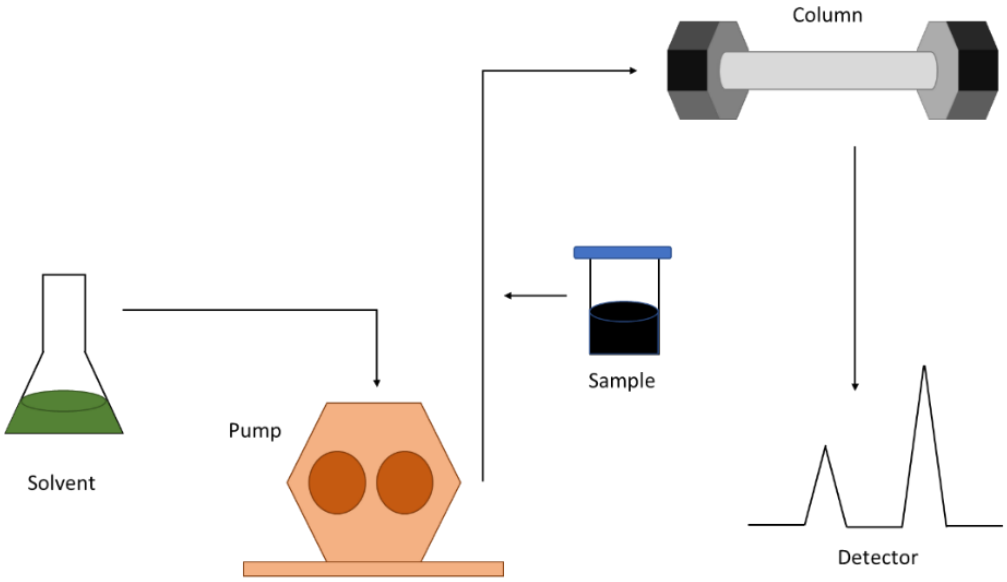

Figure 3-8 Structure of HPLC equipment

3.11. Fourier-transform infrared spectroscopy (FTIR)

Fourier-transform infrared spectroscopy (FTIR) is a technique that uses a mathematical process called the Fourier transform to obtain the absorption or transmission infrared spectrum of a substance [52]. This approach allows for easy measurement and sample preparation, and there are no limitations on the condition of the sample, as it can be a solid, liquid or gas.

The infrared spectrum is a result of the infrared absorption caused by molecular vibrations and rotational transitions. There are four types of molecular motion: translation, rotation, vibration, and electron motion, but only two of them lead to a response in infrared absorbance. The chemical bonds or functional groups in a molecule are constantly vibrating or rotating. When the vibration frequency is the same as the frequency of infrared light, the chemical bonds or functional groups in the molecule absorb the IR by vibrational absorption [52]. Different chemical bonds or functional groups have different absorption frequencies and will appear in different positions on the infrared spectrum, allowing for the identification of the chemical bonds or

functional groups present in the molecule. Molecules absorb a photon with energy hv from a lower energy level E_1 and can transition to a higher energy level E_2, in accordance with the law of energy conservation E_2-E_1=hv (h is the Planck constant and v is the frequency). The smaller the difference between the energy levels, the lower the frequency and the longer the wavelength of the light absorbed by the molecule [52].

The infrared spectrum typically involves three regions: the near-infrared region (13333-4000 cm^{-1}), the mid-infrared region (4000-400 cm^{-1}), and the far-infrared region (400-333 cm^{-1}). Generally speaking, the near-infrared spectrum is caused by the multiple frequency and combination frequency of the molecules. The mid-infrared spectrum corresponds to the fundamental frequency vibrations of the molecule, while the far-infrared spectrum is related to the rotational motion of the molecule and the vibrational motion of certain groups. Since the fundamental frequency absorption bands have been well researched for structure identification, and the bands of most organic and inorganic substances appear in the mid-infrared region, the mid-near-infrared spectrum has been widely employed [53].

According to the wavenumber of the absorption peak, the mid-infrared spectrum (4000-400 cm^{-1}) can be roughly divided into two areas: the characteristic frequency region (4000-1330 cm^{-1}) and the fingerprint region (1330 cm^{-1}-400 cm^{-1}) [54]. The absorption peaks in the characteristic frequency region are primarily generated by the stretching vibration of certain groups, and the number of peaks is relatively low but they show strong characteristics. This region is highly valuable for structure identification and is mainly used to identify functional groups. For example, carbonyl has a strong absorption peak between 1760-1665 cm^{-1} in stretching vibration, regardless of whether it is in ketones, acids, esters, or amides. If there is a strong absorption peak between

1760-1665 cm^{-1} in the spectrum, it can be roughly concluded that there is a carbonyl group in the molecule [55].

On the contrary, the fingerprint region is different. There is a large number of complex peaks in this region, and the peaks lack strong characteristics. It is mainly caused by the stretching vibration of single bonds such as C-O, C-N and C-X (halogen atoms), the bending vibration of hydrogen-containing groups such as C-H and O-H, as well as the C-C skeleton vibration [56]. When the molecular structure is slightly different, there are subtle differences in the peaks of this region.

The key component of FTIR equipment is the Michelson interferometer [57], which produces infrared light of varying wavenumber by interfering two beams of light with a different optical path difference. Michelson interferometer is an optical instrument that uses the principle of interference to measure small changes in distance or wavelength. It consists of a beam splitter that divides a light beam into two separate beams, one of which is reflected off a fixed mirror and the other off a movable mirror. The beams are then recombined and directed onto a detector. The difference in path length between the two beams causes interference, and the position of the movable mirror can be adjusted to control the phase difference between the two beams. This allows for precise measurements of small changes in distance or wavelength. The Michelson interferometer (figure 3.9) is widely used in scientific and industrial applications, including spectroscopy, metrology, and interferometry. In FTIR, the wavenumber of the IR light from the source is adjusted by the moving mirror. The infrared beam with a designed wavenumber passes through the sample before being collected by a detector and processed by Fourier-transform to obtain the final spectrum.

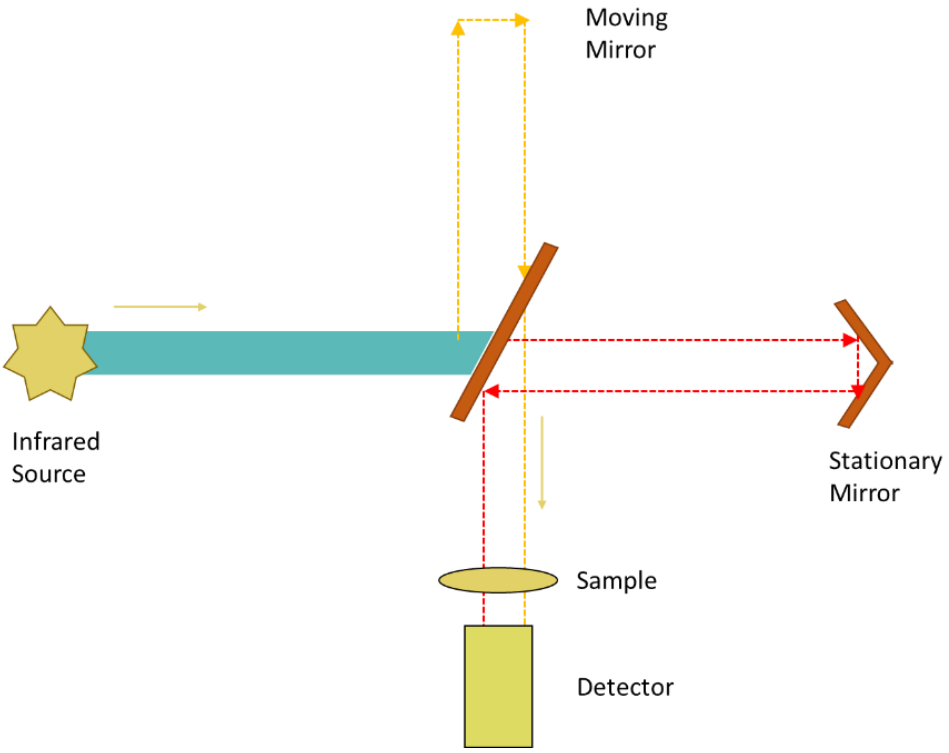

Figure 3-9 Structure of Michelson interferometer in FTIR

In summary, FTIR is a technique that uses the principles of Fourier-transform to obtain the absorption or transmission infrared spectrum of a substance. It is a versatile technique that can be used for both solid, liquid, and gas samples. The infrared spectrum is generated by the vibrations and rotations of the molecules in the sample, with different chemical bonds and functional groups absorbing at different frequencies. FTIR typically covers three regions of the spectrum: near-infrared, mid-infrared, and far-infrared. The mid-infrared region is particularly useful for structure identification, with the characteristic frequency region being used to identify functional groups and the fingerprint region being useful for subtle differences in molecular structure.

3.12. Transmission electron microscopy (TEM)

The Transmission Electron Microscope (TEM) is a microscopy technique that uses an accelerated and focused beam of electrons to image thin samples. When the electron beam

collides with atoms in the sample, it causes a change in direction, producing a solid angle scattering. The scattering angle is related to the density and thickness of the sample, resulting in images with varying light and dark areas. According to the Rayleigh Criterion, the resolution of microscopy is inversely proportional to the wavelength of the beam. Thus, a beam with a lower wavelength allows for better resolution (Eq 28).

$$d = \frac{0.61\lambda}{NA} \tag{29}$$

Because the de Broglie wavelength of electrons is accepted to be very short compared to visible light, the resolution of transmission electron microscopy (TEM) is much higher than that of optical microscopy. TEM can reach resolutions of 0.1 to 0.2 nm [58], resulting in magnifications of tens of thousands to millions of times. The electron wavelength can be calculated using the kinetic energy of the electron through the de Broglie formula. However, in TEM, the speed of electrons is close to the speed of light (c), so the wavelength must be corrected using the theory of relativity, shown in Eq 29.

$$\lambda_e = \frac{h}{\sqrt{2m_0E(1 + \frac{E}{2m_0C^2}}} \tag{30}$$

where h is the Planck's constant, m_0 is the static mass of the electron, and E is the energy of the electron after acceleration.

The use of transmission electron microscopy (TEM) is widely employed to observe the nano-structure of a sample, even the structure of a column of atoms, thousands of times smaller than the smallest structures that can be observed by optical microscopy. In terms of the image, the light and darkness are produced by different interactions based on the magnification, while the threshold depends on the type of TEM. At lower magnifications, the contrast in TEM imaging is

mainly due to the different absorption of electrons due to the different thicknesses and compositions of the material.

Turning to the equipment, TEM mainly involves three parts: the electron source, the imaging system, and the detector [59]. In terms of the light source, it mainly consists of an electron gun (Gun) that produces the electron beam and an electron gun deflector (Gun Deflector). There is an accelerating electric field between the electron gun and the deflector, which is used to accelerate the electrons generated by the electron gun. The accelerating electric field is produced by an accelerating voltage, which can be changed according to the actual situation of the experiment. The electron gun deflector is designed to deflect the electron beam coming out of the electron gun because most of the electrons are not perfectly moving along the designed beam axis, and the deflector is often required for a preliminary adjustment. There is also the condenser lens, which generally has two condenser lenses, used to focus the electron beam for interacting with the sample. There are also other adjusters to make sure the beam reaches the sample in a circular spot. Moving on to the imaging system, it mainly involves a series of lenses to improve resolution and avoid interference with the electron beam. For example, two objective lenses, one above and one below the sample, are used to focus the beam on the sample for interference and focus the beam after interference, respectively. Finally, the detector accepts the beam after interaction with the sample and produces the images. The optical path from the light source to the sample is shown in Figure 3.10.

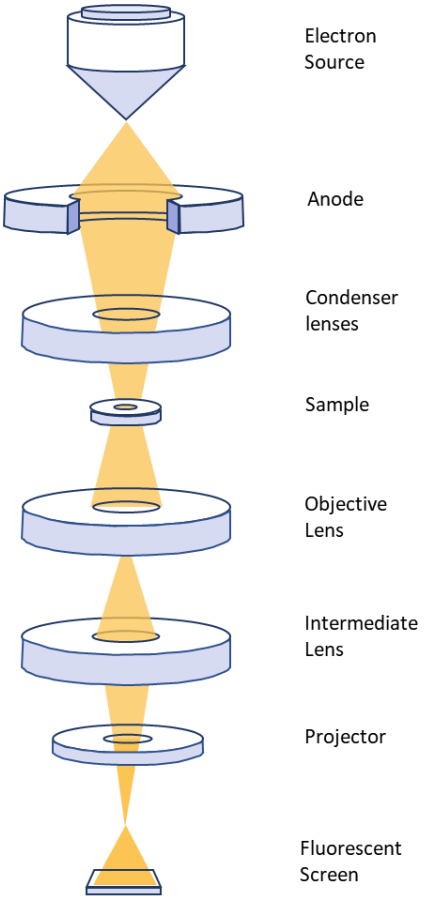

Figure 3-10 Structure of TEM

3.13. 3D-Printer

3D printing, also known as additive manufacturing, typically refers to any process of three-dimensional printing objects by injecting material powder layer by layer in a controlled manner, using inkjet printheads. The process of 3D printing is primarily additive, layering raw materials under computer control. 3D printing can be controlled by 3D models, allowing for the printing of objects with any reasonable shape and geometric features. This approach has been widely used in large-scale customisation manufacturing [60] due to its accessibility to various shapes of the printed object.

Therefore, based on the principles of 3D printing, 3D bioprinting was proposed as a method to produce scaffolds by 3D printing using bio-compatible ink. It is followed by embedding cells or

medicine, such as growth factors [61]. The benefits of this approach include high biocompatibility, which mimics natural tissue characteristics [62]. In general, 3D bioprinting utilises a layer-by-layer method to deposit materials called bioinks to create tissue-like structures that can be used in various fields of medicine and tissue engineering. Recently, bioprinting has been used to print tissue and organ models to aid in studying drugs and potential treatments [63].

Researchers in the field of 3D bioprinting has proposed several strategies to produce objects that contain living organs with appropriate biological and mechanical properties [64]. Biomimicry and self-assembly are the two main methods for 3D bioprinting. Biomimicry refers to the precise replication of natural structures through layer-by-layer and point-by-point printing [65]. The self-assembly method involves triggering the formation of target bio-objects automatically by setting cells and well-designed bioink materials together.

In the structure of a bioprinter, the machine commonly consists of inkjets and a surface. The inkjets typically include a tube that holds the ink, a nozzle for the inkjet, a pump that provides pressure to push the ink out, and a heater that controls the temperature of the ink before it is pushed out. The surface, on the other hand, serves as the printing site and provides a non-bacterial environment, as well as triggers for self-assembly, such as temperature and UV.

3.14. THT assay

Thioflavin is known as a family of fluorescent compound dyes produced by methylation of dehydrothiotoluidine with sulfonic acid, including the two most popular examples, Thioflavin T (THT) and Thioflavin S (THS). Both are reported to be used for histology staining and biophysical studies of protein aggregation, particularly the THT in the research of Alzheimer's disease and other neurodegenerative diseases [66].

In research, THT is widely used in vitro and in vivo to visualise and quantify measurement for the β-sheet. When bounding to β-sheet rich structures, such as the protein found in amyloid aggregates, the dye exhibits enhanced fluorescence and a characteristic red shift in its emission spectrum [67]. This change in fluorescence behaviour may be caused by a number of factors affecting the excited-state charge distribution of thioflavin T, including the binding to rigid, highly ordered nano pockets, and the specific chemical interactions between thioflavin T and nano pockets. Thioflavin T emits weak light around 427 nm before binding to β-sheet while the excitation peak around 450 nm was quenched due to the double ring structure in Thioflavin T molecules which can rotate freely in solution [68]. The THT contents a benzylamine and a benzothiazole ring linked by a carbon-carbon bond. When it binds with β-sheet, Thioflavin T produces a strong fluorescent signal at approximately 482 nm, by the excitation at 450 nm. It is because the double ring is fixed so the molecule can retain its excited state.

Reference

[1] Lee I B, Cho B H, Son H H, et al. Rheological characterization of composites using a vertical oscillation rheometer. Dental materials, 2007, 23(4): 425-432.

[2] Banks H T, Hu S, Kenz Z R. A brief review of elasticity and viscoelasticity for solids. Advances in Applied Mathematics and Mechanics, 2011, 3(1): 1-51.

[3] Weihs D, Mason T G, Teitell M A. Bio-microrheology: a frontier in microrheology. Biophysical journal, 2006, 91(11): 4296-4305.

[4] Klapper I, Rupp C J, Cargo R, et al. Viscoelastic fluid description of bacterial biofilm material properties. Biotechnology and bioengineering, 2002, 80(3): 289-296.

[5] Papaioannou T G, Stefanadis C. Vascular wall shear stress: basic principles and methods.

Hellenic J Cardiol, 2005, 46(1): 9-15.

[6] Skarja G A, Kinlough-Rathbone R L, Perry D W, et al. A cone-and-plate device for the investigation of platelet biomaterial interactions. Journal of Biomedical Materials Research: An Official Journal of The Society for Biomaterials and The Japanese Society for Biomaterials, 1997, 34(4): 427-438.

[7] Magnin A, Piau J M. Cone-and-plate rheometry of yield stress fluids. Study of an aqueous gel. Journal of Non-Newtonian Fluid Mechanics, 1990, 36: 85-108.

[8] Magnin A, Piau J M. Cone-and-plate rheometry of yield stress fluids. Study of an aqueous gel. Journal of Non-Newtonian Fluid Mechanics, 1990, 36: 85-108.

[9] Han C D, Jhon M S. Correlations of the first normal stress difference with shear stress and of the storage modulus with loss modulus for homopolymers. Journal of Applied Polymer Science, 1986, 32(3): 3809-3840.

[10] Soleimani A. Use of dynamic phase angle and complex modulus for the low temperature performance grading of asphalt cements. Kingston, ON: Queen's Univ, 2009.

[11] Zhang D, Mu T, Sun H. Effects of starch from five different botanical sources on the rheological and structural properties of starch–gluten model doughs. Food research international, 2018, 103: 156-162.

[12] Peter Z. Order in cellulosics: Historical review of crystal structure research on cellulose. Carbohydrate Polymers, 2021, 254: 117417.

[13] Fraser R D B, MacRae T P, Suzuki E. An improved method for calculating the contribution of solvent to the X-ray diffraction pattern of biological molecules. Journal of Applied Crystallography, 1978, 11(6): 693-694.

[14] Yun J H, Hou J, Jang W G, et al. Preparation and Optimization of Composition of Medical X-ray

Shielding Sheet Using Tungsten. Polymer (Korea), 2019, 43(3): 346-350.

[15] Liu P, Shi Q, Wang W, et al. Microstructure and XRD analysis of FSW joints for copper T2/aluminium 5A06 dissimilar materials. Materials letters, 2008, 62(25): 4106-4108.

[16] Dalmora A C, Ramos C G, Oliveira M L S, et al. Application of andesite rock as a clean source of fertilizer for eucalyptus crop: Evidence of sustainability. Journal of Cleaner Production, 2020, 256: 120432.

[17] Epp J. X-ray diffraction (XRD) techniques for materials characterization[M]//Materials characterization using nondestructive evaluation (NDE) methods. Woodhead Publishing, 2016: 81-124.

[18] Pope C G. X-ray diffraction and the Bragg equation. Journal of chemical education, 1997, 74(1): 129.

[19] Liu S, Wang Y. Application of AFM in microbiology: a review. Scanning, 2010, 32(2): 61-73.

[20] Johansson P, Apell P. Geometry effects on the van der Waals force in atomic force microscopy. Physical Review B, 1997, 56(7): 4159.

[21] Berland K, Cooper V R, Lee K, et al. van der Waals forces in density functional theory: a review of the vdW-DF method. Reports on Progress in Physics, 2015, 78(6): 066501.

[22] Domańska M, Hamal K, Jasionowski B, et al. Bacteriological contamination detection in water and wastewater samples using OD600. Polish Journal of Environmental Studies, 2019, 28(6): 4503-4509.

[23] Sonkar S K, Ghosh M, Roy M, et al. Carbon nano-onions as nontoxic and high-fluorescence bioimaging agent in food chain—an in vivo study from unicellular E. coli to multicellular C. elegans. Materials Express, 2012, 2(2): 105-114.

[24] Swinehart D F. The beer-lambert law. Journal of chemical education, 1962, 39(7): 333.

[25] Jang J, Hur H G, Sadowsky M J, et al. Environmental Escherichia coli: ecology and public health implications—a review. Journal of applied microbiology, 2017, 123(3): 570-581.

[26] Blattner F R, Plunkett III G, Bloch C A, et al. The complete genome sequence of Escherichia coli K-12. science, 1997, 277(5331): 1453-1462.

[27] Ranjbar B, Gill P. Circular dichroism techniques: biomolecular and nanostructural analyses-a review. Chemical biology & drug design, 2009, 74(2): 101-120.

[28] Pescitelli G, Kurtan T, Floerke U, et al. Absolute structural elucidation of natural products—A focus on quantum-mechanical calculations of solid-state CD spectra. Chirality: The Pharmacological, Biological, and Chemical Consequences of Molecular Asymmetry, 2009, 21(1E): E181-E201.

[29] Kelly S M, Jess T J, Price N C. How to study proteins by circular dichroism. Biochimica et Biophysica Acta (BBA)-Proteins and Proteomics, 2005, 1751(2): 119-139.

[30] Mansfield P, Pykett I L. Biological and medical imaging by NMR. Journal of Magnetic Resonance (1969), 1978, 29(2): 355-373.

[31] Alam T M, Jenkins J E. HR-MAS NMR spectroscopy in material science. Advanced aspects of spectroscopy, 2012, 10: 279.

[32] Blümich B. Introduction to compact NMR: A review of methods. TrAC Trends in Analytical Chemistry, 2016, 83: 2-11.

[33] Bluemich B. Introduction to compact NMR: A review of methods. TrAC Trends in Analytical Chemistry, 2016, 83: 2-11.

[34] Guerry P, Herrmann T. Advances in automated NMR protein structure determination. Quarterly reviews of biophysics, 2011, 44(3): 257-309.

[35] Hess S T, Huang S, Heikal A A, et al. Biological and chemical applications of fluorescence correlation spectroscopy: a review. Biochemistry, 2002, 41(3): 697-705.

[36] Wang T, Zeng L H, Li D L. A review on the methods for correcting the fluorescence inner-filter effect of fluorescence spectrum. Applied Spectroscopy Reviews, 2017, 52(10): 883-908.

[37] Eftink M R, Ghiron C A. Fluorescence quenching studies with proteins. Analytical biochemistry, 1981, 114(2): 199-227.

[38] Clegg R M. Förster resonance energy transfer—FRET what is it, why do it, and how it's done. Laboratory techniques in biochemistry and molecular biology, 2009, 33: 1-57.

[39] Rejtar T, Chen H, Andreev V, et al. Increased identification of peptides by enhanced data processing of high-resolution MALDI TOF/TOF mass spectra prior to database searching. Analytical chemistry, 2004, 76(20): 6017-6028.

[40] Jurinke C, Oeth P, van den Boom D. MALDI-TOF mass spectrometry. Molecular biotechnology, 2004, 26(2): 147-163.

[41] Pan C, Xu S, Zhou H, et al. Recent developments in methods and technology for analysis of biological samples by MALDI-TOF-MS. Analytical and bioanalytical chemistry, 2007, 387(1): 193-204.

[42] Bluemich B. Introduction to compact NMR: A review of methods. TrAC Trends in Analytical Chemistry, 2016, 83: 2-11.

[43] Iwaguch S, Matsumura K, Tokuoka Y, et al. Sterilization system using microwave and UV light. Colloids and surfaces B: Biointerfaces, 2002, 25(4): 299-304.

[44] Rodger A, Sanders K. Biomacromolecular applications of UV-visible absorption spectroscopy[M]//Encyclopedia of Spectroscopy and Spectrometry. Elsevier, 2010: 166-173.

[45] Mahoney W C, Hermodson M A. Separation of large denatured peptides by reverse phase high performance liquid chromatography. Trifluoroacetic acid as a peptide solvent. Journal of Biological Chemistry, 1980, 255(23): 11199-11203.

[46] Whitaker J R, Granum P E. An absolute method for protein determination based on difference in absorbance at 235 and 280 nm. Analytical biochemistry, 1980, 109(1): 156-159.

[47] Sweeney J A, Hennessey Jr J P. Evaluation of accuracy and precision of adenovirus absorptivity at 260 nm under conditions of complete DNA disruption. Virology, 2002, 295(2): 284-288.

[48] Gupta V, Jain A D K J, Gill N S, et al. Development and validation of HPLC method-a review. International research journal of pharmaceutical and applied sciences, 2012, 2(4): 17-25.

[49] Yang D, Yin X, Ong C, et al. Multidimensional information-based HPLC technologies to evaluate traditional Chinese medicine. Journal of Chromatographic Science, 2013, 51(7): 716-725.

[50] Williams S. Ghost peaks in reversed-phase gradient HPLC: a review and update. Journal of Chromatography A, 2004, 1052(1-2): 1-11.

[51] Swartz M. HPLC detectors: a brief review. Journal of Liquid Chromatography & Related Technologies, 2010, 33(9-12): 1130-1150.

[52] Berthomieu C, Hienerwadel R. Fourier transform infrared (FTIR) spectroscopy. Photosynthesis research, 2009, 101: 157-170.

[53] Carbonaro M, Nucara A. Secondary structure of food proteins by Fourier transform spectroscopy in the mid-infrared region. Amino acids, 2010, 38: 679-690.

[54] Bakker J M, Mac Aleese L, Meijer G, et al. Fingerprint IR spectroscopy to probe amino acid conformations in the gas phase. Physical review letters, 2003, 91(20): 203003.

[55] Mäntele W. Infrared and Fourier-transform infrared spectroscopy. Biophysical Techniques in Photosynthesis, 1996: 137-160.

[56] Magalhães S, Goodfellow B J, Nunes A. FTIR spectroscopy in biomedical research: How to get the most out of its potential. Applied Spectroscopy Reviews, 2021, 56(8-10): 869-907.

[57] Englert C R, Harlander J M, Brown C M, et al. Michelson interferometer for global high-

resolution thermospheric imaging (MIGHTI): instrument design and calibration. Space science reviews, 2017, 212: 553-584.

[58] Zaefferer S. A critical review of orientation microscopy in SEM and TEM. Crystal Research and Technology, 2011, 46(6): 607-628.

[59] Ross F M. Opportunities and challenges in liquid cell electron microscopy. Science, 2015, 350(6267): aaa9886.

[60] Dawood A, Marti B M, Sauret-Jackson V, et al. 3D printing in dentistry. British dental journal, 2015, 219(11): 521-529.

[61] Longoni A, Li J, Lindberg G C J, et al. Strategies for inclusion of growth factors into 3D printed bone grafts. Essays in Biochemistry, 2021, 65(3): 569-585.

[62] Roche C D, Brereton R J L, Ashton A W, et al. Current challenges in three-dimensional bioprinting heart tissues for cardiac surgery. European Journal of Cardio-Thoracic Surgery, 2020, 58(3): 500-510.

[63] Hinton T J, Jallerat Q, Palchesko R N, et al. Three-dimensional printing of complex biological structures by freeform reversible embedding of suspended hydrogels. Science advances, 2015, 1(9): e1500758.

[64] Jung J W, Lee J S, Cho D W. Computer-aided multiple-head 3D printing system for printing of heterogeneous organ/tissue constructs. Scientific reports, 2016, 6(1): 1-9.

[65] Greenhall J, Raeymaekers B. 3D Printing macroscale engineered materials using ultrasound directed self-assembly and stereolithography. Advanced Materials Technologies, 2017, 2(9): 1700122.

[66] Wu C, Wang Z, Lei H, et al. The binding of thioflavin T and its neutral analog BTA-1 to protofibrils of the Alzheimer's disease Aβ16–22 peptide probed by molecular dynamics simulations.

Journal of molecular biology, 2008, 384(3): 718-729.

[67] Groenning M. Binding mode of Thioflavin T and other molecular probes in the context of amyloid fibrils—current status. Journal of chemical biology, 2010, 3: 1-18.

[68] Biancalana M, Koide S. Molecular mechanism of Thioflavin-T binding to amyloid fibrils. Biochimica et Biophysica Acta (BBA)-Proteins and Proteomics, 2010, 1804(7): 1405-1412.

[69] Kuhn S, Rahe P. Discriminating short-range from van der Waals forces using total force data in noncontact atomic force microscopy. Physical Review B, 2014, 89(23): 235417.

[70] Oxford Instrument. *Atomic Force Microscopy.* Oxford, UK. 16th June 2023. https://raman.oxinst.com/techniques/scanning-probe-microscopy

4. Chapter 4. Peptide-Peptide Blending Hydrogel

Abstract

Self-assembly peptide (SAP) is becoming popular in hydrogel design, because of its convenient preparation and excellent biological properties [1]. Meanwhile, the influence of peptide sequence on produced hydrogel is widely reported in the literature [2]. The changes are attributed to the difference in net charges, hydrophobicity and specific amino interaction (such as π-π stacking) in different sequence peptides. This experiment produced hybrid hydrogels based on a self-assembly peptide (KF8K) blending with a series of peptides and well-characterise them. The second peptide included two different sequence self-assembly peptides (F8 and F9), a non-self-assembly peptide (A8) and the same sequence but opposite chirality peptide (D-KF8K). The results indicated that non-SAP does not influence the self-assembly process but leads to variations in the stiffness of blending hydrogel. It was explained that the presence of non-SAP causes variation in

fibre behaviour and network generation. On the other hand, in the two different SAP-KF8K blending hydrogels, the hydrogelation pH of the blending hydrogels changed with the ratio of compositions. The microstructures (β-sheet) were kept unchanged in the blending hydrogels while the stiffness also descended compared with the F8/F9 hydrogel and KF8K hydrogel. In terms of D-KF8K, the L- and D-KF8K blending hydrogel is highly similar to the pure L-KF8K hydrogel except for the chirality. Additionally, the distribution of peptide monomers in blending hydrogels was also revealed by FITC fluorescent quenching experiment. The SAPs (F8 / F9) were proven to homogenously distribute in the F8/F9-KF8K blending hydrogel. However, on the contrary, the peptide monomers in the hybrid hydrogel by opposite chirality KF8K assembled separately. The L- and D-KF8K formed fibre separately, suggesting the formation of the double networks in the hydrogel. The result proposed a potential strategy to prepare a biocompatible material with separate fibres.

4.1 Introduction

Typically, hydrogel is regarded as a combination of both solid and liquid due to its water-filled porous structure and hydrophobic network [3]. The hydrogel possesses characteristics of both solid and liquid. The high-water content confers fluid-like properties, while the water-filled pores provide space for cells and macromolecular drugs, as well as solubility for small molecules. The entangled fibres and network in the hydrogel contribute to its elasticity, typically seen in solid materials. This combination of solid and liquid properties makes hydrogels a versatile material, used for a variety of applications as a soft but sturdy substance.

Recently, there has been growing interest in the study of a family of self-assembled peptide hydrogels that rely on the β-sheets for potential use in 3D printing, drug delivery [4], and cell

culture media [5]. A peptide called F8, consisting of 8-12 amino acids with alternating hydrophilic and hydrophobic residues, was designed and found to form a β-sheet fibril structure through self-assembly at a pH of 4. However, this hydrogelation pH is incompatible with most cells and drugs, leading to the proposal of F9 and KF8K to produce self-assembled hydrogels at a pH of 7.

However, the effect of the peptide sequence on its microstructure (β-sheet) is still unclear. The literature reports varying effects from peptide sequence to fibre properties and shape [6]. For example, modifying the hydrophobic surface of F9 led to a loss of part of the β-sheet structure. It results in zigzag fibres instead of straight ones [6]. Hydrophobic amino acids in the sequence and the net charge difference generated also play a role in the self-assembly process, as electrostatic interactions are important in this process. In particular, the first hydrophobic amino acid in the N-terminal. If the phenylalanine in the F8 is replaced by the alanine, the peptide will not self-assemble at all and will remain in solution at all pH values. However, previous studies have not considered the properties of mixed hydrogels made of different peptide sequences, which may show different results compared to single-sequence hydrogels. This experiment aims to study the variations in mixed hydrogels made of two different sequence peptides using characterisation, mechanical property tests, and peptide monomers distribution measurements. This is an attempt to reveal how the selection of peptides affects the properties of mixed hydrogels.

On the other hand, chirality plays a critical role in determining the biological properties of amino acids and peptides. However, its influence on the properties of self-assembly peptide hydrogels is still not well understood. The properties of mixed hydrogels made of L- and D-peptides are still unknown. Natural amino acids in living organisms are typically left-handed (L-amino acids), which are also used in the self-assembly peptides [31]. The different direction of side

chains due to opposite chirality affects the 3-dimensional structure of peptides and proteins, including secondary structures. Replacing right-handed (D-amino acids) with left-handed ones can change the secondary structure, for example, disrupting the formation of α-helix [7]. As the 3-dimensional structure determines the activity of biological macromolecules and the self-assembly of β-sheet-based peptides, all proteins in living organisms only contain L-amino acids. In contrast, peptides with D-amino acids do not interact with enzymes due to their non-biological activity and "incorrect" 3-dimensional structure [8]. Therefore, previous research shows that D-amino acid hydrogels can be used in vivo for extended periods without causing toxicity to cells and tissue [9]. Therefore, this experiment compares L-KF8K, D-KF8K, and their blending hydrogel, due to the effect of opposite chirality on secondary structure. The β-sheet structure of L-KF8K and D-KF8K may be different, potentially leading to separate assembly of the two peptides. The experiment aims to study the distribution of L-KF8K and D-KF8K peptide chains in the blending hydrogel.

Besides, the distribution of different peptides in blending self-assembled peptide (SAP) hydrogels is also important, as it affects the uniformity of the hydrogel, which is crucial for applications in biological fields like cell culture [9] and tissue engineering. The uniformity of the hydrogel can also impact the mechanical properties of the fibres. However, separate assembly of different sequence SAPs can be desirable in certain cases where functional modifications need to be concentrated in a specific area. To determine whether the different peptides are randomly distributed in the blending hydrogel, an FTIC and DABCYL fluorescent quench reaction-based experiment was performed to compare the quench percentage of pure and blending KF8K hydrogels [11]. The results of the experiment can provide information about the randomness of the peptides and the distance between peptide chains in self-assembly.

4.2 Method

4.2.1 Material

F8(FEFKFEFK), F9(FEFKFEFKK), L-KF8K(KFEFKFEFKK), D-KF8K(KFEFKFEFKK), A8(AEAKAEAK), V8 (VEFKVEVK) peptide (HCl salt), FITC-mini peg-KF8K and DABCYL-min peg-KFE8 fluorescent peptide (HCl salt) were purchased from Lifetein Ltd with 95% purification (the rest 5% is chlorine salts). The purities of peptides were confirmed by reverse phase high-performance liquid chromatography (RP-HPLC) (figure S.1) and elementary analysis (table S.1). MALDI-TOF confirmed the molecular weight (figure S.2). The method of HPLC and MALDI-TOF are given in Supplement documents. Sodium hydroxide and Sodium hydrogen phosphate powder were purchased from Thermo Fisher Scientific.

4.2.2 Peptide hydrogel preparation

75 mg self-assembly peptide powder was weighed by balance and dissolved into 2.4 ml HPLC water at room temperature, followed by vortex mixing. Samples were set in a sonic bath undergoing 30 minutes of sonication for complete dissolution. 0.5 M NaOH solution adjusted the sample pH for the ideal point. The pH of the samples was measured by a pH meter (AB150 pH Benchtop Meters with 0.01 resolution).

In blending hydrogel preparation, a total of 75 mg self-assembly peptide powder was weighed while the exact weight of each sequence peptide was decided by molar mixture ratio (1:1; 1:2; 1:2.5; 1:3). The following preparation steps are the same with pure peptide hydrogel preparation. Samples' volume was adjusted by HPLC water to 3ml and stored at 4 °C overnight for hydrogelation.

4.2.3 pH Titration

Titration started from 1 ml 1mg/ml HPLC water dissolved peptide solution by adding 50mM NaOH solution. Different sequence peptide solutions were mixed by 1:1 in mole ratio in hybrid peptide samples. 5uL 0.5M NaOH is added in every step. Samples were mildly agitated before pH measurement. pH was acquired by an AB150 pH Benchtop Meters. All titration experiments were repeated three times.

4.2.4 Phase diagram

1ml 25 mg/ml peptide samples were prepared. Different sequence peptide solutions were mixed by 1:1 in mole for hybrid samples. 10uL 0.5M NaOH solution was added to adjust the pH for each step. Samples were mildly agitated before pH measurement. pH was acquired by an AB150 pH Benchtop Meters. The stage of samples was decided by eye observation [14].

4.2.5 ATR-FTIR

ATR-FTIR was employed to characterise the nanostructure of samples. 5uL samples were pipetted into the crystal surface. The absorbance spectra were collected from 400 cm^{-1} to 4000 cm^{-1} wavenumbers with 256 scans and 4 cm^{-1} steps at room temperature. For peptide samples, ranges focused on 1400 cm^{-1} to 1800 cm^{-1}. HPLC water played the role of background in room temperature measurement. The collection was by Brucker ALPHA II FTIR Spectrometer. FTIR spectra were smooth by Gaussian function between every 5 points.

Origin 9 was employed for spectra fitting. Fitting was done between 1700 cm^{-1} to 1300 cm^{-1} by Gaussian function, while four peaks around 1400, 1550, 1620 and 1660 cm^{-1} were selected. The baseline was set as a continuous line across the lower point in the fitting range.

4.2.6 CD spectroscopy

CD spectra were acquired by ChiraScan spectropolarimeter. 25 mg/ml pure and blending hydrogels were diluted 125 times with HPLC water to make the final concentration of SAP is in 0.2 mg/ml, respectively. Following vortex mixing, samples were pipetted into 1 mm path-length quartz cells without bubbles. Spectra were recorded continuously from 190 nm to 280 nm with 0.5 nm step-in at 25 °C (room temperature). HPLC water was employed as background in all measurements. The mean residual ellipticity is presented by Δε (litre mol^{-1} cm^{-1}) which means the difference in absorption coefficient between left-hand and right-hand polarised light. Data were analysed by Bestsel.

4.2.7 THT Assay

2 mmol/l THT was prepared in advance by dissolving THT powder (Sigma) into HPLC water. THT solution was further diluted to 0.05 mmol/l in pure 7.5 mg/ml KF8K as well as 7.5 mg/ml KF8K and 7,5 10 and 15 mg/ml A8 mixture hydrogels.

Fluorescence spectra were obtained by Agilent Cary Eclipse Fluorescence Spectrometer. Samples were loaded into a 2 cm path length quartz cuvette immediately after dilution, followed by 2 minutes 5000 rpm centrifuge to remove the bubble in the cuvette completely. The spectra were recorded between 420 nm and 550 nm with emission wavelength at 454 nm at 1 nm step length. The unit of fluorescent intensity is arbitrary (a.u.), meaning the relevant intensity compared with emission intensity.

4.2.8 X-ray Diffraction (XRD)

Bruker D8 Advance performed XRD experiments. The angle range was 3 to 60 degrees with a 0.02-degree step. In sample preparation, 25 mg/ml of pure hydrogels and blending hydrogels were uninformed, printed, and dried on a glass slide. Experiments were done at room temperature.

Baselines were acquired by High score software. In this condition, distance (d) was obtained by Bragg's Law

$$2d \sin \theta = n\lambda \tag{31}$$

Where θ is the angle, n is a positive integer, and λ is the wavelength of the incident wave.

4.2.9 Dynamic oscillatory rheology

The rheometer evaluated the mechanical as well as thermal properties of hydrogel samples. 180uL sample was loaded into a stainless Peltier with 45000 um gaps between Peltier and parallel plate. 20 mm diameter plate is selected, and the gap is set at 500 um in measurement. Collections underwent at room temperature.

The strain-dependent storage modulus (G') and loss modulus (G'') were collected to evaluate the linear viscosity region and shear thinning properties at fixed frequency (1 Hz).

4.2.10 AFM

7.5 mg/ml peptide samples were prepared, followed by 30 times dilution by HPLC water, giving the final concentration of 0.25 mg/ml. The sample was pipetted and vortexed, ensuring a homogeneous solution. Once the used mica was removed by stick tape and fresh mica exposed, 100 uL diluted solution was injected onto the flat mica surface. Following, Sample loaded mica was

stored in 4 °C fridges for 72 h to air dry the liquid. When the drying was completed, 1 ml HPLC water was pipetted into the mica surface for washing non-settled peptide molecules. The well-washed sample was air dried in a fume cupboard until no liquid on the mica surface.

All the AFM imaging was carried out at room temperature (20°C) and approximately 50% relative humidity. Examinations were done in an air atmosphere and dried samples in the AFM (Bruker Multimode 8). SCANASYST-AIR triangular cantilevers with a spring constant of k = 0.4 N/m and 70KHz frequency (Bruker) were used for ScanAsyst Mode imaging.

4.2.11 TEM

7.5 mg/ml sample hydrogels were diluted 10-fold using HPLC grade water and vortexed to mix evenly to 0.75 mg/ml KF8K samples. Carbon-coated copper grids (400 mesh, Electron MicroscopySciences, UK) were placed on the sample droplet for 1 min and moved to the water droplets to wash three times, then transferred to the 1% uranyl acetate droplet for the 30s. Excess liquid on the grid was subsequently removed by a 70mm filter paper (Whatman). The grid was dried for TEM imaging by FEI Tecnai12 BioTwinat 100 KeV with Gatan Orius SC1000A CCD camera.

4.2.12 FITC-Dabcyl Fluorescent Quench Reaction

For fluorescent sample preparation, sterile 7.5 mg/ml A8 solution and the solution with 0.01, 0.02, 0.03, 0.04, and 0.05 mg/ml FITC-KF8K were prepared as a standard curve. 22.5 mg/ml A8 powder was well weight by balance and dissolved into 2.4 ml HPLC water, followed by pH adjustment to 7.0 by 0.5 M NaOH. The 20, 40, 60, 80 and 100 ul previously prepared 0.1 mg/ml FITC-KF8K solution were added into corresponding samples, respectively. The volume of the sample is set to 3 ml of HPLC water.

7.5 mg/ml KF8K pure hydrogel and 3.75 mg/ml KF8K – 3.75 mg/ml F8/F9/V8/D-F8 blending hydrogels with 0.03 0.05 and 0.10 mg/ml FITC-KF8K were also prepared by the same strategy.

In the production of fluorescent quench samples, one-time (0.1 mg/ml) and five times (0.5 mg/ml) Dabcyl-KF8K were added into 0.1 mg/ml FITC-KF8K containing pure KF8K and KF8K – F8/F9/V8/D-F8 blending hydrogels by 20 and 100 ul 0.5 mg/ml Dabcyl-KF8K solution, following by pH adjustment to 7.0 by 0.5 M NaOH.

The emission spectra of all samples were acquired under 490 nm between 500 nm to 600 nm, while the samples underwent 520 nm excitation between 400 to 510 nm for full excitation spectra. The length of the cuvette was 2 cm.

4.3 Result and Discussion

4.3.1 Blending hydrogel by two self-assembly peptides

According to the literature, pH plays a critical role in the solubility and self-assembly of charged peptides, including the β-sheet family [12]. As the result, phase diagrams of F8-KF8K and F9-KF8K blending hydrogel with a series of blending ratios were explored to obtain the behaviour of hybrid hydrogel against pH (Figure 4.1 (A, B)). The corresponding net charges of the blending hydrogels are shown in figure 4.1 (C, D). Their net charges are calculated by formula 32

$$Z = \sum_i N_i \frac{10^{pK_{a_i}}}{10^{pH} + 10^{pK_{a_i}}} - \sum_j N_j \frac{10^{pH}}{10^{pH} + 10^{pK_{a_j}}} \qquad (32)$$

where i is the number of N-terminus and the side chains of Arginine, Lysine, and Histidine, and j is the number of C-terminus and the Aspartic Acid, Glutamic Acid, Cysteine, and Tyrosine.

pH is known to trigger the self-assembly of SAP to form β-sheet and hydrogel [13]. To predict the behaviour of peptides in selected concentrations against pH, the phase diagram was done in 25 mg/ml, giving the results in Figure 4.1 (A&B). In the phase diagram, with the pH increased, the peptide underwent solution to viscosity liquid, to clear hydrogel. And then it was the cloudy hydrogel and finally precipitation. The samples started from a clear solution when the over-acid pH gave rise to a high number of net charges in peptide monomer. The charges cause an over-strong repulsive force between peptide molecules. The interaction fell with the increase of pH, which brought up the decrease of net charge in the peptide. In this process, the repulsive force became weaker. As a result, the sample became increasingly viscous and, finally, hydrogel. The hydrogel network was maintained by a force equilibration where the distance and interaction intensity between molecules is suitable for β-sheet forming. The repulsive force gradually closed to the threshold where peptide molecules can form acceptable β-sheets and accumulate to fibres. There would be clouds in hydrogel if the pH keeps increasing and precipitation finally. This is because the pH affects the charge of the peptide monomers that make up the hydrogel. As the pH increases, the charge on the peptide monomers decreased, which in turn weakened the interactions that maintain the network. When the net charge was less than one, there was not enough net charge to generate repulsive force to avoid aggregation and maintain the system [32]. From the previous experiment result, for pure peptide hydrogels, F9 forms a transparent hydrogel at a pH of 4.3-4.6, while KF8K forms a transparent hydrogel at a pH of 6.5-7.5. Therefore, in this experiment, KF8K was chosen as the main self-assembly peptide as its neutral pH is more compatible to gelatin hydrogelation and has promising potential for biological applications. F9 was also used as a comparison.

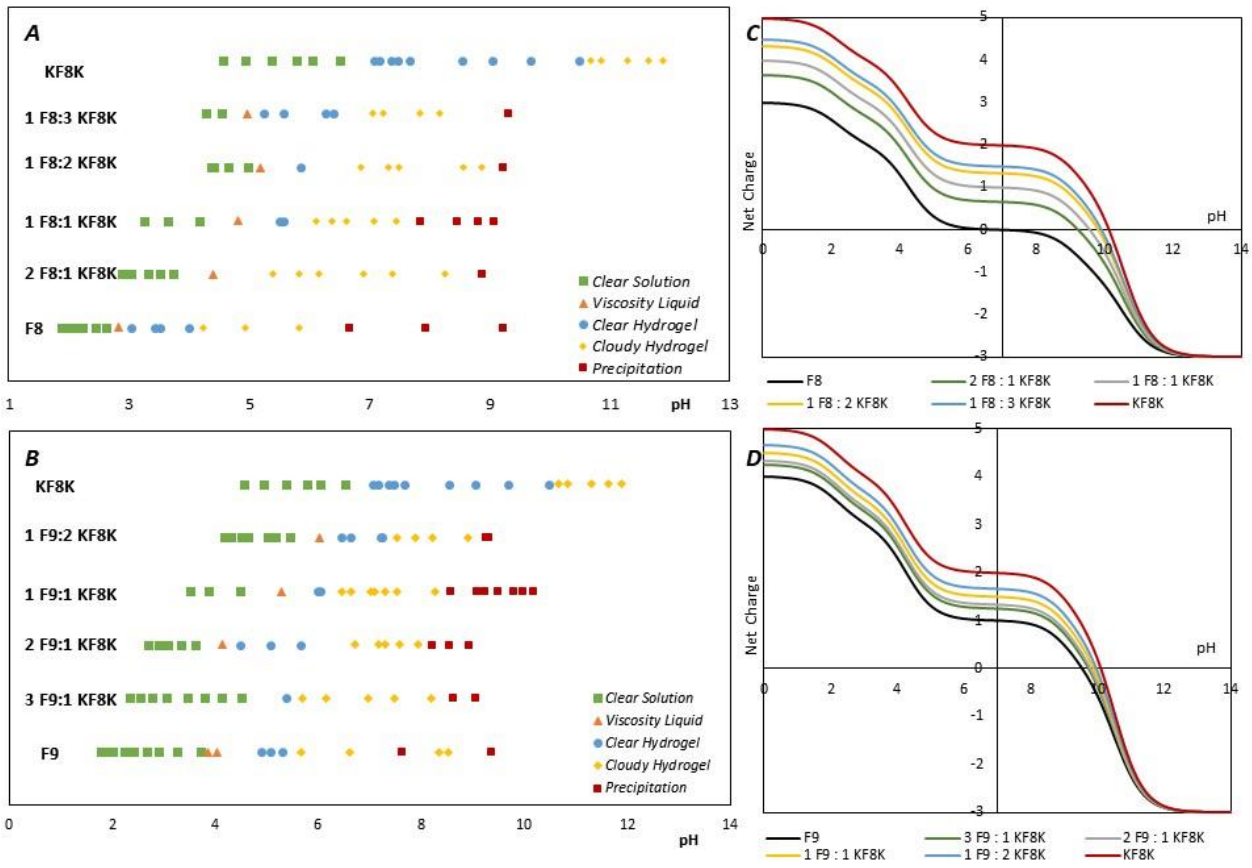

Figure 4-1 (A, C) The Phase diagram and net charge of 25 mg/ml F8-KF8K blending samples (B, D) The Phase diagram and net charge of 25 mg/ml F9-KF8K blending samples

In the phase diagram, the total peptide concentration was set at 25 mg/ml. The results show that the pH range corresponding to the appearance of hydrogels changed with the composition mixture ratio due to the net charge in the peptides switching with the variance in composites. Pure KF8K remained in a transparent hydrogel between pH 7 to 10.5, while the pH range for F8 and F9 were 3 to 4 and 4.5 to 5.5, respectively. The transparent hydrogel pH values were where the peptides hold a net charge between +1 and +2. The transparent hydrogel obtained for the 1-to-1 mixture ratio shifts to the average point compared to the two pure compositions, moving to pH 5.5-6 (F8-KF8K) and 6.5-7 (F9-KF8K). The hydrogelation pH of the blending sample was close to

the weighted average of pure peptides, indicating that the influence of the net charge of peptides on self-assembly is determined by the average net charge of different sequence peptides.

Additionally, the pH range corresponding to different hydrogel states shifted with the variance of the blending ratio. The transparent hydrogel pH range rearranged to be more neutral in higher KF8K percentage samples. Conversely, more F8/F9 led to the composites remaining in a clear hydrogel in a more acidic range. The mixture with KF8K could contribute to preventing precipitation and maintaining the transparent hydrogelation for F8 and F9 at neutral pH. This is because KF8K had more (+2) charges at neutral pH, which lead to an increase in the average net charge in the blended hydrogel. This increase in net charge helpes strengthen the interactions to maintain the hydrogel's network, preventing precipitation. The phases present in the hydrogel is determined by the average net charge in the peptides. The results suggested that different but similar sequence self-assembly peptides can form a hydrogel without a heterogeneous self-assembly process or blending hydrogel.

As most of the cell, for example, breast cell, prefers to be cultured at the neutral pH [14], producing a transparent and stiffer blending hydrogel around pH 7 was tried. F8 and F9 were blended with KF8K in a more precise ratio. The appearance of the mixed hydrogels was also consistent with the results from a phase diagram. The 1:1 and 2:1 F9-KF8K hydrogels were clear at pH 6.5, while the 2.5:1 and 3:1 samples transformed into cloudy hydrogels. In the F8-KF8K system, as F8 had less charge at pH 6.5, it was more likely to precipitate and produce a cloudy mixed hydrogel. The experimental results also agreed with the theory. The 1:1 and even 1:0.5 F8-KF8K samples were cloudy, while the same composite ratio of F9-KF8K formed a completely clear hydrogel. The threshold at which the F8-KF8K hydrogel remained clear was 1:0.4. Meanwhile,

regarding mechanical properties, F8/F9-KF8K hybrid hydrogels at a concentration of 25 mg/ml in pH 6.5 were measured. At that pH, pure F9 and F8 were in the form of precipitation, while KF8K was a transparent hydrogel with a storage modulus of over 1300 Pa. In terms of mixed samples, all clear samples showed weaker shear thinning properties compared to pure KF8K, but each cloudy composite became stronger. The clear F9-KF8K samples (2:1 and 1:1) had storage moduli of 570 Pa and 460 Pa, respectively. However, the modulus jumped up to 1300 Pa in the 2.5:1 sample, which was the starting blending ratio point of cloudiness. This sudden improvement was due to the presence of a slight solid from precipitation. However, the rigidity began to decrease with a further increase in the F9 ratio because the additional precipitation destroyed the hydrogel structure, including fibres and the network, weakening the hydrogel. The same result was also observed in F8-KF8K blending hydrogels. This tendency indicates that the simple mixture of two self-assembly peptides only adjusted the hydrogelation pH but cannot achieve an enhancement in stiffness.

Therefore, due to the failure to produce a transparent and stiffer blending hydrogel at a neutral pH, the experiment focused on researching the differences in different sequence peptides blending hydrogel with a 1-to-1 mixing ratio. KF8K was selected as the base peptide because of its neutral hydrogelation pH. In the following paragraphs, KF8K would be mixed with secondary peptides in a 1-to-1 ratio. Since the mixture ratio was kept unchanged, it would be omitted in later paragraphs. This means that samples are referred to by concentration and composite peptide. For example, '7.5 mg/ml F8-KF8K hydrogel' correspondes to a 3.75 mg/ml F8 and 3.75 mg/ml KF8K blending hydrogel.

Figure 4.2 (A, B) illustrates the storage moduli of 25 mg/ml F8, F9, KF8K, F8-KF8K, and F9-KF8K hydrogels at their hydrogelation pH. The figure illustrated that the stiffness of the 25 mg/ml F9-KF8K blending hydrogel was lower than that of both the 25 mg/ml F9 and KF8K hydrogels. The same result was observed in the F8-KF8K hydrogel. The results indicates that the 1-to-1 blending hydrogel is weaker than the pure self-assembly peptide hydrogel. This is because the hydrogelation pH for the blending hydrogel is the average value, which is unsuitable for both peptide compositions to self-assemble.

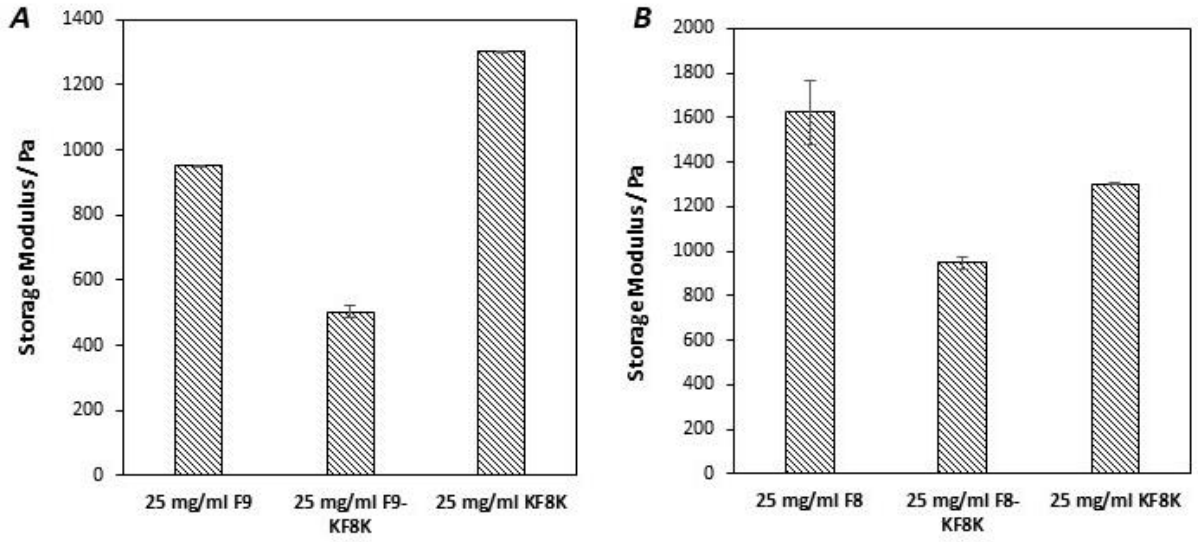

Figure 4-2 (A) The storage modulus of 25 mg/ml F9, 25 mg/ml KF8K, 12.5 mg/ml F9 & 12.5 mg/ml KF8K blending hydrogel in hydrogelation pH (B) The storage modulus of 25 mg/ml F8, 25 mg/ml KF8K, 12.5 mg/ml F8 & 12.5 mg/ml KF8K blending hydrogel in hydrogelation pH

Because hybrid peptide hydrogels have weaker mechanical strength compared to single peptide hydrogels, research into the microstructure variations in hybrid peptide hydrogels is needed. The 25 mg/ml F8, F9, KF8K, F8-KF8K and F9-KF8K five hydrogels underwent characterisation, including FTIR, CD, and XRD spectroscopy to reveal their microstructure. The comparison between the spectra provided insights into the microstructure variations after mixing.

The pH for each sample still was in their hydrogelation pH. The results are shown in Figure 4.3 (A-C).

Regarding FTIR, all three single peptide hydrogels and two blending hydrogels were observed with a band of β-sheet at 1622 cm^{-1} and an anti-parallel β-sheet at 1695 cm^{-1} [15,16]. The peak at 1077 cm^{-1} (NaH_2PO_4) was used as the standard for peak intensity normalisation [17]. After normalisation, the β-sheet peak intensity of the five samples was also similar. The similarity in spectra suggests that the same concentration of different sequence self-assembly peptides form similar structures under their hydrogelation pH. Relatively speaking, the peak for the anti-parallel β-sheet is relatively more difficult to observe in FTIR than the β-sheet. The band of anti-parallel β-sheet was not detected in 7.5 mg/ml F8, F9 and KF8K samples. Additionally, the bands between 1520 and 1556 cm^{-1} were attributed to the amide II [16]. The band at 1522 cm^{-1} illustrated the presence of the amide group. The corresponding peak for the carboxyl group was at 1556 cm^{-1}. The intensity of these two peaks showed a noticeable variation in different samples. This is because the pH of the samples was different (at their hydrogelation pH), and therefore the protonation of carboxyl and amide groups varied. The peak at 1397 cm^{-1} was due to the double bond in the benzene ring in phenylalanine. The three single peptide hydrogels and two hybrid hydrogels showed high similarity in the FTIR spectra. This similarity implies a random and homogeneous distribution of F8/F9 peptide monomers with KF8K monomers in the mixed hydrogels. Otherwise, separate structures should appear in the spectra of the mixed hydrogels.

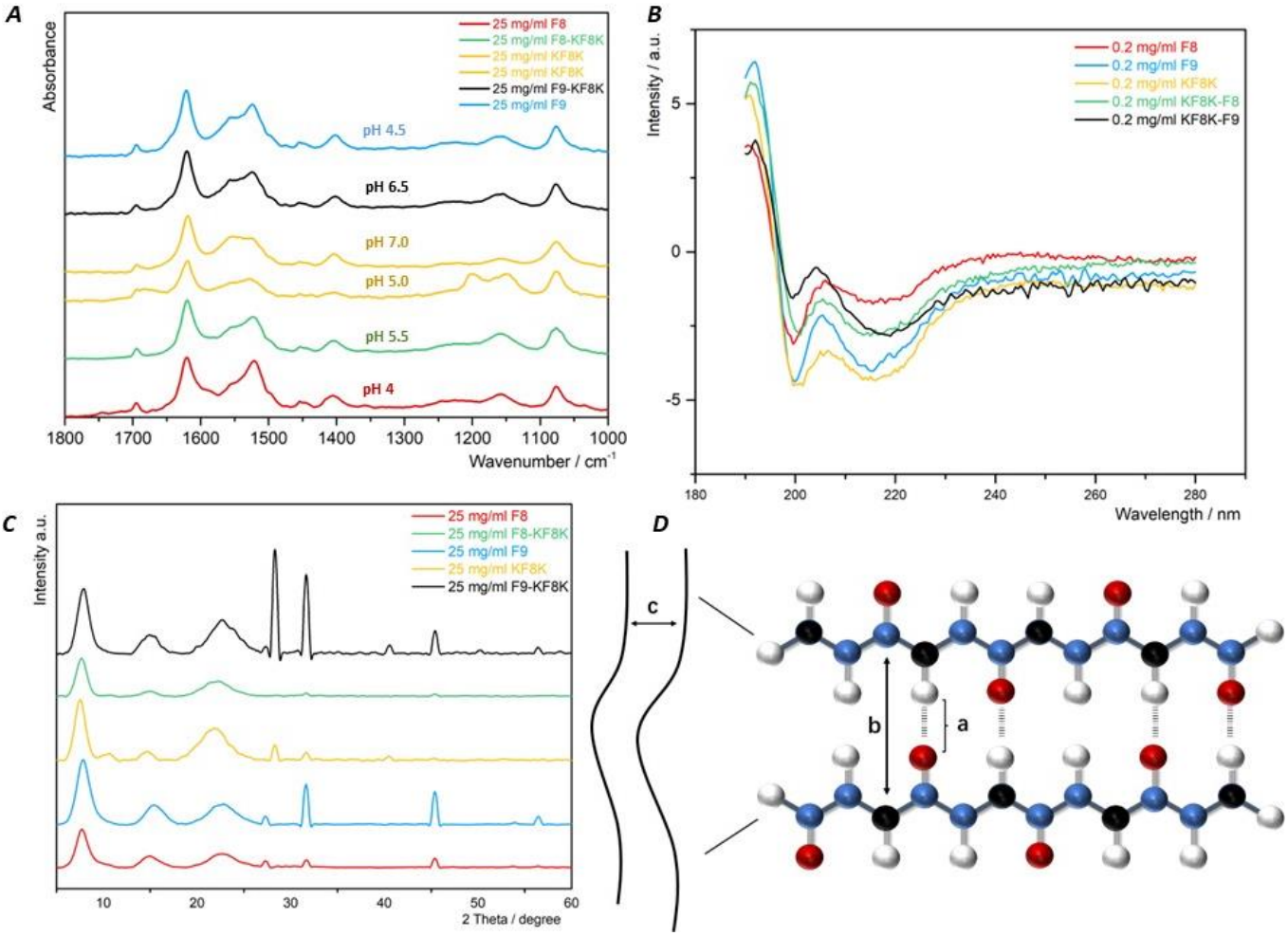

Figure 4-3 (A) FTIR of 25 mg/ml F8, F9, KF8K, 1:1 F8-KF8K and 1:1 F9-KF8K blending hydrogel in hydrogelation pH (B) CD spectra of 25 mg/ml F8, F9, KF8K, 1:1 F8-KF8K and 1:1 F9-KF8K blending hydrogel in hydrogelation pH (C) XRD of 25 mg/ml F9, KF8K and 1:1 F9-KF8K blending hydrogel (D) Schematic of corresponding structures observed in XRD

To confirm the accuracy of the results from FTIR, samples were also characterised by CD spectroscopy to prove that the explanations of FTIR peaks are reasonable. The use of CD spectroscopy was driven by the fact that most self-assembly peptides produce corresponding results from FTIR and CD spectra in secondary structure [18]. Therefore, F8, F9, KF8K single peptide hydrogel and F8-KF8K, F9-KF8K blending hydrogels were measured between 190 to 280 nm with a 0.5 nm step using HPLC water as the background. All samples were dominated by β-sheet with

around 60% in total secondary structure. The combination of the positive peak in 190-195 nm and the negative peak in 220 nm illustrated the presence of the β-sheet, which was evident in Figure 4.3 (B) [19]. Additionally, others, particularly random coil, occupy 35% of the secondary structure in peptide hydrogels, which led to the negative peak at 200 nm. Additionally, the α-helix percentage was lower than 3%, indicating that there is no α-helix in the samples, in line with the results from FTIR.

Moving on to XRD, patterns and reflections are shown in Figure 4.3(C & D) and Table 4.1 for pure F9, F8, KF8K, F8-KF8K and F9-KF8K hydrogels.

Table 4-1 The reflection corresponding structure in XRD

Distance / Å	Corresponding structure
22.8	Around two times of 10.9 '(a) structure' (influence since small angle)
10.9 (c)	sheet-sheet separation (lamination distance) upon lateral stacking of β-sheet
5.8 (b)	Peptide-peptide distance in β-sheet
4.1 (a)	Distance in hydrogen bonds

An XRD comparison of 25 mg/ml KF8K against pH was made first to clarify the relationship between the reflection and the structure. The reflections at 11.2 Å and 5.8 Å showed intensity variations against pH, with a higher peak at hydrogelation pH (pH 7) but weaker in solution pH (pH 4). This indicates that these two reflections are related to the β-sheet. This is due to the fact that in KF8K, there is more the β-sheet forming at its hydrogelation pH (pH 7).

Therefore, in the XRD spectra of the five experimental samples, the reflection at around 10.9-11.2 Å was explained as the sheet-sheet separation in β-sheet [20], confirming the presence of β-sheet in samples. The structure also caused the peak at 23.1 Å, attributed to the repetition of the 10.9 A peak. The peak corresponding to 4.1 Å was due to the hydrogen bonds in the β-sheet between two peptide monomers. The bond length of hydrogen and oxygen atoms contributed to the decrease in the distance in hydrogen bonds compared to the gap between two peptide chains. On the other hand, there was also an obvious diffraction at 5.7 Å in F8 and F9 spectra, while it was relatively weaker in KF8K. It corresponded to the distance of strand-strand distance in β-sheets [21]. The intensity change is explained as the result of the presence of one more lysine in KF8K. When there is an extra lysine in the N-terminal, the phenylalanine is masked and leads to a decrease in the gap between chains. The blending hydrogel samples showed similar patterns to their compositions, close to the average addition of their refined compositions. The reflections for the β-sheet were clearly observed in the two blending hydrogel samples' spectra. The reflection at 5.7 Å in blending samples was more evident than KF8K but weaker than F8/F9. The shift in β-sheet peaks also appeared in blending hydrogel samples, while the shift intensity was between the intensity of KF8K and F8/F9. The reflections over 30° were related to the salt, particularly sodium chloride, which was present in the hydrogel sample preparation due to the peptide powder containing hydrochloric acid. The salt concentration was different in samples, leading to the difference in reflection intensity.

4.3.2 Fluorescent Quenching reaction

The next section is concerned with the distribution of different sequence peptide chains in the blending hydrogel. The above comparison between KF8K and its blending hydrogel with F8 and

F9 suggests the non-variations in the formation of β-sheet in blending hydrogel. The result from rheology and characterisations both recommended the homogeneity of the blending SAP hydrogels. However, the distribution of different sequence peptide monomers in the blending hydrogels still needs to be clarified. Due to the high similarity between SAPs, non-homogeneous microscopic peptide monomer distribution is also potential in macroscopically homogeneous blending hydrogels. The discrepancy between designed self-assembly peptides was not obvious enough to produce mechanical or characterisation differences. Therefore, the experiment to expose the distribution of peptide monomers in blending hydrogels was proposed. If the two different sequence peptide monomers assemble separately, it still is a double-network hydrogel.

As a result, an experiment was designed relying on the fluorescent quenching reaction to assess the fibre distribution. The significant advantage of this pairing is that their quenching is distance depended, related to the distribution density of peptides in fibres. Fluorescein isothiocyanate (FITC) was accepted as fluorescent, which has been widely utilised in biomolecule labelling due to its good biocompatibility. It is a fluorescent molecule functionalised with an isothiocyanate reactive group (-N=C=S). The excitation and emission inspiration wavelengths of FITC are approximately 520 nm and 500 nm [33], respectively. Besides, pH is a critical factor that decides the fluorescent intensity for FITC. There is an approximately ten times intensity enhancement when pH is reduced to 9 from 2 [24]. A series of molecules are able to quench the fluorescent from FITC, including halide ions, heavy metal ions, oxidising organic compounds and aromatic compounds. One of the most well-known quenchers for FITC is 4-((4-(dimethylamino)phenyl)azo)benzoic Acid (DABCYL) [22]. The azo bond in Dabcyl makes the main contribution to fluorescent quenching. The quenching is explained by the fact that the azo group works as the electron acceptor in fluorescence resonance energy transfer (FRET) [25]. The primary

benefit of FITC and Dabcyl reaction is that the quenching process is distance dependent, which only finishes when the gap between FITC is 1 to 10 nm in any direction [33]. This feature gives access to analyse of the distance between labelled peptides, which helps to assess the density and distribution of the target peptide. Besides, the excitation and emission inspiration wavelengths of Dabcyl are 336 nm and 490 nm, without any overlap in the corresponding wavenumber in FITC [26].

The FITC and Dabcyl are labelled in the basic peptide, KF8K. The Schematic of the quenching reaction is given in figure 4.4 (A). The quenching reaction of FITC-Dabcyl will only occur when they are close together, between 1 and 10 nm. At that moment, a weaker fluorescent signal will be observed. In contrast, when the above molecules are more than 10 nm apart, a fluorescence signal will be detected. As a result, the distance depended on quenching can indicate the density of KF8K monomers in the blending hydrogel by measuring the percentage of quenching.

The control in the experiments is the quenching ratio when the designed concentration KF8K-FITC and KF8K-Dabcyl are introduced into the pure KF8K hydrogel. Subsequent experiments involved mixing the same concentration of the KF8K-FITC and KF8K-Dabcyl peptides into the KF8K and other sequence peptide blending hydrogels. The change in the quench percentage is monitored. If the secondary peptide co-assembles to the KF8K, no change in the possibility of KF8K-FITC meeting KF8K-Dabcyl. Therefore, the quench ratio should be unchanged. Otherwise, the separate assembly causes the increase of KF8K density, increasing the probability of meeting. Therefore, a ratio increase will be observed.

Besides, when both KF8K-FITC and Dabcyl-KF8K are present in the hydrogel, the quenching can be in both the same fibre and cross fibre (figure 4.4 C). The ideal percentage of cross-fibre quenching cannot be estimated. However, the cross-fibre quenching can be eliminated by dilution.

As dilution increases, the concentration of fibres decreases. The fibre spacing exceeds the quenching distance between Dabcyl and FITC. At that time, there is only in-fibre quenching which can be predicted by the formulation in Figure 4.4 (B). The distance between peptide monomers can be acquired by X-ray and microscopy.

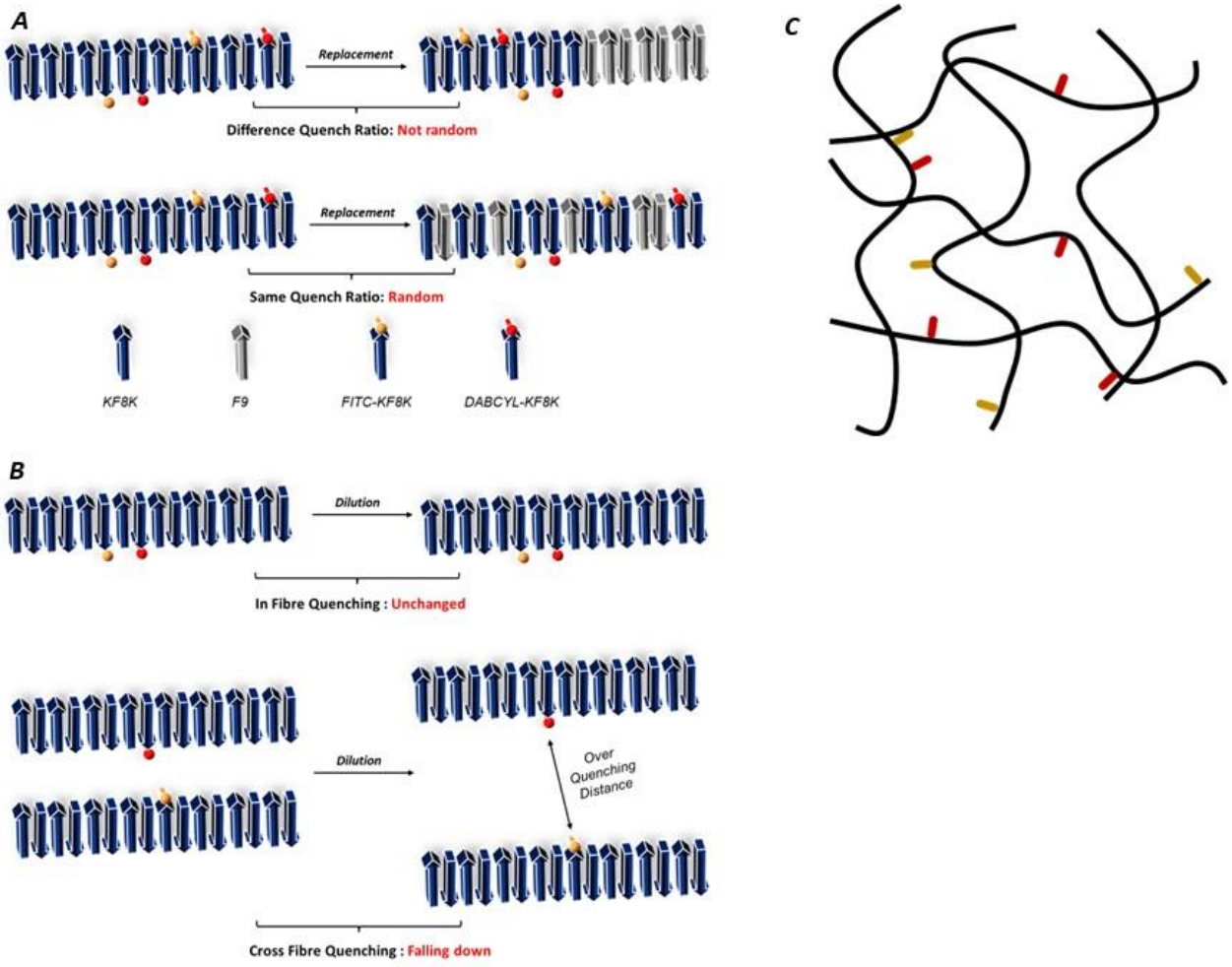

Figure 4-4 (A) The pathway of FITC-Dabcyl quenching experiment (B) The pathway of FITC-Dabcyl quenching dilution experiment (C) Schematic of FITC and Dabcyl in peptide fibre

As the above paragraph, a large and growing body of literature has reported the relationship between pH and FITC fluorescent intensity. From the literature, for FITC, the preferred pH is 8, but it is acceptable from pH 6 [27]. Therefore, the pH was set at pH 6.5, which is the hydrogelation pH of the KF8K. Besides, a considerable amount of literature has been published on the quenching of

FITC from the benzyl ring, which appears in the side chain of phenylalanine [28]. As a result, before the quenching reaction, the influence from background self-assembly peptide hydrogels needs to be assessed. The background hydrogels mean the peptide hydrogels without Fluorophore (FITC-KF8K) and Quenching (DABCYL-KF8K).

In the pre-experiment, 7.5 mg/ml was selected as the concentration of background peptide hydrogels. The value corresponds to the previous mechanical and characterisation experiments. The concentration was also kept in the later quenching reaction. However, it is not surprised that the fluorescent intensity for the 0.01 mg/ml FTIC-KF8K in 7.5 mg/ml KF8K hydrogel was decreased compared to the same concentration FITC-KF8K in HPLC water without extra quencher (Dabcyl). The intensity weakening is attributed to the influence from KF8K. Besides, the intensity decrease, regarded as quenching, was also found in the other background peptide hydrogels, for example, 3.75 mg/ml KF8K – 3.75 mg/ml F9 blending hydrogel. The fluorescent intensity of 0.01 mg/ml FITC decreases to around 200 a.u. in 7.5 mg/ml KF8K-F9 peptide. However, the value was 1428 a.u. in HPLC water. The result suggests the family of self-assembly peptides causing quenching, fixed with the result in the literature. Based on the literature, the influence from phenylalanine (F) in KF8K is proposed. The phenylalanine holds a benzyl ring in its side chain which can lead to the quenching to FITC [29]. Additionally, Self-assembly also has the potential to trigger the self-quenching of FITC. Due to the distance between FITC decreasing drastically in assembled fibres, the FITC molecules in fibre are over closed causing the self-quenching.

Therefore, a series of experiments were designed to evaluate the derivation of the quenching from background peptides, KF8K, F9 and F8. Firstly, the influence of phenylalanine, whose side chain is a benzyl ring, was assessed. The benzyl ring is able to quench FITC by attracting the

activated electron from FITC. A titration of the poly-F into the FITC solution was designed to monitor the change of fluorescent intensity against the concentration of poly-F (poly-phenylalanine). It was designed to prove that phenylalanine plays a dominating role in quenching. Figure 4.5 (A) shows the fluorescent intensity of 0.01 mg/ml FITC-KF8K with polyphenylalanine in a series of concentrations. From the diagram, it can be clearly seen that the 0.01 mg/ml KF8K-FITC produced at approximately 800 a.u. with no poly-F. However, only 650 a.u. left when 0.01 mg/ml poly-F was involved and finishing at 350 a.u. (37% intensity left) when the concentration was raised to 0.20 mg/ml. The extreme intensity falling was observed following the addition of poly-F proves the quenching stemming from the presence of phenylalanine.

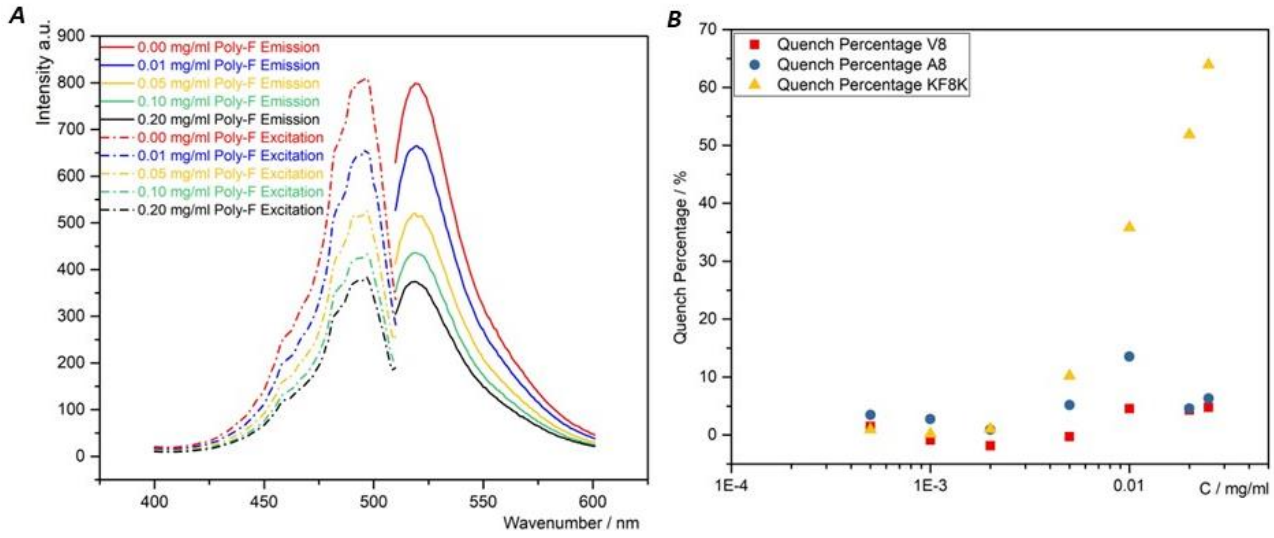

Figure 4-5 (A) The quenching percentage of titration A8, V8 and KF8K into 0.01 mg/ml FITC-KE8K (B) the fluorescent spectra of 0,0.01,0.02,0.05, 0.10 poly-F in 0.01 mg/ml FITC-KF8K

On the other hand, in order to evaluate the effectiveness of self-assembly to quenching, a titration of KF8K, A8 and V8 into 0.01 mg/ml FITC-KF8K in pH seven was performed. The result is shown in figure 4.5 (B). V8 is a peptide which replaces all phenylalanine (F) in F8 with valine (V) as a hydrophobic and non-charged amino acid. It also self-assembles into β-sheet and fibre under

suitable pH. Therefore, valine was employed as the peptide which can self-assemble but not phenylalanine. There was less than 10% quenching monitored in A8 and V8 titration. And their concentration had no effect on the quenching rate. On the contrary, the FITC fluorescence quenching was observed after the addition of KF8K. Further quenching was observed with increasing KF8K concentrations. The titration result suggests the phenylalanine (F) in self-assembly peptides (KF8K, F9 and F8) causes the quenching for FITC.

Due to the quenching from SAPs, the influence from background peptides hydrogels is demanded to assess first. The ideal result is that the same intensity of quenching was observed in pure KF8K and KF8K containing hybrid hydrogels. The same intensity means the quenching is equal in each background hydrogel and can be offset. The fluorescent intensity of FITC-KF8K in 7.5 mg/ml KF8K, KF8K-F8, KF8K-F9 and KF8K-(D)-KF8K hydrogels was measured. In all blending samples, KF8K was mixed with secondary peptides in the 1-to-1 ratio. The total peptide concentration was controlled at 7.5 mg/ml unchanged. This means the blending sample is equal to replacing half of KF8K with the same amount of another peptide. Figure 4.6 (A) shows the emission intensity of 0.003, 0.005 and 0.01 mg/ml FITC-KF8K under pH 6.50 in 7.5 mg/ml KF8K, KF8K-F9 and KF8K-F8 blending hydrogels. In the above three background peptide hydrogels, a similar FITC fluorescent intensity was detected when the same amount of FITC was present. This result indicates that the quenching from the four SAPs is similar in intensity and can therefore be counteracted. Further, fortunately, the proportion of FITC quenched in these hydrogels did not vary with the FITC-KF8K concentration. The value kept at around 83.5%. The result is explained that the quench from SAPs to FITC has been saturated. As a result, the slight change in FITC-KF8K concentration will not lead to a difference in the quenching ratio. Therefore, in short, the

quenching from the SAPs will not interfere with the FITC-Dabcyl quench experiment to expose the distribution of peptide chains in KF8K-based blending hydrogel.

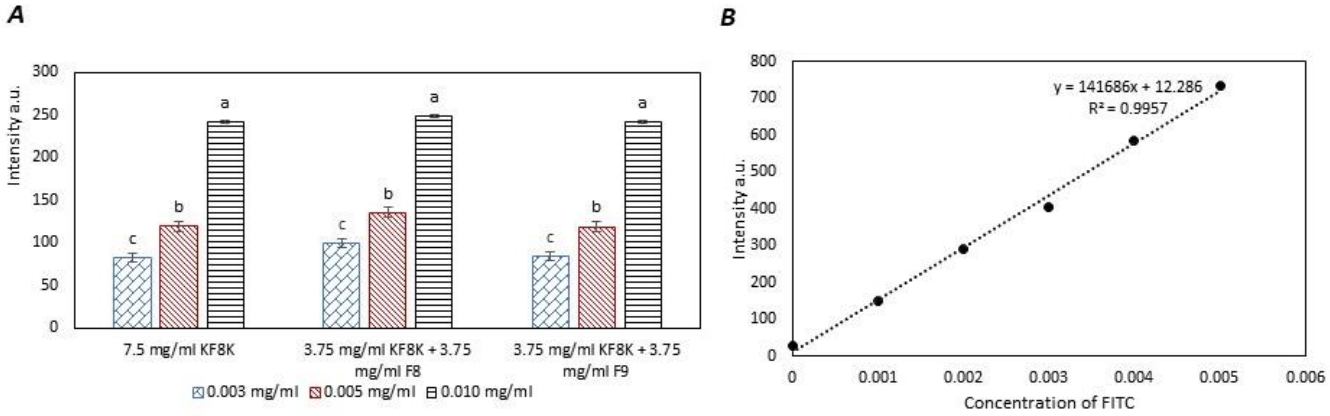

Figure 4-6 (A) the fluorescent of the intensity of 0.003, 0.005 and 0.010 mg/ml FITC-KF8K in 7.5 mg/ml KF8K pure, KF8K-F8 and KF8K-F9 (B) the fluorescent intensity against the FITC-KE8K concentration standard curve

Prior to the quenching reaction, the standard curve between activated FITC concentration and fluorescent intensity is demanded. The curve was produced by measuring a series of different concentrations of FITC-KF8K in 7.5 mg/ml A8 solution, whose result is shown in figure 4.6 (B). The reason for employing A8 for the standard curve is that there is no fluorescent quenching for FITC. The A8 also has good solubility in water between pH 2 and 12. Besides, the high similarity between A8 and F8/F9/KF8K sequence is another reason. The distribution between hydrophilic and hydrophobic amino acids and positive and negative charging in the A8 peptide chain is the same as the F8/F9/KF8K peptides. Similarly, the pH for the standard curves was also 6.50. The concentration of FITC was set from 0.000 mg/ml to 0.005 mg/ml to prevent intensity saturation (1000 a.u.) with 0.001 mg/ml intervals. A relevantly lower concentration of FITC-KF8K was introduced compared to the concentration in the above experiment, so that there was no quenching from A8. In the fluorescent spectra, the emission intensity of 0.005 mg/ml FITC-KF8K

reaches 792 a.u. Meanwhile, the value was 152 a.u. in 0.001 mg/ml FITC-KF8K. The value in emission spectra was adopted for linear fitting to establish a function to calculate the predicted activated FITC concentration from the fluorescent intensity in pH 6.50. Fortunately, the intensity of the peak in emission spectra and excitation spectra was closed. The produced fitting results from emission spectra and excitation spectra were same. The produced fitting formulation is Intensity(a.u.) = 141686 × FITC-KF8K concentration (mg/ml) + 12.268 with 0.9957 R^2 which proves the linearity of the fitting function.

Table 4-2 Result of Quenching percentage after the addition of Dabcyl in KF8K-F9 blending hydrogel

Sequence	7.5 mg/ml KF8K Efficient FITC: 0.00162 mg/ml			3.75 mg/ml KF8K + 3.75 mg/ml F9 Efficient FITC: 0.00164 mg/ml		
Quench Ratio	No quench	1-1 FITC-DABCYL	1-5 FITC-DABCYL	No quench	1-1 FITC-DABCYL	1-5 FITC-DABCYL
Intensity a.u.	242.68	229.03	170.97	247.39	243.60	172.39
Fluorescent Concentration mg/ml	0.00163	0.00153	0.00112	0.00166	0.00163	0.00113
Quench Percentage	0.00	5.62	30.88	0.00	1.93	31.78

Turning to the Dabcyl quenching reaction, the fluorescent intensity for 0.010 mg/ml FITC-KF8K with Dabcyl-KF8K in 7.5 mg/ml KF8K pure hydrogel and 7.5 mg/ml KF8K-F9 blending hydrogel are given in table 4.2 and figure 4.7. The molecular ratio between FITC-KF8K and Dabcyl-KF8K was 1-1 (0.01 mg/ml FITC-KF8K and 0.01 mg/ml Dabcyl-KF8K) and 1-5 (0.01 mg/ml FITC-KF8K and 0.5 mg/ml Dabcyl-KF8K). The concentration of FITC-KF8K was 0.01 mg/ml, unchanged. 0.01 mg/ml Dabcyl-KF8K failed to achieve obvious quenches in both pure KF8K and KF8K-F9 hydrogel. Only 5.8% of FITC-KF8K was quenched in pure KF8K and 1.93% in blending hydrogel. The result is attributed to the ratio of active FITC-KF8K being so low that Dabcyl-KF8K was hard to meet with it

in the quenching range. Because of the quenching from KF8K and F9, the activated concentration of FITC-KF8K in KF8K and KF8K-F9 hydrogel was only 0.00162 and 0.00164 mg/ml, respectively. Meanwhile, the concentration of the general peptide was 7.5 mg/ml, which was 4573 times that of FITC-KF8K. However, the quenching percentage increased to around 31% in KF8K hydrogel when the ratio of Dabcyl-KF8K was improved to 5 times. Additionally, the value reached 32% in KF8K-F9 hydrogel. A strongly closed quench percentage was detected in pure KF8K and KF8K-F9 blending hydrogel. The similarity indicates that the replacement of un-labelled KF8K by F9 does not influence the quench percentage by Dabcyl-KF8K, which means the F9 and KF8K peptide monomers assemble homogeneously in the blending hydrogel.

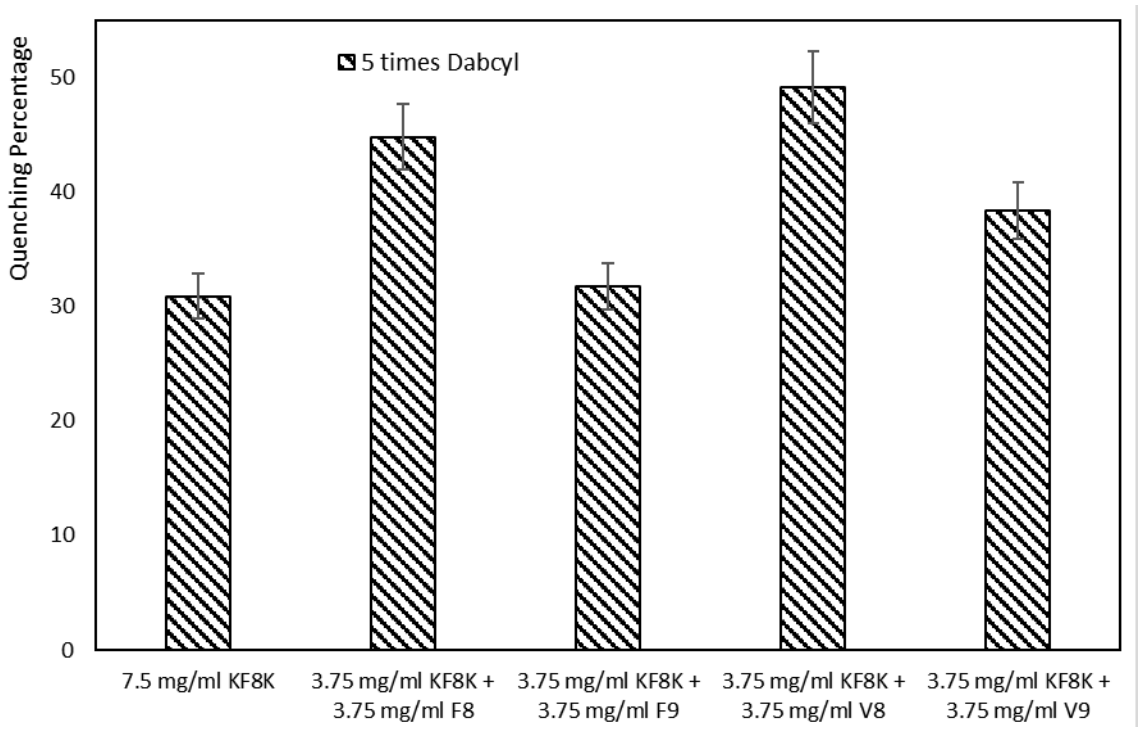

Figure 4-7 The Quenching percentage of 7.5 mg/ml KF8K, KF8K-F8, KF8K-F9, KF8K-V8 and KF8K-F9 hydrogels with 1 and 5 molar times Dabcyl

The same experiment was also done in the KF8K-F8 system. The result is shown in table 4.4 and figure 4.7. Despite the high similarity between F8 and F9 in the peptide sequence, the two

self-assembly peptides showed completely different results when mixed with KF8K. The quenching from the background peptide, KF8K-F8, was the same as KF8K. The value still was approximately 83%. However, for the Dabcyl quenching ratio, 5 times Dabcyl-KF8K caused 44.77% of quenching in 7.5 mg/ml KF8K-F8. The total FITC-KF8K concentration still was 0.10 mg/ml. This apparent difference in quenching rate demonstrates the separate assembly between KF8K and F8 monomers. The separation of two peptide monomers is attributed to the pH. F8 peptide precipitates in the experiment pH, 6.50. Therefore, in the blending hydrogel, the KF8K monomer self-assembles to fibre but F8 monomers aggregate and precipitate.

Table 4-3 Result of Quenching percentage after the addition of Dabcyl in L-KF8K and F8 blending hydrogel

Sequence	7.5 mg/ml KF8K Efficient FITC: 0.00162 mg/ml			3.75 mg/ml L-KF8K + 3.75 mg/ml F8 Efficient FITC: 0.00164 mg/ml		
Quench Ratio	No quench	1-1 FITC-DABCYL	1-5 FITC-DABCYL	No quench	1-1 FITC-DABCYL	1-5 FITC-DABCYL
Intensity a.u.	242.68	229.03	170.97	249.38	248.89	142.63
Fluorescent Concentration mg/ml	0.00163	0.00153	0.00112	0.00167	0.00166	0.00092
Quench Percentage	0.00	5.62	30.88	0.00	1.72	44.77

Similar results have been observed for V8 (sequence: VEVKVEVK) and V9 (sequence: VEVKVEVKK). In figure 4.8 (A), it is clear that with 5 times Dabcyl-KF8K, the quenching percentage in V9-KF8K (34.37%) was close to the value of KF8K (30.88%). As a result, V9 was believed to be co-assembled with KF8K. However, an obvious quenching ratio increase was observed in V8-KF8K (49.08%). The V8 peptide monomers also precipitate at pH 6.50. In short, the behaviour of the V8 and V9 in KF8K blending hydrogel is the same as the F8 and F9. The similarity between V-peptide

and F-peptide demonstrates that the difference in hydrophobic amino acid will not interfere with the co-assembly preference with KF8K peptide.

Finally, the KF8K hydrogel containing the fluorophore and quencher was diluted to verify that this fluorescence quenching matched the expected values. When dilutions are sufficient, quenching from Dabcyl to FITC occurs only within the peptide fibrils. Thus, the expected quenching rate within the fibril can be calculated by the peptide monomer spacing. The distances between peptide monomers are obtained by the experiment. Usually, the values are obtained by X-ray diffraction. Additionally, the signal for sufficient dilution (no cross fibres quenching) should be the moment when the quench percentage is unchanged against dilution times. It is because the cross-fibre quenching will be weaker with dilution continuously, but the single fibre quenching is unchanged with dilution. Therefore, if there are no cross fibres quenching, the quench percentage is unchanged against dilution times. When the quenching occurs only within the fibre, the abstract quench percentage should be 20.68%. The result was calculated based on the KF8K peptide chain distance measured by X-ray diffraction, which is 0.58 nm. The 7.5 mg/ml KF8K hydrogel with 0.01 mg/ml FITC-KF8K and 0.05 mg/ml Dabcyl-KF8K were diluted to disperse fibres making sure the quench by Dabcyl-KF8K only presents in single fibres. The dilution result is given in Figure 4.8 (B). It appeared that the 7.5 mg/ml KF8K hydrogel with 0.01 mg/ml FITC-KF8K and 0.05 mg/ml Dabcyl-KF8K presented around 44.07% FITC-KF8K quench. However, the value decreased to 23.38% and 25.86% after 2- and 5-times dilution, respectively. Further, the quenching percentage reached 20.59% when the sample underwent dilution 10 times. From this date, the in-fibre quenching was calculated at around 23%, corresponding to the theoretical calculation result (20.68%) based on the peptide chains' distance from X-ray diffraction. The result strongly suggests the reliability of the FITC-Dabcyl quenching reaction.

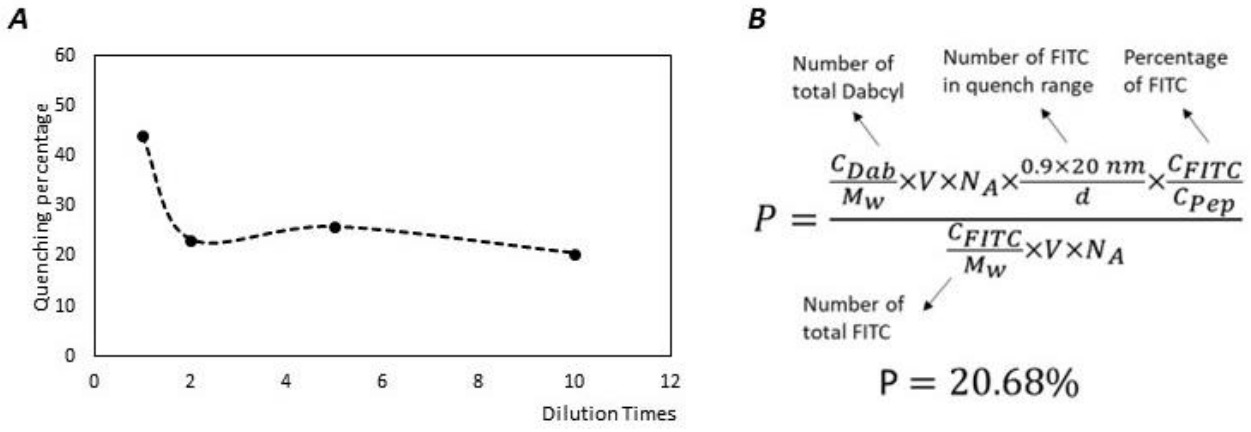

Figure 4-8 (A) the Quenching percentage of 0.01 mg/ml FITC-KF8K, 0.05 mg/ml Dabcyl-KF8K in 7.5 mg/ml KF8K after 2-, 5- and 10-times dilution. (B) the formulation of calculation ideal quenching percentage

In short, in the blending hydrogels, V9 and F9 can homogeneously distributes with KF8K. The result indicates the slight difference in peptide sequence does not cause the separately assembly in blending hydrogel. However, the V8 and F8 monomers showed separately assembly with KF8K monomer. It is attributed to the precipitation of the V8 and F8 at the pH.

4.3.3 Blending hydrogel by self-assembly peptide and non-self-assembly peptide

This section discusses about the A8 (sequence: AEAKAEAK) and KF8K. A8 is a non-self-assembling peptide [34]. In the A8 sequence, all phenylalanine (F) is replaced by alanine (A), which is unable to form pi-pi interactions and has significantly lower hydrophobicity (F has a value of 100 while A has a value of 41 at pH 7). However, the distribution of hydrophobic and hydrophilic amino acids, as well as the location of charged amino acids, remain unchanged. As a result, A8 only acts as a well-dissolved peptide with the same design without interfering with the self-assembly process. A phase diagram of 7.5, 15 and 25 mg/ml A8 against pH was created. All samples remain in a transparent liquid in a pH range of 2 to 12.

In terms of A8, since the critical role of the β-sheet in driving the self-assembly of peptides, the influence of A8 on the formation of secondary structure in KF8K was researched first. The FTIR spectra between 1000 to 1800 cm^{-1} of pure A8 and its hybrid samples with KF8K are shown in figure 4.9 (A). The ratio of the two blending samples was 7.5 mg/ml A8 - 7.5 mg/ml KF8K and 15 mg/ml A8 - 7.5 mg/ml KF8K, meaning a 1-to-1 and 2-to-1 A8-KF8K mixing ratio. NaH_2PO_4 was also used as a reference peak for normalization, which did not influence the self-assembly of peptides. The band of amide I in A8 stayed at 1638 cm^{-1}, proving that there was no secondary structure forming in pure A8. However, the amide I peaks were divided into two A8-KF8K blending samples. Besides the peak in 1638 cm^{-1}, there is another separated peak shifted to 1616 cm^{-1} (the bond of β-sheet). Further, the intensity of the shifting peak in those two blending samples was close and also similar to the peak in pure 7.5 mg/ml KF8K. The intensity similarity verified the presence of β-sheet isolation with the addition of A8. Additionally, the band of amide II stayed at 1552 cm^{-1} in all samples. The area increased with the increase of total peptide concentration, regardless of whether the peptide was A8 or KF8K. Amide II derives from the amide group in all amino acids.

In the above FTIR spectrum, the shape of peaks in FTIR was similar between each blending sample. To expose the relationship between peak intensity and A8 peptide concentration better, a further FTIR peak fitting in the 1300-1700 cm^{-1} zone was done. The fitting forced on analysing the composition of the amide I band in the blending sample. The amide I band of 7.5 mg/ml KF8K was at 1615 cm^{-1}, which corresponded to the β-sheet. However, the band was at 1638 cm^{-1} in 15 mg/ml A8. The amide I peak of the 7.5/15 mg/ml A8 – 7.5 mg/ml KF8K blending samples was separated into two peaks. Based on the amide I of pure A8 and KF8K, the peaks at 1615 cm^{-1} and 1638 cm^{-1} were choices. The fitting results are shown in figure 4.9 (B) and table 4.4. The concentration of KF8K was unchanged in the blending samples, while the area for the β-sheet peak

was stable with an increase of A8 concentration. The tendency indicates that the concentration of KF8K is the only factor that decides the generation of the β-sheet in this system.

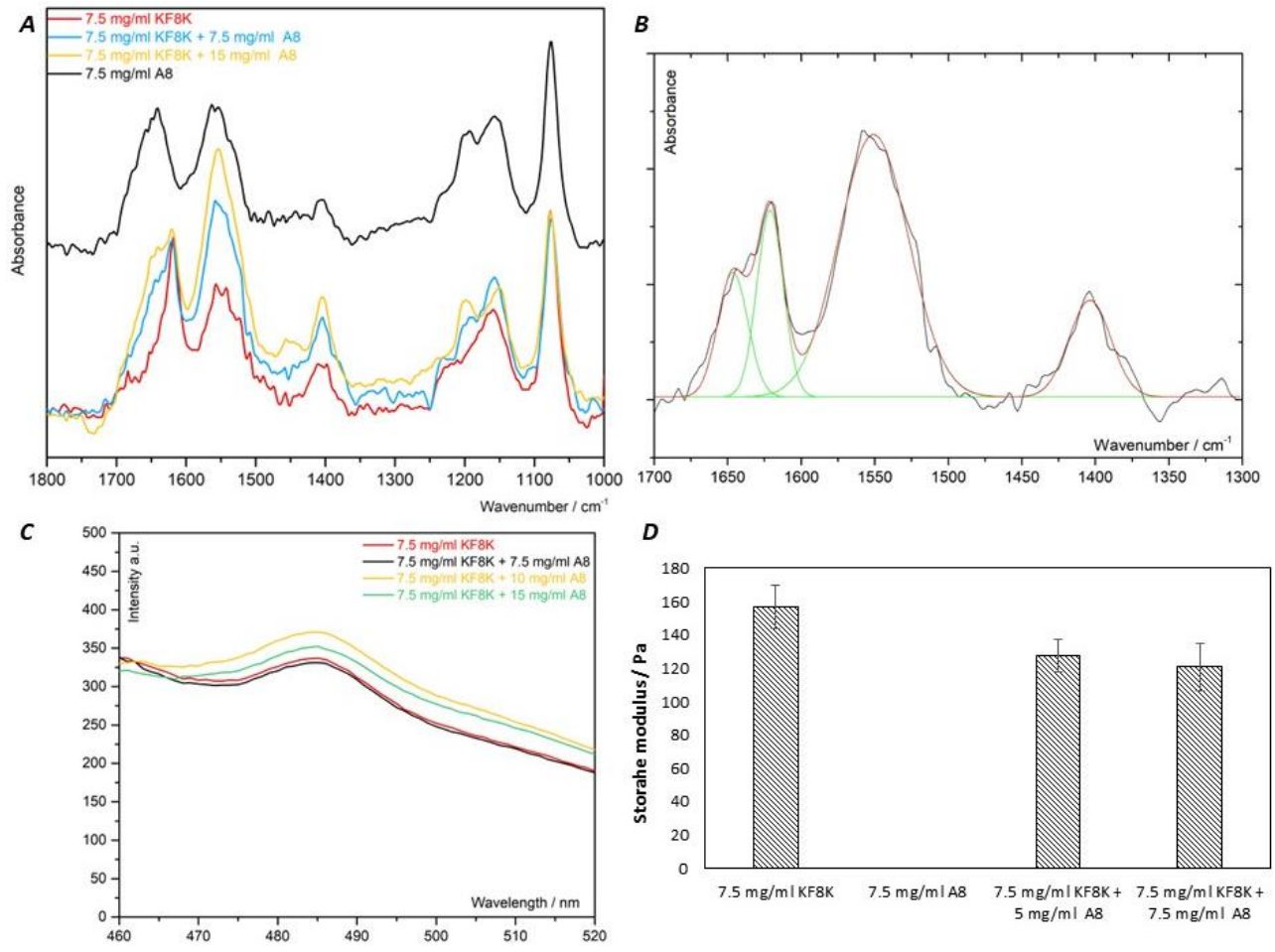

Figure 4-9 (A) The FTIR of 7.5 mg/ml KF8K with 0, 7.5 and 15 mg/ml A8 blending hydrogel (B) Fitting of FTIR of 7.5 mg/ml KF8K and 15 mg/ml A8 blending hydrogel (C) THT assay of 7.5 mg/ml KF8K with 0, 7.5,10 and 15 mg/ml A8 blending hydrogel (D) Storage modulus of 7. 5mg/ml KF8K with 0, 5 and 7.5 mg/ml A8 hydrogel.

Table 4-4 The area of β-sheet and Amide I after fitting in KF8K and A8 blending hydrogels

Samples	B-Sheet Area	Amide I Area
7.5 mg/ml KF8K	**0.07104**	\
7.5 mg/ml KF8K + 7.5 mg/ml A8	**0.07273**	0.05532
7.5 mg/ml KF8K + 15 mg/ml A8	**0.07233**	0.06679
15 mg/ml A8	\	0.06337

Because of the results from the FTIR fitting, a series of A8 and KF8K blending samples were also tested using the Thioflavin T (THT) assay. The intensity of THT in the fluorescence spectrum is proportional to the amount of β-sheet in the samples [23]. This is because THT binds to the β-sheet structures and produces a molecule with fluorescent at 286 nm. The THT assay was used to confirm the accuracy of the results from FTIR and peak fitting for the KF8K-A8 samples. In Figure 4.9 (C), the concentration of KF8K was kept constant at 7.5 mg/ml, while A8 was varied at concentrations of 0, 7.5, 10, and 15 mg/ml. However, the intensity of the peaks at 286 nm was nearly unchanged, with a maximum difference of only 10%. This trend indicates that the amount of β-sheet formed is independent of the concentration of A8. The existence of A8 does not contribute to the self-assembly process.

Even though the results of the characterizations suggest that A8 does not interfere with the formation of the β-sheet, the storage moduli of A8-KF8K blending hydrogels decreased with an increase in A8 concentration. The storage modulus started from 150 Pa in 7.5 mg/ml KF8K. However, with 15 mg/ml, the value fell to 120 Pa, with a 20% degradation (Figure 4.9 (D)). Since the evidence proved the non-interference with the self-assembly process, the phenomenon can be explained by the influence on fibre from A8 molecules. A possible reason is that the A8

molecules mixed into KF8K fibres, leading to a decrease in the density of KF8K in the fibres. Therefore, the strength of the fibres decreased.

At the same time, A8 was also included in the fluorescent quenching experiment as a non-self-assembling peptide. A8 was mixed with KF8K for the blending hydrogel. And FITC-KF8K and Dabcyl-KF8K were added to the blending hydrogel to measure the quenching percentage. In corresponding to the above experiments, the total peptide concentration of peptide was still kept at 7.5 mg/ml in the blending sample, and the ratio between A8 and KF8K was 1 to 1 unchanged (3.75 mg/ml A8 and 3.75 mg/ml KF8K). Ideally, due to A8 not self-assembling and forming fibre with KF8K, the A8 monomers should not interfere with the self-assembly of KF8K. As the result, the 7.5 mg/ml A8-KF8K sample should work similarly to the 3.75 mg/ml KF8K. The quenching results are given in figure 4.9. In the 7.5 mg/ml A8-KF8K blending hydrogel, 53.01% of the FITC-KF8K fluorescence was quenched by the 5 times concentration of Dabcyl -KF8K. However, this value was only 30.99% in the 7.5 mg/ml KF8K hydrogel. There was a significant difference in the quenching percentage of two samples with the same amount of Dabcyl. Besides, the FITC quenching percentage in 3.75 mg/ml KF8K hydrogel is also shown in figure 4.10. In that hydrogel, the 5 times concentration of Dabcyl-KF8K produced 50.88% quenching for FITC-KF8K. The value was highly close to the percentage acquired in 7.5 mg/ml A8-KF8K. This data justifies the hypothesis presented at the beginning of the paragraph. The A8 monomer was not involved in the KF8K self-assembly. Furthermore, compared to 7.5 mg/ml KF8K, 3.75 mg/ml KF8K exhibited an obviously higher FITC fluorescence quenching rate. This data demonstrates the effect of background peptide concentration decreases on quenching rates. The above reduction in background peptide concentration affects the quenching rate in two ways. On the one hand, the concentration of peptide fibre decreased due to a decrease in the concentration of background

peptides. Therefore, the quenching across the fibres was reduced. However, on the other hand, a decrease in the concentration of background peptides led to a relative increase in the concentration of FITC/Dabcyl-modified peptides. Thus, the probability of encounter between FITC fluorophore and Dabcyl quencher was improved. The results of the experiment showed the latter to be dominant. The decrease in background peptide concentration led to an increase in the FITC fluorescence quenching rate by Dabcyl.

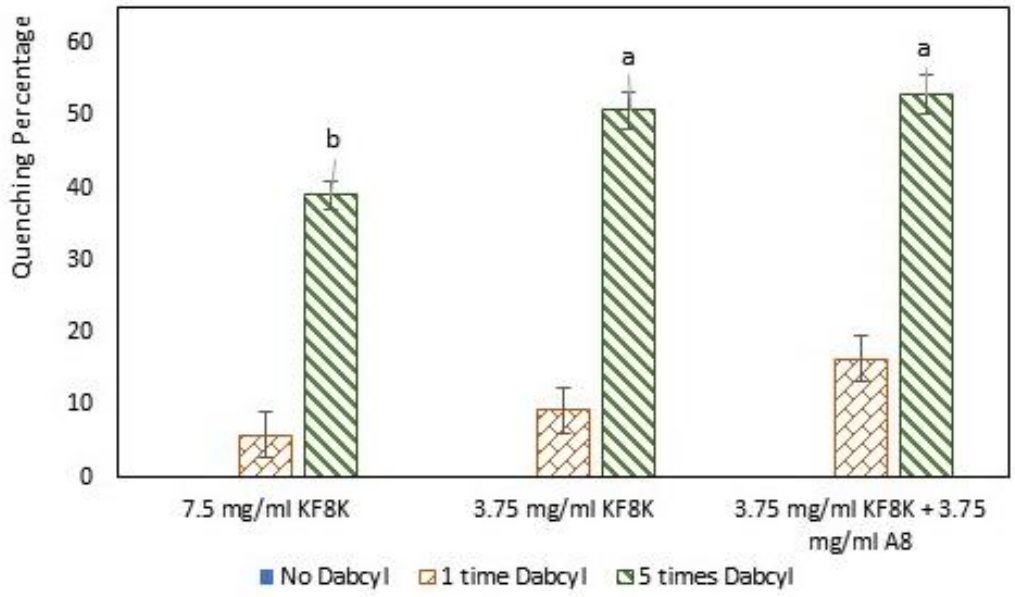

Figure 4-10 The Quenching percentage of 7.5 mg/ml KF8K, KF8K-A8 and 3.75 mg/ml KF8K hydrogels with 1 and 5 molar times Dabcyl

In summary, the A8 does not co-assemble and influence the assembly of KF8K. The replacement of KF8K by A8 produced the same result of the dilution of KF8K.

4.3.4 Blending hydrogel by opposite chirality self-assembly peptides

The following section assesses the influence of chirality on self-assembly by comparing L- and D-KF8K. D-KF8K, whose sequence is the same as L-KF8K, but with all amino acids in the D configuration (figure 4.11 A), is also included in the study. Its contribution is to compare the

influence of chirality on self-assembly hydrogel and as a potential candidate to form a double-network with L-KF8K. It is explained that the different directions of side chains between L- and D-KF8K might affect the spatial interactions. For example, π-π stacking. Therefore, Prior to the fluorescent quenching experiment, a series of characterisation, mechanical tests, and microscopy imaging were done on A8, D-KF8K and their blending hydrogels with L-KF8K to monitor their influence on self-assembly, and ultimately, the hydrogel.

Firstly, a pH against phase diagram was adopted to ensure the hydrogelation ability given in figure 4.11 (C). Unsurprisingly, no significant difference was detected in the hydrogelation pH between D- and L-KF8K, which were clear solutions before pH 6.5. At the same time, they started to be viscous and formed a transparent hydrogel from pH 6.70. With the increase in pH, the cloudy hydrogel was observed in pH 6.78 and 6.80 in D- and L-KF8K, respectively. The finding suggests the similarity of the two opposite chirality peptides in the hydrogelation behaviour against pH. Meanwhile, the appearance of hydrogel was still unaffected by chirality, as given in figure 4.11 (B).

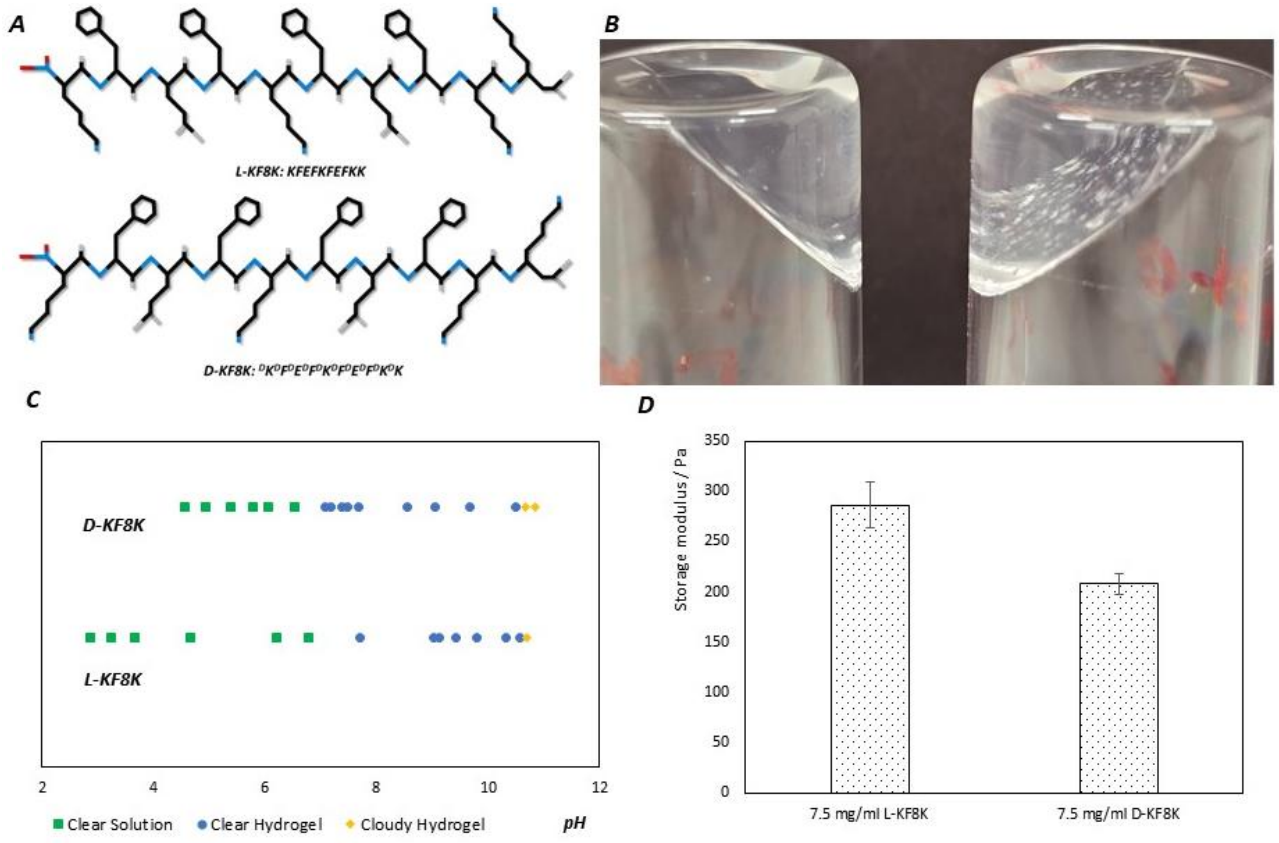

Figure 4-11 (A) Structure of L-KF8K and D-KF8K (B) Appearance of 7.5 mg/ml L-KF8K and D-KF8K (C) The Phase diagram of 25 mg/ml L-KF8K and D-KF8K samples (D) Storage modulus of 7.5 mg/ml L-KF8K and D-KF8K hydrogel in pH 6.5

Due primarily to the reliance on the β-sheet in the self-assembly of KF8K, those two samples also underwent FTIR in order to monitor the difference of secondary structures (figure 4.12 B). The analysis forced on the wavenumber between 1800 cm^{-1} to 1300 cm^{-1} which covered the main bonds of amino acid and peptide, involving amide I and amide II. From the D- and L-KF8K spectra, it can be seen that a sharp peak presented at 1618 cm^{-1} with a weak peak at 1681 cm^{-1}. The two peaks were related to the parallel and anti-parallel β-sheet, respectively. Identically, the β-sheet peaks in the L- and D-KF8K spectra also reached approximately the same intensity, proving the high similarities of the two peptides in another view.

It was followed by circular dichroism spectroscopy (CD). Its benefit not only involves access to the secondary structure but also allows the measurement of the molecule's chirality directly. Figure 4.12 (A) highlighted the peaks corresponding to the β-sheet. However, the signal was in opposite ellipticity in D- and L-KF8K. For L-KF8K, a negative peak at 220 nm and a positive peak at 195 nm can be seen clearly, which is attributed to the presence of a β-sheet. Meanwhile, peaks in the same wavelength were also detected in D-KF8K while the positive and negative were reversed, accepted as the β-sheet but anti-chirality.

Turning to the XRD (X-ray diffraction), the results are shown in figure 4.12 (C). The reflections at 4.1 Å, 5.8 Å, and 11.0 Å were also present in the D-KF8K sample, which are assigned to the length of hydrogen bonds, the distance between peptide chains, and sheet-sheet separation distance, respectively. The diffraction spectrum was similar to that of L-KF8K. In summary, the characterization results indicate the similarity of D- and L-KF8K in the secondary structure after self-assembly, except for chirality.

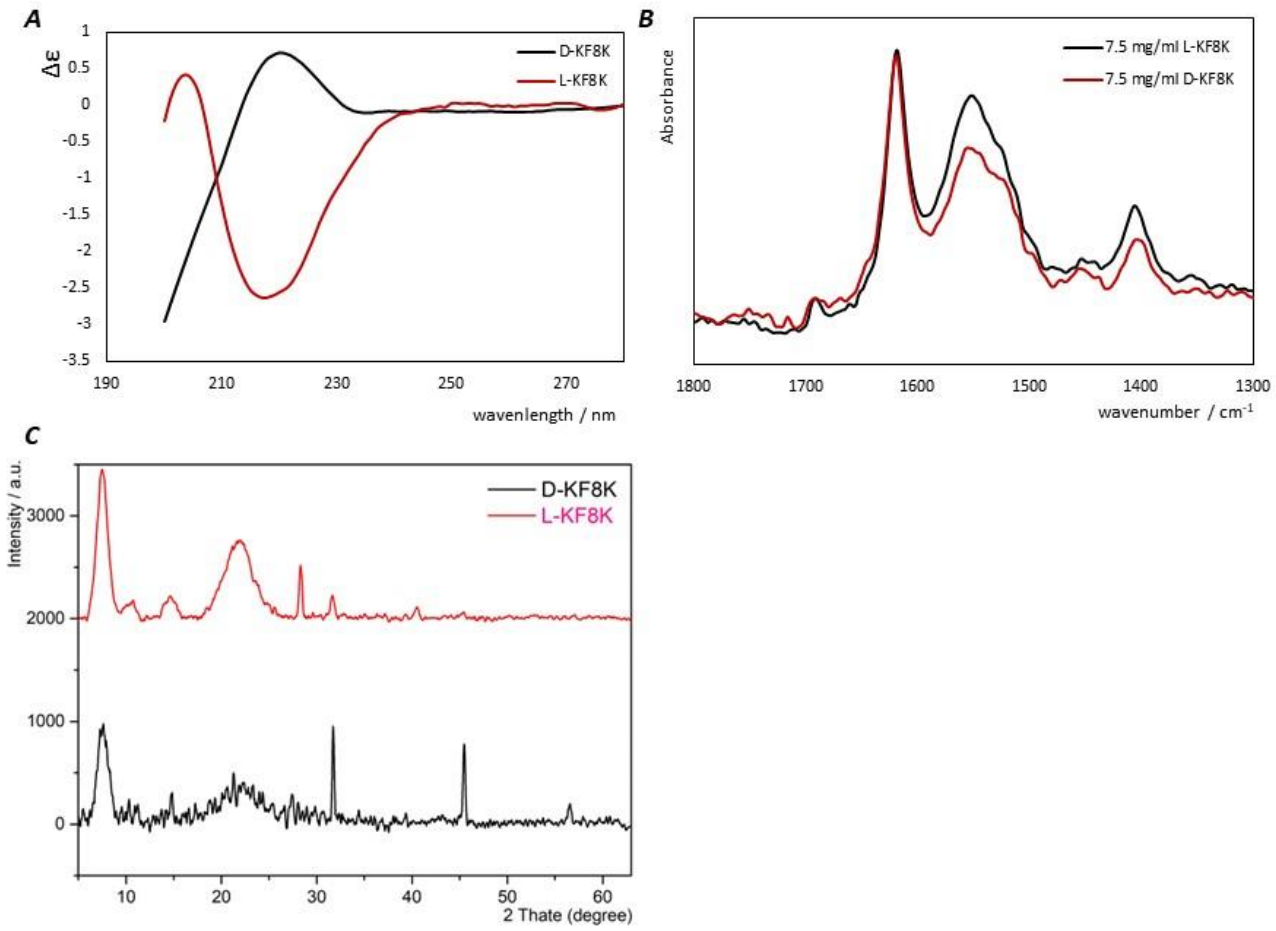

Figure 4-12 (A) CD spectra of 7.5 mg/ml L-KF8K and D-KF8K (B) FTIR spectra of 7.5 mg/ml L-KF8K and D-KF8K (C) XRD of 25 mg/ml L-KF8K and D-KF8K (D) OD600 of E. coli in 5 mg/ml A8, F8, F9, L-KF8K and D-KF8K in 18 hours

Additionally, the two KF8K samples also underwent microscopy to make the comparison in the morphology view. The AFM images are given in figure 4.13 (A, B), revealing that both peptides formed fibres when their concentration was over CHC (critical hydrogel concentration). In L-KF8K, the sample was at a diluted concentration of 0.25 mg/ml. In the diluted L-KF8K sample, fibrils of $\sim 15.6 \pm 0.5$ nm in diameter were detected. Larger fibrils were also imaged with up to $\sim 23.9 \pm 1.0$ nm in diameter, which is attributed to the assembly of individual signal fibrils to fibres. Meanwhile, an indistinguishable fibrils image was caught in D-KF8K with the same concentration, 0.25 mg/ml. The single fibrils were imaged in two different fibres, which were 9.3 ± 0.5 nm and

$\sim 19.8 \pm 0.5$ nm in diameter whose number was relevantly smaller than L-KF8K. However, the diameter results from AFM were reported not to be highly reliable because the interaction between mica and peptide may cause variations in morphology. Besides, once the curvature of AFM is larger than the fibre diameter, the result in the image will be larger than the actual one. In that, the slight difference in fibril diameter from AFM between L- and D-KF8K is likely related to the interference from AFM and mica. Due to the limitation in AFM, TEM was also employed for a more precise diameter detection, whose images are displayed in figure 4.14 (A, B). A clear and good network structure was observed in TEM images in both L- and D-KF8K samples under 0.375 mg/ml concentration. The shape and density of the fibres were close to each other. The fibre diameter is 4.21 ± 0.37 and 5.31 ± 0.19 nm, respectively.

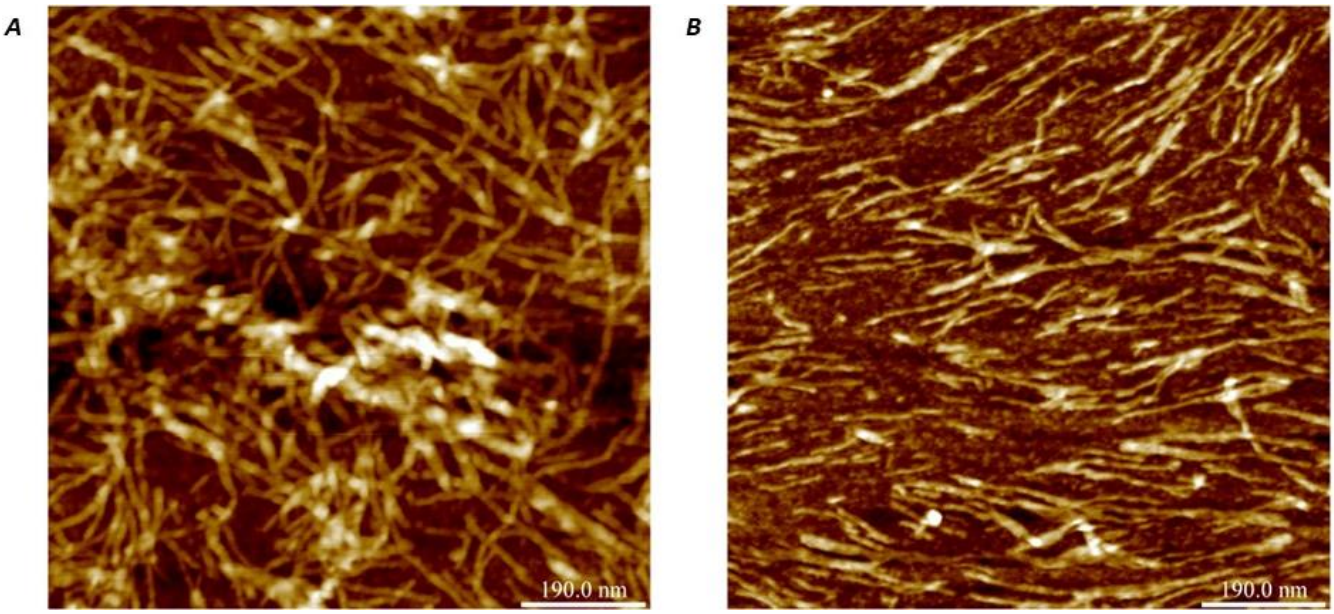

Figure 4-13 (A-B) AFM image of 0.25 mg/ml L-KF8K and D-KF8K in mica surface

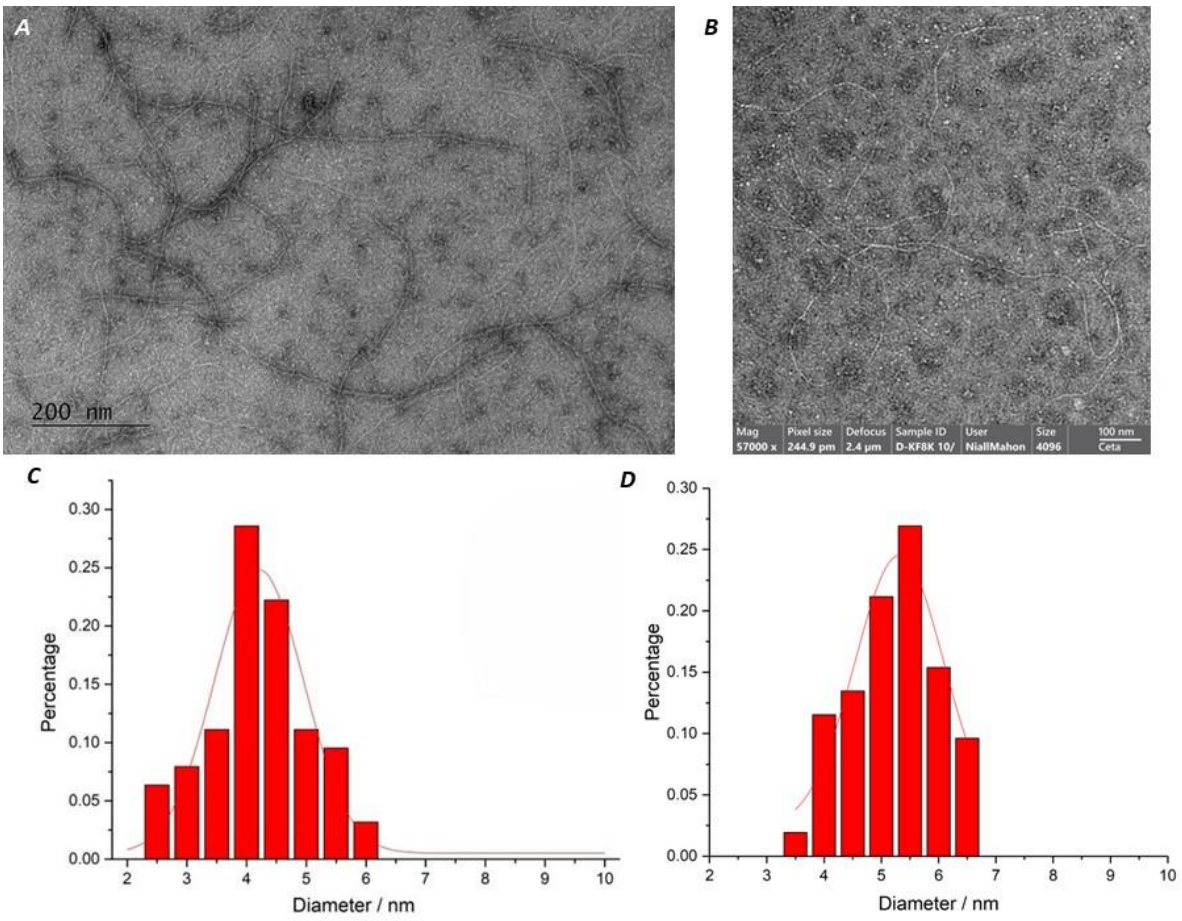

Figure 4-14 (A -B) TEM of 0.375 mg/ml L- KF8K and D- KF8K hybrid hydrogel (C-D) 0.375 mg/ml L-KF8K's and D- KF8K's fibres' diameter distribution.

Finally, in terms of the mechanical properties test, the results are shown in Figure 4.11 (D). The results also provide evidence for the similarity of the two peptide hydrogels, consistent with the results from previous experiments. The storage modulus reached 208 Pa in 7.5 mg/ml D-KF8K, with no significant difference compared to 7.5 mg/ml L-KF8K, which is 286 Pa. In summary, according to the results, L- and D-KF8K perform similarly in microstructure formation and mechanical properties, except that the chirality of monomers and secondary structure is reversed.

The following section was concerned with the effect of peptide chirality on the co-assembly of peptide monomers. The same sequence but opposite chirality peptides, L-KF8K and D-KF8K, were employed in the FITC-Dabcyl reaction. D-KF8K hydrogel has been proven to have a similar stiffness to L-KF8K hydrogel in the previous paragraphs. D-KF8K was thought to be a peptide that

can self-assemble separately with L-KF8K to form a double network hydrogel. In literature, the partial replacement of D-amino in the L peptide was reported to produce wide changes in the secondary structures [30]. However, the above characterisation proved the same secondary structure (β-sheet) presenting in both L- and D-KF8K. As a result, the two opposite chiral peptides are likely to form separate β-sheets and further form fibres separately. If the hypothesis works, ideally, the Dabcyl-KF8K in a 7.5 mg/ml L-KF8K - D-KF8K blending hydrogel would yield a higher quenching percentage for FITC-KF8K compared to in the 7.5 mg/ml KF8K hydrogel. Because D-KF8K did not participate in the assembly of L-KF8K, in the 7.5 mg/ml L-KF8K - D-KF8K hybrid hydrogel, the L-KF8K monomers are accumulated passively. As a result, the relative density of Dabcyl/FITC-modified L-KF8K against general L-KF8K was higher compared to in the 7.5 mg/ml L-KF8K. It means the possibility of Dabcyl-KF8K meeting FITC-KF8K is higher. The results of the quenching experiment are given in figure 4.15 and table 4.5. When the same concentration of Dabcyl-KF8K and FITC-KF8K was present, Dabcyl-KF8K showed 14.36% quenching of FITC in the blending L-KF8K and D-KF8K hydrogels. However, the value was 5.81% in the pure KF8K hydrogels. Further, if the concentration of Dabcyl-KF8K was increased to 5 times of FITC-KF8K, 46.99% of FITC-KF8K fluorescent was quenched by Dabcyl-KF8K in 7.5 mg/ml L-KF8K – D-KF8K. Meanwhile, the ratio was only 30.88% in 7.5 mg/ml L-KF8K hydrogel. This rises in FITC quenching rate in L-KF8K - D-KF8K blending hydrogels proved the separate assembly of the two peptides. This finding helps us to establish the self-assembly hydrogel with homogeneous macro properties but inhomogeneous micro fibre. The extra outside triggers or stimulations still are not needed in preparation for the micro inhomogeneous double-network hydrogel.

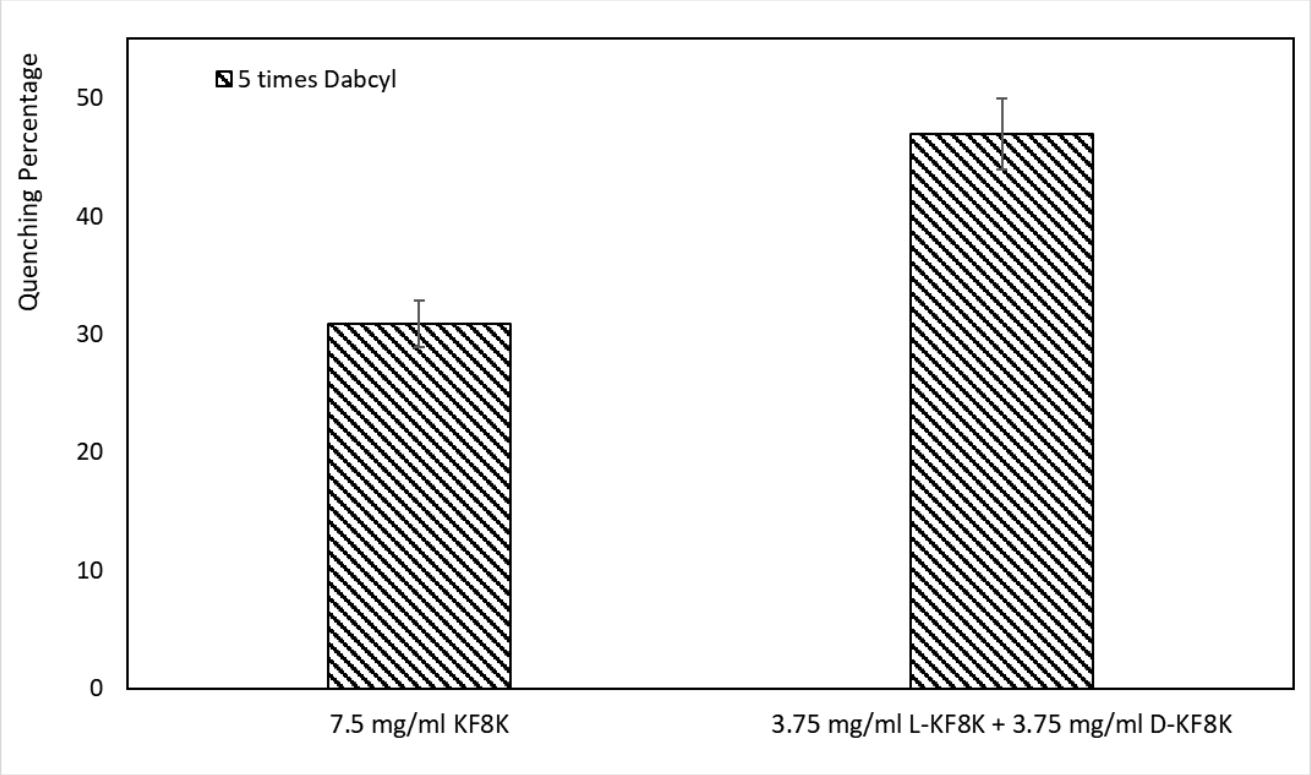

Figure 4-15 The Quenching percentage of 7.5 mg/ml KF8K and L-KF8K-D-KF8K hydrogels with 5 molar times Dabcyl

Table 4-5 Result of Quenching percentage after the addition of Dabcyl in L-KF8K-D-KF8K blending hydrogel

Sequence	7.5 mg/ml KF8K Efficient FITC: 0.00162 mg/ml			3.75 mg/ml L-KF8K + 3.75 mg/ml D-KF8K Efficient FITC: 0.00164 mg/ml		
Quench Ratio	No quench	1-1 FITC-DABCYL	1-5 FITC-DABCYL	No quench	1-1 FITC-DABCYL	1-5 FITC-DABCYL
Intensity a.u.	242.68	229.03	170.97	268.52	232.52	148.30
Fluorescent Concentration mg/ml	0.00163	0.00153	0.00112	0.00181	0.00155	0.00096
Quench Percentage	0.00	5.62	30.88	0.00	14.36	46.99

In short, D-KF8K produced a similar assembly process and hydrogel to L-KF8K. However, when they were blended together, their monomers will assemble separately.

4.4 Conclusion

In summary, the hydrogels with multiple sequence peptides were produced successfully, while the properties and structure differed depending on the type of consisting peptides. The ingredient peptide covered self-assembly peptide, non-self-assembly peptide, and D-peptide.

In the mixture with SAPs (F8 and F9), the modification by lysine in terminals did not drive apparent variance in the self-assembly process where two self-assembly peptides formed β-sheet and fibres together and randomly. This means the blending hydrogel behaved like a physical average of its two ingredient pure peptide hydrogels. The hydrogelation pH was determined by the ratio of composition peptides, where the more KF8K there is, the more neutral pH the transparent blend hydrogel acquires. At the same time, the increase of F8/F9 led to transparent hydrogel in more acid conditions. However, unfortunately, in pH 7, F8/F9-KF8K blending system cannot produce transparent and stiffer hydrogel compared with the pure same total concentration of KF8K. The increase of F8/F9 contributed to higher stiffness, while it led to hydrogel becoming cloudy at pH 7. KF8K played the contrary role, helping blending hydrogel keep clear in neutral pH but with weaker storage modulus. Further, even though in the hydrogelation pH, the half-half ratio blending hydrogels still presented lower stiffness than pure SAP hydrogels, as in blending hydrogel, the compositions are not in the preferable hydrogelation pH. However, the characterisation results did not suggest any change in the secondary structure after blending via CD, XRD or FTIR. Besides, relying on the FITC-Dabcyl quenching reaction, the homogeneous distribution of different sequence self-assembly peptides in blending hydrogels was also proved. The quench percentage in pure KF8K hydrogel and V9/F9-KF8K mixing hydrogel were the same.

When A8, the non-self-assembly peptide, is blending with KF8K, the pH and β-sheet amount are determined solely by KF8K. A8 did not affect the self-assembly process but decreased the stiffness of blending hydrogel as A8's concentration increases. This is because A8 weakens the fibre network of KF8K. Besides, in the A8-KF8K blending hydrogel, the FITC fluorescent quenching ratio by Dabcyl was improved, further proving that the non-self-assembly peptide was independent of the KF8F peptide fibres and self-assembly. Therefore, the replacement of KF8K by A8 in the blending sample made the result like dilution of KF8K.

The blending hydrogel by L-KF8K and D-KF8K achieved the primary aim of the experiment, establishing double-network hydrogel successfully.

The double network hydrogel exhibited similar microstructure except for chirality, as revealed by rheology test, characterisations and TEM/AFM imaging. Further, the fluorescent quenching reaction showed the separate assembly of the two peptides. Replacing half of L-KF8K with D-KF8K increased Dabcyl quenching more effectively than diluting KF8K. This double-network hydrogel enables the accumulation of functional modifications in the designed specific area. A future work of this double-network hydrogel is the need for further research on developing a peptide to connect the D-peptide and L-peptide assembly blocks in the hydrogel fibre. The L- and D- hybrid peptide potentially works as the linker.

Surprisingly, the quenching caused by the self-assembling peptide, KF8K, was observed in the FITC fluorescent quenching process. Through the comparison between KF8K, A8 and V8, the quenching was attributed to the presence of phenylalanine, which has a quenching benzyl ring on its side chain. Self-assembly was not the cause of the quenching. This study highlighted the

potential interference of aromatic amino acids on fluorescent intensity in fluorescent-based experiments.

Finally, through the well-dilution, which means there wass not cross-fibre quench in the hydrogel, the in-fibre quenching percentage of the Dabcyl to FITC in KF8K hydrogel was revealed. The obtained value closely aligned with the quench ratio, as calculation through the result from X-ray diffraction (XRD).

Reference

[1] Fong C, Le T, Drummond C J. Lyotropic liquid crystal engineering–ordered nanostructured small molecule amphiphile self-assembly materials by design. Chemical Society Reviews, 2012, 41(3): 1297-1322.

[2] Jun S, Hong Y, Imamura H, et al. Self-assembly of the ionic peptide EAK16: the effect of charge distributions on self-assembly. Biophysical journal, 2004, 87(2): 1249-1259.

[3] Ahmed E M. Hydrogel: Preparation, characterization, and applications: A review. Journal of advanced research, 2015, 6(2): 105-121.

[4] Sheehan F, Sementa D, Jain A, et al. Peptide-based supramolecular systems chemistry. Chemical Reviews, 2021, 121(22): 13869-13914.

[5] Modepalli V N, Rodriguez A L, Li R, et al. In vitro response to functionalized self-assembled peptide scaffolds for three-dimensional cell culture. Peptide Science, 2014, 102(2): 197-205.

[6] Elsawy M A, Smith A M, Hodson N, et al. Modification of β-sheet forming peptide hydrophobic face: effect on self-assembly and gelation. Langmuir, 2016, 32(19): 4917-4923.

[7] Hong S Y, Oh J E, Lee K H. Effect of D-amino acid substitution on the stability, the secondary structure, and the activity of membrane-active peptide. Biochemical pharmacology, 1999, 58(11): 1775-1780.

[8] Melchionna M, E Styan K, Marchesan S. The unexpected advantages of using D-amino acids for peptide self-assembly into nanostructured hydrogels for medicine. Current topics in medicinal chemistry, 2016, 16(18): 2009-2018.

[9] Asano Y, Lübbehüsen T L. Enzymes acting on peptides containing D-amino acid. Journal of bioscience and bioengineering, 2000, 89(4): 295-306.

[10] Jayawarna V, Ali M, Jowitt T A, et al. Nanostructured hydrogels for three-dimensional cell culture through self-assembly of fluorenylmethoxycarbonyl–dipeptides. Advanced materials, 2006, 18(5): 611-614.

[11] Sapsford K E, Sun S, Francis J, et al. A fluorescence detection platform using spatial electroluminescent excitation for measuring botulinum neurotoxin A activity. Biosensors and bioelectronics, 2008, 24(4): 618-625.

[12] Caplan M R, Moore P N, Zhang S, et al. Self-assembly of a β-sheet protein governed by relief of electrostatic repulsion relative to van der Waals attraction. Biomacromolecules, 2000, 1(4): 627-631.

[13] Ligorio C, Vijayaraghavan A, Hoyland J A, et al. Acidic and basic self-assembling peptide and peptide-graphene oxide hydrogels: Characterisation and effect on encapsulated nucleus pulposus cells. Acta Biomaterialia, 2022, 143: 145-158.

[14] Michl J, Park K C, Swietach P. Evidence-based guidelines for controlling pH in mammalian live-cell culture systems. Communications biology, 2019, 2(1): 144.

[15] Zou Y, Li Y, Hao W, et al. Parallel β-sheet fibril and antiparallel β-sheet oligomer: New insights into amyloid formation of hen egg white lysozyme under heat and acidic condition from FTIR spectroscopy. The Journal of Physical Chemistry B, 2013, 117(15): 4003-4013.

[16] Grdadolnik J. Saturation effects in FTIR spectroscopy: intensity of amide I and amide II bands in protein spectra. Acta chimica slovenica, 2003, 50(4): 777-788.

[17] Fresenius' Zeitschrift Für Analytische Chemie[M]. 1989.

[18] Krysmann M J, Castelletto V, McKendrick J E, et al. Self-assembly of peptide nanotubes in an organic solvent. Langmuir, 2008, 24(15): 8158-8162.

[19] Zhang S, Altman M. Peptide self-assembly in functional polymer science and engineering. Reactive and Functional Polymers, 1999, 41(1-3): 91-102.

[20] Roeters S J, Iyer A, Pletikapić G, et al. Evidence for intramolecular antiparallel beta-sheet structure in alpha-synuclein fibrils from a combination of two-dimensional infrared spectroscopy and atomic force microscopy. Scientific reports, 2017, 7(1): 1-11.

[21] Von Bergen M, Barghorn S, Biernat J, et al. Tau aggregation is driven by a transition from random coil to beta sheet structure. Biochimica et Biophysica Acta (BBA)-Molecular Basis of Disease, 2005, 1739(2-3): 158-166.

[22] Sapsford K E, Sun S, Francis J, et al. A fluorescence detection platform using spatial electroluminescent excitation for measuring botulinum neurotoxin A activity. Biosensors and bioelectronics, 2008, 24(4): 618-625.

[23] Ajmal M R, Nusrat S, Alam P, et al. Differential mode of interaction of ThioflavinT with native β structural motif in human α 1-acid glycoprotein and cross beta sheet of its amyloid: Biophysical and molecular docking approach. Journal of molecular structure, 2016, 1117: 208-217.

[24] Mahata M K, Lee K T. Development of near-infrared sensitized core–shell–shell upconverting nanoparticles as pH-responsive probes. Nanoscale Advances, 2019, 1(6): 2372-2381.

[25] Feltrup T M, Singh B R. Development of a fluorescence internal quenching correction factor to correct botulinum neurotoxin type A endopeptidase kinetics using SNAPtide. Analytical chemistry, 2012, 84(24): 10549-10553.

[26] Guo J, Xu C, Li X, et al. A simple, rapid and sensitive FRET assay for botulinum neurotoxin serotype B detection. PLoS One, 2014, 9(12): e114124.

[27] Lanz E, Gregor M, Slavík J, et al. Use of FITC as a fluorescent probe for intracellular pH measurement. Journal of Fluorescence, 1997, 7(4): 317-319.

[28] Faust A, Waschkau B, Waldeck J, et al. Synthesis and evaluation of a novel hydroxamate based fluorescent photoprobe for imaging of matrix metalloproteinases. Bioconjugate chemistry, 2009, 20(5): 904-912.

[29] Wang W L, Xu J, Sun Z, et al. Effect of transannular π− π interaction on emission spectral shift and fluorescence quenching in dithia [3.3] paracyclophane− fluorene copolymers. Macromolecules, 2006, 39(21): 7277-7285.

[30] Hong S Y, Oh J E, Lee K H. Effect of D-amino acid substitution on the stability, the secondary structure, and the activity of membrane-active peptide. Biochemical pharmacology, 1999, 58(11): 1775-1780.

[31] Fernandez-Lopez S, Kim H S, Choi E C, et al. Antibacterial agents based on the cyclic D, L-α-peptide architecture. Nature, 2001, 412(6845): 452-455.

[32] Wan S, Borland S, Richardson S M, et al. Self-assembling peptide hydrogel for intervertebral disc tissue engineering. Acta biomaterialia, 2016, 46: 29-40.

[33] Feltrup T M, Singh B R. Development of a fluorescence internal quenching correction factor to correct botulinum neurotoxin type A endopeptidase kinetics using SNAPtide. Analytical chemistry, 2012, 84(24): 10549-10553.

[34] Mohammed A, Miller A F, Saiani A. 3D Networks from Self-Assembling Ionic-Complementary Octa-Peptides[C]//Macromolecular Symposia. Weinheim: WILEY-VCH Verlag, 2007, 251(1): 88-95.

5. Chapter 5. Peptide-Gelatin Hybrid Hydrogel

Abstract

The three-dimensional network and porous structure help hydrogels to be widely used as the scaffold in the biological and medical fields, including tissue engineering and cell culture [1]. Self-assembly peptide (SAP) hydrogels are a promising family of hydrogels due to their biocompatibility and biodegradability. The self-assembly of the SAP hydrogels, such as F9 and KF8K, relies on the formation of the β-sheet. Meanwhile, gelatin is also a well-researched hydrogel with temperature sensitivity [2]. Therefore, in this experiment, the aim was to create a hybrid hydrogel by mixing SAP into gelatin. The results showed that the new hybrid hydrogel has improved, and controllable mechanical properties and temperature sensitivity compared to pure SAP hydrogel. The β-sheet structure from SAP was maintained in the mixture, while the gelatin took on the helix structure. Furthermore, the SAP-gelatin hybrid hydrogel still showed good strain-breaking recoverability and improved anti-bacterial properties compared to pure gelatin hydrogel.

5.1 Introduction

Self-assembly (SA) is a process where disordered molecules interact with each other through physical bonds to form periodic structures spontaneously, given the right conditions [3]. There is growing interest in using self-assembly for the preparation of hydrogels due to the spontaneous nature of the hydrogelation process [4]. In recent years, self-assembly peptide hydrogels (SAPH) have gained attention for their biocompatibility and biodegradability [5]. The β-sheet-based SAPH family is one example that has been well-researched, and it includes the peptides used in this experiment, F9 and KF8K.

Unfortunately, the mechanical properties of self-assembly peptide hydrogels are not sufficient for certain applications, such as bacterial storage [6] and soft glass [7]. As a result, the double network (DN) hydrogel was proposed as a strategy to produce hydrogels with improved and controllable mechanical properties. One example is the PEG-peptide DN hydrogel [8], which is a soft-and-tough material composed of a rigid first network and a soft second network. The two networks interpenetrate or are connected through physical or chemical interactions. Since the self-assembly of peptide hydrogels is driven by physical interactions, the physical DN strategy is employed to retain the benefits of physical crosslinking, such as the reversibility of physical interaction.

The selection of the substance to blend into the peptide as the secondary network is crucial. The candidate substance must have hydrogelation ability, compatibility with the peptide, and favourable biological properties. So far, a number of natural biopolymers have been used in hydrogel preparation [9] and they can form a network without extra crosslinkers, making them

strong candidates as secondary materials. Thus, in this experiment, gelatin was selected as the secondary network material, since it is also a natural peptide same as the SAP.

Gelatin contains all the natural amino acids except tryptophan, isoleucine, threonine, and methionine and has an unusual protein amino acid, hydroxyproline. The major amino acids in gelatin chains are glycine, proline, and hydroxyproline, making up 50% of the total amino acids in gelatin [10]. Therefore, as a peptide, gelatin has higher compatibility with the self-assembly peptides. The biocompatibility and biodegradability of gelatin have been established through research [11]. Like collagen, gelatin has coil and helix structures. Studies suggest that the hydrogelation of gelatin occurs when triple-helixes and coil structures aggregate together. The aggregation typically occurs in the proline-rich zone, which is maintained by physical interactions, resulting in network crosslinking. As the crosslink is driven by hydrogen bonds, the crosslinking is a thermal-controlled process, making the gelatin hydrogel temperature sensitive and melting around 30°C [12]. The temperature sensitivity is another reason why gelatin was chosen for this experiment, giving new features to the hybrid DN hydrogel.

So far, several double-network hydrogels have been produced using gelatin as one of the components, such as a gelatin/polyacrylamide DN hydrogel [13] and a gelatin/gellan gum DN hydrogel [14]. However, these hydrogels have limitations in terms of recoverability and anti-bacterial properties, which restrict their use in biological and medical fields. For instance, the gelatin-based hydrogel is prone to breakage during injection from needles or 3D printing nozzles due to high strains. Additionally, the gelatin-based hydrogel is susceptible to contamination by bacteria in the air.

The aim of the experiment is to develop an SAP-gelatin hybrid hydrogel that has improved but controllable stiffness and combines the benefits of both gelatin and self-assembly peptides (SAPs). For example, temperature responsiveness from gelatin and strain-breaking recoverability from SAP. Besides, it also tries to overcome the limitations of traditional gelatin hydrogel by mixture with SAP. The hybrid hydrogel was designed to form a double network structure. The SAP served as the first network and gelatin as the second network. The hybrid hydrogel was expected to form spontaneously through the self-assembly of peptides at high temperatures. And the stiffness of the hydrogel would be increased by the crosslink of gelatin as the temperature cools down. This feature help the hybrid hydrogel could potentially replace the traditional bio-printing ink, Gel-Ma, with improved biocompatibility and no extra crosslinker [15].

5.2 Method

5.2.1 Material

F9(FEFKFEFKK) and KF8K(KFEFKFEFKK) peptide (HCl salt) were purchased from were purchased from Lifetein Ltd with 95% purification (the rest 5% is chlorine salts). The purities of peptides were confirmed by reverse phase high-performance liquid chromatography (RP-HPLC) (figure S.1) and elementary analysis (table S.1). MALDI-TOF confirmed the molecular weight (figure S.2). The method of HPLC and MALDI-TOF are given in Supplement documents. Sodium hydroxide and Sodium hydrogen phosphate powder were purchased from Thermo Fisher Scientific.

Type B pork gelatin was obtained from Acros Organics with analysis purification. Sodium hydroxide was purchased from Thermo Fisher Scientific.

5.2.2 Pure peptide hydrogel preparation

22.5 mg F9/KF8K peptide powder was weighed by balance and dissolved into 2.4 ml HPLC water at room temperature, followed by a vortex mixture. Samples were set in a sonic bath undergoing 30 minutes of sonication for complete dissolution. 0.5 M NaOH solution adjusted the sample pH to the ideal point. The pH of the samples was measured by a pH meter (AB150 pH Benchtop Meters with 0.01 resolution). The sample was adjusted by HPLC water to 3ml and stored at 4 °C overnight for hydrogelation.

5.2.3 Pure gelatin hydrogel preparation

30, 90 and 150 mg gelatin powder were weighed, respectively, and dissolved into 3 ml HPLC water with 50 °C heating, followed by a good string. Samples were 5000rpm centrifuged for 5 minutes to remove the bubble and set in a 4 °C fridge overnight for hydrogelation and storage.

5.2.4 Gelatin-Peptide Hybrid Hydrogel Preparation

22.5 mg F9/KF8K peptide powder was weighed by balance and dissolved into 1.4 ml HPLC water at room temperature, followed by a vortex mixture. The samples' pH was adjusted to their hydrogelation pH by 0.5 ml NaOH. 30, 90 and 150 mg gelatin powder were weighed and dissolved into 1 ml HPLC water with 50 °C heating, followed by a good string. Gelatin solutions were cold to 40 °C before being added to the well-pH peptide solution. Hybrid samples were kept at 40 °C and gently stirred for 5 minutes. Samples were stored in a 4 °C fridge overnight for hydrogelation.

5.2.5 ATR-FTIR

ATR-FTIR was employed to characterise the nanostructure of samples. 5uL samples were pipetted into the crystal surface. The absorbance spectra were collected from 400 cm^{-1} to 4000

cm^{-1} wavenumbers with 256 scans and 4 cm^{-1} steps at room temperature. For peptide samples, spectra focused on 1400 cm^{-1} to 1800 cm^{-1}. HPLC water played the role of background in room temperature measurement. The collection was by Brucker ALPHA II FT-IR Spectrometer. FTIR spectra were smooth by Gaussian function between every 5 points.

5.2.6 X-ray Diffraction (XRD)

XRD experiments were performed by Bruker D8 Advance. The angle range was 3 to 60 degrees with the 1-degree step. In sample preparation, 100 uL 50 mg/ml gelatin hydrogel, 7.5 mg/ml F9/KF8K hydrogel and 50 mg/ml + 7.5 mg/ml hybrid hydrogel were prepared, printed and dried on a glass slide. Experiments were done at room temperature.

Baselines were acquired by High score software. In this condition, distance (d) was obtained by Bragg's Law [29].

5.2.7 AFM

7.5 mg/ml peptide samples were prepared, followed by 30 times dilution by HPLC water, giving the final concentration of 0.25 mg/ml. The sample was pipetted and vortexed, ensuring a homogeneous solution. Once the used mica was removed by stick tape and fresh mica exposed, 100 uL diluted solution was injected into the flat mica surface. Following, Sample loaded mica was stored in 4 °C fridges for 72 h to air dry the liquid. When the drying was completed, 1 ml HPLC water was pipetted into the mica surface for washing non-settle peptide molecules. The well-washed sample was air dried in a fume cupboard until no liquid on the mica surface.

All the AFM imaging was carried out at room temperature (20°C) and approximately 50% relative humidity. Examinations were done in an air atmosphere and dried samples in the AFM

(Bruker Multimode 8). SCANASYST-AIR triangular cantilevers with a spring constant of k = 0.4 N/m and 70KHz frequency (Bruke) were used for ScanAsyst Mode imaging.

5.2.8 TEM

Sample hydrogels were diluted 10-fold using HPLC grade water and vortexed to mix evenly to 0.75 mg/ml F9, 5 mg/ml gelatin and 0.75 mg/ml F9 & 5 mg/ml gelatin hybrid samples. Carbon-coated copper grids (400 mesh, Electron MicroscopySciences, UK) were placed on the sample droplet for 1 min and moved to the water droplets to wash three times, then transferred to the 1% uranyl acetate droplet for the 30s. Excess liquid on the grid was subsequently removed by a 70mm filter paper (Whatman). The grid was dried for TEM imaging by FEI Tecnai12 BioTwinat 100 KeV with Gatan Orius SC1000A CCD camera.

5.2.9 Dynamic oscillatory rheology

The mechanical, as well as thermal properties of hydrogel samples, were evaluated by the TA Discovery™ Hybrid Rheometer HR 20 rheometer. 180uL sample was loaded into a stainless Peltier with a 45000-um gap between the Peltier and parallel plate. 20 mm diameter plate is selected, and the gap is set at 500 um in measurement. Collections underwent at room temperature.

Strain-dependent storage modulus (G’) and loss modulus (G’’) were collected to evaluate the linear viscosity region and shear thinning properties at fixed frequency (1 Hz).

Particular, gelatin-containing samples were assessed for mechanical properties variation with temperature by a 10 to 40 °C temperature ramp with a 2 °C / min rate. Meanwhile, a time sweep at 10 °C was given to gelatin and gelatin peptide hybrid samples to assess how long samples would finish hydrogelation. Storage modulus was regarded as a standard to evaluate whether

hydrogenation was completed or not. All of these experiments were done in 1 Hz and 0.2% strain. In the term of the recovery test, 0.2% strain and 1000% strain were introduced to samples for 300s and 60s, respectively. All samples were incubated in a Peltier at a designed temperature of 300s and repeated three times to avoid occasional errors.

The analysis and fitting of recovery curve relied on classical mechanical model (one spring element in parallel with two springs + dash pot elements) [16]

$$G' = G_0' + G_1'\left(1 - e^{-t/\tau_1}\right) + G_2'\left(1 - e^{-t/\tau_2}\right) \quad (33)$$

where G'_0 is storage modulus when high shear strain removed and G'_1, G'_2, are two characterise storage shear moduli in two recovery process. τ_1 and τ_2 are two time- parameters.

5.2.10 3D-Printing

15 mg/ml KF8K with 30 mg/ml gelatin hybrid hydrogel was employed as ink in 3D printing. The hydrogel was injected into an ink storage tube mildly by syringe and undergone 5000 rpm centrifuged for 2 minutes to remove bubbles completely. Printing was done at room temperature in the blank group, while samples were heated to 45 °C in the experimental group to melt hydrogel into a solution completely.

22-gauge nozzles were employed in printing, and pressure was set to 15 kPa. 10 nm×10 nm×3 nm cube was the printing modulus, and it was printed in a petri dish.

5.2.11 CD spectroscopy

CD spectra were acquired by ChiraScan spectropolarimeter. In gelatin samples, 50 mg/ml gelatin hydrogels are dilute to 1,2,2.5 and 5 g/ml final concentration. Meanwhile, 7.5 mg/ml F9/KF8K hydrogels and 50 mg/ml gelatin- 7.5 mg/ml F9/KF8K hybrid hydrogels were diluted 37.5

times by HPLC water to make the final concentration of SAP is in 0.2 mg/ml. Following vortex mixing, samples were pipetted into 1 mm path-length quartz cells without any bubbles. Spectra were recorded continuously from 190 nm to 280 nm with 0.5 nm step-in at 25 ℃ at room temperature. HPLC water is employed as background in all measurements. The mean residual ellipticity is presented by Δε (litre mol-1 cm-1) which means the difference in absorption coefficient between left-hand and right-hand polarised light. Data were analysed by Bestsel.

5.2.12 THT Assay

Two mmol/l THT was prepared in advance by dissolving THT powder (Sigma) into HPLC water. THT solution was further diluted to 0.05 mmol/l in 50 mg/ml gelatin hydrogel, 7.5 mg/ml F9/KF8K hydrogels and 50 mg/ml gelatin-7.5 mg/ml F9/KF8K blending hydrogels.

Fluorescent spectra were obtained by Agilent Cary Eclipse Fluorescence Spectrometer. Samples were loaded into 2 cm path length quartz cuvette immediately after dilution, followed by 2 minutes 5000 rpm centrifuge to remove the bubble in the cuvette completely. The spectra were recorded between 420 nm and 550 nm with emission wavelength at a 1 nm step. The peak ideally is at 454 nm. The unit of fluorescent intensity is an arbitrary unit (a.u.), meaning the relevant intensity compared with emission intensity.

5.2.13 Anti-bacterial Assay

Hydrogels were pre-prepared by the above process and separated into 96-well tissue culture plates (Costar). In the experimental group, 50 ul pure 7.5 mg/ml F9, 7.5 mg/ml KF8K, 50 mg/ml Gelatin, 7.5 mg/ml F9- 50 mg/ml Gelatin and 7.5 mg/ml KF8K- 50 mg/ml Gelatin hydrogels were introduced into wells, respectively, while each sample repeated in three wells. It was followed by

100 ul E Coil. in LB culture medium in each well. The OD600 of the resulting well was measured by a Plate reader with 37 °C incubation for 18 hours. Blank groups only introduced 50 ul corresponding hydrogels or 100 ul E.coil solution, which were repeated in three wells.

Bacterium solution was prepared by transferring from the single-colony bacterium to a solid LB-agar petri dish. E coil in the solid medium is transferred to 5 ml LB liquid medium twice in 24 hours and 4 hours before the experiment, followed by 37 °C incubation. The bacterium solution is further diluted by LB medium until the OD600 approaches 0.005.

5.3 Result and discussion

5.3.1 Sample Preparation

The first question is about the suitable ingredients for a double network. The self-assembly peptides KF8K and F9 were used as the first network, as previously discussed in chapter 4. Additionally, gelatin was chosen as the secondary biopolymer due to its excellent biological properties, easy hydrogelation strategy, and established research. However, different sources of gelatin have significant variations in their amino acid ratios, particularly in the percentage of glycine and proline [17]. As a result, the two main types of gelatins, fish and pork, were compared. The results of the storage modulus at room temperature are shown in figure 5.1(A). It was clear from this figure that pork gelatin formed a hydrogel at room temperature, while fish gelatin remained a solution. Furthermore, when hybrid hydrogels with SAPs were examined, pork gelatin in combination with peptides resulted in approximately four times the stiffness improvement when compared to pure peptide samples. On the other hand, there was a slight decrease in stiffness in fish gelatin and peptide mixture hydrogels. This is because fish gelatin has a relatively lower ratio of proline and hydroxyproline, which are essential amino acids for gelation in gelatin,

as well as a lower average chain molecular weight. Additionally, the presence of β and γ chains in fish gelatin has a negative effect on its hydrogelation ability [17]. Therefore, pork gelatin was deemed a better choice and was used in this experiment.

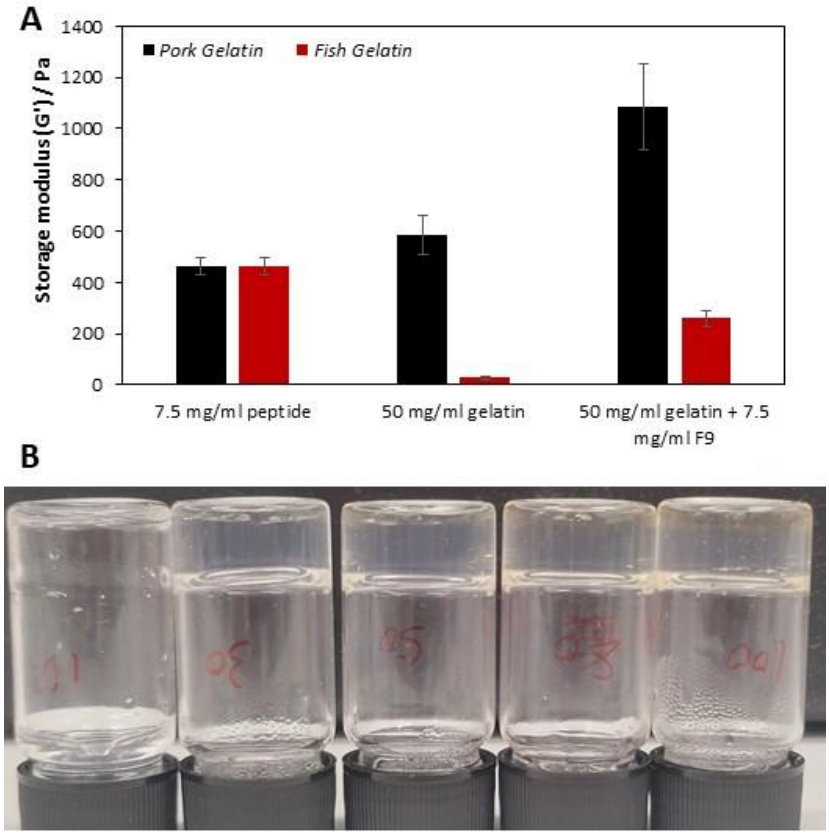

Figure 5-1 (A) Storage moduli of Pork and fish gelatin and their hybrid hydrogel peptide at room temperature. (B) The appearance of 10, 30, 50, 80 and 100 mg/ml gelatin at room temperature

The concentration of peptide and gelatin is still crucial in this experiment. If the concentration is too low, they cannot form a stable hydrogel, but too high of a concentration will also cause inhomogeneity after blending. Based on the results in the previous chapter, 7.5 mg/ml was selected as the concentration of self-assembly peptide in the hybrid hydrogel, which was above the critical hydrogel concentration (CHC) for both KF8K and F9. Under this concentration, both KF8K and F9 formed a stable and transparent hydrogel. Similarly, 10, 30 and 50 mg/ml were set as

concentration series of gelatin, whereas 10 mg/ml was designated as a group unable to form a hydrogel. 30 and 50 mg/ml were the concentrations that produce hydrogel at room temperature. Additionally, the concentration also impacted the appearance of the gel. It was colourless and transparent with less than 50 mg/ml of gelatin, but it became cloudy above the threshold concentration. The cloudiness of the hydrogel harms the optical properties of the hydrogel, so it is preferred to be avoided (Figure 5.1 (B)).

Furthermore, the pH of the hybrid hydrogel is critical because it determines the net charge of the peptides. The importance of net charge in self-assembly has been widely reported in recent studies, particularly in self-assembly peptide hydrogels [18]. The number of net charge and positive/negative charge conditions determine the intensity and direction of electrostatic force, which plays a crucial role in self-assembly. The relationship between pH, net charge, and the phase of peptide hydrogels has been well discussed in chapter 4. Fortunately, gelatin does not hold any charge from pH 4 to 9, meaning the net charge of the blending sample is the same as the charge in the self-assembly peptides. Additionally, since the hydrogelation of gelatin is not affected by net charge, the pH of the hybrid hydrogel was set at the hydrogelation pH of SAPs, which were 4.5 and 6.5 for F9 and KF8K, respectively.

5.3.2 Characterisation & Imaging

Due to the variance in micro-structure, which typically leads to changes in hydrogel properties, a series of characterisations were performed on samples to expose structural changes after blending. FTIR was used, focusing on the β-sheet from SAP and triple helix from gelatin in the wavenumber range of 1400-1800 cm^{-1}, which involved most of the critical bands of peptide, including amide I and amide II. The result for KF8K-gelatin and F9-gelatin are shown in Figures 5.2

(A&B), respectively. Fortunately, in both figures, the formation of the above two key structures can be seen clearly. The peptide spectrum involved the bond of β-sheet in 1618 cm^{-1}. And the peak in 1644 cm^{-1} was the triple helix in the gelatin spectrum. Similar spectra were seen in F9-gelatin and KF8K-gelatin blending samples. The band in 1554 cm^{-1} stemmed to amide II (N-H bending) structure which was contained in both pure gelatin and SAPs (F9 and KF8K). Therefore, the amide II bond was seen in gelatin, SAPs and their blending samples. However, a large difference was observed in the amide I zone in different samples. Typically, amide I (C=O stretching vibration) is generally utilised to monitor the presence of secondary structures. It is because a large number of hydrogen bonds appearing in the secondary structures causes a redshift of the amide I band. The separated peaks are widely employed to distinguish secondary structures. The three critical examples involved α-helix in 1654 cm^{-1}, random coil in 1642 cm^{-1} and β-sheet in 1620 cm^{-1} [12]. The spectra of the blending samples were detected like a physical addition of SAP's and gelatin's spectra. The bond of the β sheet from SAP was kept. The intensity of peaks still was unchanged with more gelatin. The increase in gelatin concentration only made contributes to the intensity of gelatin stemmed peaks. They were the amide II in 1554 cm^{-1} and the triple helix in 1644 cm^{-1}. The results from FTIR suggest the critical structure of the two ingredients is well-kept. The two networks dis not interfere each other after blending.

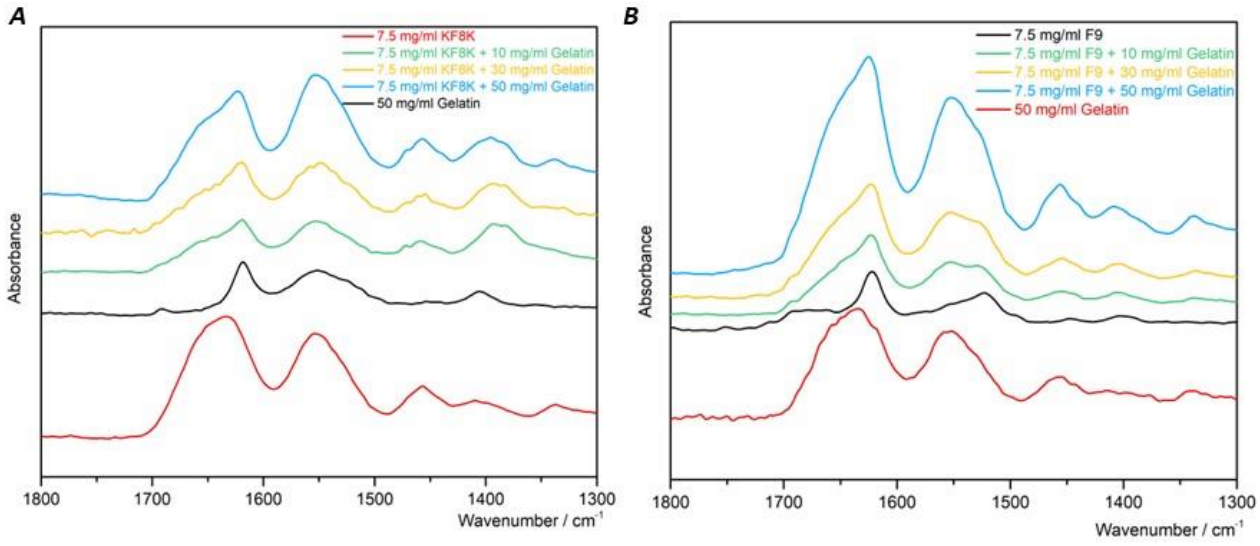

Figure 5-2 (A) FTIR spectra of gelatin, KF8K and their hybrid hydrogels (B) *FTIR spectra of gelatin, F9 and their hybrid hydrogels*

The following section discusses the use of Circular Dichroism (CD) spectroscopy in observing the secondary structure of peptides and proteins. In the spectra of pure gelatin samples (figure 5.3(A)), a negative peak at 197 nm was observed, which increased intensity with the increase in gelatin concentration. This peak is attributed to the presence of triple helices in the sample [30]. The results of blending hydrogels are shown in figures 5.3 (B&C), where the helix structure also dominates in the 30 and 50 mg/ml gelatin - 7.5 mg/ml F9/KF8K hybrid hydrogel. This indicates a large presence of triple helix structure in the hybrid hydrogel. The CD spectrum of 50 mg/ml gelatin – 7.5 mg/ml KF8K also exhibited a negative peak at 235 nm, which suggests the presence of 310 helices. The primary difference between 3_{10} helices and α helices are in the site of hydrogen bonds. Each amino acid in residue i forms a hydrogen bond with i+3 instead of i+4, making 3_{10} helices appear tighter and thinner [31]. Pure gelatin and SAP samples did not show this structure in the CD spectra, indicating a potential structural variation after blending. Additionally, in 10 mg/ml gelatin-contained hybrid samples, a positive peak of 195 nm was observed, indicating the

presence of β-sheets. However, as the concentration of SAP was relatively lower compared to gelatin in the blending sample, the positive peak was completely offset and disappeared in samples with higher gelatin concentration. Combining the results of FTIR and CD, it can be seen that the β-sheet from SAP and triple helix from gelatin were retained in the blending hydrogel. However, slight structural variations were still observed, indicating an enhancement in the blending hydrogels.

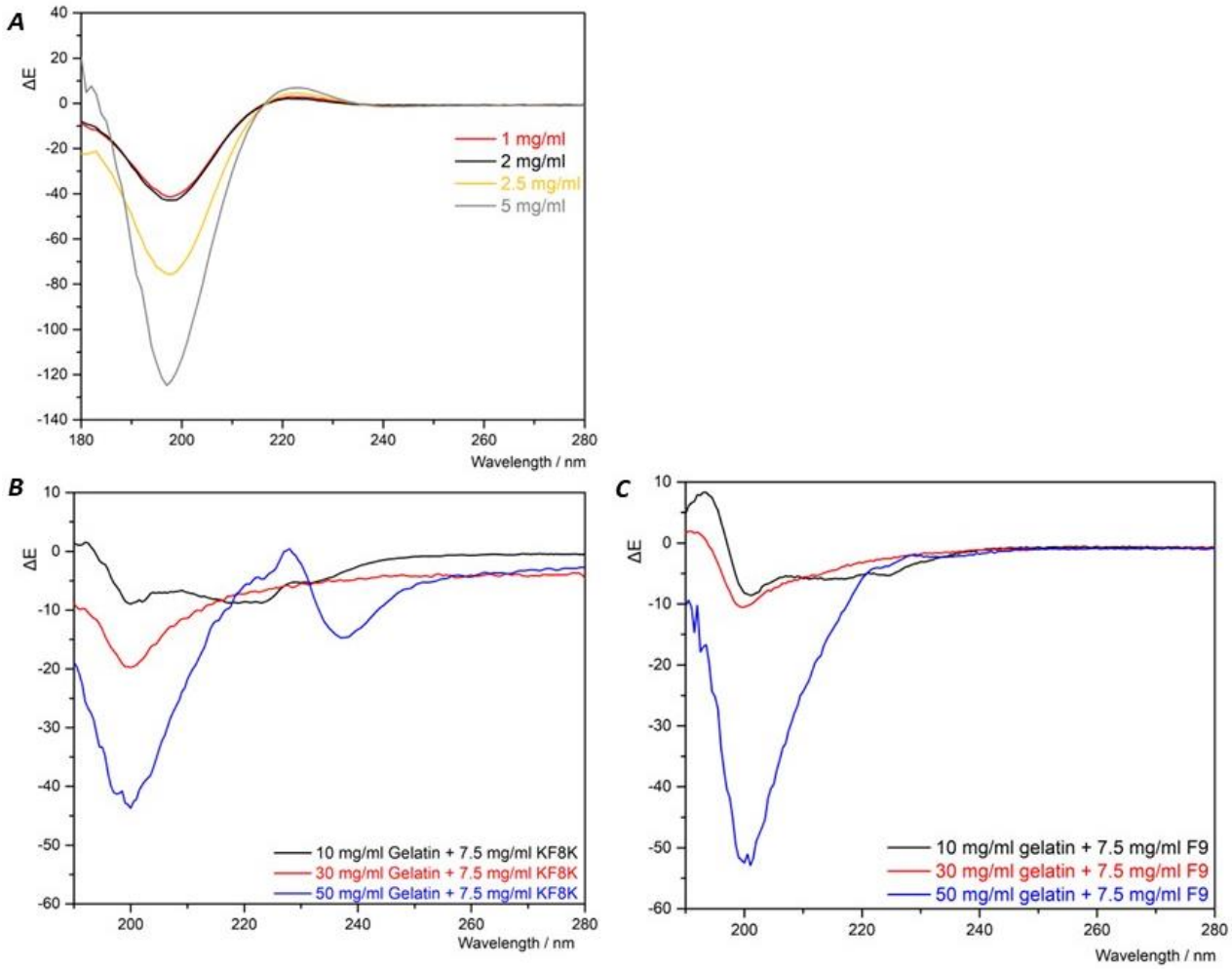

Figure 5-3 (A) CD spectra of 1, 2, 2.5 and 5 mg/ml Gelatin (B) CD spectra of gelatin, KF8K and their hybrid hydrogels (C) *CD spectra of gelatin, F9 and their hybrid hydrogels*

Meanwhile, the variation in the number of β-sheets is also a critical factor in the properties of blending hydrogels. This variation can also contribute to stiffness improvement in the hydrogel.

The number of β-sheets was measured by the peak intensity at 485 nm in the THT fluorescent spectrum (Figures 5.4 (A&B)). THT is a molecule that can bind to β-sheet molecules, creating fluorescence. The effect on β-sheets was evaluated by comparing the fluorescent intensity in pure peptides, gelatin, and their hybrid hydrogel. The presence of β-sheets in pure gelatin was indicated by the emission peak at 485 nm, but the intensity was significantly weaker in comparison to self-assembly peptides and hybrid hydrogels. The F9 and KF8K hydrogel samples showed a fluorescent peak with three times the intensity of gelatin, reaching approximately 600 a.u. Based on the linear quantitation relationship between fluorescent intensity and β-sheet concentration, the detected number confirmed that gelatin only formed one-third the number of β-sheets as SAP hydrogel. This result was consistent with results from CD and FTIR. Additionally, in terms of hybrid hydrogels, F9 -gelatin had a typical β-sheet signal with similar intensity to pure F9, suggesting that the β-sheet concentration is unchanged after blending. However, the signal intensity was enhanced in the KF8K-gelatin blending sample compared to pure KF8K hydrogel. This difference demonstrates the improvement of β-sheet concentration in the blended hydrogel. The difference in the β-sheet amount in F9 -gelatin and KF8K-gelatin hybrid hydrogels can be attributed to the pH difference. Neutral pH is more conducive to gelatin folding into helix structures and hydrogelation. The reduction in gelatin's storage modulus and the strain-breaking threshold is well-known when pH is lower than 5 or higher than 9 [19].

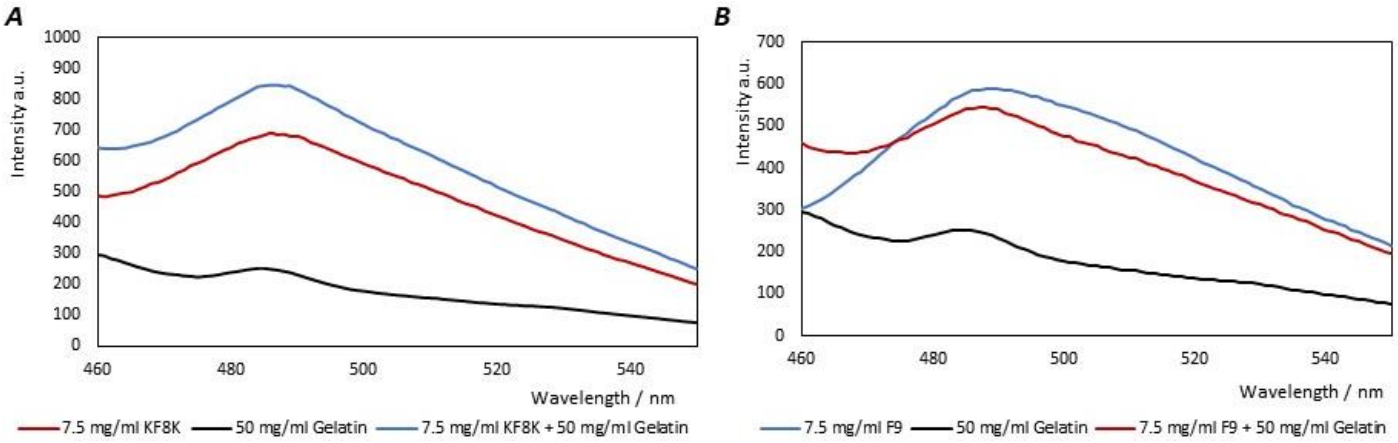

Figure 5-4 (A) THT assay of gelatin, KF8K and their hybrid hydrogels (B) *THT assay of gelatin, F9 and their hybrid hydrogels*

Additionally, the hydrogels were measured by XRD to reveal the distance and gap in the microstructures. Additionally, the variance in the reflection also gave information about the difference in microstructures after the mixture. In Figure 5.5(A), the broad peak in pure gelatin at 5.3 A was explained as the triple helix [32], agreeing with the results of FTIR and CD, which showed the existence of a triple helix in the gelatin hydrogel. The broadness of this peak in gelatin is because gelatin is not a crystal. Meanwhile, there were reflections in 4.1 Å and 10.9 Å in the KF8K and gelatin spectra, which are attributed to the length of hydrogen bonds and the gap in the sheet-sheet separation of β-sheet, respectively. The gap between strands and strands in β-sheets is 5.7 Å, as proven by the reflection in 15.07° in the KF8K spectrum. The peak was not seen in the gelatin spectrum because it was masked by the peak from the triple helix. The above four reflections were also observed in the KF8K-gelatin hybrid, suggesting that the β-sheet peaks from KF8K and the helix peaks from gelatin were kept after the mixture. The result of XRD also proved the presence of a β-sheet in KF8K, gelatin, and blending hydrogel, agreeing with the FTIR and THT spectra. The peaks in 23.0 Å were two times the reflection of peaks in 10.9 Å, and they were only observed in pure KF8K and mixing samples, which explains that the concentration of β-sheets in

gelatin was too low. Similarly, the F9 spectrum (Figure 5.5(B)) held peaks in 4.1 Å, 5.3 Å, 10.9 Å, and 23.0 Å. The F9 -gelatin hybrid hydrogel exhibited the reflections from F9 for the β-sheet and helix from gelatin. In particular, the reflection intensity at 5.7 Å was obviously higher in F9 compared to KF8K, indicating that the amount of β-sheet in F9 was higher than in KF8K. This is because one more lysine at the N-terminal interferes with the formation of the β-sheet [18].

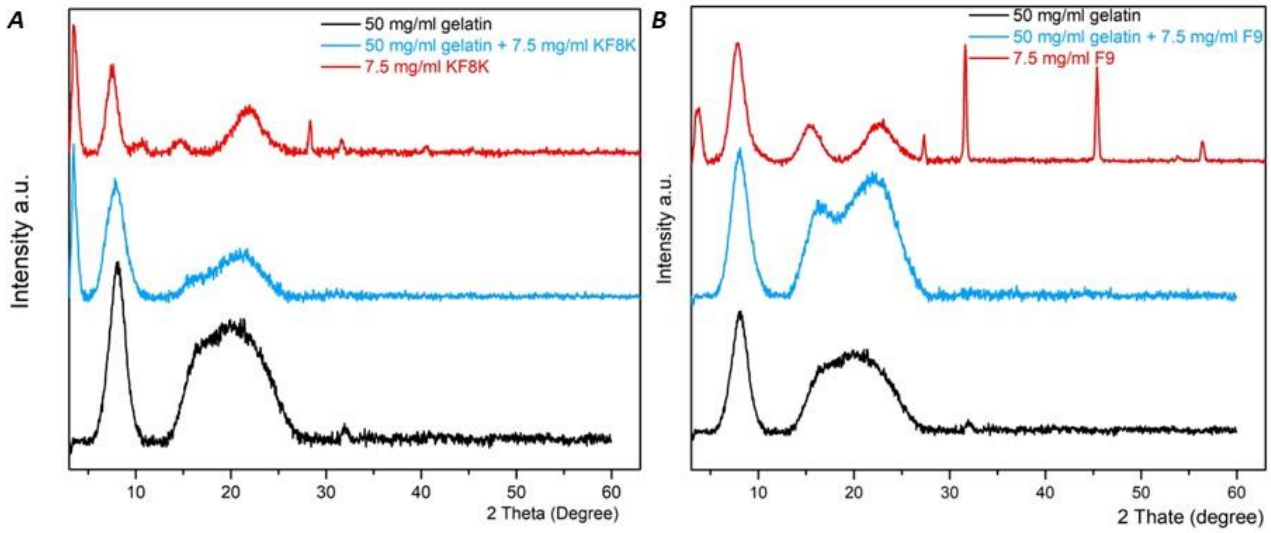

Figure 5-5 (A) XRD spectra of gelatin, KF8K and their hybrid hydrogels (B) *XRD spectra of gelatin, F9 and their hybrid hydrogels*

The internal structure of the material was revealed through characterization techniques, but information about morphologies, including changes in fibres and networks, was still lacking. Therefore, the samples were imaged using TEM (Figure 5.6 A&B). Unfortunately, the structure of the gelatin sample could not be imaged using TEM as the gelatin molecules were completely dissolved in water after dilution. Additionally, the fibres of gelatin were too thin to be observed using general TEM. In contrast, well-defined entangled fibres and networks were observed in the pure F9 and KF8K samples. The pictures of KF8K were well discussed in chapter 4. Similarly, clear fibres and networks were also seen in the KF8K-gelatin and F9 -gelatin hybrid hydrogel samples.

The pictures and fibre diameter distributions are shown in Figure 5.6 (C&D). In the microscopy images, the fibres were well extended and entangled together, forming crosslinking and networks. The diameter distribution showed a well-normal distribution in fibres, indicating the uniformity of fibres and hydrogels. In particular, the average diameter of pure 7.5 mg/ml KF8K reached 4.12 nm, while it was 5.19 nm in 7.5 mg/ml KF8K – 50 mg/ml gelatin samples. The 1 nm improvement indicates the potential for stiffness improvement in the hybrid hydrogel compared to pure hydrogels. Similarly, another 1 nm increase was also observed in the single fibre's diameter of the F9-gelatin hybrid hydrogel, which also supported the stiffness enhancement of hybrid hydrogels from a micro view.

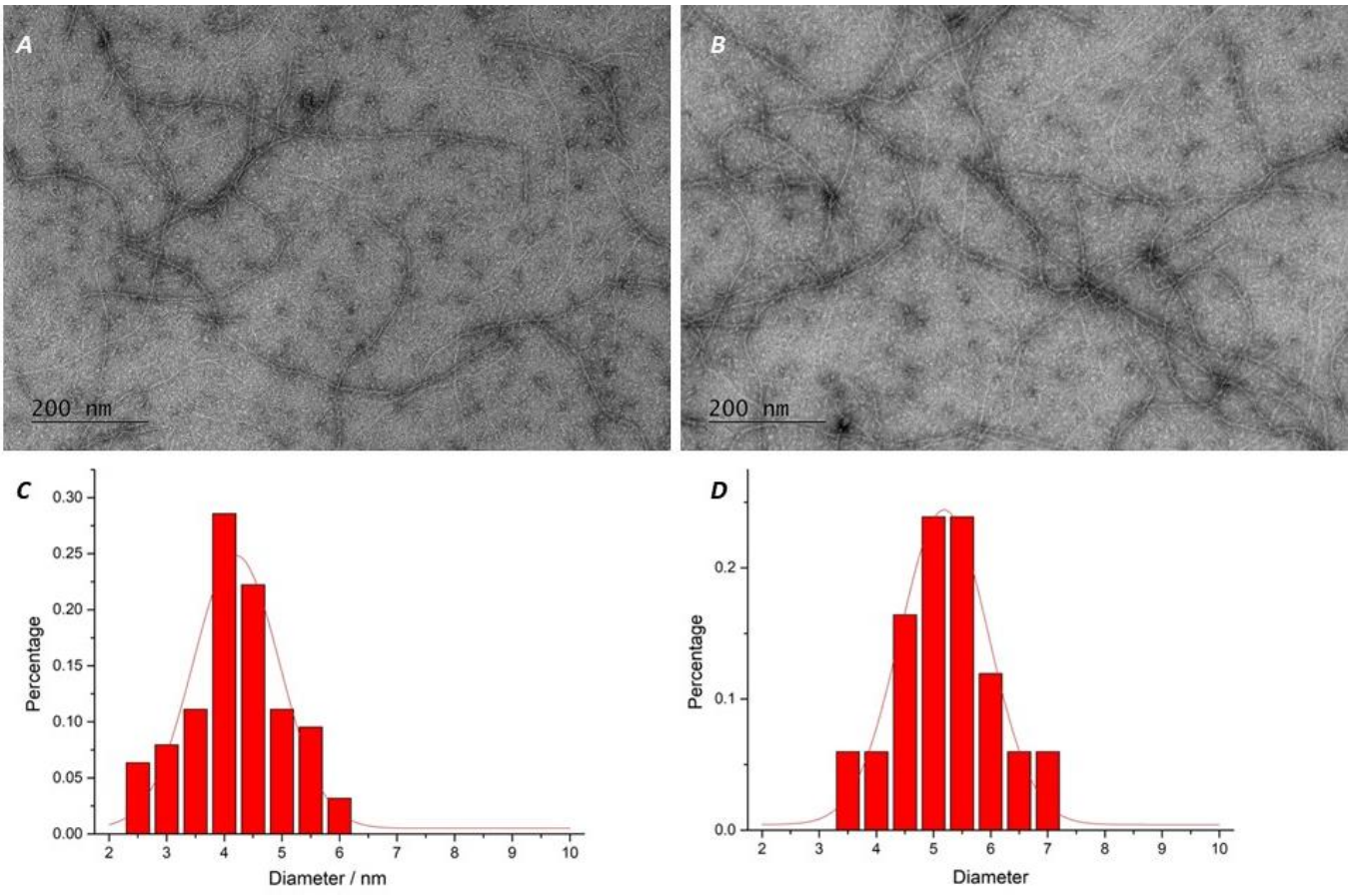

Figure 5-6 (A -B) TEM of Gelatin- KF8K and Gelatin- F9 hybrid hydrogel (C-D) Gelatin- KF8K's and Gelatin- F9's fibres' diameter distribution.

In summary, a series of characterization and microscopy imaging results indicate that key structures were well-preserved after blending. The shape of fibres and networks were also unchanged in blending hydrogels. The presence of new microstructures and an increase in fibre diameter suggests the potential for stiffness improvement in blending hydrogels.

5.3.3 Mechanical Properties & Model

The previous results indicate an enhancement in stiffness. To compare the stiffness of pure peptide, gelatin, and their hybrid hydrogels, a pre-experiment was conducted to monitor the stiffness of the materials over time. The results, shown in Figure 5.7(A), indicated that the storage modulus of the peptide was stable after one day, while the value of gelatin continued to increase for three days. A drastic improvement in storage modulus value (409 Pa) was observed after one day, but there was still an additional 200 Pa produced after three days. In terms of the hybrid hydrogel, although there was a slight increase in stiffness between day 1 and day 3, most of the stiffness was produced after one day. These results suggest that the primary hydrogelation of the hybrid hydrogel occurred on day 1. Additionally, the change in the error bar suggests that a relatively strong inhomogeneity was observed in the hybrid sample on day 3. Therefore, day 1 was chosen as the time to measure the stiffness of the samples.

As a result, the storage modulus value of pure peptide (F8K and KF8K) hydrogels, gelatin hydrogel, and their hybrid hydrogels is given in figure 5.7 (B&C). The peptide concentration in the hydrogel was kept unchanged at 7.5 mg/ml, while a series of gelatin concentrations (10, 30, and 50 mg/ml) were used. The hybrid hydrogel consisted of 7.5 mg/ml peptide and the corresponding gelatin concentrations. It is clear that a 10 mg/ml concentration of gelatin remained in a liquid state at room temperature. Therefore, no contribution was found in the 10 mg/ml gelatin and

peptide blending hydrogels. As expected, compared to the KF8K peptide hydrogel, there was only a 50 Pa increase in the KF8K-10 mg/ml gelatin sample. Furthermore, even a 100 Pa decrease in the F9-10 mg/ml gelatin hydrogel was measured, as 10 mg/ml did not reach the CHC of gelatin at room temperature. In contrast, 30 mg/ml gelatin was found to be a stable hydrogel at room temperature, and a noticeable improvement in storage moduli was also achieved in its hybrid hydrogel with SAPs. The value of 30 mg/ml gelatin-F8K reached three times that of pure F9 hydrogel, and the improvement was even greater in the 30 mg/ml gelatin-KF8K compared to pure KF8K hydrogel. In this case, 30 mg/ml is considered the threshold concentration for achieving enhancement in hybrid hydrogels. Furthermore, the enhancements were further enlarged when the gelatin concentration was raised to 50 mg/ml. The storage modulus reached around 1800 Pa when 50 mg/ml gelatin was blended with 7.5 mg/ml F9 or KF8K. In short, a significant improvement in stiffness is achieved by blending DN hydrogels with gelatin and peptides, and the value can still be controlled by adjusting the concentration of gelatin.

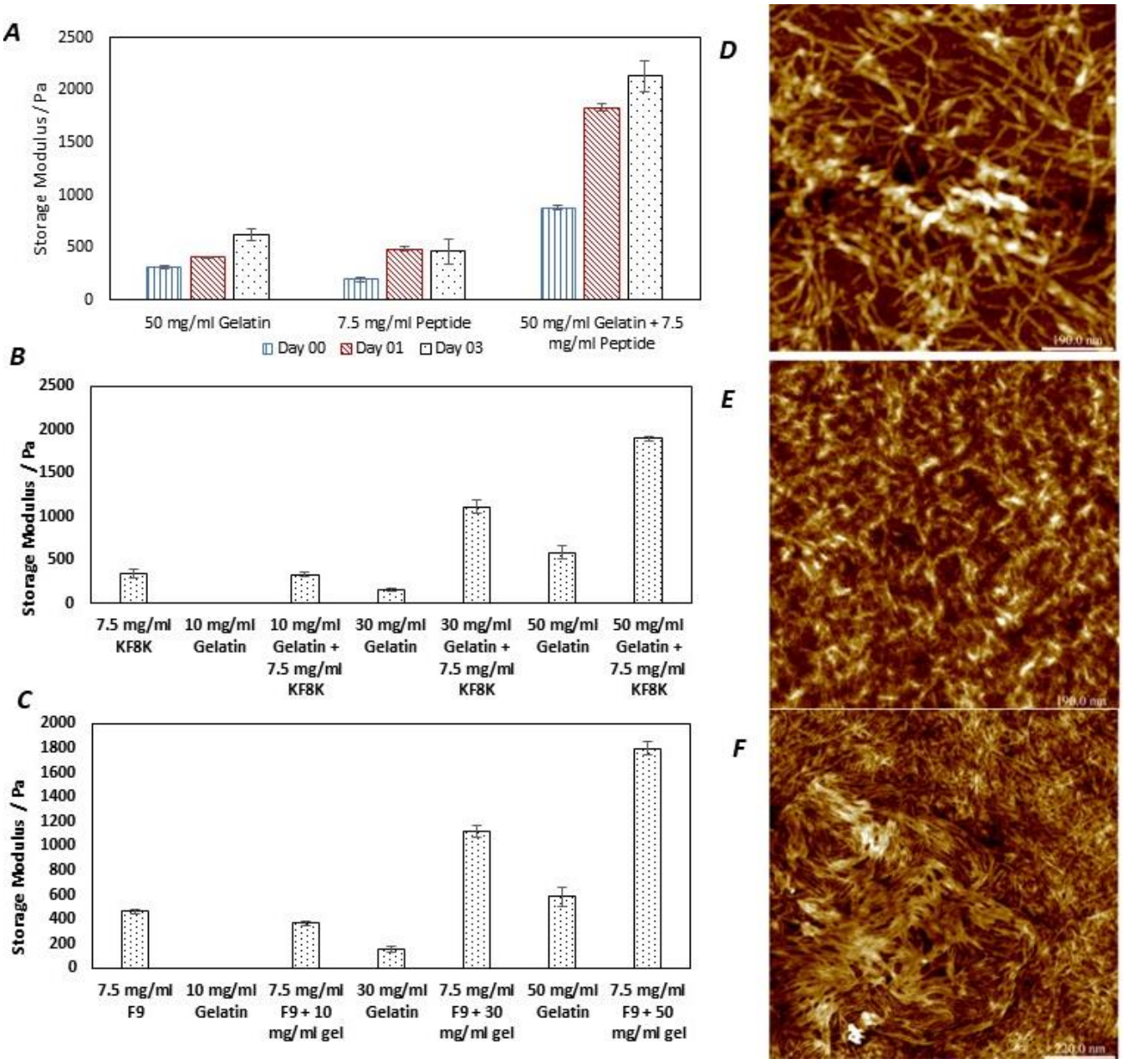

Figure 5-7 (A) The storage modulus of 7.5 mg/ml F9, 50 mg/ml gelatin and their hybrid hydrogel in days 00, 01 and 03. (B-C) The storage modulus of 10,30, and 50 mg/ml gelatin and their blending hydrogel with 7.5 mg/ml KF8K and F9. (D-F) AFM image of 0.25 mg/ml KF8K, 10 mg/ml Gelatin and their Gelatin-KF8K hydrogel.

Fortunately, a predicted stiffness improvement was observed in the hybrid hydrogel. However, the characterization results are not strong enough to explain such a significant enhancement. As a result, the improvement is attributed to the interaction between gelatin and

peptide network behaviours. The failure of imaging gelatin fibre and network by TEM led to the use of AFM as a replacement. The KF8K was employed as the representation for AFM. The imaging of KF8K, gelatin, and their hybrid hydrogel is shown in Figure 5.7 (D, E, & F). The high sensitivity to the interaction with the sample surface helps AFM draw the contour of the sample, including the fibres, network, and porous structure. Similar to TEM, a clear fibre and its entangled network were imaged in the KF8K peptide sample. However, for the gelatin, it showed a clear, high-density porous structure under AFM without separated fibres or networks. Meanwhile, in the image of the blending hydrogel, the highlight was the fibre clusters which were accepted as the result of the bonding of the peptide fibres. The dense gelatin structure extruded the peptide fibres together, forming wider and stronger clusters by several single fibres that entangle each other. Meanwhile, there were still single peptide fibres observed. The fibres went through the pores in the gelatin network, strengthening the structure further. Therefore, the combination of the gelatin network and peptide fibres produced a synergistic double network. In the structure, gelatin worked as the hard background, and the peptide fibre and fibre cluster were the soft one going through the gelatin network. The AFM result gave the reason why there was a drastic improvement in stiffness after peptide and gelatin blending without strong new physical interaction or chemical bond formation between the two networks.

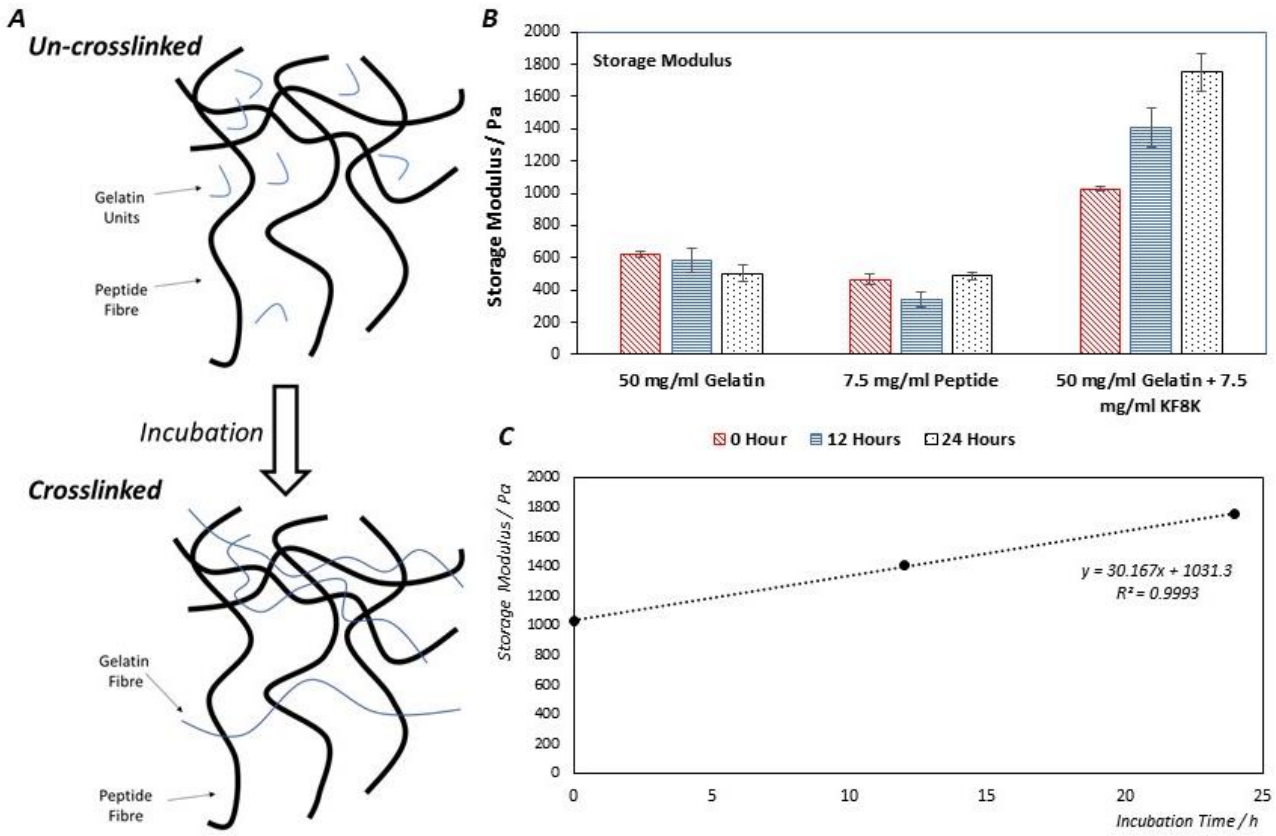

Figure 5-8 (A) Process of incubation-time relied on the model (B) Storage modulus of hybrid hydrogel against incubation time in room temperature (C) Fitting formula of storage modulus against incubation time.

The peptide fibre cluster core structure observed under AFM suggests that the gelatin-peptide hybrid hydrogel may be sensitive to incubation time. In the preparation of the hybrid hydrogel, the SAP self-assembles first when the pH was adjusted to a suitable range at room temperature. Before the gelatin was set into a cold environment to form a hydrogel, the gelatin molecules were still free. As a result, during the incubation period, the gelatin molecules can interact with the peptide fibres, entangling them. This was followed by the crosslinking of the gelatin at 4℃, where the gelatin units in the peptide fibres also potentially interacted with other units, forming fibres and networks. Therefore, a model of the two networks was established, shown in figure 5.8 (A). Free gelatin molecules enter the peptide network, playing a role as pivots

that connect the peptide fibres and the gelatin network. An experiment comparing the stiffness variance against different incubation times was designed as evidence of this sensitivity. If the model is correct, an increase in incubation time will enhance the stiffness of the hybrid hydrogel. The storage moduli of 7.5 mg/ml KF8K, 50 mg/ml gelatin and their hybrid hydrogel with 0-, 12-, and 24-hours incubation can be seen in Figure 5.8 (B). The stiffness of the pure gelatin and KF8K samples did not change with incubation time, with a difference of less than 100 Pa after an extra 24-hour incubation in both the gelatin and peptide hydrogel. However, the hybrid samples differed significantly from each other. Every 12 hours gave roughly a 350 Pa increase in storage moduli. After 24 hours of incubation, there was approximately an 80% increase in storage moduli in the DN hybrid hydrogel. This trend strongly supports the rationality of the model, explaining the enhancement of the hydrogel after blending from another perspective.

5.3.4 Temperature Sensitivity & Printability

Since the presence of gelatin, the hybrid hydrogel potentially exhibits temperature sensitivity. The temperature-sensitivity of gelatin is because the weak bonds maintaining helices are broken at high temperatures. Gelatin completely loses helices structure in heating but recovering back to the coil after cooling [20]. As a result, the following experiment forced to assess the stiffness of hybrid hydrogel against temperature. Figure 5.9 (A) revealed the relationship between the storage modulus of gelatin and environment temperature. The gelatin hydrogel showed a weakening in stiffness with the increase in temperature. It can be clearly seen that both 50 and 30 mg/ml gelatin samples were kept in the stiff gel at 10 ℃. After that, their stiffness started to fall gently with heating until 25 ℃. At that point, the decrease of hydrogel modulus started to accelerate sharply. Latterly, at around 35 ℃, the G’ of gelatin hydrogel decreased to lower than G’’. That

relationship indicates that the hydrogel has already completely transformed into liquid. The G' and G'' crossing point was accepted as the melting point of gelatin which is 37 ℃. A similar behaviour was also observed in the hybrid hydrogel, whose result is given in figure 5.9 (B). The hydrogel remained steady at 10 ℃, but the storage modulus dropped down after heating. In contrast, when the temperature reached the melting point (37 ℃), the stiffness of the hybrid hydrogel was approximately the same value as pure peptide hydrogel (KF8K) instead of 0. It is explained by the stiffness of peptide hydrogel is not impacted by temperature. In particular, the KF8K peptide hydrogel was stable and unchanged between the 10- and 45-℃ temperature zone, staying in around 300 Pa. Another highlight in figure 5.7(B) was the stiffness recovery of the hybrid hydrogel after the heating-cooling cycle. When the hydrogel was cooled down, the sample showed a higher storage modulus. At 37 ℃, the sample started to transform back to the hydrogel. Further, at 10 ℃, the sample formed a stable hydrogel again. This result proved the temperature responsibility of gelatin was kept in gelatin-peptide hybrid hydrogel and the melting points were the same as pure gelatin, at around 37 ℃. Besides, a storage modulus rising was found when recovered hydrogel was placed at 10 ℃ and showed a higher value after increasingly heating-cooling cycles. The value increase after more cycles was derived from the rheometer equipment. Thus, the above number proved that gelatin-peptide hybrid hydrogel forms a stiff hydrogel at room temperature but weakened with increasing temperature. Therefore, relying on the feature, the hybrid hydrogel held promising prospects as the delivers sealing drugs or molecules at room temperature and releases in vivo, which is 37 ℃.

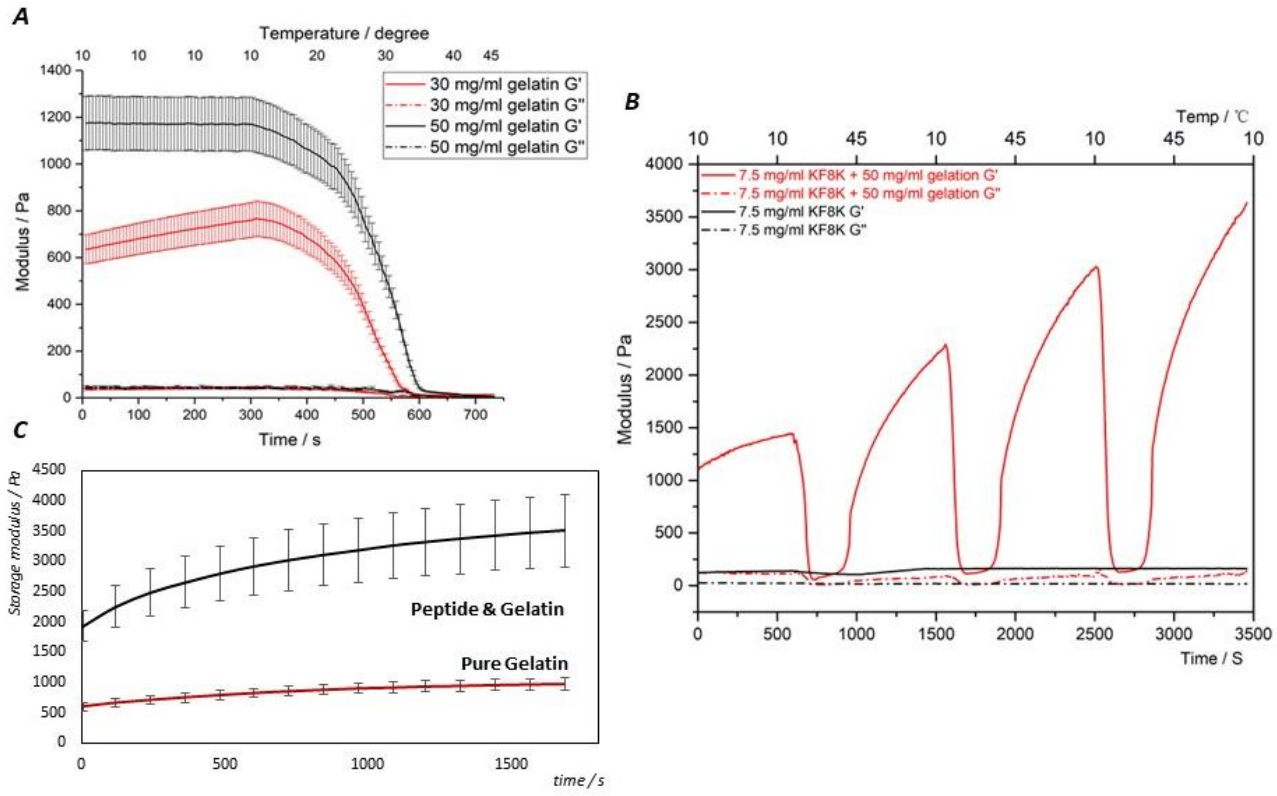

Figure 5-9 (A) The storage modulus of gelatin against temperature (B) Temperature recovery cycle of gelatin-KF8K hybrid hydrogel (C) Storage modulus of gelatin and gelatin-KF8K hydrogel with time in 10 ℃. The gelatin concentration is 50 mg/ml, while it is 50 mg/ml Gelatin and 7.5 mg/ml KF8K in the hybrid hydrogel.

The excellent stiffness and temperature sensitivity of the gelatin-SAP hydrogel suggest its potential use as an ink in bio-3D printing. Figure 5.9 (C) illustrates the change in storage modulus with time for both pure gelatin and a hybrid hydrogel made of 50 mg/ml gelatin and 7.5 mg/ml peptide (KF8K) at 10 ℃. The samples were pre-heated to 25 ℃ to weaken the hydrogel stiffness before measuring. The pure gelatin reached 900 Pa after 1000 seconds and remained stable from that point on, with only a further 70 Pa (less than 10%) increase in the last 800 seconds. In contrast, the storage modulus of the hybrid sample continued to increase during the 1800 seconds, although the rate of increase slowed after 1500 seconds. This suggests that the presence of

peptide fibres prolongs the hydrogelation process, as interpenetration between the peptide fibres is required for the crosslinking of the gelatin, increasing the time needed to achieve a stiff gel.

The potential use of hybrid hydrogel as an ink in 3D printing raises the question of its strain recovery ability. In 3D printing, hydrogels experience high strain during injection from the nozzle. The following experiment focused on the recoverability of the double-network hydrogel, as a lack of strain recovery is a major limitation of gelation hydrogel in applications. In the recovery test, the sample underwent three strain-removing and strain-breaking cycles, referred to as the second, third, and fourth recovery cycles. The period from the start to the first strain breaking was referred to as the first cycle. The storage modulus of the gelatin hydrogel after high-strain breaking can be seen in Figure 5.10 (A&B). The stiffness of the 50 mg/ml gelatin hydrogel decreased over time after high-strain breaking. All recovery cycles showed a declining tendency. The modulus recovered approximately 95% when the high strain was removed. In contrast, in 30 mg/ml gelatin, there was only roughly 50% stiffness left after the first breaking and stain removal. Furthermore, the higher concentration gelatin (50 mg/ml) showed better recoverability than the 30 mg/ml one. The 30 mg/ml gelatin did not return to its previous stiffness after strain removal. These results demonstrate the limited strain recoverability of the gelatin hydrogel.

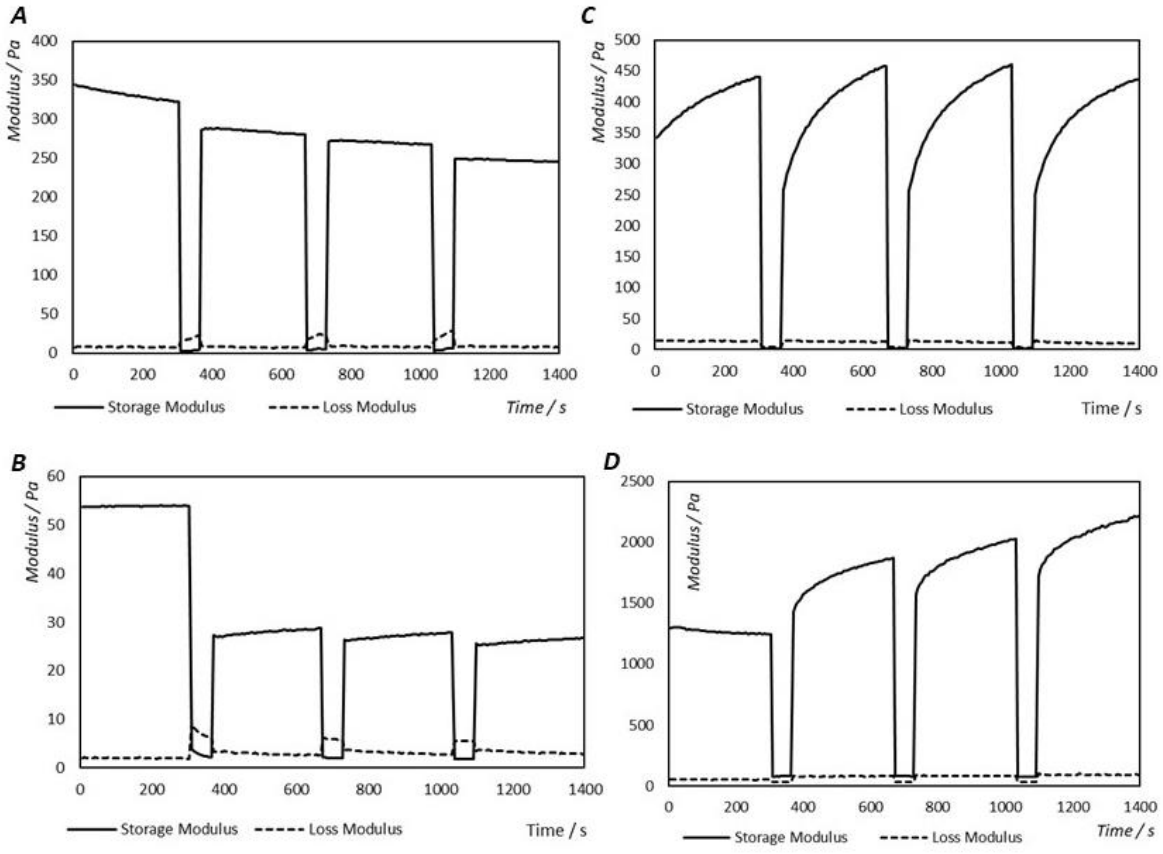

Figure 5-10 (A) Strain breaking and recovery cycle of 50 mg/ml gelatin (B) Strain breaking and recovery cycle of 30 mg/ml gelatin (C) Strain breaking and recovery cycle of 7.5 mg/ml KF8K hydrogel (D) Strain breaking and recovery cycle of 50 mg/ml gelatin- 7.5 mg/ml KF8K hydrogel

On the other hand, a high-speed recovery was observed in the KF8K peptide hydrogel (Figure 5.10 (C)), as reversible physical interactions dominate the maintenance of SAP networks. The physical bonds can be immediately rebuilt upon the removal of strain. The KF8K hydrogel started from 300 Pa and completely returned to a similar value after three strain breakings. This result was also consistent with F9.

In terms of the gelatin-KF8K hybrid hydrogel, a decent recovery was observed in all strain-breaking and recovery cycles (Figure 5.10 D). The modulus in the first cycle was clearly different from later recovery cycles. This is attributed to the influence from the rheometer. The sample was interfered with when it was loaded in the plate in the rheometer. Therefore, the presence of SAP

(KF8K) played a role in promoting the recovery of gelatin in the hybrid hydrogel. The same result was also obtained in the F9-gelatin hydrogel. The hybrid hydrogels were proven to have strain-breaking recoverability.

To further understand the recovery process, a fitting model was employed. Currently, models have been proposed in the literature to establish the relationship between mechanical properties and network topologies for hydrogel samples [21]. The model is considered to be a helpful strategy for measuring how the recovery process works. The classical mechanical model (one spring element in parallel with two spring + dashpot elements) was adopted as a reasonable model used the for β-sheet-based peptide hydrogel family. Based on the model, the recovery is divided into two processes, long-time recovery and short-time recovery [22]. The recovery hydrogel can be divided into two processes. There is a short-time process finishing quickly but with weaker recovery and a long-time process that produces more robust storage modulus recovery but is done over a relevant long time. The fast and short-time recovery is explained by the fast recovery of physical interactions. However, the long-time one is attributed to the movement of peptide monomers.

The shortcoming of recoverability in gelatin hydrogel was further exposed from the fitting result. In the 50 mg/ml gelatin hydrogel (figure 5.11), both G_1' and G_2' were negative in all four recovery cycles (table 5. 1). It means the 50 mg/ml gelatin hydrogel was becoming weaker as time went by after high shear strain breaking. Furthermore, the G_∞ is proposed, which is given by $G_\infty=G_0+G_1+G_2$ representing the storage modulus of the sample with infinite time after breaking. Still, the value dropped to zero in 50 mg/ml gelatin. The G_∞ suggests the 50 mg/ml gelatin cannot keep in hydrogelation when the time is long enough after meeting with high shear strain.

Table 5-1 Fitting result of the recovery cycles of 50 mg/ml gelatin hydrogel

	G_0	G_1	τ_1	G_2	τ_2	G_∞
0-5 min	0.344	-7.00E-03	1.43E+02	-4.99E+00	9.79E+04	0.000
6-11 min	0.286	-5.00E+00	5.68E+05	-4.92E+00	5.77E+05	0.000
12-17 min	0.270	-2.88E-04	2.44E-02	-2.88E-04	3.11E-02	0.000
18-23 min	0.249	-5.000E+00	7.18E+05	-5.00E+00	7.18E+05	0.000

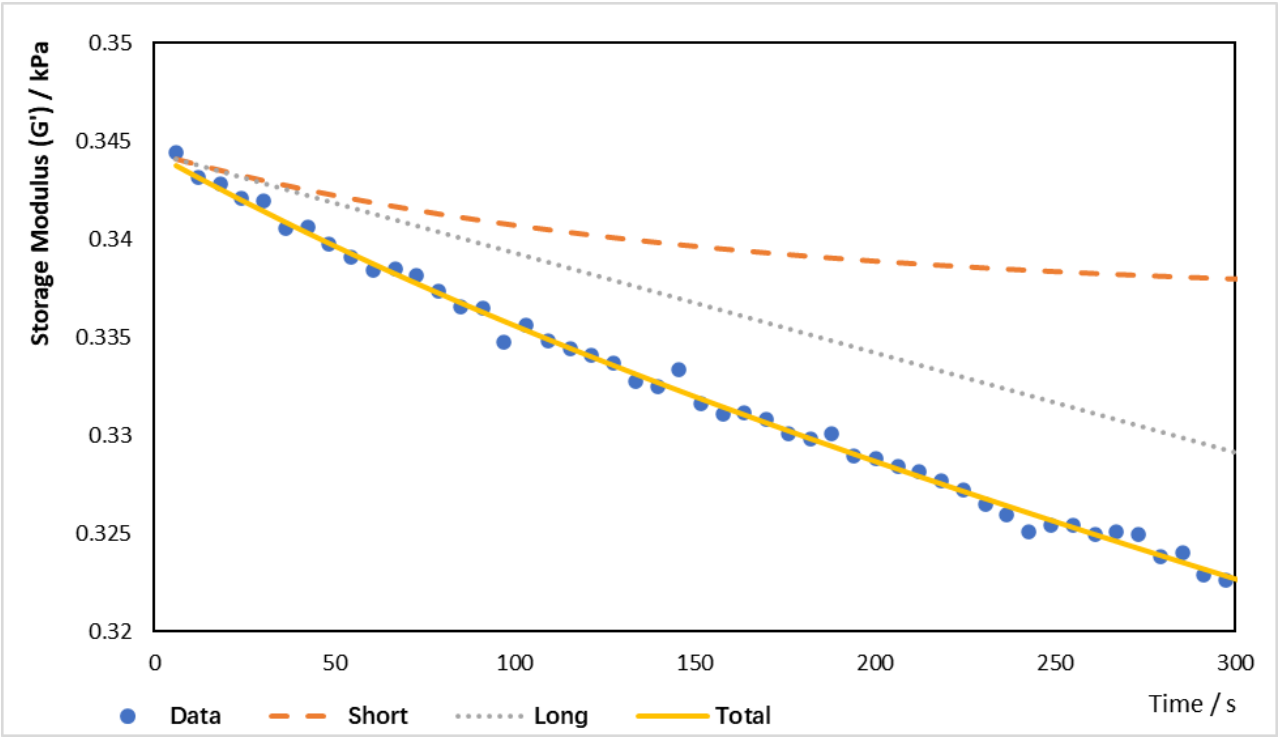

Figure 5-11 Fitting result of the 3rd recovery cycle of 50 mg/ml gelatin hydrogel

Conversely, self-assembly peptide (KF8K) showed better recovery than gelatin. It is evident that the G_∞ of all four cycles were a positive value. KF8K held the same G_∞ in cycle 2nd (6-11 min), 3rd (12-17 min) and 4th (18-23 min), confirming its capacity for full recovery after high strain breaking. In particular, the first cycle (0-5 min) exhibited a critical difference value in G_∞ compared

with the later three cycles. It was explained by the deposition of materials on the rheometer plate and the lag time between sample setting up and experiment starting [18].

The purpose of the following experiment is to investigate the recoverability of a double-network hydrogel composed of a mixture of gelatin and KF8K peptide. The fitting result of 50 mg/ml gelatin- 7.5 mg/ml KF8K hydrogel is given in table 5.2 & figure 5.12. The table highlighted that G_1 and G_2 shifted to positive in KF8K-Gelatin hydrogel in all three later cycles. Therefore, undoubtedly, the G_∞ also was a positive value in the later cycles. It proved that hybrid hydrogels recover with time after high shear strain breaking. It is not surprising that the hybrid hydrogels showed an unstable recovery process in 1st cycle, like pure SAP. This phenomenon was derived from the impact of rheometer equipment. Meanwhile, in the later three cycles, the G1 also kept unchanged while there was a fluctuation in the value of G_2. The second and fourth cycles produced similar values but were different to the third cycle. The fluctuation suggested the recoverability of the hybrid hydrogel was not as good as pure KF8K peptide hydrogel. Similar to the KF8K peptide hydrogel, the G_1 was stable in each cycle, suggesting the short-time recovery was entirely dominated by the self-assembly peptide. On the contrary, the difference in G_2 indicates the long-time process was impacted by gelatin. In summary, the peptide-gelatin DN hydrogel acquired decent recoverability even though the recovery was not as good and stable as peptide hydrogel.

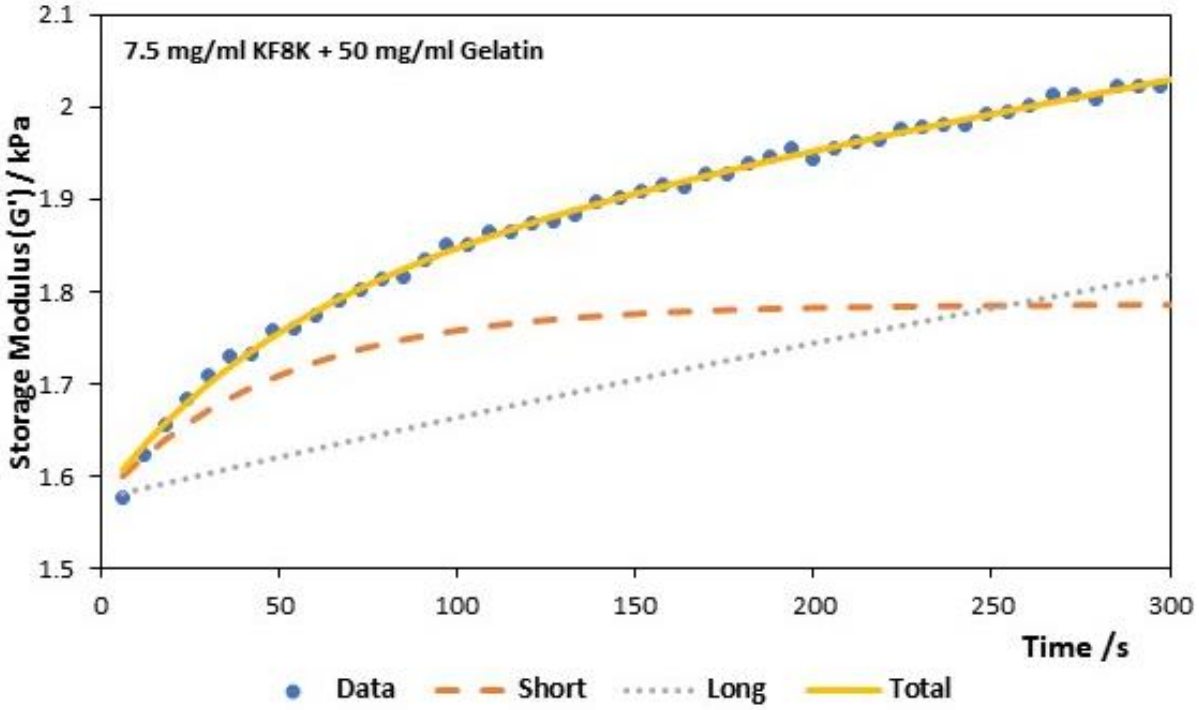

Figure 5-12 Fitting result of the 3rd recovery cycle of 50 mg/ml gelatin- 7.5 mg/ml KF8K hydrogel

Table 5-2 Fitting result of the recovery cycles of 50 mg/ml gelatin- 7.5 mg/ml KF8K hydrogel

	G_0	G_1	τ_1	G_2	τ_2	G_∞
0-5 min	1.297	-0.045	346.22	-0.045	346.18	1.207
6-11 min	1.429	0.251	63.50	2.999	4499.17	4.541
12-17 min	1.575	0.211	49.73	1.073	1.2E+03	2.859
18-23 min	1.726	0.240	48.96	3.000	3531.25	4.966

For the above result, SAP hydrogel has been viewed as a promising ink in 3D printing. 30 mg/ml gelatin and 15 mg/ml KF8K blending hydrogel was employed for 3D bio-printing as the ink. Figure 5.13 (A-C) shows the printing result. The hybrid hydrogel established a precise structure with high resolution. The clear and precise edge of the structure can be seen under the

magnification of microscopy. In the printing, the hydrogel was pre-heated to 25 ℃ to make the gel weaker. The weakened hydrogel can be pressed out more easily. Meanwhile, the surface of the printing bed was designed at 4 ℃. At there, the gelatin in the hybrid hydrogel can crosslink quickly. Besides, 10 mg/ml gelatin and 50 mg/ml gelatin were also blended into 15 mg/ml KF8K as ink. Unfortunately, 10 mg/ml has been proven to be low for gelatin forming a hydrogel. It led to the hybrid hydrogel working close to pure KF8K in printing. In contrast, 50 mg/ml gelatin and peptide produced an over high stiffness that the ink cannot be pressed out from nozzle by designed pressure.

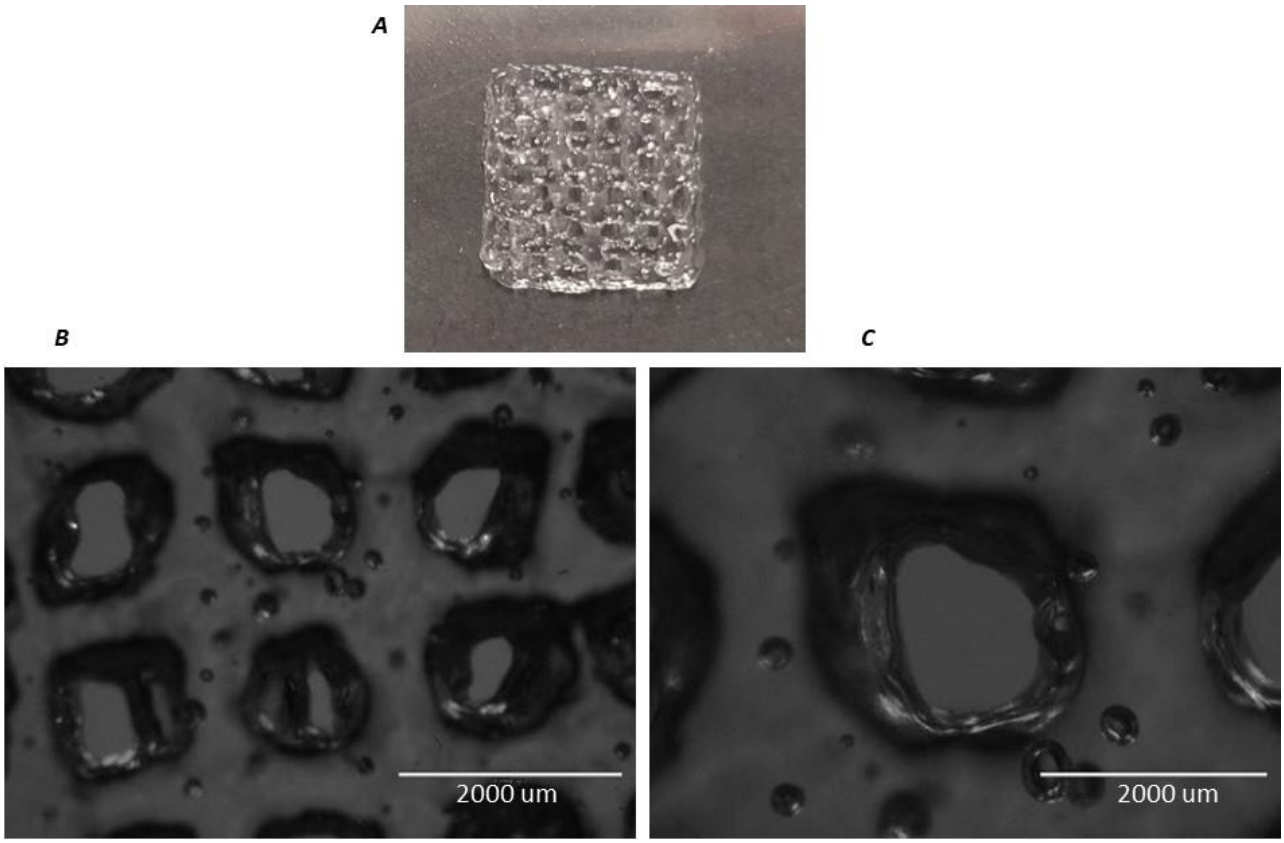

Figure 5-13 (A) 3D printing by the 15 mg/ml KF8K and 30 mg/ml gelatin hybrid hydrogel (1 cm x 1 cm x 5 mm cuboid). (B-C) 2 times and 4 times zooming under optical microscopy.

5.3.5 Anti-bacterial

In the final part of the experiment, the antibacterial ability in the gelatin and peptide double network hydrogel was assessed. The assessment was achieved by the anti-bacterial assay. The variance of bacteria concentration in the assay would be monitored for 18 hours. LB (Lysogeny Broth) medium and 70% ethanol were employed as the negative control and positive control. The reason for the test is unsatisfactory gelatin's anti-bacterial ability. Gelatin was also used as a medium for bacterial culture [23,24]. The limitation of gelatin sets a boundary for its applications, for example, in the food industry and medicine [25]. On the contrary, the lysine and phenylalanine in the KF8K (self-assembly peptides) sequence contribute promising anti-bacterium properties. The positive charge for lysine interferes with the bacteria's growth [26]. Meanwhile, the phenylalanine triggers oxidative and variation of osmotic stress leading to a series of alterations in the membrane of bacterial cells. The change includes differences in permeabilisation and integrity [27,28].

Figure 5.14 compared the bacterial concentration variance in pure gelatin, KF8K peptide and their hybrid samples with the above negative and positive controls. Bacterium proliferated in the pure gelatin gel, reaching 0.811 a.u. after 0.3 days. The absorbance of E. Coil stayed unchanged in the next 0.5 days. The bacteria growth curve was the same as the LB medium, containing the lag phase, exponential phase and stational phase. The result suggests the shortcoming of antibacterial ability in gelatin. The bacterial concentration reached 30% of pure LB medium, whose value was 2.698 a.u. after 18 hours.

The OD260 absorbance of E. coil in the KF8K was only 0.089 a.u. Compared to the LB medium and the gelatin sample, the absorbance value of KF8K was strongly close to the value of 70%

ethanol. There was only 0.005 UV absorbance in the 70% ethanol sample. Besides, there was no bacterial proliferation observed in the KF8K sample. The concentration of bacteria was kept at a low level for 18 hours. The absorbance value kept unchanged for 18 hours. The excellent anti-bacterial ability is attributed to the four lysines in the KF8K sequence, particularly the two in N- and C- terminals. Phenylalanine also contributed to inhibiting bacterial growth. Meanwhile, the gelatin and KF8K hybrid sample produced a lower bacterial concentration after 18 hours than the pure KF8K sample. The UV absorbance number was 0.033 a.u. The bacteria proliferation was still not detected in the hybrid sample. The blending with KF8K (SAP) is believed strongly contributes to overcoming the shortcoming of antibacterial ability in gelatin. In particular, the hybrid sample produced better antibacterial than pure KF8K. The high fibre diameter and density network in the hybrid hydrogel is the reason for the difference. In the higher density network, bacteria cannot avoid connect with the antibacterial amino acids in hydrogel fibres.

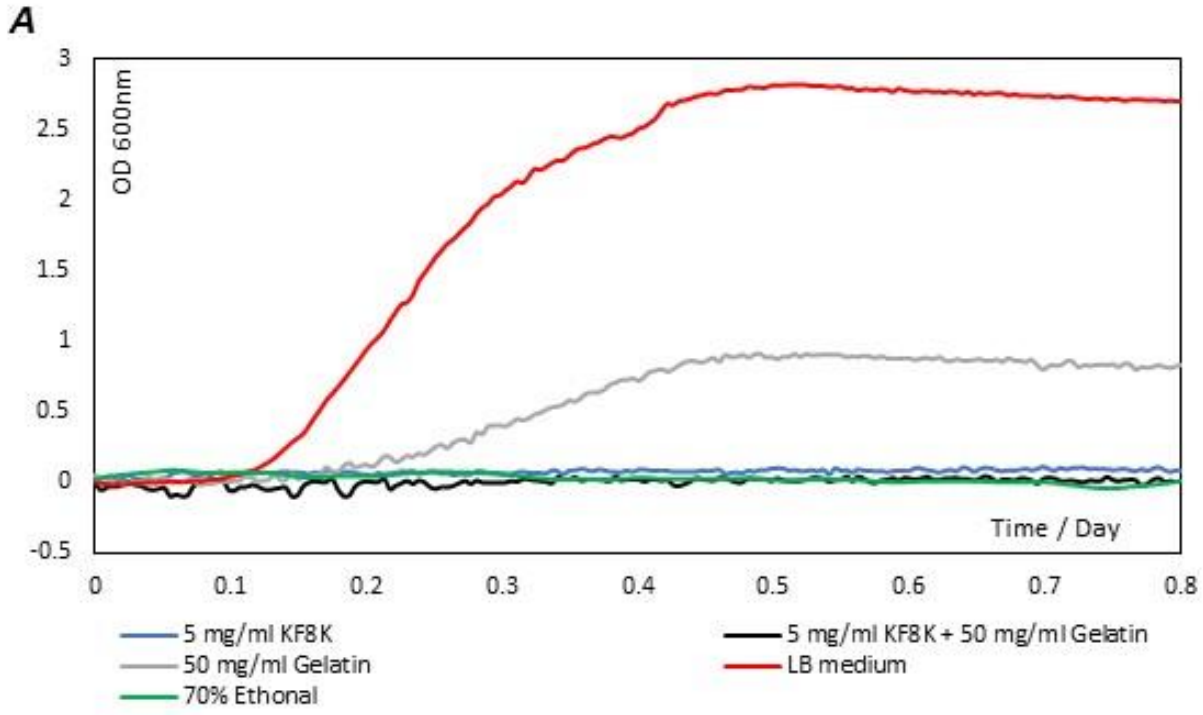

Figure 5-14 OD 600 of gelatin, peptide and hybrid hydrogel after 18 hours. LB medium and 70% ethanol were employed as control groups

5.4 Conclusion

In summary, a hybrid hydrogel of self-assembled peptides and gelatin has been developed. The desired properties, including controllable mechanical properties, excellent temperature sensitivity, biological compatibility, and anti-bacterial capabilities, have been successfully achieved in the hybrid hydrogel.

When the gelatin concentration reached its threshold value (30 mg/ml), a significant stiffness enhancement was observed in the gelatin and self-assembly peptide blending hydrogel. Additional improvements in stiffness were observed when the gelatine concentration continued to increase to 50 mg/ml. 50 mg/ml of gelatin - 7.5 mg/ml of KF8K mixture resulted in a stiffness value of 2000 Pa. This value was more than six times higher than that of pure 7.5 mg/ml KF8K (300 Pa) and two times higher than that of pure 50 mg/ml gelatin. Therefore, the stiffness of the blending hydrogel can be adjusted by controlling the concentration of gelatin.

The improvement in stiffness is attributed to the network interactions. The network structure of the hybrid hydrogel was clearly imaged using AFM, revealing that gelatin formed a higher-density network, compressing the peptide fibres together into clusters. TEM imaging also showed an increase in fibre diameter, with an improvement of approximately 1 nm in the hybrid hydrogel compared to pure peptide hydrogels.

Additionally, the hybrid hydrogel retains its temperature sensitivity. As the temperature increased to 37 degrees Celsius, the strength of the hybrid hydrogel weakened and reached the

same value as that of pure KF8K hydrogel. Upon cooling, the strength of the hybrid hydrogel was restored. These results suggest the potential of hybrid hydrogels as 3D printing inks, which can be softened and extruded at high temperatures and cross-linked and hardened at low temperatures. Furthermore, the hybrid hydrogel has demonstrated good printability, as evidenced by its strain-breaking recoverability.

Finally, the hybrid hydrogel has also been demonstrated to have good antibacterial properties.

In the future, modified gelatins such as Gelatin-MA are expected to hold potential as a replacement for gelatin in hybrid hydrogels. These modified gelatins have more active sites for cross-linking and attachment of target molecules.

Reference

[1] Cascone S, Lamberti G. Hydrogel-based commercial products for biomedical applications: A review. International journal of pharmaceutics, 2020, 573: 118803.

[2] Jaipan P, Nguyen A, Narayan R J. Gelatin-based hydrogels for biomedical applications. Mrs Communications, 2017, 7(3): 416-426.

[3] Thorkelsson K, Bai P, Xu T. Self-assembly and applications of anisotropic nanomaterials: A review. Nano Today, 2015, 10(1): 48-66.

[4] Akiyoshi K, Deguchi S, Tajima H, et al. Microscopic structure and thermoresponsiveness of a hydrogel nanoparticle by self-assembly of a hydrophobized polysaccharide. Macromolecules, 1997, 30(4): 857-861.

[5] Liang L, Xu X D, Chen C S, et al. Evaluation of the biocompatibility of novel peptide hydrogel in rabbit eye. Journal of Biomedical Materials Research Part B: Applied Biomaterials, 2010, 93(2): 324-332.

[6] A. Nakayama,A. Kakugo,J. P. Gong,Y. Osada,M. Takai,T. Erata,S. Kawano, Advanced Functional Material, Volume14, Issue11, November, 2004, Pages 1124-1128

[7] Orsborn G, Dumbleton K. Eye care professionals' perceptions of the benefits of daily disposable silicone hydrogel contact lenses. Contact Lens and Anterior Eye, 2019, 42(4): 373-379.

[8] Li L, Zhang K, Wang T, et al. Biofabrication of a biomimetic supramolecular-polymer double network hydrogel for cartilage regeneration. Materials & Design, 2020, 189: 108492.

[9] Catoira M C, Fusaro L, Di Francesco D, et al. Overview of natural hydrogels for regenerative medicine applications. Journal of Materials Science: Materials in Medicine, 2019, 30: 1-10.

[10] Imeson A P. Thickening and gelling agents for food[M]. Springer Science & Business Media, 2012.

[11] Xu J, Fang H, Zheng S, et al. A biological functional hybrid scaffold based on decellularized extracellular matrix/gelatin/chitosan with high biocompatibility and antibacterial activity for skin tissue engineering. International Journal of Biological Macromolecules, 2021, 187: 840-849.

[12] Ki C S, Baek D H, Gang K D, et al. Characterization of gelatin nanofiber prepared from gelatin–formic acid solution. Polymer, 2005, 46(14): 5094-5102.

[13] Yan X, Chen Q, Zhu L, et al. High strength and self-healable gelatin/polyacrylamide double network hydrogels. Journal of Materials Chemistry B, 2017, 5(37): 7683-7691.

[14] Shin H, Olsen B D, Khademhosseini A. The mechanical properties and cytotoxicity of cell-laden double-network hydrogels based on photocrosslinkable gelatin and gellan gum biomacromolecules. Biomaterials, 2012, 33(11): 3143-3152.

[15] Yue K, Trujillo-de Santiago G, Alvarez M M, et al. Synthesis, properties, and biomedical applications of gelatin methacryloyl (GelMA) hydrogels. Biomaterials, 2015, 73: 254-271.

[16] Majumder P, Zhang Y, Iglesias M, et al. Multiphase assembly of small molecule microcrystalline peptide hydrogel allows immunomodulatory combination therapy for long-term heart transplant survival. Small, 2020, 16(38): 2002791.

[17] Karim A A, Bhat R. Fish gelatin: properties, challenges, and prospects as an alternative to mammalian gelatins. Food hydrocolloids, 2009, 23(3): 563-576.

[18] Wychowaniec J K, Smith A M, Ligorio C, et al. Role of sheet-edge interactions in β-sheet self-assembling peptide hydrogels. Biomacromolecules, 2020, 21(6): 2285-2297.

[19] Anirudhan T S, Mohan A M. Novel pH switchable gelatin based hydrogel for the controlled delivery of the anti cancer drug 5-fluorouracil. Rsc Advances, 2014, 4(24): 12109-12118.

[20] Duconseille A, Astruc T, Quintana N, et al. Gelatin structure and composition linked to hard capsule dissolution: A review. Food hydrocolloids, 2015, 43: 360-376.

[21] Gao J, Tang C, Elsawy M A, et al. Controlling self-assembling peptide hydrogel properties through network topology. Biomacromolecules, 2017, 18(3): 826-834.

[22] S. Yousaf, P. King, A.F. Miller, A. Saiani, D. Clarke, L. Trivoluzzi, H. Aojula, E. Bichenkova; Analytical Chemistry, 91, 10016-10025 (2019)

[23] Antwi M, Geeraerd A H, Vereecken K M, et al. Influence of a gel microstructure as modified by gelatin concentration on Listeria innocua growth. Innovative food science & emerging technologies, 2006, 7(1-2): 124-131.

[24] Doktycz M J, Sullivan C J, Hoyt P R, et al. AFM imaging of bacteria in liquid media immobilized on gelatin coated mica surfaces. Ultramicroscopy, 2003, 97(1-4): 209-216.

[25] Wu J, Sun X, Guo X, et al. Physicochemical properties, antimicrobial activity and oil release of fish gelatin films incorporated with cinnamon essential oil. Aquaculture and Fisheries, 2017, 2(4): 185-192.

[26] Lin L, Gu Y, Li C, et al. Antibacterial mechanism of ε-Poly-lysine against Listeria monocytogenes and its application on cheese. Food Control, 2018, 91: 76-84.

[27] Gahane A Y, Ranjan P, Singh V, et al. Fmoc-phenylalanine displays antibacterial activity against Gram-positive bacteria in gel and solution phases. Soft matter, 2018, 14(12): 2234-2244.

[28] Singh H, Gahane A, Singh V, et al. Antibiofilm activity of Fmoc-phenylalanine against Gram-positive and Gram-negative bacterial biofilms. The Journal of Antibiotics, 2021, 74(6): 407-416.

[29] Kacher J, Landon C, Adams B L, et al. Bragg's Law diffraction simulations for electron backscatter diffraction analysis. Ultramicroscopy, 2009, 109(9): 1148-1156.

[30] Jenness D D, Sprecher C, Johnson Jr W C. Circular dichroism of collagen, gelatin, and poly (proline) II in the vacuum ultraviolet. Biopolymers: Original Research on Biomolecules, 1976, 15(3): 513-521.

[31] Toniolo C, Bonora G M, Bavoso A, et al. A long, regular polypeptide 310-helix. Macromolecules, 1986, 19(2): 472-479.

[32] Shankar S, Teng X, Li G, et al. Preparation, characterization, and antimicrobial activity of gelatin/ZnO nanocomposite films. Food Hydrocolloids, 2015, 45: 264-271.

6. Chapter 6. Peptide-Oligonucleotide Hybrid Hydrogel

Abstract

Recently, double-network hydrogels relying on the preparation of two self-assembled

materials have been more and more widely proposed [1]. The convenience of the preparation process is its advantage over other double-network hydrogels. Two widely used and studied examples are peptides and oligonucleotides [2]. This experiment designed a hybrid hydrogel by well-designed peptide (KF8K) and oligonucleotide (A16) self-assembling by β-sheet and based pairing, respectively. The two structures were linked by a peptide and oligonucleotide consisting of the conjugate. The conjugate was produced through the maleimide and thiol clicks reaction. The hybrid hydrogel exhibited obvious stiffness improvement compared to pure SAP hydrogel. The stiffness can also be adjusted by changing the mixture ratio between peptide and oligonucleotide.

6.1 Introduction

As a wide-distributed biological macro-molecule, the oligonucleotide has been well-researched [3]. It is known as a short-nuclear nucleoside with less than 20 bases, also seen as a short piece of DNA. The single-strand (ss) oligonucleotide can pair with a complementary strand forming a double-strand (ds). The pairing is the result of the principle of the complementary base pairing rule. In the rule, Adenine-nucleotide (A) pairs with Thymine-nucleotide (T,) and Guanine-nucleotide (G) pairs with Cytosine-nucleotide (C) with strict selectivity. The base pairing is a spontaneous process without extra demand, such as enzymes.

The oligonucleotide is also regarded and applied as a self-assembly material based on the stable and high-selective bases pairing rule. Well-designed oligonucleotides can form fibres and networks by overlapping oligonucleotide chains, and some of them also produce hydrogel under suitable conditions [4,5]. The ladder is a basic design unit where ss DNA pairs with adjacent ss DNAs one by one, forming more complex structures, including tubes [6]. However, the strand pairing strength of this approach is not strong enough to form complex structures sufficiently due to the

pairing domain in strands being too short. In that, to overcome the limitation, Y and cross-shape oligonucleotide blocks are recently proposed [7]. The two units are established by 3 and 4 single strands, respectively. There are multiple arms at the end of the units for the junction between other units forming blocks. The specific units play the role of tiles to establish three-dimensional (3D) objects [8].

As a result, self-assembly oligonucleotide hydrogel is proposed as responsive material and extracellular matrix (ECM) [9]. Hydrogel is a hydrophilic polymer with a good crosslink and complex network that does not dissolve into water. The hydrophilic backbone brings a high-water content ability to the hydrogel. DNA hydrogels show excellent biocompatibility and biodegradability since DNA is a natural biological molecule. The oligonucleotide hydrogel has been reported as 3D printing ink [10], drug delivery [11], diagnostics [12] and cell culture [13].

Besides, the self-assembly of peptides driven by pH and electronic static forces is also reported to produce hydrogels. The family of self-assembly peptides, including the KFEFKFEFKK (KF8K), forms β-sheet structures. The accumulation of these peptides results in the formation of fibres, networks, and a hydrogel. The self-assembly process is influenced by the alternating hydrophilic and hydrophobic amino acids in the peptides. The net charge of the peptides, determined by pH, influences the electronic static force and triggers the self-assembly process. Therefore, the concept of linking the oligonucleotide chain into the peptide fibres to strengthen the peptide network is proposed (Figure 6.1). A conjugate of oligonucleotide and peptide is needed to connect the two molecules. The conjugate first participates in the assembly of pure peptides, forming fibres through its peptide terminal. Then, the free oligonucleotide is added and pairs with the conjugate's oligonucleotide terminal. Thanks to the conjugate, the oligonucleotide further connects the peptide fibres, contributing to an improvement in the network's stiffness.

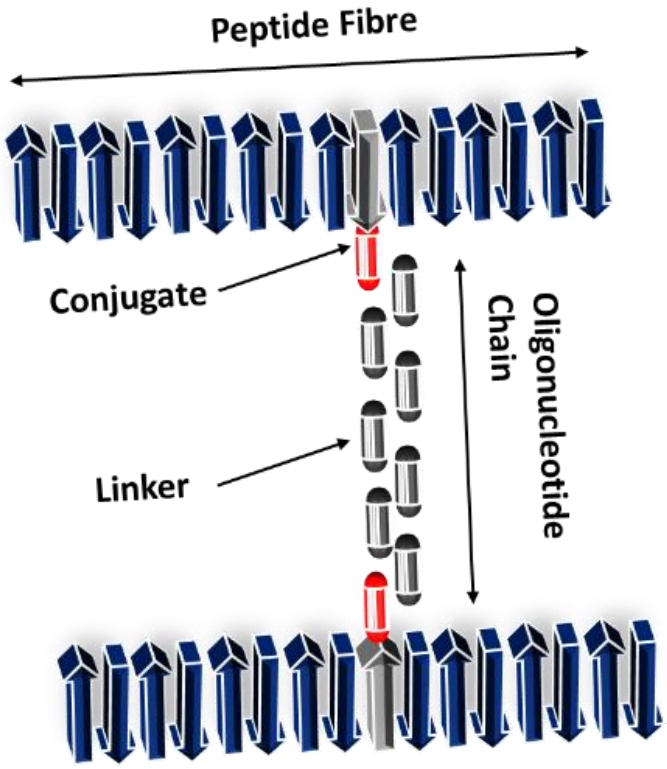

Figure 6-1 Schematic of the hybrid hydrogel

This experiment aimed to produce a self-assembly peptide hydrogel with improved and controllable stiffness by the extra link from oligonucleotide. A 16 bp single-strand oligonucleotide would react to a 12-amino acids peptide to produce the conjugate by the thiol-maleimide reaction to connect the peptide fibre and oligonucleotide. The hybrid hydrogel was looking forward to adjusting its strength by changing the ratio of the oligonucleotide.

6.2 Method

6.2.1 Peptide

Maleimide-GGKKFEWEFEKK (Mal-W10) and KFEFKFEFKK (KF8K) were purchased from Lifetein with 95% purification and HCl salt. The Mal-W10 was called Mal-Pep in the later paragraph. The purification was tested by elementary analysis (table S.1), HPLC (figure S.1) and MALDI-TOF (figure S.2), which showed the purification of peptide, designed length peptide and demanded molecular

weight peptide, respectively. The solvent in HPLC was 0.1% TFA contained water, and 0.1% TFA contained ACN when the C-12 column was employed in the HPLC. It was followed by the MALDI-TOF mass spectroscopy, where the matrix contained the solution of absorbent (ACN+0.1% TFA) and organic compounds (sinapic acid and α-Cyano-4-hydroxycinnamic acid).

6.2.2 Oligonucleotide

Desalted 5'-AGGCGCCTTTAGCTAA-SH-3' (Thiol-A16) and 5'-AGGCGCCTTTAGCTAA-3' (A16) were purchased from ATDbio Ltd. The Thiol-A16 and A16 are called Thiol-oligo and linker in the later paragraph, respectively. The thiol group was typically oxidised to disulfide bonds by oxygen. The purification was proved by HPLC and mass spectroscopy.

6.2.3 Conjugate Producing Reaction

Prior to the reaction, the disulfide bond protection in thiol-oligonucleotide was reduced to thiol by ten times TECP in 10-folds PBS (phosphate-buffered saline) at pH three overnight. It was followed by the cleaning of the NAP-25 column removing the salt and TECP away. The acquired thiol-oligonucleotide underwent a vacuum freeze-drying to remove water.

5 umol maleimide-peptide was decently dissolved into 0.95ml ten times PBS (no oxygen) and 0.05 ml DMSO blending solution. The solution was treated with nitrogen gas in advance overnight removing oxygen. 1 umol well-prepared thiol-oligonucleotide was added to the solution. It was followed by adjusting pH to 7.0 by 0.5 M NaOH. The reaction solution was fixed by parafilm isolated to the oxygen and mildly stirred overnight.

6.2.4 Conjugate separation and purification

The solution after the reaction underwent the reversed-phase HPLC to separate the targeting

conjugate. It uses the C-18 column under solvent A 0.05 M LiClO4 in water and B 0.05 M LiClO4 in ACN. The eluent is in a gradient from 0% to 50% of solvent B for 60 min. The unreacted oligonucleotide fractions, unreacted peptide and conjugate were monitored by the UV absorbance under 210 nm. Through the retention times, the conjugate was separated from the reaction solution. The separated sample was measured by Nanodrop UV to assess the purification and oligonucleotide concentration after the reaction. Prior to final lyophilising, the collected fractions underwent dialysis under 2000 MW semipermeable membrane overnight at room temperature. It removes the ACN and LiClO4 salt from the HPLC solvent.

6.2.5 NMR spectrum

0.04 umol lyophilizate was dissolved into 500 uL D_2O solvent to 0.08 umol/ml concentration. The sample was measured by 400 MHz NMR for proton nuclear magnetic resonance (^1H spectrum). The spectrum background is D_2O.

6.2.6 MALDI-TOF

The lyophilizate was mixed into the MALDI matrix, which was 25 mg/mL THAP 2,4,6-trihydroxyacetophenone monohydride) with 5 mg/mL ammonium citrate in 50% ACN and 0.1% TFA. The mass spectrum was acquired from Bruker Daltonics Ultraflex ToF/ToF mass spectrometer. The measuring method was 10k Da positive ion without reflection.

6.2.7 FTIR

The lyophilizate powder was measured by ATR-FTIR between 1800 cm^{-1} and 1300 cm^{-1} with 256 scans and 4 cm^{-1} steps. The air was employed as background. The collection was by Brucker A-P FT-IR Spectrometer. FTIR spectra were smooth by Gaussian function between every 5 points.

6.2.8 Hydrogel preparation

Half hydrogel samples were prepared in aqueous 100 mM Tris buffer (pH 7.2) containing 200 mM KCl, while the rest was in pure HPLC water. 5 mM KF8K were used for hydrogel samples as the final peptide concentrations. In the Tris containing sample, once KF8K peptide was dissolved by half the total volume of water, buffer and reaction-acquired conjugate were added into the solution, followed by the pH adjustment by 0.5 M NaOH. The no tris samples were prepared by dissolved KF8K peptide powder into 80% designed volume HPLC water. After a clear solution was obtained, the above conjugate was blended, and the pH was adjusted to 7.2 immediately. Adding water or buffer to adjust the volume of samples to the designed number was the final step.

6.2.9 Rheology Test

180uL sample was loaded into a stainless Peltier with 45000 um gaps between the Peltier and parallel plate. 20 mm diameter plate is selected, and the gap is set at 500 um in measurement. Collections underwent at room temperature. Strain-responsible storage modulus (G') and loss modulus (G'') were collected to evaluate the linear viscosity region and shear thinning properties at fixed strain (0.2%) and frequency (1 Hz).

6.3 Result and discussion

6.3.1 Reaction Design

In the experiment, the self-assembling peptide KF8K acts as the backbone of a hydrogel, which has been extensively studied in chapters 4 and 5. The hydrogelation occurs at neutral pH and bonds with the pH-fixed oligonucleotide. The oligonucleotide chain reinforces the network and scaffold by linking the peptide fibres, as depicted in figure 6.2. To connect these two structures, a

peptide-oligonucleotide conjugate is required. This conjugate allows the peptide and oligonucleotide fragments to assemble into KF8K fibres and free oligonucleotide chains, respectively.

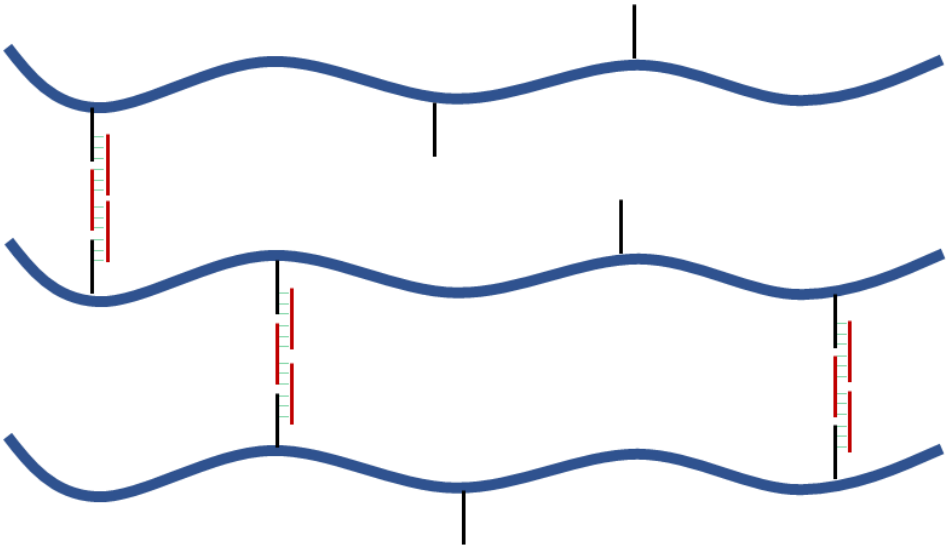

Figure 6-2 Schematic of the peptide-oligonucleotide connection

So far, many reports have shown that maleimide (Mal) and thiol (SH) reactions can effectively and selectively establish biological composites, offering the benefits of Michael-type additions [14]. The reaction occurs when the sulfur atom's free electron pair reacts with the double bond in the maleimide group's heterocycle (figure 6.3), linking the sulfur atom and heterocycle. The high reactivity of the double bond is mainly due to ring strain from bond angle distortion and the positioning of carbonyl groups in a cis conformation. Maleimide reacts preferentially with thiol groups when pH is between 6.5 and 7.5, the reaction being a thousand times faster than with primary amines. If pH is over 7.5, amines will compete with the activated site in maleimide and obstruct the reaction [14]. Thus, the reaction was performed in a ten times PBS buffer to maintain neutral pH.

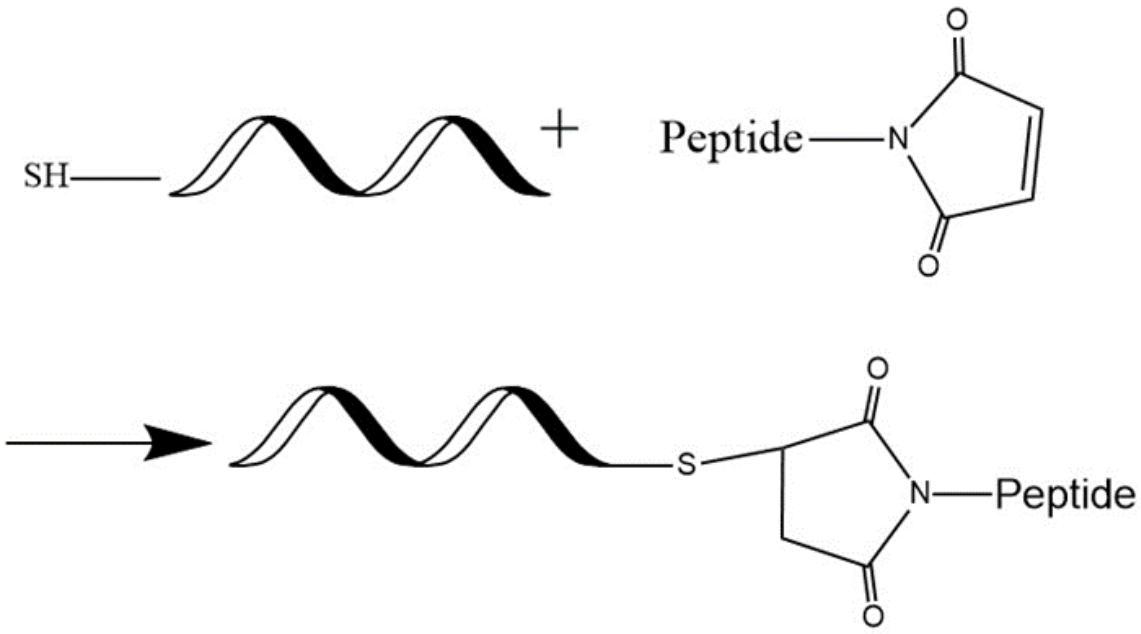

Figure 6-3 Reaction active site between Thiol and Maleimide group

In the experiment, a 16 bp oligonucleotide, whose sequence is 5'-AGGCGCCTTTAGCTAA-3', was used. The 5’ means the end of DNA or RNA single strand with a free 5'-hydroxyl group or one of its phosphate and the 3’ means the end of DNA or RNA single strand with a free 3'-hydroxyl group or one of its phosphate. The oligonucleotide was modified with a thiol in the 3’ terminal. Literature suggests that 12 bp oligonucleotides can form stable double strands [15], leading to a 16 bp design in this experiment. The oligonucleotides were created using a combination of two palindrome sequences, S1 and S2: S1 (5'-AGGCGCCT-3') and S2 (5'-TTAGCTAA-3'). The two fragments can pair with the same sequence but in opposite directions. The oligonucleotides can form long chains via a lattice structure as they half overlap with each other (Figure 6.4). The sequence wass designed to avoid complete pairing between two same sequence fragments to prevent the extension of the oligonucleotide chain.

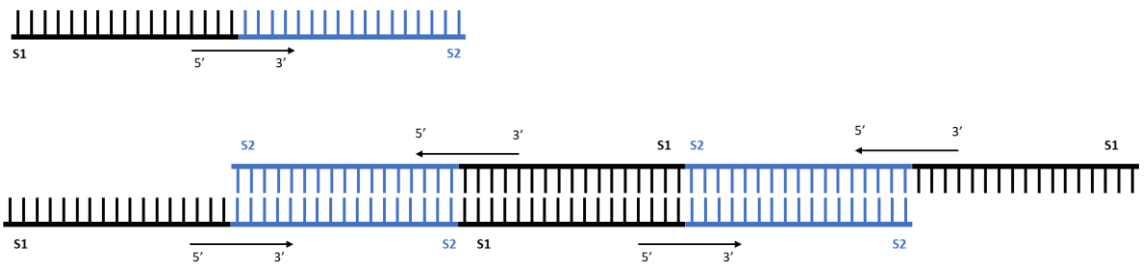

Figure 6-4 Schematic of oligonucleotide pairing to the lattice structure

Meanwhile, the maleimide group replaces the amide group at the N-terminal of the peptide, reducing its positive charge. For an admirable amino acid sequence, the peptide must have good solubility between pH 6.5 and 7.2 in a 10 times PBS buffer. The high salt concentration in the buffer can harm the peptide's solubility. Four potential peptide sequences were proposed, each with alternative hydrophilic and hydrophobic amino acids. They were Mal-GGKKFEWEFEKK (WE), Mal-GGKKFEWKFEKK (WK), Mal-GGKKFEFEFEKK (FE) and Mal-GGKKFEFKFEKK (FK), where G is Glycine, E is Glutamic Acid and F is Phenylalanine. The idea of alternative hydrophilic and hydrophobic amino acids came from the self-assembly peptide due to the conjugate would be blended into the SAP forming hydrogel finally. At the same time, E and K provided charges for Coulomb force, contributing to better solubility. Meanwhile, considering the potential spatial impact, the sequence designed two glycines between the maleimide group and peptide, ensuring all reaction target atoms are well exposed to the thiol group. Surprisingly, the WE peptide was the only one fully dissolved in PBS buffer at pH 7, whereas the rest all precipitated. The replacement of glutamic acid by lysine took two more positive charges in WK and FK peptides, causing a strong electrostatic interaction with ions and poor stability in PBS. Additionally, a possible explanation for the precipitation of FE might be the strong hydrophobicity in phenylalanine. Therefore, WE peptide was employed in this experiment. The peptide is called W10 in the later paragraph.

Prior to the conjugate reaction, the compatibility of W10 and KF8K in fibre was assessed. The

FITC-Dabcyl quenching reaction was used. Figures 6.5(A & B) show the fluorescent spectra of FITC-KF8K in 7.5 mg/mL KF8K and 3.75 mg/mL KF8K + 3.75 mg/mL W10 with Dabcyl. A slight improvement (3%) in quenching was observed in the W10-KF8K blend compared to pure KF8K, due to higher activated FITC concentration and less phenylalanine in W10. However, the W10-KF8K blend was not as homogeneous as F9-KF8K. W10 showed better solubility in PBS buffer than KF8K, meaning it was less hydrophobic. But it did not separately assemble like A8 and D-KF8K. Overall, W10 in the conjugate should be in the KF8K fibre decently.

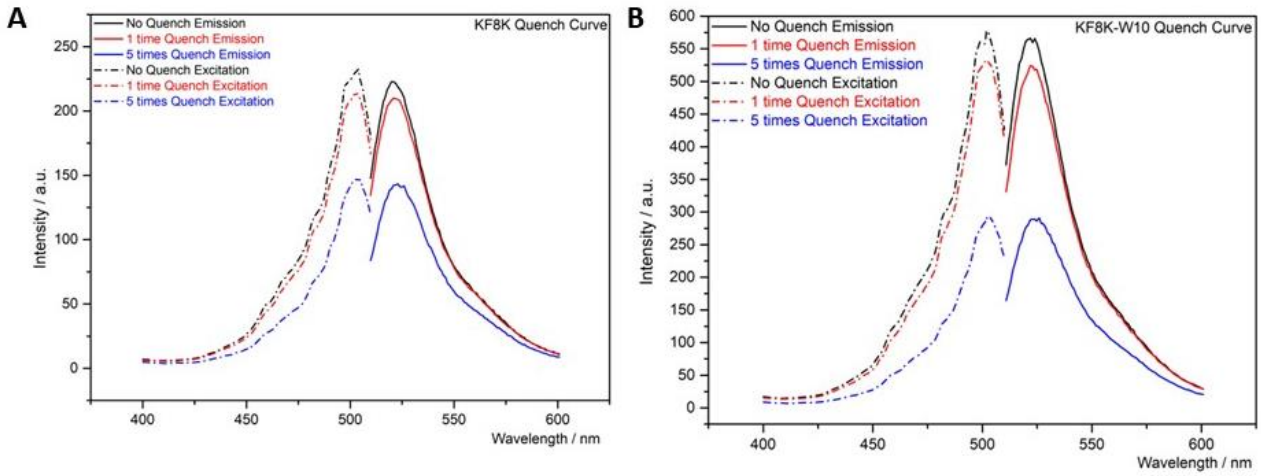

Figure 6-5 (A) Fluorescent intensity of 0.01 mg/ml FITC-KF8K with 0, 1 and 5 molar times Dabcyl-KF8K in 7.5 mg/ml KF8K (B) Fluorescent intensity of 0.01 mg/ml FITC-KF8K with 0, 1 and 5 molar times Dabcyl-KF8K in 3.75 mg/ml KF8K + 3.75 mg/ml W10

6.3.2 Reaction and Purification

The step in conjugate preparation is shown in figure 6.6 The reaction began with pre-treatment (reduction) of the disulfide bond to create thiol groups. TCEP (tris(2-carboxyethyl)phosphine) is commonly used to protect the thiol group from oxidation. The thiol groups were then reduced with TCEP and cleaned with the NAP-25 column to remove salt and TCEP which would interfere with the maleimide-thiol reaction [16]. After lyophilization, flocculation

was observed while it was a white solid before treatment. The clean thiol-oligonucleotide was dissolved in 10x PBS with Mal-Pep and DMSO was added to prevent self-assembly and hydrogelation. The solution was adjusted to the designed pH for the reaction.

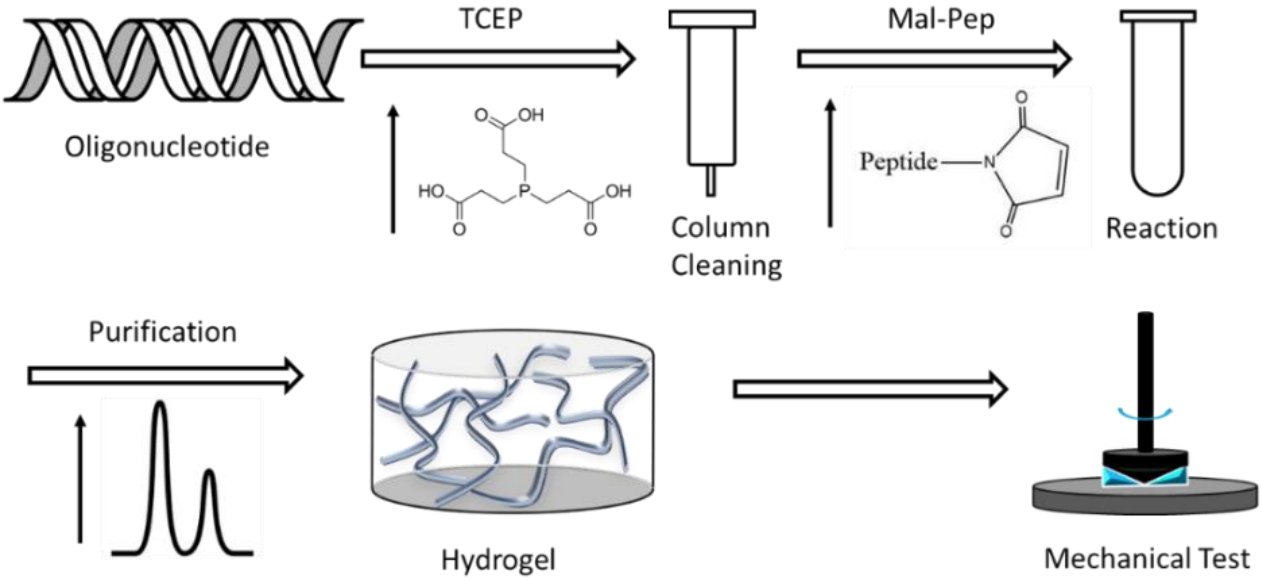

Figure 6-6 Steps in the conjugate preparation process

After the conjugation reaction, the targeting conjugate was separated and purified using HPLC. HPLC separates molecules based on their retention time, which is determined by the molecule's solubility with the solvent. Figure 6.7 compares the retention time of the Mal-peptide, Thiol-oligonucleotide, and mixture solution after the reaction under 210 nm. 210 nm is the UV absorbance for peptide bonds and nucleobases. In the spectrum of the reacted solution, the peaks between 30-40 minutes were from the Mal-peptide, which was also seen clearly in the spectrum of Mal-pep. There was an excess of Mal-peptide in the reaction, causing a large amount to remain after the reaction. The slight variance in the 30–40-minute zone was due to impurities in the maleimide peptide, including hydrochloric acid, from the synthetic process. The pure oligo was separated from the column in approximately 17 minutes, as seen in figure 6.7 (B). Despite the reaction, a small peak was still present at the same time, indicating a small volume of thiol-oligo

leaving. At the same time, a strong single signal appeared at 21.5 minutes, which was identified as the conjugate. The peak was expected to shift slightly to a longer retention time due to the increased volume and decreased solubility of the conjugate compared to the pure oligo. This was also reported by S. Yousaf (2019) [17] with the same retention time. A slight shift in peak retention time was also observed in the leftover Mal-peptide and Thiol-oligo after the reaction, compared to their pure spectra. This was because DMSO was used in the reaction, which changed the system's polarity and influenced the molecule's solubility in the solvent.

Due to the noted time range, the 21–23-minute sample was accepted as the produced conjugate collection. Samples underwent a standard run every time before final collection to ensure accurate collection time. A 16–18-minute sample was also collected for UV assessment as a potential pure thiol-oligo.

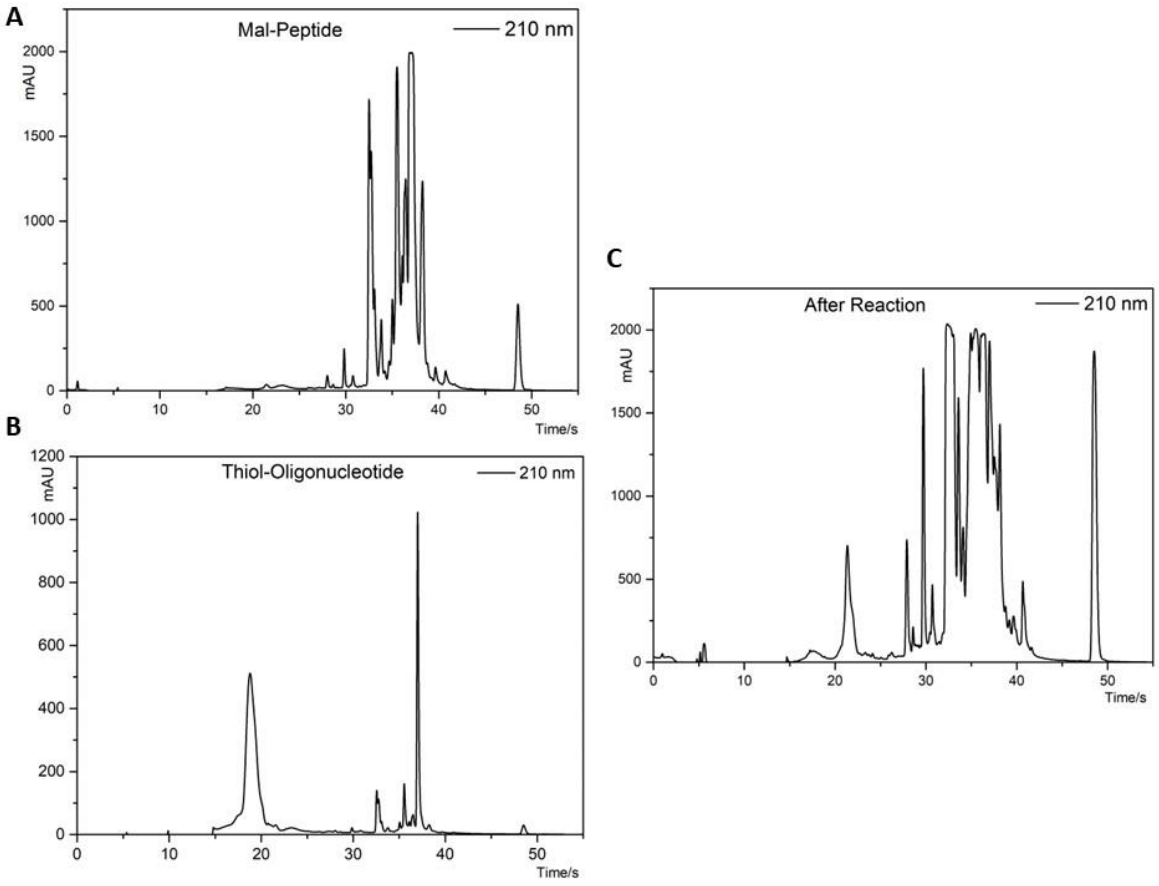

Figure 6-7 (A) The HPLC of Mal-peptide (B) The HPLC of Thiol-oligo (C) The HPLC of productor

after the reaction

The samples from HPLC at 16-18 minutes and 21-23 minutes were first assessed by UV. UV is a commonly used method for determining oligonucleotide amount and purity, and for measuring pairing based on the hyperchromic effect. The nanodrop UV was used because it allows UV measurement in a small volume of only 1 uL, which is ideal for the small reaction sample. The samples were measured by UV twice: firstly when they are freeze-dried and re-dissolved into 50 uL, and then after they are dialysed to remove salt and solvent from HPLC. The UV results indicated improved purification after dialysis. The 260/230 ratio was around 1.450 in both collected samples before dialysis but increased to 1.590 and 1.618 in the 16-18- and 21-23-minute samples, respectively, after dialysis. However, the predicted oligonucleotide concentration dropped in the 16–18-minute sample, suggesting that unreacted oligo was present which was lost in the dialysis. However, the conjugate's molecular weight was too high to be lost through dialysis. In contrast, the 21–23-minute sample maintained its value stability, indicating it was the target product.

6.3.3 Characterisation

Traditionally, NMR is widely used to assess the success of reactions [18]. This is done by monitoring changes in signals from reactive groups. If the signal from the reaction site group disappears after the reaction, it indicates that the reaction has proceeded as designed. Figure 6.8 displays the NMR spectra of unreacted Mal-Pep, Thiol-Oligo, and the conjugate (sample collected at 21-23 minutes and cleaned by dialysis). The experiment focused on the signal at 6.7 ppm [19], which corresponded to the double bond in the maleimide ring and reacts with the sulfur atom in thiol. The absence of this peak in the conjugate's spectrum indicates that the maleimide group has reacted and the reaction was successful.

Additionally, besides the maleimide group, the Mal-peptide NMR spectrum showed peaks between 1 and 4 ppm and around 7 ppm, which correspond to the backbone of the peptide (W10). At the same time, the thiol-oligonucleotide NMR spectrum also revealed signals between 1 and 4 ppm, attributed to the backbone of the oligonucleotide. Since both the peptide and oligonucleotide showed signals in this area, these peaks were not used for structure identification in the experiment. Conversely, the most critical signal of the Thiol-oligonucleotide spectrum was the one between 7 and 9 ppm, which corresponded to the base pairs and proves the presence of the oligonucleotide. In the conjugate spectrum, the signal around 7 ppm was still present, coming from the peptide backbone. However, the signal from the oligonucleotide base pairs was not seen, due to the low concentration of oligonucleotide after the reaction. A series of NMR spectra for Thiol-oligonucleotide at different concentrations between 0.1 to 2 umol/ml are shown in Figure 6.9. The oligonucleotide signal was detected in the 2 umol/ml sample, weakened in the 1 umol/ml sample, and cannot be seen in the 0.1 umol/ml sample. The threshold for detecting the signal was 0.2 umol/ml. The conjugate after purification had a concentration of 0.08 umol/ml, lower than the signal threshold.

In short, the NMR result gave a strong suggestion about the success of the reaction. However, the shortcoming of oligonucleotide signals after the reaction has driven the further characterisation of the conjugate.

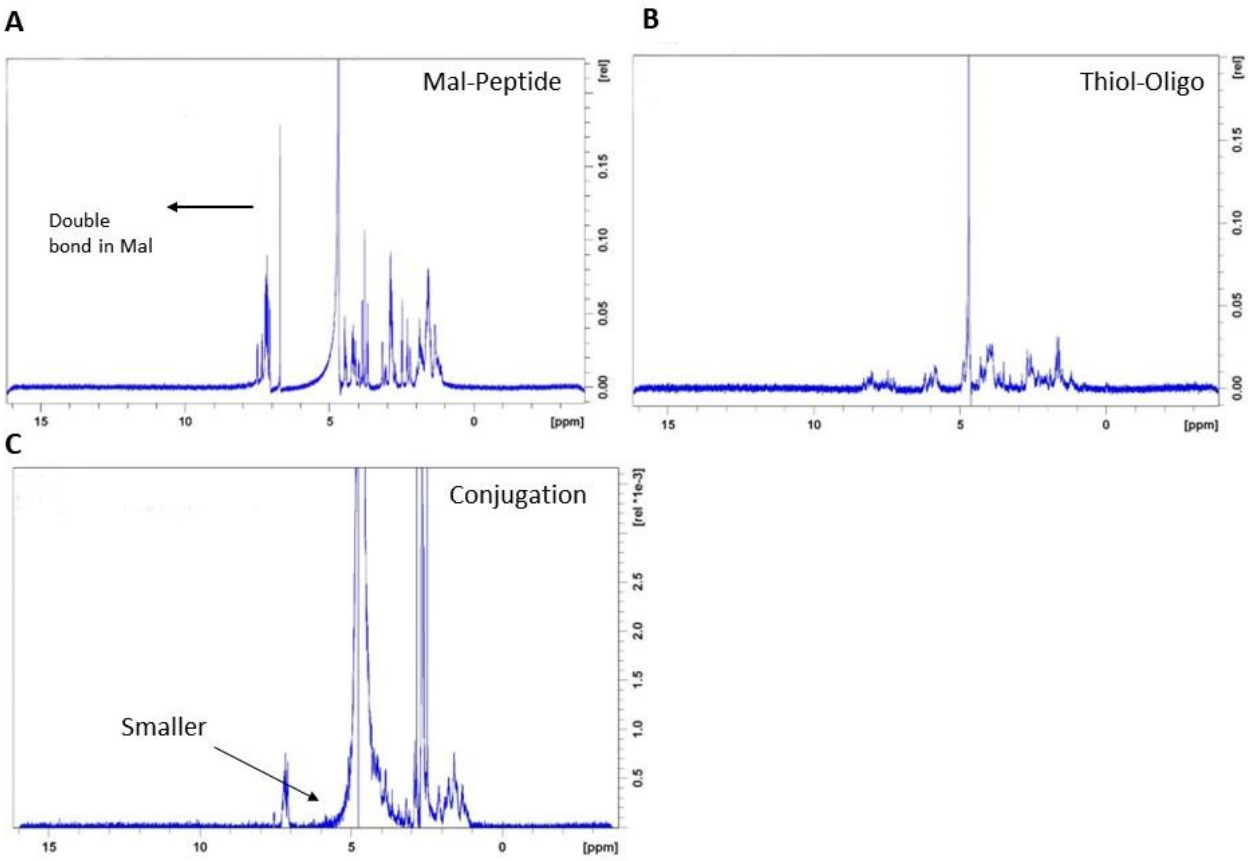

Figure 6-8 (A) The NMR of unreacted Mal-peptide (B) The NMR of unreacted Thiol-oligo (C)

The NMR of cleaned conjugate (collected from 21-23 mins)

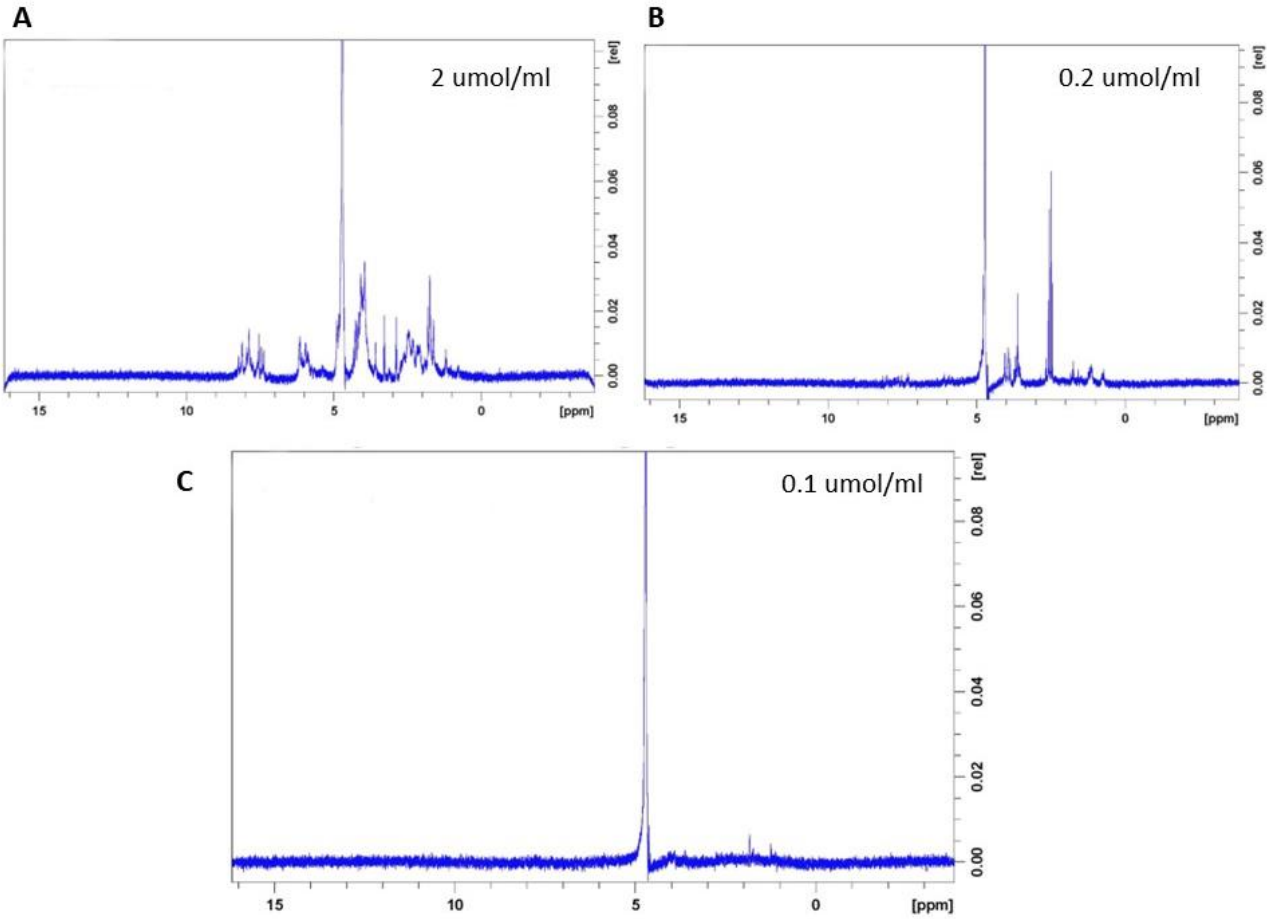

Figure 6-9 The NMR spectrum of thiol-oligonucleotide in 2, 1, 0.2, 0.1 umol/ml

Due to the unsatisfactory results seen in the NMR spectra, the separated samples were analysed using MALDI-TOF mass spectrometry (Figure 6.10) to verify successful oligo-peptide linking. In the mass spectrum, the peak with the highest mass-to-charge ratio (m/z) corresponded to the molecular weight of the sample, as typically only one charge is present in the sample. The advantage of MS is that it easily assesses the success of the reaction by comparing the signal and molecular weight of target molecules. The sample collected between 21-23 minutes showed a signal with the highest m/z of 6731, which was consistent with the estimated molecular weight of the targeted conjugate. The molecular weight of the thiol-modified oligonucleotide (A16, 16 bp) is 5125, while the maleimide peptide (10 amino acids) is 1607, with 97 from the maleimide group. The estimated molecular weight is 6732 m/z, with a shortcoming of 1 Dalton attributed to the

diproton of the carboxyl group in the side chain of glutamic acid and C terminal. The sample collected between 16-18 minutes did not show a peak of this value. The spectrum also revealed information on oligo fragments, including an 11 bp fragment (AGGCGCCTTTA) at 3357 and a five bp fragment (GCTAA-SH) at 1670. The MS results confirmed that the sample collected at 21-23 minutes was the target conjugate and that the reaction was completed successfully.

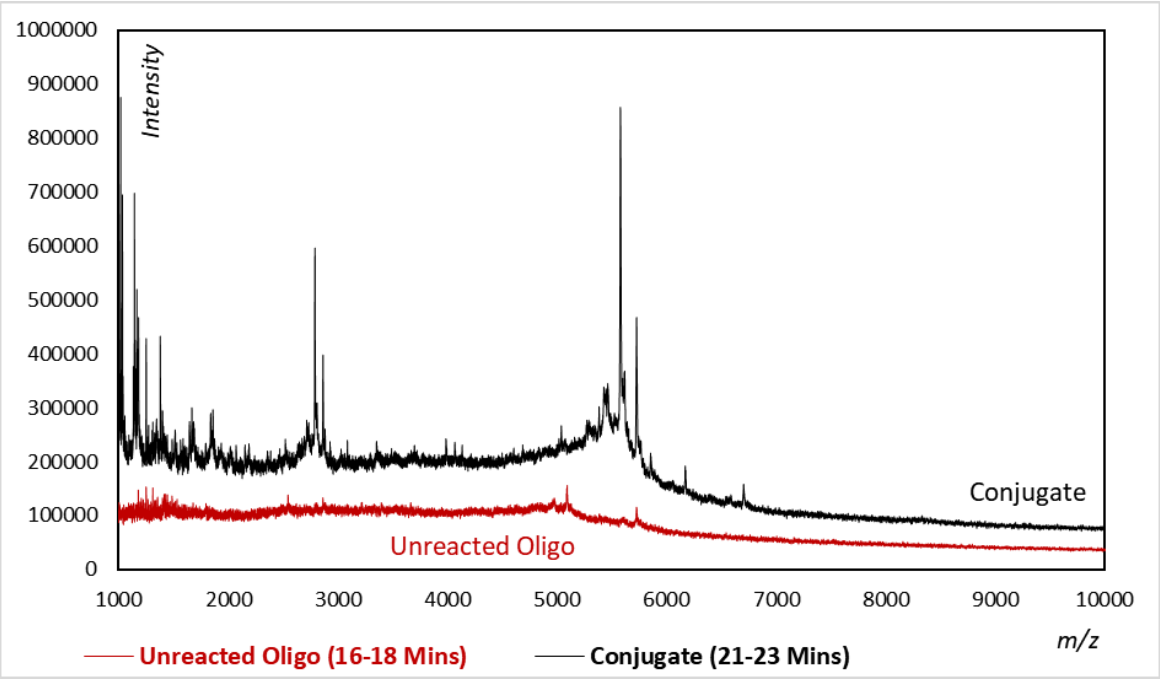

Figure 6-10 The MALDI-TOF Mass Spectrum of conjugate sample (collected between 21-23 mins, black) and Unreacted Oligo (collected between 16-18 mins, red)

Besides, to reveal the microstructure of the produced conjugate, the sample was analysed by FITR, shown in figure 6.11. In the Mal-peptide spectrum, the peaks at 1709 and 1208 cm^{-1} were crucial, arising from the C=O and -C-O-C- bonds in the maleimide group [20]. The signal can indicate whether the reaction is done or not. These two bonds were absent in the conjugate's spectrum, confirming the reaction between the maleimide group and the thiol group. The peaks at 1512-1567 cm^{-1} and 1640-1673 cm^{-1} in the Mal-peptide spectrum were also evident, representing amide II and amide I, respectively. These peaks were also present in the conjugate spectrum but with

weaker intensity, proving the presence of the peptide in the conjugate. The unreacted oligonucleotide's spectrum did not show these peaks, indicating the absence of peptides. The dominant peak at 1100 cm^{-1} in the unreacted oligo spectrum was attributed to the phosphate group in the oligonucleotide. Fortunately, the critical bond in oligonucleotide was also kept in the conjugate spectrum. The conjugate's spectrum included the bond for amide I, II and the phosphate group but without the maleimide group. It is believed to the evidence for the success of the conjugate reaction.

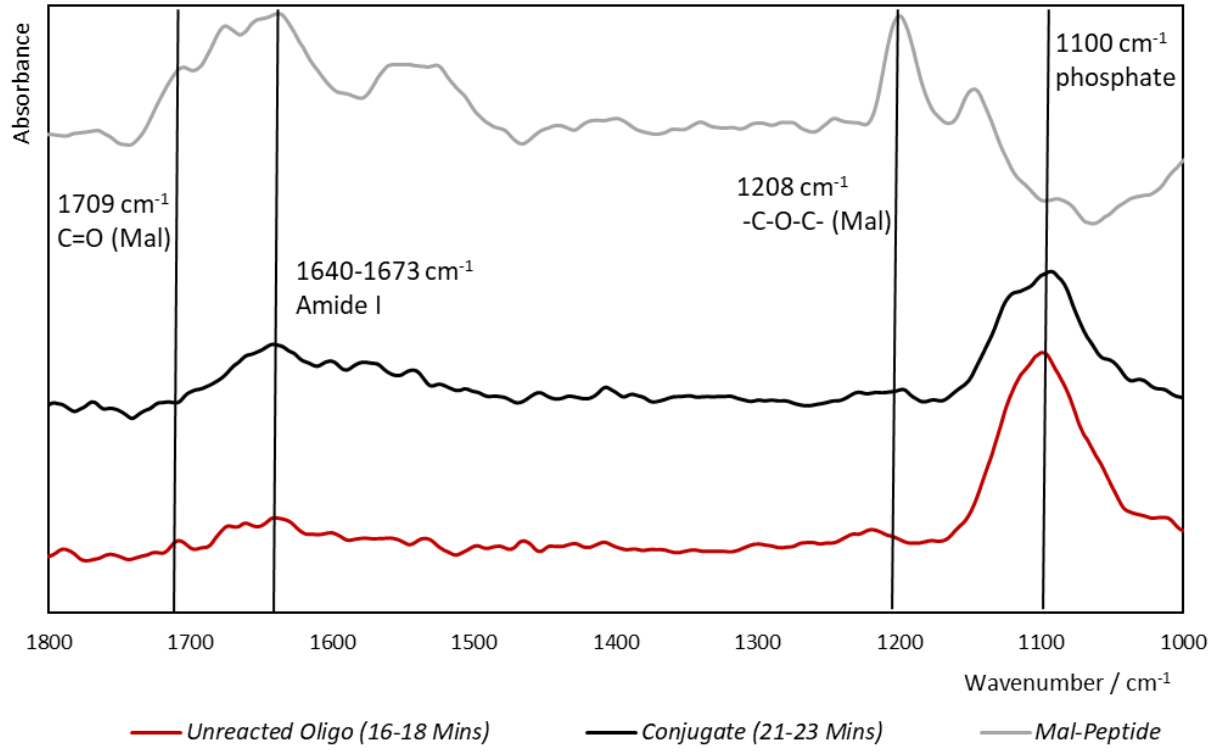

Figure 6-11 The FTIR spectra of conjugate sample (collected between 21-23 mins, black), Unreacted Oligo (collected between 16-18 mins, red) and Mal-peptide (grey)

6.3.4 Hydrogel Preparation

After the confirmation of the conjugation reaction, the next step in this experiment is to prepare the hybrid hydrogel. Before mixing, the complementary pairing of the conjugate and free oligonucleotide must be evaluated using Nanodrop UV based on the hyperchromic effect. Results

are shown in Table 6.1. Both the conjugate and linker were measured at UV 260 nm absorbance at room temperature. The samples were then heated above the melting point (to 45°C), breaking the pairing. If an increase in absorbance is observed after heating, it indicates the double strands have transformed into single strands, proving that the samples were in double-strand form at room temperature. The table shows that the OD 260 of both the conjugate and linker increased rapidly after heating, confirming their double-strand structure at room temperature. When the linker and conjugate were combined, the absorbance reached 118.562, which was lower than the average absorbance of the separate linker and conjugate, proving the pairing between the two. However, the results cannot determine whether the pairing is cross-linked between the conjugate and linker or only within the linker itself, requiring further rheology comparison to be conducted.

Table 6-1 The OD260, 260/280, 260/230 for conjugate, free oligonucleotide linker and their blending samples

Sample	OD 260 nm	260/280	260/230
Conjugate-ds	1.984	1.666	1.313
Conjugate-ss	4.104	1.682	1.323
Linker-ds	354.899	1.624	2.380
Linker-ss	426.153	1.622	2.402
Conjugate + Linker	118.562	1.661	2.338

In the rheology test, the experiment's primary goal of improving hydrogel stiffness was verified. The results also provided evidence of the oligonucleotide pairing between the linker and conjugate in the hydrogel. The value is given in Figure 6.12. Adding conjugate decreased the storage modulus of pure KF8K peptide samples due to the interference from the conjugate charge

on peptide assembly and the lack of linker-assisted pairing. The gap between peptide fibres was over the length of single oligonucleotides. The sample with a linker showed stiffness improvement with different ratios of the peptide to the oligo linker, with the improvement increasing with more oligo linkers. However, there still was a limitation in the mixture ratio. The threshold for blending was at 1:20 where the peptide starts to precipitate. The presence of conjugate enhanced the storage modulus, proving the pairing was between conjugate and linker, not linker and linker. Blending peptide hydrogel with both linker and conjugate resulted in over 2 times increase in storage modulus for a 1:40 ratio, 75% improvement for 1:80, and 50% for 1:160, suggesting successful optimisation of mechanical properties.

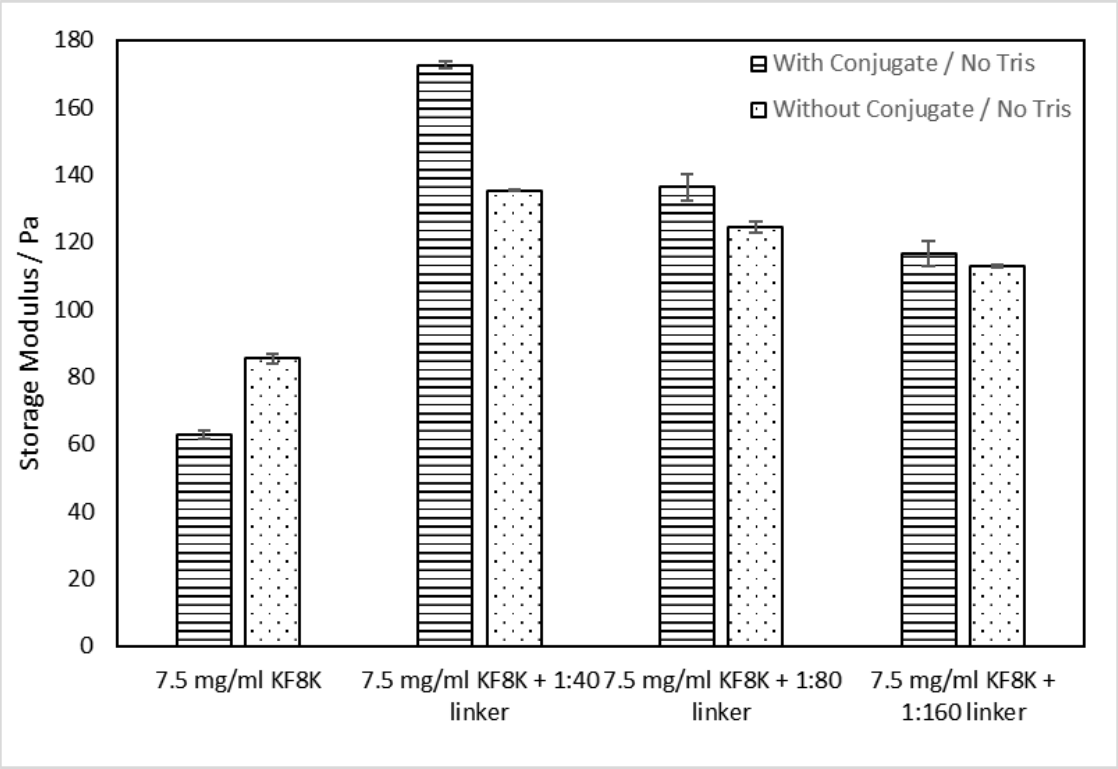

Figure 6.12 The storage Modulus of 7.5 mg/ml KF8K and its hybrid samples with or without conjugate

According to the literature, tris buffer is commonly used in helping the formation of double strands in DNA [21]. However, it can interfere the self-assembly of KF8K peptides by masking

electrostatic forces with high ion concentrations. The comparison between hydrogels with and without tris buffer was made and the results in Figure 6.13 suggest both peptide and peptide-oligonucleotide hybrid hydrogels perform better without tris buffer. This is due to the self-assembly of peptides dominating the hydrogel with oligonucleotides serving as auxiliary connections. Tris buffer helps with oligonucleotide pairing but hinders peptide self-assembly.

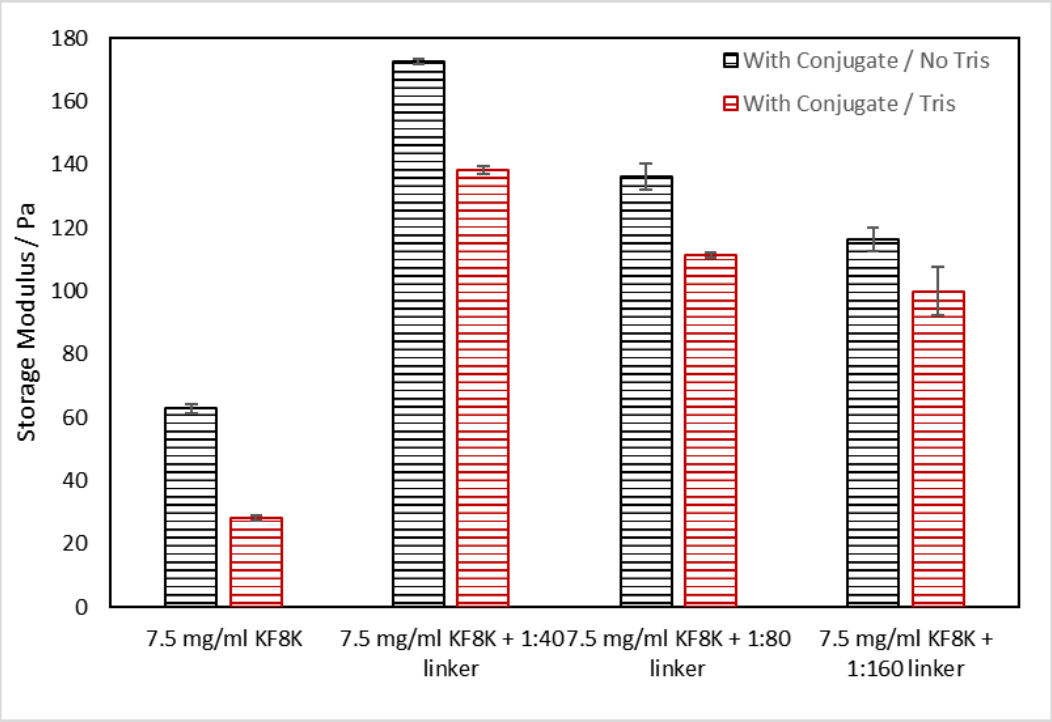

Figure 6.13 The storage Modulus of 7.5 mg/ml KF8K and its oligonucleotide-containing hybrid samples with or without tris buffer

6.4 Conclusion

In conclusion, the hybrid self-assembly peptide and oligonucleotide hydrogel was successfully prepared with improved and controllable stiffness. The peptide fibre of this hydrogel was connected by an oligonucleotide. The oligonucleotide-peptide conjugate was used to connect the self-assembly fibres. The conjugate was produced through a thiol-maleimide click reaction.

The results of this study suggest that the self-assembly of the two biological macromolecules

was not compromised after reaction and blending. They were compatible with each other to form a hydrogel under the designed mixing ratio. Furthermore, the combination of the two networks resulted in increased stiffness, and the storage modulus can be controlled by adjusting the proportion of conjugate and linker oligonucleotide.

However, there are still unsatisfactory results needing further work. For instance, the conjugate structure needed better characterisation in the NMR spectrum. And the reaction yield was lower than predicted. The shortcoming encourages more optimisation in the reaction process. Additionally, in future, more imaging and characterisation would be helpful to expose the hydrogel structure better. It includes the micro imaging (TEM) of the oligonucleotide chain as well as the characterisation of the oligonucleotide network.

Reference

[1] Hivare P, Gangrade A, Swarup G, et al. Peptide functionalized DNA hydrogel enhances neuroblastoma cell growth and differentiation. Nanoscale, 2022, 14(24): 8611-8620.

[2] Li F, Tang J, Geng J, et al. Polymeric DNA hydrogel: Design, synthesis and applications. Progress in Polymer Science, 2019, 98: 101163.

[3] McLaughlin C K, Hamblin G D, Sleiman H F. Supramolecular DNA assembly. Chemical Society Reviews, 2011, 40(12): 5647-5656.

[4] Si Y, Li L, Wang N, et al. Oligonucleotide cross-linked hydrogel for recognition and quantitation of microRNAs based on a portable glucometer readout. ACS applied materials & interfaces, 2019, 11(8): 7792-7799.

[5] Liu J. Oligonucleotide-functionalized hydrogels as stimuli responsive materials and biosensors. Soft Matter, 2011, 7(15): 6757-6767.

[6] Winfree E, Liu F, Wenzler L A, et al. Design and self-assembly of two-dimensional DNA crystals. Nature, 1998, 394(6693): 539-544.

[7] Cheng E, Xing Y, Chen P, et al. A pH-triggered, fast-responding DNA hydrogel. Angewandte Chemie International Edition, 2009, 48(41): 7660-7663.

[8] Chhabra R, Sharma J, Liu Y, et al. DNA self-assembly for nanomedicine. Advanced drug delivery reviews, 2010, 62(6): 617-625.

[9] Shao Y, Jia H, Cao T, et al. Supramolecular hydrogels based on DNA self-assembly. Accounts of chemical research, 2017, 50(4): 659-668.

[10] Li C, Faulkner-Jones A, Dun A R, et al. Rapid formation of a supramolecular polypeptide–DNA hydrogel for in situ three-dimensional multilayer bioprinting. Angewandte Chemie International Edition, 2015, 54(13): 3957-3961.

[11] Tang H, Duan X, Feng X, et al. Fluorescent DNA–poly (phenylenevinylene) hybrid hydrogels for monitoring drug release. Chemical communications, 2009 (6): 641-643.

[12] Yan L, Zhu Z, Zou Y, et al. Target-responsive “sweet” hydrogel with glucometer readout for portable and quantitative detection of non-glucose targets. Journal of the American Chemical Society, 2013, 135(10): 3748-3751.

[13] Wu Y, Li C, Boldt F, et al. Programmable protein–DNA hybrid hydrogels for the immobilization and release of functional proteins. Chemical communications, 2014, 50(93): 14620-14622.

[14] Demers L M, Mirkin C A, Mucic R C, et al. A fluorescence-based method for determining the surface coverage and hybridization efficiency of thiol-capped oligonucleotides bound to gold thin films and nanoparticles. Analytical chemistry, 2000, 72(22): 5535-5541.

[16] Burns J A, Butler J C, Moran J, et al. Selective reduction of disulfides by tris (2-carboxyethyl) phosphine. The Journal of Organic Chemistry, 1991, 56(8): 2648-2650.

[17] Maximillian T W. A mild TCEP-based para-azidobenzyl cleavage strategy to transform reversible cysteine thiol labelling reagents into irreversible conjugates. Chemical Communications, 2015, 51(25): 5279-5282.

[18] Dispinar T, Sanyal R, Sanyal A. A Diels-Alder/retro Diels-Alder strategy to synthesize polymers bearing maleimide side chains. Journal of Polymer Science Part A: Polymer Chemistry, 2007, 45(20): 4545-4551

[19] Gomez M V, de la Hoz A. NMR reaction monitoring in flow synthesis. Beilstein journal of organic chemistry, 2017, 13(1): 285-300.

[20] Vermeesch I M, Groeninckx G, Coleman M M. Poly (styrene-co-N-maleimide) copolymers: preparation by reactive extrusion, molecular characterization by FTIR, and use in blends. Macromolecules, 1993, 26(24): 6643-6649.

[21] Kejnovsky E, Kypr J. Tris buffer protects DNA backbone against breakage upon irradiation with ultraviolet light. General Physiology and Biophysics, 1993, 12: 317-317.

7. Chapter 7. Conclusion

7.1 General Conclusion

In summary, three different types of double network hydrogels were prepared successfully by three different design strategies. The primary aim, improved and controllable stiffness, was well achieved in the three hybrid hydrogels. The opposite chirality SAP, gelatin and oligonucleotide showed excellent compatibility with self-assembly peptides without interference in the hydrogelation process. The β-sheet from SAP was proved unchanged in three hybrid hydrogels.

Meanwhile, the critical structure of gelatin (triple helix) and oligonucleotide (helix structure) were also observed after blending.

The opposite chirality SAPs blending hybrid hydrogel was designed for a hydrogel with homogeneous macro-properties, for example, mechanical properties, but separately assembled monomers.

D-KF8K presented high similarity in mechanical properties and micro-structure to the L-KF8K except for the chirality. B-sheet was observed in FTIR, CD and XRD. On the contrary, the two peptides assembled to fibres separately in the blending hydrogel which was evidenced by the FITC fluorescent quenching reaction. A clear quenching percentage change was measured in L- and D-KF8K blending hydrogel compared to pure L-KF8K hydrogel. The similar but separately assembled hydrogel gives accessibility to accumulate target functional groups in a designed specific area in a homogeneous stiffness hydrogel.

In terms of gelatin-SAP hybrid hydrogel, the gelatin and SAP formed networks successfully. The β-sheet and triple helix were kept in the hybrid hydrogel. A strong enhancement in stiffness was achieved which is attributed to the interaction between the gelatin network and peptide fibres. A large amount of peptide fibre clusters was observed which hold several times wider diameters than single peptide fibres. Additionally, the temperature sensitivity from gelatin and the recoverability from SAP were also kept and combined in the hybrid hydrogel together. Therefore, the hybrid hydrogel showed promising prospects as the ink for 3D printing.

Finally, the oligonucleotide-peptide hybrid hydrogel was also established. The reaction connected the peptide and oligonucleotide producing the conjugate, which played the role of linking the peptide and oligonucleotide together. The hybrid hydrogel exhibited a strong stiffness

enhancement compared to pure peptide hydrogel. Besides, the hydrogel was also regarded as a two-step crosslinking hydrogel which formed a weaker hydrogel firstly for the designed target and strengthens later.

7.2 Future Work

In future, β-amino acid is a potential candidate to replace D-amino acid producing DN hydrogel [1]. Its extra carbon in the backbone may interfere with the hydrogen bonds with α-amino acids in the β-sheet. β-amino acids are relatively rare in nature, but have been synthesised and studied for their potential as drug delivery molecules, and as precursors to other compounds [2]. The unique properties of β-amino acids, such as their conformational rigidity and reduced tendency to form hydrogen bonds, make them useful in the development of new pharmacologically active compounds. β-amino acid is accepted to cause the separate assembly with α-amino acids. Another strategy is blending D-amino acids and L-amino acids hybrid peptides into the D-peptide and L-peptides. The hybrid peptide can work as the adapter to connect the D- and L-peptide fibres. Therefore, the hydrogel whose fibre consists of opposite chirality peptide blocks is possible to be produced.

On the other hand, modified gelatine has also been proposed as the potential candidate to establish the double-network hydrogels with self-assembly peptide. Gelatin methacryloyl (GelMA) is one of the examples. The methacryloyl group in GelMA l can be polymerized with other monomers to form a three-dimensional network, which gives the resulting hydrogel its gel-like properties. The use of GelMA in these applications takes advantage of the biocompatibility and biodegradability of gelatin [3], as well as the ability to manipulate its mechanical and swelling properties through the crosslinking process.

Reference

[1] Wei J, Zhu L, Lu Q, et al. Recent progress and applications of poly (beta amino esters)-based biomaterials. Journal of Controlled Release, 2023, 354: 337-353.

[2] Zhang X X, Gao Y, Hu X S, et al. Recent Advances in Catalytic Enantioselective Synthesis of Fluorinated α-and β-Amino Acids. Advanced Synthesis & Catalysis, 2020, 362(22): 4763-4793.

[3] Amonpattaratkit P, Khunmanee S, Kim D H, et al. Synthesis and characterization of gelatin-based crosslinkers for the fabrication of superabsorbent hydrogels. Materials, 2017, 10(7): 826.

Supplement documents

S.1 Method

RP-HPLC

The HPLC model is a Dionex® Ultimate 3000 Reversed Phase HPLC. The solvent are HPLC water + 0.1% trifluoroacetic acid (TFA) (solvent A) and acetonitrile (ACN)+ 0.1% TFA (solvent B) while the stationary phase is the C12 column. The column model was Jupiter Proteo 90 Å C12 (non-polar) and the size was 250×10.0 mm.

All samples were injected 0.05 ml. The elution gradient starts at 95 solvent A (5% solvent B) to 65% solvent A (35% solvent B) during 60 minutes.

S.2 Figures

Table S-0-1 Elementary analysis result for purchased KF8K peptide purification

Element	Expected	Found	Charge
C	61.47%	51.46% ± 3.22%	-
H	7.04%	6.15% ± 0.86%	-
N	13.45%	10.21% ± 0.77%	-
Cl	0.00%	0.00% ± 0.00%	-

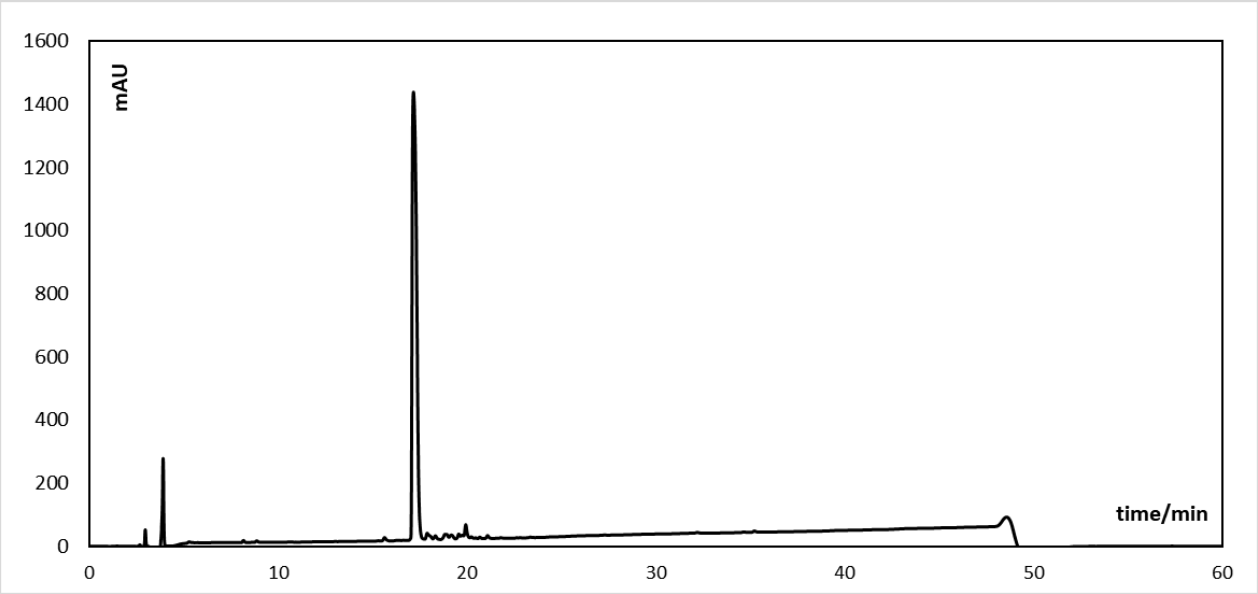

Figure S-0-1 HPLC test result for purchased KF8K peptide purification

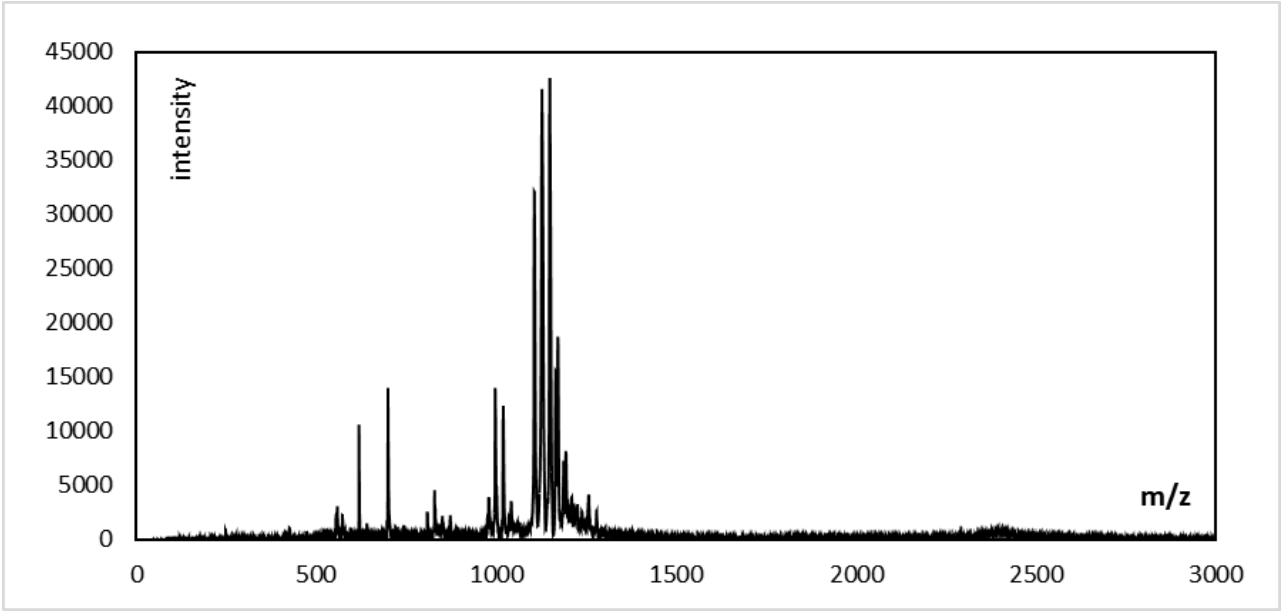

Figure S-0-2 MALDI test result for purchased KF8K peptide purification